Numerical simulations on the dynamics of charged particles in the inner magnetosphere associated with a magnetic storm

by

Yusuke EBIHARA

MARCH 1999

Department of Polar Research,

the Graduate University for Advanced Studies

Contents

Figure contents

Table contents

Acknowledgement

I would like to express my thanks to Prof. Masaki Ejiri for his valuable instruction and guidance on this work. I am most grateful for having had the opportunity to study under his guidance.

Thanks are also due to all the staffs of Department of Polar Science, the Graduate University for Advanced Studies and Upper Atmosphere Physics division of National Institute of Polar Research, Prof. Takeo Hirasawa, Prof. Takehiko Aso, Prof. Natsuo Sato, Dr. Hiroshi Miyaoka, Dr. Hisao Yamagishi, Dr. Makoto Taguchi, Mr. Akira Kadokura, Mr. Akira Yukimatsu, Dr. Masaki Okada, Dr. Masayuki Kikuchi, and Dr. Masaki Tutsumi for their helpful discussions and many suggestions.

I gratefully acknowledge helpful discussions and comments with Prof. Toshifumi Mukai at ISAS and Prof. Toshio Terasawa at University of Tokyo on the relation between the solar wind and the plasma sheet density. The GEOTAIL/LEP momentum data sets provided by the GEOTAIL/LEP team have been used in this dissertation. I wish to thank Prof. Toshifumi Mukai, all members of the GEOTAIL/LEP team and the whole GEOTAIL community, who provided valuable data sets.

The numerical simulation was carried out at Information Science Center (ISC), National

Institute of Polar Research. I would like to thank all the staffs of ISC, especially Dr. Masaki Okada and Mr. Yasukazu Suzuki who have maintained the computer system of ISC and I thank them for their efforts.

I used the solar wind and the IMF data sets observed by the MFI and SWE instruments aboard WIND satellite through the ISTP Key Parameters. I am grateful to the PIs, Dr. R. Lepping and Dr. K. Ogilvie, for the permission to use the data sets. The provisional and final Dst indices were provided from the WDC-C2 for Geomagnetism, Kyoto University.

Preface

This dissertation is concerned with the study of the dynamic behavior of the energetic charged particles trapped by the earth's magnetic field in the inner magnetosphere associated with magnetic storms. The magnetosphere is defined as the near-earth space environment inside which the geomagnetic field are confined.

After the discovery in 1958 that the earth is surrounded by energetic charged particles known to be *Van-Allen radiation belts*, many direct observations in geospace by sounding rockets and artificial satellites have given us knowledge about the dynamic feature in the magnetosphere.

One of drastic phenomena in the magnetosphere, *magnetic storms*, is noticeable for a long time because magnetograms at equatorial latitudes are unusually disturbed during a magnetic storm. The cause is the existence of the ring current flowing at altitudes of ~20000 - 30000 km. The ring current mainly consists of trapped energetic ions. During a magnetic storm, abundant energetic ions are injected into the ring current and the ions dissipate within a few days. Although many ground and satellite observations have been carried out, the whole physical mechanism of the magnetic storm and related phenomena are still open questions.

The primary purpose of this dissertation is to examine the dynamic behavior of trapped charged particles in the inner magnetosphere associated with a magnetic storm by the newly developed numerical simulation scheme; it seems to be essential to understand the physical process concerned with the magnetic storm.

In Chapter 1, a general introduction is described toward the objects of this dissertation.

In Chapter 2, the dynamic behavior of charged particles in the inner magnetosphere is reviewed. The inner magnetosphere can be categorized into several regions by their characteristic behavior; (1) the plasmasphere where the cold and dense plasma is filled, (2) the ring current where particles that most contribute to the energy density in the inner magnetosphere are trapped, and (3) the radiation belt where relativistic particles are trapped. In addition to the basic concepts of the regions, the motion of charged particles and the particle's differential flux are also described.

In Chapter 3, the Coulomb collision loss of ions in the inner magnetosphere is dealt with. To evaluate the Coulomb collision loss effect on the ring current ions, the time-dependent three-dimensional plasmaspheric model is newly constructed. The calculated plasma density is evaluated with the result observed by the EXOS-B satellite and the result of the calculation is in good agreement with the observed one. Using this plasmaspheric model, the spatial variation of the loss lifetime of the ions is calculated. As an application, decay of storm-time energy density (plasma pressure) due to the Coulomb collision loss of ions is examined for a particular storm. The other major loss process, charge exchange loss with neutral hydrogen, is also compared with the Coulomb collision loss. These calculation and evaluation are basically important for the ring current dissipation.

In Chapter 4, an enhancement of the differential flux of ions accompanied with a characteristic energy dispersion structure (so-called 'nose' structure) observed by the Explorer 45 satellite is investigated. The calculated differential flux is compared with that observed. The source distribution function and an induction electric field that causes the flux enhancement are derived from the numerical simulation. The inferred distribution function in the near-earth plasma sheet is consistent with the statistical results made by direct satellite observations.

In Chapter 5, a model that deals with the ring current buildup and its decay depending on the solar wind density and the interplanetary magnetic field (IMF) is developed. A first attempt to calculate the magnetic disturbance due to the ring current by the Biot-Savart integral over the whole three-dimensional distribution of the calculated current density, without using the Dessler-Parker-Scopke relation, is made. At first, the relation between the solar wind and the plasma sheet (as a direct source of the ring current) densities is statistically examined; they are well correlated. Next, the magnetic disturbance induced by the calculated current density (ring current) is compared with the observed one for particular storms in April 1997. Furthermore, the following items are discussed; (1) the energy injection rate from the near-earth plasma sheet into the ring current, (2) dependence of corrected Dst on the plasma sheet temperature, (3) electric current distribution of the ring current, (4) effects of charge exchange loss, (5) energy composition of the pressure, (6) response time of the plasma sheet density to the solar wind density, (7) the relation of total kinetic energy of the ring current ions, and (8) a diamagnetic effect of the ring current.

Unless otherwise mentioned MKS unit is used throughout this dissertation.

Chapter 1

General introduction

1.1 Discovery of the ring current

Dynamics of charged particles in the earth's magnetosphere is one of major topics of space physics. Many particles having various energies and pitch angles are trapped by the earth's dipolar magnetic field in the region of <8 earth radii. Existence of the charged particles trapped by the earth's magnetic field had been predicted by theories and unusual variations appeared in magnetograms on earth's surface before the so-called space age. After the discovery in 1958 that the earth is surrounded by energetic charged particles known to be *Van-Allen radiation belts*, many direct observations in geospace by sounding rockets and artificial satellites have given us knowledge about the dynamic feature of the geospace and related phenomena, e.g, *geomagnetic storms* and *auroras*.

In early 1960's, the feature of the ring current was revealed by satellites which observed the charged particles and the magnetic fields. Using a modeled pressure distribution having

a Gaussian type distribution along an equatorial radius, so-called V_3 model deduced from the magnetic perturbation in the equatorial plane observed by Explorer 6, *Akasofu and Chapmen* [1961] and *Akasofu et al.* [1961] inferred the ring current distributions that flow westward in the outer region and eastward in the inner region in a meridian plane. *Hoffman and Bracken* [1965] applied the observed ion energy spectra with energies above 100 keV by Explorer 12 to the *Akasofu and Chapmen* [1961]'s model, and they calculated the current distribution for the quiet time ring current. Moreover *Hoffman and Bracken* [1967] included the self-consistency in the current calculation.

1.2 Flux enhancements associated with storm/substorm

During a magnetic storm, it has been observed that the particle fluxes of the ring current drastically enhanced. Using the result of the OGO 3 particle observations, *Frank* [1967] found the proton flux with energies 31-49 keV increased by factors above 30 over the prestorm intensities during a magnetic storm at $L = 3.5$ near the equatorial region; they suggested that the total energy of these protons with energies 3-50 keV within the earth's magnetosphere is sufficient to account for the depression of the Dst index.

Detectors aboard Explorer 45 (S^3-A) provided the first total ion and electron energy density measurements in the equatorial region from 2.5 to 5.5 Re [*Longanecker and Hoffman*, 1973]. *Smith and Hoffman* [1973] showed that the storm-time ring current constitutes an enormous enhancement of protons in the energy range 10-120 keV. *Berko et al.* [1975] calculated the distortion magnetic field deduced from the proton's distribution. They compared with the direct measurement of the magnetic field and they concluded that protons

with energies 1-872 keV can account for the observed ring current magnetic field in the equatorial region for a particular storm.

Smith and Hoffman [1973] found that during a main phase of the storm, additional injections of protons related to substorms were observed, i.e., they were superposed on the gradual increase in proton energy density. The characteristic features of this additional enhancement in the evening region are consistent with flow patterns resulting from a combination of inward convection, corotation and gradient-curvature drift motion, being carried from the plasma sheet into the inner region; this features are accompanied with the nose structure in the observed E-t (energy versus time) spectrograms [*Smith and Hoffman*, 1974]. Using McIlwain's electric field model $E3$, *Konradi et al.* [1975] backtracked protons of the nose structure observed by Explorer 45 and they concluded that the protons came from beyond the McIlwain's injection boundary [*McIlwain*, 1961] located at

$$R_b = \frac{122 - 10Kp}{\phi - 7.3}, \tag{1.1}$$

where R_b and ϕ are a geocentric distance of the injection boundary in earth radii and magnetic local time in hour, respectively. However, the injection boundary in the morning quadrant that they estimated from the McIlwain's boundary by reflecting from the afternoon quadrant is debatable because the reflected boundary may have no physical meaning.

Chen [1970], *Grebowsky and Chen* [1975], and *Cowley and Ashour-Abdalla* [1976] predicted the forbidden regions of newly injected particles under the steady convection field to interpret the nose dispersion structure. They showed that the steady state ion drift trajectories depending on their energies and pitch angles lead to a 'nose' structure. How-

ever, comparison of these results with Explorer 45 data showed that the calculated 'nose' locations appear at lower L value region than those observed. *Cowley* [1976] argued that particle's strong pitch angle diffusion might limit inward penetration of particles.

Ejiri [1978] and *Ejiri et al.* [1980] succeeded to reconstruct the nose dispersion observed by Explorer 45 by tracing particles having various energies and pitch angles under their basic concept that the 'nose' structure is caused by a temporal enhanced convection field: First the plasma sheet plasma is convected from the tail region toward the earth primarily in the radial direction with little energy and pitch angle dispersion under a weak convection (first stage). Following the convection enhancement (second stage), this population moves further toward the earth and begins dispersing with energy and pitch angle. They noted that the appearance of the nose dispersion is essentially arising from the time-dependent particles' trajectories. So far, the appearance of the 'nose' structure has been studied by a single particle tracing scheme. It seems to be essential for quantitative understanding the 'nose' structure to investigate the enhancement of the differential flux that constitutes the 'nose' structure. One can also speculate the source distribution function in the near-earth plasma sheet that causes the 'nose' dispersion structure. In Chapter 4, the differential flux enhancement accompanied with the 'nose' structure is quantitatively examined by the numerical simulation.

1.3 Decay of the ring current ions

The decay of the ring current is also one of significant topics. Historically, the ring current decay is estimated by the energy balance equations [e.g. *Gonzalez et al.*, 1994 for

review] as

$$\frac{dE(t)}{dt} = U(t) - E(t)/\tau, \tag{1.2}$$

where $E(t), U(t)$ and τ are the total energy of the ring current particles, the energy input rate into the ring current, and the decay time, respectively. Since the total energy of the ring current E is considered to correlate linearly with the corrected Dst index (Dst*) [*Dessler and Parker*, 1959; *Sckopke*, 1966], Eq.(1.2) can be rewritten as

$$\frac{d\mathrm{Dst^*(t)}}{dt} = U'(t) - \mathrm{Dst^*}(t)/\tau. \tag{1.3}$$

Although the typical τ value is 5-10 hours during a typical recovery phase of storms [e.g. *Gonzalez et al.*, 1994], the τ value has not been determined exactly; it is natural because the decay time constant τ depends on the energy, pitch angle and location of ions of the ring current.

Thus to accumulate each ions's loss effect is essential to investigate the ring current decay. Previously, four major loss processes are proposed for decay of the ions constituting the ring current as listed below:

1. *Convection outflow.* Particles transported by the large-scale convection field flow sunward. The particles that encounter the dayside magnetopause may be lost [e.g., *Takahashi et al.*, 1990; *Ebihara et al.*, 1998b].

2. *Charge exchange with neutral hydrogen.* The neutral hydrogen exists steadily with the density of $\sim$700 $\mathrm{cm^{-3}}$ at a geocentric distance of 3 Re and $\sim$300 $\mathrm{cm^{-3}}$ at 4 Re

[*Rairden et al.*, 1986]. A proton exchanges its charge with the neutral hydrogen as $H^+ + H \rightarrow H + H^+$. Many authors have mentioned that the charge exchange is the major loss process for the ring current ions [e.g., *Liemohn*, 1961; *Swisher and Frank*, 1968; *Prülss*, 1973; *Smith et al.*, 1976; *Chamberlain*, 1977; *Smith and Bewtra*, 1978; *Solomon and Picon*, 1981; *Kistler et al.*, 1989; *Noël*, 1997; *Chen et al.*, 1997; *Ebihara and Ejiri*, 1998]. The resultant energetic hydrogen is called an energetic neutral atom (ENA), which are used to obtain the two-dimensional image of the ring current distribution [e.g., *Roelof*, 1987; *Beutir et al.*, 1996; *Henderson et al.*, 1997]. Recently, *Bishop* [1996] suggested that the ENAs generate a secondary ring current in the inner region.

3. *Coulomb collision with thermal plasmas.* The Coulomb collision has been also considered as one of significant loss processes comparable to the charge exchange. *Wentworth* [1959] investigated the lifetimes of trapped ions due to the Coulomb collision. They assumed the distribution of thermal plasmas to be expressed by a delta function. *Fok et al.* [1991] derived the Coulomb lifetime from the assumption that the thermal plasma has a Maxwellian distribution. The Coulomb collision may be an important loss process for a particular energy range ions (especially below 10 keV) [*Fok et al.*, 1991]. The Coulomb collision loss with the plasmaspheric thermal plasmas may be ignored relative to the charge exchange loss for the ring current decay because the plasmasphere shrinks during a magnetic storm [*Ebihara et al.*, 1998b].

4. *Wave-particle interaction.* Wave-particle interaction with the electromagnetic ion cyclotron (EMIC) wave as a loss mechanism of ions has also been proposed. However,

the wave-particle interaction loss of the ring current ions is an unresolved question because the loss rate strongly depends on the assumed wave amplitude. [*Kozyra et al.*, 1997 for reviews].

The neutral hydrogen distributes relatively steadily. Hence the charge exchange loss of ring current ions with the neutral hydrogen has been established by many investigators. On the other hand, the distribution of the (plasmaspheric) thermal plasma is highly affected and drastically changed by the strength of the large-scale electric field (convection field) with a time scale within approximately 1 hour. Therefore the evaluation of the storm-time Coulomb collision loss of ring current ions with the thermal plasma is difficult; a time-dependent distribution model of the thermal plasma is required. So far, quantitative and realistic evaluation of the storm-time Coulomb collision loss of ring current ions has not been made. In Chapter 3, after constructing a time-dependent three-dimensional plasmaspheric model, the storm-time Coulomb collision loss of the ring current ions is quantitatively evaluated. Moreover, the effects of the Coulomb collision loss on the ring current energy density (plasma pressure) are compared with the charge exchange loss effect for a particular magnetic storm.

1.4 Development of the ring current

The development of the ring current is one of noticeable subjects for the solar-terrestrial physics. In the early years, magnetic field reconnection between the southward interplanetary magnetic field (IMF) and the earth's magnetic field is the most widely accepted

mechanism for developing the magnetic storm. Many authors have proposed the quantitative coupling functions between them [e.g., *Rostoker et al.*, 1972; *Gonzalez and Mozer*, 1974; *Burton et al.*, 1975; *Kan and Lee*, 1979; *Akasofu*, 1981; *Vasyliunas et al.*, 1982; *Doyle and Burke*, 1983; *Wygant et al.*, 1983; *Gonzalez et al.*, 1989]. The coupling functions cannot explain the strength of the ring current development completely because the essential element for the ring current development is the dynamics of ions of the ring current. Thus one must trace ions' trajectories under specified magnetospheric conditions to understand the physics of the ring current development.

Several processes have been proposed to explain the global ring current enhancement empirically and theoretically; (1) inward transport of plasma sheet particles by enhanced convection electric field [e.g., *Williams*, 1981; *Wodnicka*, 1989; *Takahashi et al.*, 1990; *Lui*, 1993; *Bourdarie et al.*, 1997; *Wolf et al.*, 1997; *Jordanova et al.*, 1998; *Ebihara and Ejiri*, 1998], (2) particle injection associated with a substorm [e.g., *Kamide and Fukushima*, 1971; *Lui et al.*, 1987; *Fok et al.*, 1996; *Ebihara et al.*, 1998c], (3) diffusive transport due to the magnetic and/or electric fluctuation [e.g., *Lyons and Schulz*, 1989; *Riley and Wolf*, 1992; *Lui*, 1993; *Chen et al.*, 1993; *Chen et al.*, 1994; *Bourdarie et al.*, 1997; *Chen et al.*, 1998] (4) inward displacement of preexisting trapped particle distribution due to a large-scale convection [e.g., *Lyons and Williams*, 1980] (5) direct entry from the ionosphere in the cusp/cleft and/or the polar cap region into the ring current [e.g., *Cladis and Francis*, 1985; *Delcourt et al.*, 1990; *Peroomian and Ashour-Abdalla*, 1996]. However, there is very little agreement among them on the physical mechanism of the ring current buildup and its essential source.

Previous ring current models have failed to explain the characteristic negative bay and its intensity of Dst index as compared with observations. The primary reason may be that the realistic source population in the plasma sheet and the realistic convection field have not been modeled well. Recently, *Jordanova et al.* [1998] showed that the superdense plasma sheet is one of main sources for the ring current buildup for a particular storm by their model calculation. After examining the solar wind density and the near-earth plasma sheet density, *Borovsky et al.* [1997] and *Terasawa et al.* [1997] have concluded that they are highly correlated. This means that the near-earth plasma sheet density is well responsive to change of the solar wind density, i.e., the enhancements of the solar wind density may affect the plasma sheet density and the enhanced plasma sheet density resultantly may cause the ring current buildup. After examining the relation between the solar wind and the plasma sheet densities by using the result of satellite observations, the ring current buildup depending on the solar wind is examined in Chapter 5.

Chapter 2

Review of dynamics of charged particles in the inner magnetosphere

2.1 Earth's inner magnetosphere

In a vacuum, the earth's magnetic field would appear roughly dipolar with its magnetic moment axis tilted by 11° from its rotation axis. However, the magnetic field is filled with a plasma and it is distorted by external currents. The entire region where the earth's magnetic field governs is called the earth's magnetosphere. The dynamic pressure of the solar wind compresses the magnetosphere so that it resembles a comet's tail. Night side region of the earth's magnetosphere is a region called the magnetotail. The magnetotail extends out far beyond the moon's orbit. In one part of the magnetotail, the stretched magnetic field forms a thin region of relatively hot plasma known to be the *plasma sheet*. Average particle energies in the near-earth plasma sheet are typically around 5 keV and the

number density in the near-earth plasma sheet is approximately ~0.3-1 cm^{-3} [e.g., *Peterson et al.*, 1981; *Lennartsson and Shelley*, 1986; *Baumjohann et al.*, 1989; *Paterson et al.*, 1998]. In the near-earth plasma sheet, there is a large-scale electric field being dominantly in the duskward direction; this large-scale convection field is so-called the *convection electric field*. The plasmas stored in the near-earth plasma sheet convect sunward due to the convection electric field, and they become trapped in the inner magnetosphere where earth's dipolar magnetic field dominates.

Since the convected plasma has a sufficient energy, they can contribute to the formation of the large-scale current surrounding the earth as if a current flows in a ring; this current is called a *ring current*. The growth and decay of the ring current can be observed by magnetograms placed in the earth's surface. At certain times more particles than usual are convected (or injected) from the magnetotail into the ring current by the large-scale convection field. The resultant current depresses the horizontal-component of equatorial earth's magnetic field. The depression usually lasts several hours or a few days and reaches its minimum field of ~1 % of the earth's internal field. Such strong depressions of the earth's field have been noticed in magnetograms for a long time; this is called *magnetic storms*.

Various charged particles are trapped in the earth's magnetosphere. The inner magnetosphere can be categorized into several regions by their characteristic behavior; the plasmasphere, the ring current and the radiation belt. The basic concepts of the regions are described below.

2.1.1 Plasmasphere

The *plasmasphere* is the region where the cold and dense plasma originated from the ionosphere corotates with the earth. As a consequence, the ionospheric plasma fills in the closed field line until the plasma pressure distribution is in hydrostatic equilibrium. The plasmasphere consists of cold plasmas with its temperature of ~1 eV [*Comfort et al.*, 1985; *Olsen et al.*, 1987]. The plasmaspheric density ratio He^+/H^+ is generally of the order of 0.2 [*Horwitz et al.*, 1986] or 0.1 [Olsen et al., 1987]. Plasmaspheric enhancements of O^+ are often accompanied with the distinct increase in ionospheric electron temperature [*Horwitz et al.*, 1986].

Usually, the plasma density inside the plasmasphere is significantly higher than outside, because in the outer region where the convection field dominates the corotation field the plasma convects to the dayside magnetopause [*Nishida*, 1966; *Brice*, 1967]. **Figure 2.1** shows the model calculation of the plasmaspheric electron density as a function of McIlwain's L [*McIlwain*, 1961] (or the geocentric distance in the equatorial plane in earth radii) given by *Carpenter and Anderson* [1992].

The steep gradient as shown in **Figure 2.1** is called the *plasmapause*. The plasmapause position has been studied both by using *in situ* satellite measurements [e.g., *Taylor et al.*, 1968; *Chappell et al.*, 1970a; *Chappell et al.*, 1970b; *Chappell et al.*, 1971; *Carpenter and Chappell*, 1973; *Maynard and Grebowsky*, 1977; *Chappell*, 1982; *Reasoner et al.*, 1983; *Higel and Wu*, 1984; *Nagai et al.*, 1985; *Horwitz et al.*, 1990] or by ground-based measurements and analysis of whistler waves triggered in the ionosphere by lightning flashes [e.g., *Carpenter*, 1962; *Carpenter*, 1963; *Carpenter*, 1966; *Park*, 1974]. The historically presented

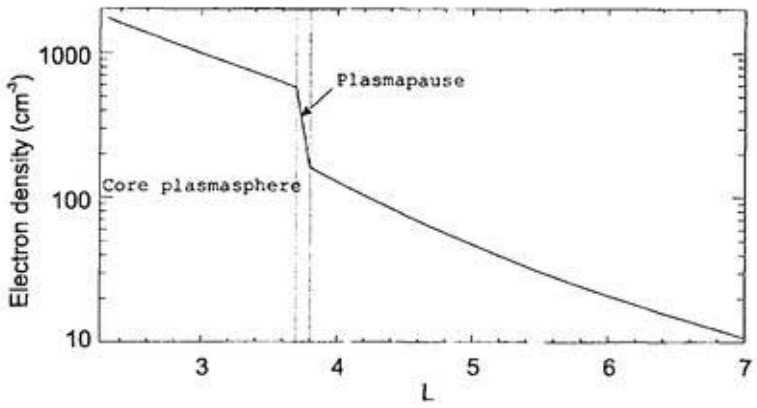

Figure 2.1. A model calculation of the plasmaspheric electron density in the equatorial plane as a function of L-value given by *Carpenter and Adnerson* [1992].

shapes of the plasmapause are shown in **Figure 2.2**.

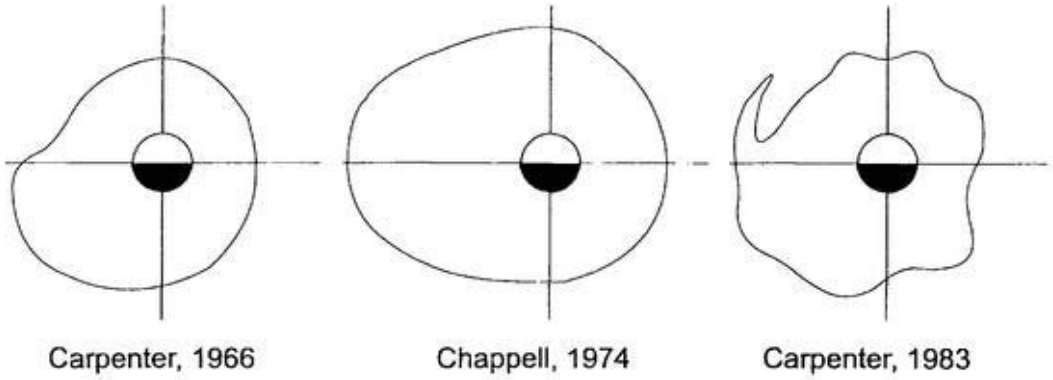

Figure 2.2. Historical plasmapause shapes in the equatorial plane. From left to right, the shapes were presented by *Carpenter* [1966], *Chappell* [1974] and *Carpenter* [1983], respectively. (After *Carpenter et al.* [1993])

Equatorial projection of plasmapause is typically located near 2-7 Re (earth radii); they are drastically changed by the strength of the convection electric field. **Figure 2.3** represents a composite density profiles in the night side region given by *Chappell et al.* [1970a]; it is clearly shown that the density gradient around the plasmapause is sensitive to the

magnetic activity as indicated by Kp.

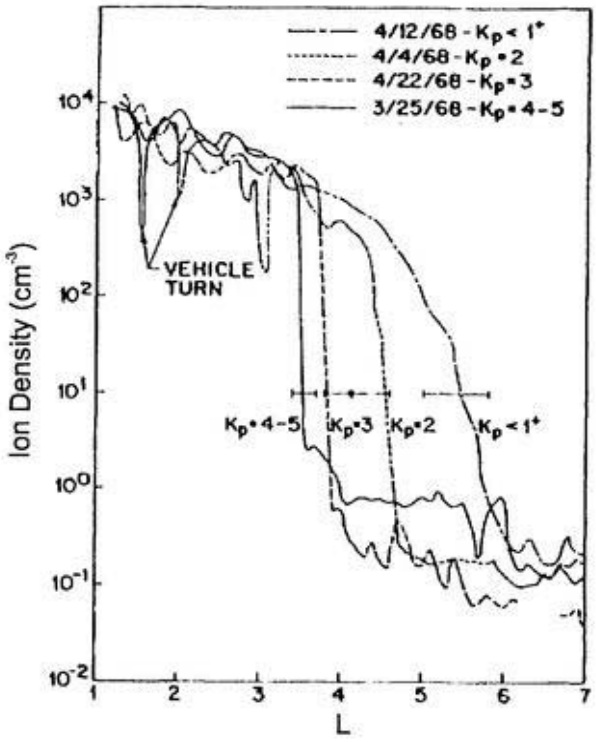

Figure 2.3. A composite density profiles showing the reaction of the plasmasphere in the night side region. (After *Chappell et al.* [1970a])

In the nightside region, the plasmapause density gradient is typically found while the sharp density gradient is not always observed in the dayside region [*Nagai et al.*, 1985]. Moreover, *Horwitz et al.* [1990] reported that the transition region of the density around the plasmapause is generally complicated and they can be classified into six different categories, being represented in **Figure 2.4**. After examining 515 radial profiles of the ion density observed by the DE-1 satellite, *Horwitz et al.* [1990] found that *featureless* (labeled as A) or *multiple plateau* (labeled as C) are mostly observed.

During increasing activity, the stronger convection electric field pushes the plasmapause

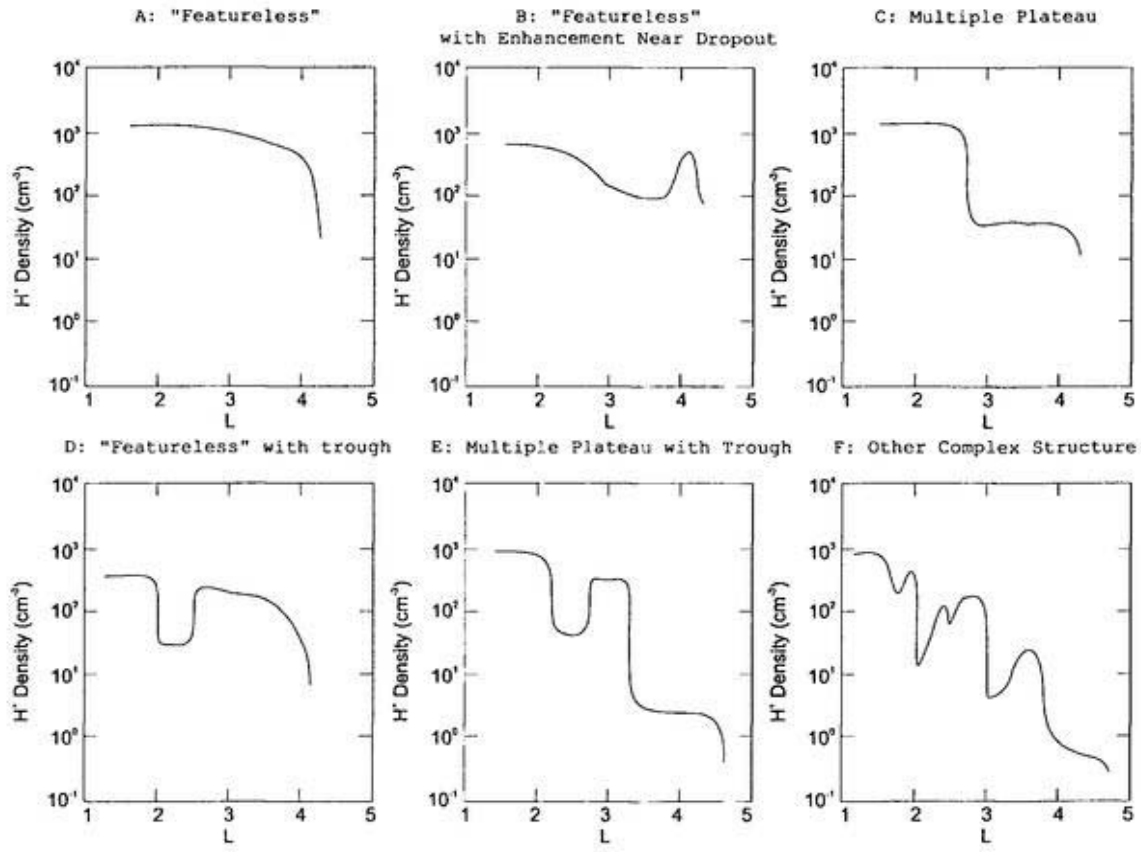

Figure 2.4. Six schematic plasmaspheric density profiles categorized by *Horwitz et al.* [1990]. (After *Horwitz et al.* [1990])

closer to the earth and peels off the outer layers of the old plasmasphere. The peeled plasmasphere connecting with the core plasmasphere is called detached plasmasphere [e.g., *Chappell et al.*, 1971; *Chappell*, 1974] or plasmatail [e.g., *Chen and Grebowsky*, 1974; *Grebowsky et al.*, 1974; *Grebowsky et al.*, 1975; *Chen et al.*, 1975; *Maynard and Chen*, 1975] (see **Figure 2.5**).

The plasmatail extends beyond the geosynchronous orbit (6.6 Re) so that geosynchronous satellites often observe the plasmatail (or a bulge of the core plasmasphere) in the dusk region. *Higel and Wu* [1984] statistically examined the magnetic activity dependence of the

plasmatail (or a bulge) crossing of the geosynchronous satellite (GEOS-2) and they found that the geosynchronous satellite encounters the plasmatail in early local time (closer to noon) as the magnetic activity increases. *Elphic et al.* [1997] speculated that the plasmaspheric particles convecting from the core plasmasphere are carried by the reconnection into nightside region when they encounter the dayside magnetopause. However, we have no definitive information to confirm their speculation.

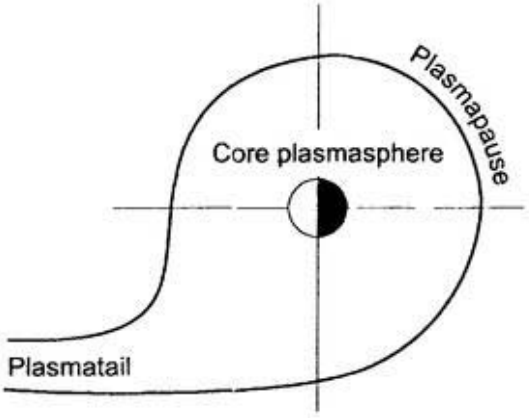

Figure 2.5. Schematic for the plasmatail extending from the core plasmasphere in the equatorial plane.

Conversely, during decreasing activity, plasmapause moves outward, and a refilling process from the topside ionosphere begins; the new plasmasphere forms in a several days. To measure the plasma flow properties of refilling flux tubes is most essential for understanding the refilling process. *Hoffman and Dodson* [1980] documented the high latitude polar wind outflow in terms of light ion densities, flow velocities and fluxes. However, the properties observed by them seem to be different from the properties related to the plasmaspheric refilling. The retarding ion mass spectrometer (RIMS) [*Chappell*, 1982] aboard DE 1 succeeded to illuminate the plasma flow properties of the refilling flux tubes. *Chandler and*

Chappell [1986] found interhemispheric flows of the order of 1 km/s or less for H^+. Such flows are quite subsonic, as the thermal speeds are of the order of 6 km/s or higher. They also found that the counterstreaming generally occurs at solstice; H^+ ions flow from the summer hemisphere and He^+ ions from the winter hemisphere. *Olsen et al.* [1985] found both an isotropic background and a low-energy field-aligned flow in the plasmasphere; the isotropic population is primarily composed of H^+ ions, with 10 % of $He^+$and 0.1-1 % of O^+. The field-aligned population has a density of ~2-3 cm^{-3} and thermal energies of 0.25-1 eV, being flowing at 5~20 km/s. Using the suprathermal ion mass spectrometer (SMS) aboard EXOS-D, *Watanabe et al.* [1992] reported the ion flow velocities in the refilling of the outer plasmasphere; they found rather high flow speed of 12 km/s or greater for H^+ , 7 km/s for He^+ and 3 km/s for O^+. *Olsen et al.* [1987] investigated the trapped ion population confined within a few degrees latitude of the equator; the heated H^+ ions have bi-Maxwellian distribution of temperature of 0.5-1.0 and 5-50 eV with densities of 10-100 cm^{-3}. They noted that this trapped and heated population in the near equatorial region are often observed.

2.1.2 Ring current

The ring current consists of geomagnetically trapped 10-200 keV ions [e.g., *Willaimas*, 1981] (mainly H^+, He^+ and O^+) that drift azimuthally around the earth at geocentric distance of 2-8 Re; they are overlapping the radiation belt (Van Allen radiation belt).

The global strength of the ring current can be monitored by ground-based magnetograms at mid- and low-latitudes. The Dst index calculated from the observed geomagnetic field

gives an estimate of the strength of the ring current. This index has been used to monitor the development of geomagnetic storm.

The ring current has been considered that the current always flows westward because of the two reasons: (1) The gradient and curvature drift motion of ions is westward and eastward for electrons so that the direction of the current is westward. (2) The negative excursion of the Dst index during a magnetic storm is well explained by the existence of the enhancement of the westward ring current.

Such a classical idea of the ring current is incorrect. In early 1960's, the dynamic feature of the ring current was revealed by satellites which observed the charged particles and the magnetic fields. Using a modeled pressure distribution having a Gaussian type distribution along an equatorial radius, so-called V_3 model, *Akasofu and Chapmen* [1961] and *Akasofu et al.* [1961] inferred the ring current distributions that flow westward in the outer region and eastward in the inner region in a meridian plane. The V_3 model was deduced from the magnetic perturbation in the equatorial plane observed by Explorer 6. *Hoffman and Bracken* [1965] applied the observed ion energy spectra with energies above 100 keV by Explorer 12 to the *Akasofu and Chapmen* [1961]'s model, and they calculated the current distribution for the quiet time ring current. Moreover *Hoffman and Bracken* [1967] included the self-consistency in the current calculation. *Frank* [1967] found the proton flux with energies 31-49 keV increased by factors above 30 over the prestorm intensities during a magnetic storm at $L = 3.5$ near the equatorial region by using the result of the OGO 3 particle observations (see **Figure 2.6**); they suggested that the total energy of these protons with energies 3-50 keV within the earth's magnetosphere is sufficient to account

for the depression of the Dst index.

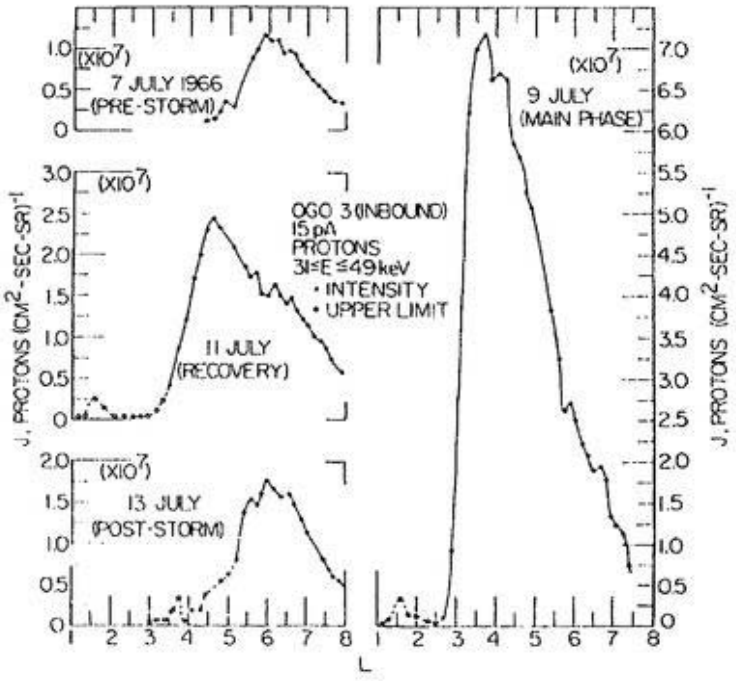

Figure 2.6. Flux of protons in an energy range of 31-49 keV as a function of L near the equatorial region during the pre-storm, main phase, recovery phase and post-storm periods of the July 1966 storm. (After *Frank* [1967].)

Detectors aboard Explorer 45 (S^3-A) provided the first total ion and electron energy density measurements in the equatorial region from 2.5 to 5.5 Re [*Longanecker and Hoffman*, 1973]. *Smith and Hoffman* [1973] showed that the storm-time ring current constitutes an enormous enhancement of protons in the energy range 10-120 keV. *Berko et al.* [1975] calculated the distortion magnetic field deduced from the proton's distribution. They compared with the direct measurement of the magnetic field and they concluded that protons with energies 1-872 keV can account for the observed ring current magnetic field in the equatorial region for a particular storm.

Smith and Hoffman [1973] also showed that during a main phase of the storm, additional injections of protons related to substorms were observed; they were superposed on the gradual increase of the proton energy density. The characteristic features of this additional enhancement in the evening region are consistent with flow patterns resulting from a combination of inward convection, corotation and gradient-curvature drift motion, being carried from the plasma sheet into the inner region; this features are accompanied with the nose structure in the observed E-t (energy versus time) spectrograms [*Smith and Hoffman*, 1974]. *Ejiri* [1978] and *Ejiri et al.* [1980] succeeded to reconstruct the nose dispersion structure by tracing particles having various energies and pitch angles under their basic concept that the 'nose' structure is caused by a temporal enhanced convection field: First the plasma sheet plasma is convected from the tail region toward the earth primarily in the radial direction with little energy and pitch angle dispersion under a weak convection (first stage). Following the convection enhancement (second stage), this population moves further toward the earth and begins dispersing with energy and pitch angle. The time-dependent particle penetration into the lower L region is indicated in **Figure 2.7**.

The CHEM (Charge-Energy-Mass Spectrometer) aboard AMPTE/CCE (Active Magnetospheric Particle Tracer Explorers / Charge Composition Explorer) has an ability to observe the charge composition of ions in the energy range of 0.3-315 keV/e [*Gloeckler et al.*, 1985a]. Prior to the mission of AMPTE/CCE, the charge composition of ring current ions had been inferred from the different charge exchange loss rates among species [*Smith et al.*, 1981].

One of the intense storms in the whole AMPTE/CCE mission, on September 4-7, 1984,

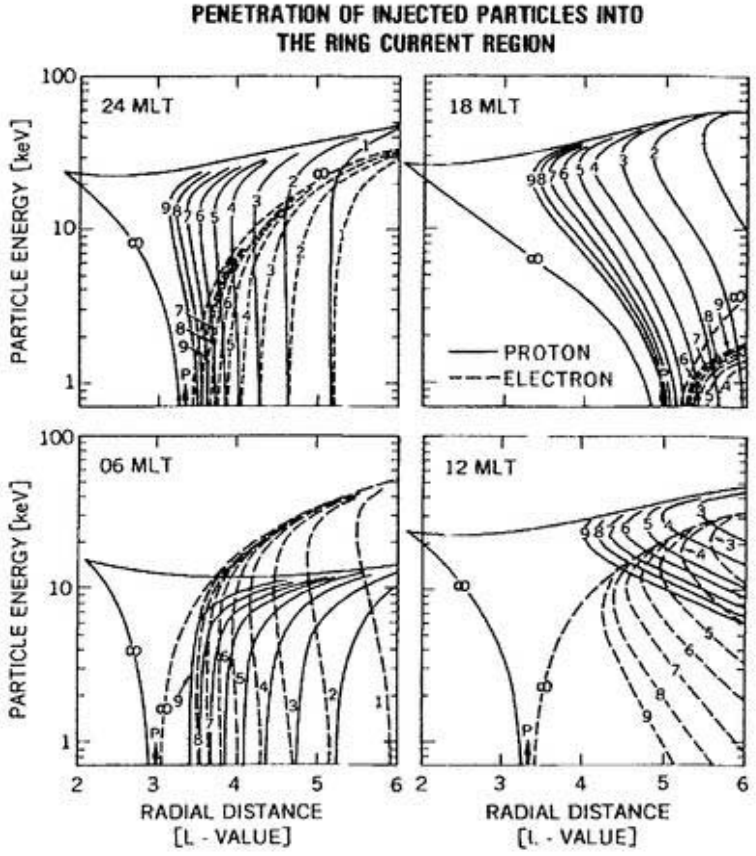

Figure 2.7. Reulsts of simulations of the particle penetration into the ring current region. The MLT dependence of particle penetration distances for ions (solid lines) and for electrons (dashed lines) after an electric field enhancement is clearly shown. (After *Ejiri et al.* [1980].)

Gloeckler et al. [1985b] reported that the energy density of O^+ increased up to a fraction 29% of total during a main phase of the storm in the region 3.7-4.7 Re while O^+ contributed only 2.7% to the total energy density in a quiet-time. The other intense storm during the AMPTE/CCE mission, in February 1986, the O^+ energy density dominated that of H^+ in the most disturbed period [*Hamilton et al.*, 1988]. *Hamilton et al.* [1988] speculated that the large increase of the O^+ energy density is caused by the large amount of ionospheric outflow O^+ ions in the auroral or cusp/cleft region. The magnetic activity dependent

outflow of O^+ ions was previously reported by *Yau et al.* [1985], that is,

$$F(H^+) = 1.5 \times 10^{25} \exp(0.26Kp) \text{ sec}^{-1}, \tag{2.1}$$

$$F(O^+) = 9.0 \times 10^{24} \exp(0.56Kp) \text{ sec}^{-1}, \tag{2.2}$$

where $F(H^+)$ and $F(O^+)$ are the outflow rates of H^+ and O^+ ions, respectively. Comparing with Eq.(2.1) and Eq.(2.2), it is suggested that the outflow rate of O^+ ions is sensitive to Kp as compared with that of H^+. The drastic enhancement of the O^+ energy density seems to be a common feature during a large or an intense storm [e.g., *Roeder et al.*, 1996; *Daglis*, 1997]. The magnetic activity dependence of O^+ ions has been observed not only in the ring current, but also in the near-earth plasma sheet [*Peterson et al.*, 1981; *Sharp et al.*, 1982; *Ipavich et al.*, 1985; *Lennartsson and Shelley*, 1986; *Daglis et al.*, 1994; *Daglis and Axford*, 1996]. However, the whole mechanism that the O^+ energy density in the ring current and/or in the inner plasma sheet depends on the magnetic activity has not been understood.

Lui et al. [1987] examined the time development of the plasma pressure, current density and plasma beta value as a function of a radial distance during the large storm of September 4-7, 1984 (see **Figure 2.8**). The current density $\boldsymbol{J}_\perp$ perpendicular to the magnetic field was calculated from the observed ion pressure P as

$$\boldsymbol{J}_\perp = \frac{\boldsymbol{B}}{B^2} \times \left[\nabla P_\perp + (P_\parallel - P_\perp) \frac{(\boldsymbol{B} \cdot \nabla)\boldsymbol{B}}{B^2} \right], \tag{2.3}$$

where $\boldsymbol{B}$ is the local magnetic field and the subscripts $\perp$ and $\parallel$ represent the value perpen-

dicular and parallel to the local magnetic field, respectively. Eq.(2.3) is given by *Parker* [1957]. The results are as followings: (1) Enhancements in the plasma pressure occur initially in the outer region and reach the inner region in the recovery phase. (2) Particle injection structure can be seen. (3) The plasma beta in some region exceeds 1.

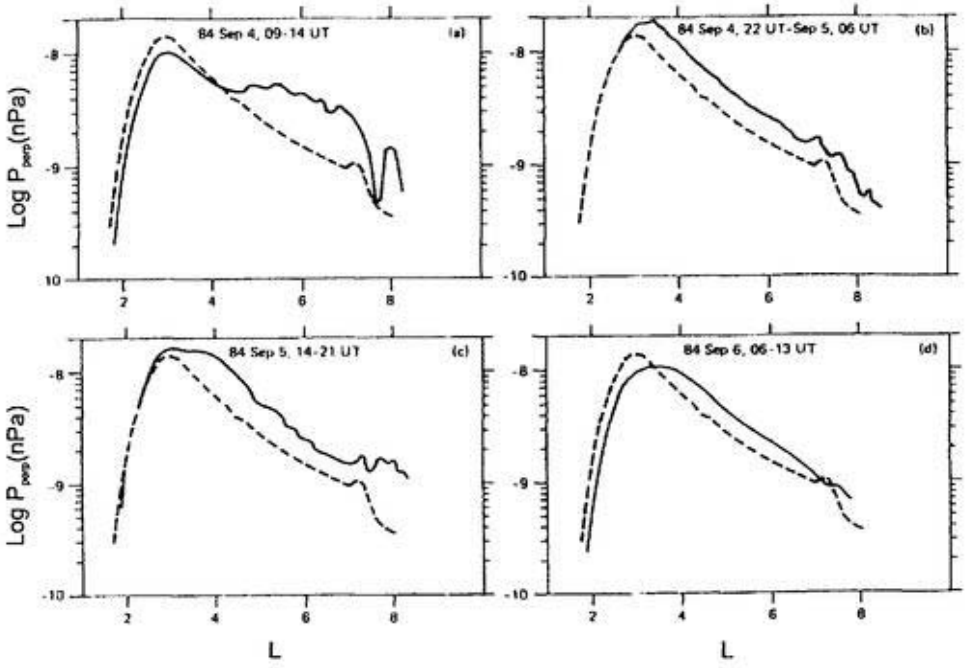

Figure 2.8. The perpendicular plasma pressure as a function of L during a magnetic storm on September 4-7, 1984. Dashed lines represent the perpendicular pressure obtained from the reference pass before the commencement of the storm (After *Lui et al.* [1987].)

Several processes have been proposed to explain the global ring current enhancement;

1. inward transport of plasma sheet particles by enhanced convection electric field [e.g., *Williams*, 1981; *Wodnicka*, 1989; *Takahashi et al.*, 1990; *Lui*, 1993; *Bourdarie et al.*, 1997; *Wolf et al.*, 1997; *Jordanova et al.*, 1998; *Ebihara and Ejiri*, 1998],

2. particle injection associated with a substorm [e.g., *Lui et al.*, 1987; *Fok et al.*, 1996;

Ebihara et al., 1998c],

3. diffusive transport due to the magnetic and/or electric fluctuation [e.g., *Lyons and Schulz*, 1989; *Riley and Wolf*, 1992; *Lui*, 1993; *Chen et al.*, 1993; *Chen et al.*, 1994; *Bourdarie et al.*, 1997; *Chen et al.*, 1998],

4. inward displacement of preexisting trapped particle distribution due to a large-scale convection [e.g., *Lyons and Williams*, 1980],

5. direct entry from the ionosphere in the cusp/cleft and/or the polar cap region into the ring current [e.g., *Cladis and Francis*, 1985; *Delcourt et al.*, 1990; *Peroomian and Ashour-Abdalla*, 1996].

However, There is very little agreement on the physical mechanism of the ring current buildup and its essential source.

The decay of the ring current is also one of significant topics. Four major loss processes are proposed for decay of the ions constituting the ring current as listed below:

1. *Convection outflow.* Particles transported by the large-scale convection field flow sunward. The particles that encounter the dayside magnetopause may be lost [e.g., *Takahashi et al.*, 1990; *Ebihara et al.*, 1998b].

2. *Charge exchange with neutral hydrogen.* The neutral hydrogen exists steadily with the density of ~700 cm^{-3} at a geocentric distance of 3 Re and ~300 cm^{-3} at 4 Re [*Rairden et al.*, 1986]. A proton exchanges its charge with the neutral hydrogen as $H^+ + H \rightarrow H + H^+$. Many authors have mentioned that the charge exchange is the major loss process for the ring current ions [e.g., *Liemohn*, 1961; *Swisher and*

Frank, 1968; *Prülss*, 1973; *Smith et al.*, 1976; *Chamberlain*, 1977; *Smith and Bewtra*, 1978; *Solomon and Picon*, 1981; *Kistler et al.*, 1989; *Noël*, 1997; *Chen et al.*, 1997; *Ebihara and Ejiri*, 1998]. The resultant energetic hydrogen is called an energetic neutral atom (ENA), which are used to obtain the two-dimensional image of the ring current distribution [e.g., *Roelof*, 1987; *Beutir et al.*, 1996; *Henderson et al.*, 1997]. *Bishop* [1996] suggested that the resultant ENAs generate a secondary ring current in the inner region.

3. *Coulomb collision with thermal plasmas.* The Coulomb collision has been also considered as one of significant loss processes comparable to the charge exchange. *Wentworth* [1959] investigated the lifetimes of trapped ions due to the Coulomb collision. They assumed the distribution of thermal plasmas to be expressed by a delta function. *Fok et al.* [1991] derived the Coulomb lifetime from the assumption that the thermal plasmas has a Maxwellian distribution. The Coulomb collision may be an important loss process for a particular energy range (especially below 10 keV) [*Fok et al.*, 1991]. The Coulomb collision loss with the plasmaspheric thermal plasmas may be ignored relative to the charge exchange loss for the ring current decay because the plasmasphere shrinks during a magnetic storm [*Ebihara et al.*, 1998b].

4. *Wave-particle interaction.* Wave-particle interaction with the electromagnetic ion cyclotron (EMIC) wave as a loss mechanism of ions has also been proposed. However, the wave-particle interaction loss on the ring current ions is an unresolved question because the loss rate strongly depends on the assumed wave amplitude. [*Kozyra et al.*, 1997 for reviews].

2.1.3 Radiation belt

The trapping regions of high energy charged particles surrounding the earth are called *radiation belts* (or *Van Allen radiation belts*). There is a clear distinction between protons and electrons.

For electrons, there are two belts; the inner belt located between about 1.1-2.0 Re in the equatorial plane, and the outer belt located between about grater than 3.5 Re. The inner belt exists stably while the outer belt is sensitive to the magnetic activity. The region between the inner and outer belts is called a *slot region*. Wave-particle interaction with the whistler mode waves has been considered to be the primary source to make the slot region [e.g., *Lyons et al.*, 1972]. After a large magnetic storm, the slot region is filled with the newly transported electrons.

High energy protons with energies exceeding 10 MeV are located between 1.1-3.0 Re in the equatorial plane and they form a proton radiation belt. The proton radiation belt is a fairly stable population but this is disturbed after an extremely large storm (e.g., after the storm in March 1991 [e.g., *Hudson et al.*, 1997]). The inner proton radiation belt varies with 11-year solar cycle. The main source of protons in this region is the decay of cosmic ray induced albedo from the atmosphere.

Figure 2.9 shows the model calculation of the radiation belts for 2 MeV electrons and 10 MeV protons, being given by NASA's empirical models, AE8-MIN for electrons and AP-8-MIN for protons.

Recently, a new belt was found within the inner belt. It contains heavy nuclei (mainly oxygen, but also nitrogen and helium, and very little carbon) with energies below 50

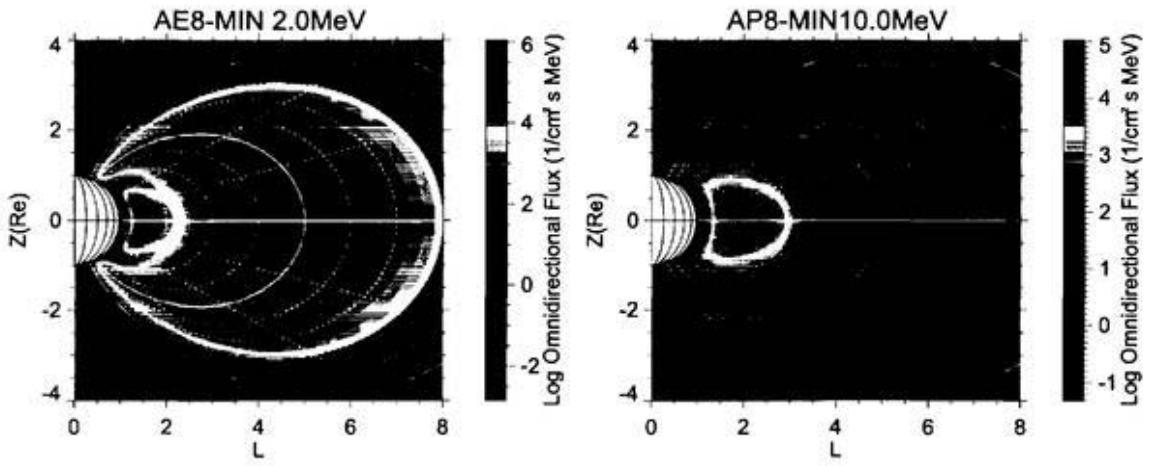

Figure 2.9. Model calculation of the omnidirectional flux for 2 MeV electrons (left) and 10 MeV protons (right) in the meridian plane. The flux distribution is given by NASA AE-8 model for electrons and AP-8 model for protons.

MeV/nuclei. The source of these particles are the so-called *anomalous cosmic rays* of interstellar origin [e.g., *Mewaldt et al.*, 1996].

The radiation belts are also important because the high energy particles are harmful: (1) It degrades satellite components, particularly semiconductor and optical devices. (2) It induces background noise in particle detectors. (3) It induces errors in digital circuits. (4) It induces electrostatic charge-up in insulators. (5) It is also threat to the astronauts.

2.2 Adiabatic drift motion in the magnetosphere

2.2.1 Lorentz force

In dealing with the dynamics of charged particles in the magnetosphere, one should first know the force acting on each charged particle. The dominant force acting each non-

relativistic particle in most cases is the Lorentz force as

$$m\frac{d^2\boldsymbol{r}}{dt^2} = q\left(\boldsymbol{E} + \frac{d\boldsymbol{r}}{dt} \times \boldsymbol{B}\right), \tag{2.4}$$

where $\boldsymbol{r}, m, q, \boldsymbol{v}, \boldsymbol{E}$ and $\boldsymbol{B}$ are particle position, mass, charge, a velocity vector, an electric field vector and a magnetic field vector, respectively.

Assuming that the magnetic field B is uniform and constant and that the electric field E is zero, Eq.(2.4) becomes

$$\left(\frac{dv_\parallel}{dt}\right)_\parallel = 0, \tag{2.5}$$

$$\left(\frac{dv_\perp}{dt}\right)_\perp = \frac{q}{m}(\boldsymbol{v}_\perp \times \boldsymbol{B}), \tag{2.6}$$

where $v_\parallel$ and $v_\perp$ are the velocity parallel to the magnetic field and the velocity perpendicular to the magnetic field, respectively. Integrating Eq.(2.5), it becomes

$$v_\parallel = \text{constant}, \tag{2.7}$$

that is, the particle moves parallel to $\boldsymbol{B}$ at a constant speed. The trajectory projected on to a plane perpendicular to $\boldsymbol{B}$ is a circle of radius r_L whose gyrating period of Ω as

$$r_L = \frac{mv_\perp}{Bq}, \tag{2.8}$$

$$\Omega = \frac{v_\perp}{r_L} \tag{2.9}$$

$$= \frac{Bq}{m}. \tag{2.10}$$

The particle motion in this case is helical; the *pitch angle* of the helix is the angle between the particle velocity and the magnetic field, being defined by

$$\alpha = \tan^{-1} \frac{v_\perp}{v_\parallel}, \tag{2.11}$$

where α is the pitch angle. Particle with its pitch angle of 90° moves essentially in circle. Particle with its pitch angle of 0° moves along a magnetic field line.

2.2.2 Guiding center approximation

Under the basic assumption that the gyro radius r_L is smaller than the characteristic scale of $|\nabla B|$, *Northrop* [1963] gives equations of the guiding center motion for the steady fields as

$$\frac{d\boldsymbol{R}_\perp}{dt} \approx \frac{\boldsymbol{b}}{B} \times \left\{ -\boldsymbol{E} + \frac{\mu}{q}\nabla B + \frac{m}{q} v_\parallel^2 \frac{\partial \boldsymbol{b}}{\partial s} \right\}, \tag{2.12}$$

$$\frac{dv_\parallel}{dt} \approx -\frac{\mu}{m}\frac{\partial B}{\partial s}, \tag{2.13}$$

$$\frac{d\boldsymbol{R}_\parallel}{dt} = v_\parallel, \tag{2.14}$$

$$\frac{dW}{dt} \approx q\frac{d\boldsymbol{R}}{dt} \cdot \boldsymbol{E}, \tag{2.15}$$

where $\boldsymbol{R}, \boldsymbol{b}, \mu, s$ and W are a position vector of the guiding center, a unit vector of $\boldsymbol{B}$, a magnetic moment of a particle, a line element align a field line, and the kinetic energy, respectively. The equation of the perpendicular displacement Eq.(2.12) consists of three terms; the $E \times B$ drift, the grad-B (∇B) drift and the curvature drift. Eq.(2.13) indicates that the particle motion parallel to the magnetic field is accelerated in a direction oppo-

site to the gradient of the magnetic field. If a particle is moving into a stronger magnetic field, it will be repelled. Considering the earth's magnetic field that connects with both the northern and southern hemispheres, a particle becomes trapped between the northern and southern hemispheres. Therefore Eq.(2.13) is called the *mirroring force*. Those equations are applicable for tracing the particle motion under the relatively steady electric and magnetic fields in the magnetosphere, e.g., the cusp/cleft region, the distant neutral sheet.

2.2.3 Adiabatic invariants

The concept of invariants is extremely useful in describing the motion of particles in the magnetic field. Considering the motion of a particle described by a pair of variables (p_i, q_i) that are generalized momenta and coordinates, the action integral J_i over a complete period of oscillation of q_i with specified initial conditions, which is written as

$$J_i = \oint p_i dq_i, \tag{2.16}$$

is an invariant of motion.

This action integral will remain invariant even if some property of the system is allowed to change. However, it is required that the temporal change is slow as compared to relevant periods of the system and that the spatial change must not be related to the periods.

There are three type invariants associated with the motion in the magnetosphere; the gyration motion around a magnetic field line, the bounce motion along a field line and the drift motion perpendicular to a magnetic field.

First adiabatic invariant

The first invariant is associated with the gyro motion of a particle. Multiplying each side of Eq.(2.13) by $v_{\parallel}$ and m, we obtain the equation in the steady magnetic field as

$$\begin{aligned} \frac{d}{dt}\left(\frac{mv_{\parallel}^2}{2}\right) &= -\mu\frac{\partial B}{\partial s}\frac{ds}{dt} \\ &= -\mu\frac{dB}{dt}. \end{aligned} \tag{2.17}$$

From the requirement of conservation of the total energy of the particle, the conservation equation is derived as

$$\begin{aligned} \frac{d}{dt}\left(\frac{1}{2}mv_{\parallel}^2+\frac{1}{2}mv_{\perp}^2\right) &= \frac{d}{dt}\left(\frac{1}{2}mv_{\parallel}^2+\mu B\right) \\ &= 0. \end{aligned} \tag{2.18}$$

After substituting Eq.(2.17) into Eq.(2.18), we obtain

$$-\mu\frac{dB}{dt}+\frac{d}{dt}(\mu B)=0, \tag{2.19}$$

that is,

$$B\frac{d\mu}{dt}=0. \tag{2.20}$$

Eq.(2.20) means that the magnetic moment μ is independent of time and is a constant in the guiding center motion. The constancy of the magnetic moment implies that the total magnetic flux enclosed by the motion must also remain constant. This constancy of the

first invariant of guiding center motion leads to magnetic trapping of particles.

Second adiabatic invariant

The longitudinal invariant is associated with the $v_\parallel$ motion. Since charged particles traveling in the direction of B behave as if the magnetic field is not there; the momentum is simply $mv_\parallel$. The action integral for this motion is usually represented by J

$$J = \oint mv_\parallel ds. \tag{2.21}$$

From the definition of the total energy T as

$$T = \frac{mv_\parallel^2}{2} + \mu B, \tag{2.22}$$

the second invariant indicated in Eq.(2.21) becomes

$$\begin{aligned}
\frac{dJ}{dt} &= \frac{\partial J}{\partial t} + \left(\frac{\partial J}{\partial T}\right)\frac{dT}{dt} + \left(\frac{\partial J}{\partial s}\right)\frac{ds}{dt} \\
&= \int_{s_1}^{s_2} \left[\frac{2}{m}(T-\mu B)\right]^{-1/2} \left[-\frac{\mu}{m}\frac{\partial B}{\partial t}\right] ds \\
&\quad + \left[v_\parallel \frac{dv_\parallel}{dt} + \frac{\mu}{m}\frac{\partial B}{\partial t}\right] \int_{s_1}^{s_2} \left[\frac{2}{m}(T-\mu B)\right]^{-1/2} ds \\
&\quad + v_\parallel \left[\frac{2}{m}(T-\mu B)\right]^{1/2},
\end{aligned} \tag{2.23}$$

where s_1 and s_2 are the two mirror points. Since the parallel velocity $v_{\parallel}$ is zero at the mirror points, all terms including $v_{\parallel}$ vanish. Then Eq.(2.23) becomes

$$\begin{aligned}\frac{dJ}{dt} &= -\int_{s_1}^{s_2} \frac{\mu}{m}\left[\frac{2}{m}(T-\mu B)\right]^{-1/2}\frac{\partial B}{\partial t}ds \\ &\quad + \left(\frac{\partial B}{\partial t}\right)\int_{s_1}^{s_2}\frac{\mu}{m}\left[\frac{2}{m}(T-\mu B)\right]^{-1/2}ds. \end{aligned} \tag{2.24}$$

If $\partial B/\partial t$ is slowly varying and it can be considered constant over s_1 and s_2, $\partial B/\partial t$ can be taken outside of the integral. Then, the two terms in Eq.(2.24) cancel;

$$\frac{dJ}{dt} = 0. \tag{2.25}$$

This invariant J is conserved if the perturbation time scale is longer than the transit time of particles between the two mirror points.

Third adiabatic invariant

The first invariant is associated with the gyration motion. The second invariant is associated with the longitudinal motion. For the particle motion in the magnetosphere, the third invariant is associated with the drift motion around the earth. The guiding center drift motion conserves the total magnetic flux within its drift path. The third invariant J_3 can be written as

$$J_3 = \int mV_{\perp}d\phi, \tag{2.26}$$

where $V_\perp$ and ϕ are the drift velocity perpendicular to the magnetic field and the azimuthal angle, respectively, being conserved as long as the perturbation time scale is longer than the drift times of the particles.

2.2.4 Loss cone

Consider a particle in the equator where $B=B_{eq}$, having arbitrary pitch angle of α_0. Arising from the conservation of the first invariant, the cut off pitch angle α_i is called the 'loss cone', being expressed as

$$\sin \alpha_i = \sqrt{\frac{B_{eq}}{B_m}}, \tag{2.27}$$

where B_m is the magnetic intensity at the mirror point. If the particle with its equatorial pitch angle of α_0 is less than α_i, it will mirror below the earth's surface or below the absorbing region of the earth's atmosphere and thus it cannot be bounce motion. In the dipolar magnetic field, the loss cone angle α_i is given by

$$\sin \alpha_i = \frac{\left(\frac{R_i}{Re}\right)^3}{L^3 \left(4 - \frac{3R_i}{ReL}\right)^{1/2}}, \tag{2.28}$$

where R_i, L and Re are the geocentric distance of the absorption layer, McIlwain's L-value and the earth's radius, respectively. **Figure 2.10** shows the loss cone angle as a function of L; the altitude of the absorption layer R_i is taken to be 300 km.

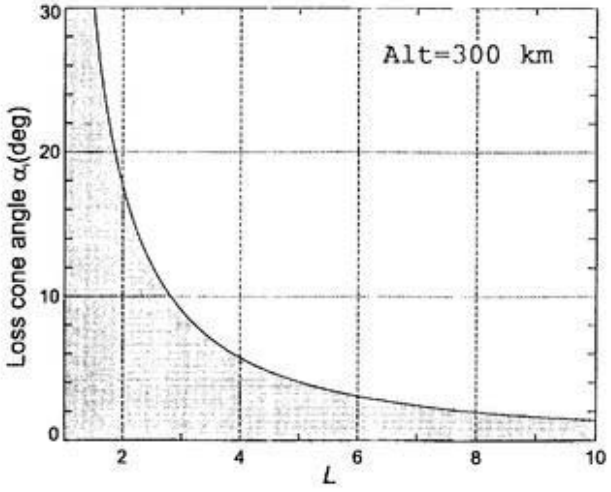

Figure 2.10. Loss cone angle α_i as a function of L. The absorption altitude is take to be 300 km.

2.2.5 Bounce-average drift velocity

When a particle bounces along a field line, it also drifts perpendicularly to the magnetic field. The field line along which a particle is bouncing at a given time is called the *guiding field line*. Each guiding field line is limited by the particle's mirror points. The mirror points generate the two limiting curves m_1 and m_2, called *mirror point paths*. The drift shell Σ (see **Figure 2.11**) is defined by the following procedure; (1) identifying the initial guiding field line, (2) finding the velocity with which the particle is changing guiding field lines, and (3) integrating this velocity.

In general case, there may be a minimum-B point along a given field line. Consider a given, fixed reference surface Ω (**Figure 2.11**) orthogonal to all field lines through each minimum-B point, we define it a magnetic equatorial plane. The minimum-B surface is always perpendicular to the field lines if there is no field-aligned current.

The velocity of the reference point 0 in **Figure 2.12** is called the particle's bounce-

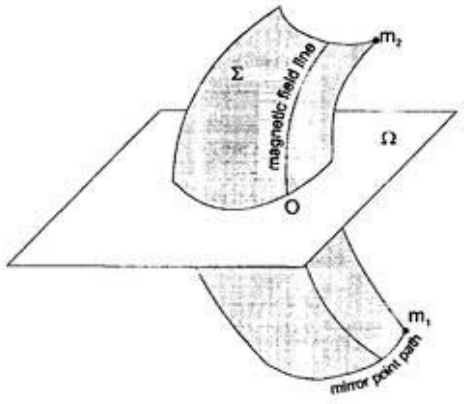

Figure 2.11. A surface Ω orthogonal to all field lines.

average drift velocity. If $\boldsymbol{V}_s$ is the actual, instantaneous drift velocity of the particle while its guiding center is passing through point P_s, the displacement of point 0 associated with the instantaneous displacement $V_s \Delta t$ will be given by $\boldsymbol{OO'}$. O' is obtained by tracing the field line l' that goes through P_s' down to the reference surface Ω. The bounce-average drift velocity of O will then be given by the bounce-average of all associated velocities $\boldsymbol{V}_O$ as

$$\langle \boldsymbol{V}_O \rangle = \frac{2}{\tau_b} \int_{s_1}^{s_2} \boldsymbol{V}_{Os} \frac{ds}{v_\parallel}, \tag{2.29}$$

where τ_b is the bounce period. The associated velocity $\boldsymbol{V}_{Os}$ is related to the actual drift velocity $\boldsymbol{V}_s$ by a purely field-geometric transformation as

$$\boldsymbol{V}_{Os} = \vec{\boldsymbol{T}} \boldsymbol{V}_s. \tag{2.30}$$

In a dipolar magnetic field, the tensor $\vec{\boldsymbol{T}}$ becomes a scalar $\cos^{-3}\lambda$, where λ is the latitude of the point P_s.

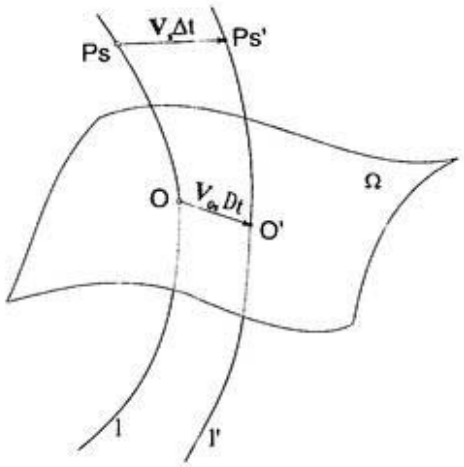

Figure 2.12. Schematics for the bounce-average drift velocity.

The curvature drift velocity $\boldsymbol{V}_C$ and the grad-B drift velocity $\boldsymbol{V}_G$ are

$$\boldsymbol{V}_C = \frac{mv_\parallel^2}{qB^4}\boldsymbol{B}\times(\boldsymbol{B}\cdot\nabla)\boldsymbol{B}, \tag{2.31}$$

$$\boldsymbol{V}_G = \frac{mv_\perp^2}{2qB^3}\boldsymbol{B}\times\nabla\boldsymbol{B}. \tag{2.32}$$

If there is no external current, i.e., $\nabla\times\boldsymbol{B}=0$, the curvature drift velocity becomes

$$\boldsymbol{V}_C = \frac{mv_\parallel^2}{qB^4}\boldsymbol{B}\times\nabla B. \tag{2.33}$$

Then, the gradient-curvature drift can be expressed as

$$\begin{aligned}\boldsymbol{V}_{CG} &= \boldsymbol{V}_C+\boldsymbol{V}_G\\ &= \left(\frac{mv^2}{2}\right)\frac{\boldsymbol{B}\times\nabla B}{qB^3}(1+\cos^2\alpha)\\ &= \frac{mv^2}{qB^3}(\boldsymbol{B}\times\nabla B)\left(1-\frac{1}{2}\frac{B}{B_m}\right)\end{aligned} \tag{2.34}$$

$$= \frac{mv^2}{2qBR_C}(2-\sin^2\alpha)\boldsymbol{b}\times\boldsymbol{n}, \tag{2.35}$$

where R_C and $\boldsymbol{n}$ are the curvature radius and the normal vector toward the opposite direction to the center of the curvature, respectively.

In the dipolar magnetic field, the gradient-curvature drift $\boldsymbol{V}_{CG}$ is westward for protons and eastward electrons, including no radial component. As shown in **Figure 2.13**, the drift displacement of the guiding field line's reference point O is related to the instantaneous velocity as

$$\begin{aligned} OO' &= V_{Os}\Delta t \\ &= \frac{V(\lambda)}{\cos^3\lambda}\Delta t. \end{aligned}$$

Hence, for the angular bounce-average drift velocity is given by

$$\left\langle\left(\frac{d\phi}{dt}\right)_{CG}\right\rangle = \frac{2}{\tau_b}\int_{s_1}^{s_2}\frac{V_{CG}}{v_\parallel R\cos^3\lambda}ds, \tag{2.36}$$

$$= \frac{2}{S_b}\int_0^{\lambda_m}\frac{V_{CG}(4-3\cos^2\lambda)^{1/2}}{\cos^2\lambda\left(1-\frac{\sin^2\alpha_0(4-3\cos^2\lambda)^{1/2}}{\cos^6\lambda}\right)^{1/2}}d\lambda. \tag{2.37}$$

To derive Eq.(2.37), the following equations are used

$$ds = R\cos\lambda(4-3\cos^2\lambda)^{1/2}d\lambda, \tag{2.38}$$

$$\sin^2\alpha = \sin^2\alpha_0\frac{(4-3\cos^2\lambda)^{1/2}}{\cos^6\lambda}. \tag{2.39}$$

The dipole magnetic field is expressed by

$$B(\lambda) = B_0 \frac{(4 - 3\cos^2\lambda)^{1/2}}{\cos^6\lambda}, \tag{2.40}$$

where B_0 is the magnetic field at L=1. The curvature radius R_C is

$$R_C = \frac{R}{3}\cos\lambda \frac{(4 - 3\cos^2\lambda)^{3/2}}{2 - \cos^2\lambda}. \tag{2.41}$$

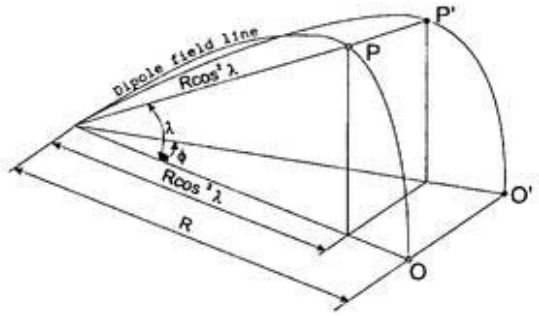

Figure 2.13. Geometry for the drift displacement of the guiding field line's reference point O and the instantaneous position P.

Substituting Eq.(2.39), Eq.(2.40) and Eq.(2.41) into Eq.(2.35), we obtain the instantaneous magnetic drift velocity in the dipolar magnetic field as

$$V_{CG} = \frac{3mv^2}{2qRB_0} \frac{\cos^5\lambda(1 + \sin^2\lambda)}{(4 - 3\cos^2\lambda)^2} \left\{ 2 - \frac{\sin^2\alpha_0(4 - 3\cos^2\lambda)^{1/2}}{\cos^6\lambda} \right\}. \tag{2.42}$$

Then, using Eq.(2.37) and Eq.(2.42), the bounce-average drift velocity becomes

$$\left\langle \left(\frac{d\phi}{dt} \right)_{CG} \right\rangle = \frac{3mv^2}{2qR^2B_0} \left[\frac{\displaystyle\int_0^{\lambda_m} \frac{2 - \frac{\sin^2\alpha_0(4-3\cos^2\lambda)^{1/2}}{\cos^6\lambda}}{\left\{1 - \frac{\sin^2\alpha_0(4-3\cos^2\lambda)^{1/2}}{\cos^6\lambda}\right\}^{1/2}} \left\{ \frac{\cos^3\lambda(1+\sin^2\lambda)}{(4-3\cos^2\lambda)^{3/2}} \right\} d\lambda}{\displaystyle\int_0^{\lambda_m} \frac{\cos\lambda(4-3\cos^2\lambda)^{1/2}}{\left\{1 - \frac{\sin^2\alpha_0(4-3\cos^2\lambda)^{1/2}}{\cos^6\lambda}\right\}^{1/2}} d\lambda} \right] \tag{2.43}$$

Since Eq.(2.43) includes a complicated term to solve it, *Ejiri* [1978] gives approximation formulae for Eq.(2.37) as

$$\left\langle \left(\frac{d\phi}{dt} \right)_{CG} \right\rangle \equiv \frac{3mv^2}{2qR^2B_0} \frac{g(\alpha_0)}{f(\alpha_0)}, \tag{2.44}$$

$$\equiv \frac{3mv^2}{2qR^2B_0} G(\alpha_0), \tag{2.45}$$

with

$$f(y) = \alpha - \beta(y + y^{1/2}) + a_1 y^{1/3} + a_2 y^{2/3} + a_3 y + a_4 y^{4/3}, \tag{2.46}$$

$$\begin{aligned} 3g(y) &= 2\alpha - (5\beta - \alpha)y - (\beta - a_3)y \ln y \\ &\quad -\beta y^{1/2} + \frac{3}{2} a_1 y^{1/3}(1 - y^{1/3}) + 6a_4 y(y^{1/3} - 1), \end{aligned} \tag{2.47}$$

$$y = \sin\alpha, \tag{2.48}$$

where

$$a_1 + a_2 + a_3 + a_4 = 0, \tag{2.49}$$

$$\alpha = 1 + \ln(2 + \sqrt{3})/2\sqrt{3}$$

$$\simeq 1.38, \tag{2.50}$$

$$\beta = (\alpha/2) - (\pi/12)\sqrt{2}$$

$$\simeq 0.32. \tag{2.51}$$

The coefficients are

$$a_1 = 0.055,$$

$$a_2 = -0.037,$$

$$a_3 = -0.074,$$

$$a_4 = 0.056. \tag{2.52}$$

The approximate functions $f(\alpha_0), g(\alpha_0)$ and $G(\alpha_0)$ are shown in **Figure 2.14**

Then, the bounce-average drift velocity can be written as

$$\langle \boldsymbol{V} \rangle = \boldsymbol{V}_E + \left\langle \left(\frac{d\phi}{dt} \right)_{CG} \right\rangle \boldsymbol{e}_\phi, \tag{2.53}$$

where $\boldsymbol{e}_\phi$ is a unit vector toward azimuthal direction and $\boldsymbol{V}_E$ is the $E \times B$ drift velocity, being expressed as

$$\boldsymbol{V}_E = \frac{\boldsymbol{E} \times \boldsymbol{B}}{B^2}. \tag{2.54}$$

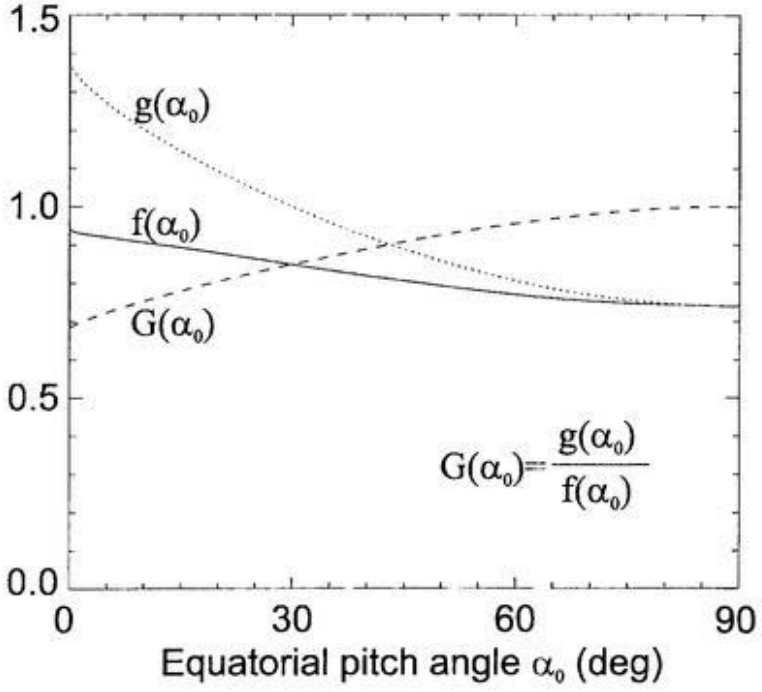

Figure 2.14. The functions, $f(\alpha_0), g(\alpha_0)$ and $G(\alpha_0)$, as a function of the equatorial pitch angle α_0. A solid line, a dotted line and a dashed line are the functions of $f(\alpha_0), g(\alpha_0)$ and $G(\alpha_0)$, respectively.

2.2.6 Electric field model

Convection field

The Volland-Stern type [*Volland*, 1973; *Stern*, 1975] convection model gives the equatorial electric potential distribution Φ_{dd} of the convection, being expressed as

$$\Phi_{dd} = AR^{\gamma} \sin \phi, \tag{2.55}$$

where R is a geocentric distance, ϕ a magnetic local time, γ a shielding factor being taken to be 2 and A a factor indicating the strength of the convection. This simple convection model is used throughout this dissertation.

Following *Maynard and Chen* [1975], the intensity factor A as a function of Kp is adopted to examine the drift trajectories of particles for instance. The intensity factor given by *Maynard and Chen* [1975] is

$$A = \frac{0.045}{(1 - 0.159Kp + 0.0093Kp^2)^3} \ (\mathrm{kV/Re^2}), \tag{2.56}$$

and it is shown in **Figure 2.15**. This Kp dependent model is used in Chapter 3 and Chapter 4. In Chapter 5, the solar wind and IMF dependent model is introduced instead of this Kp dependent model.

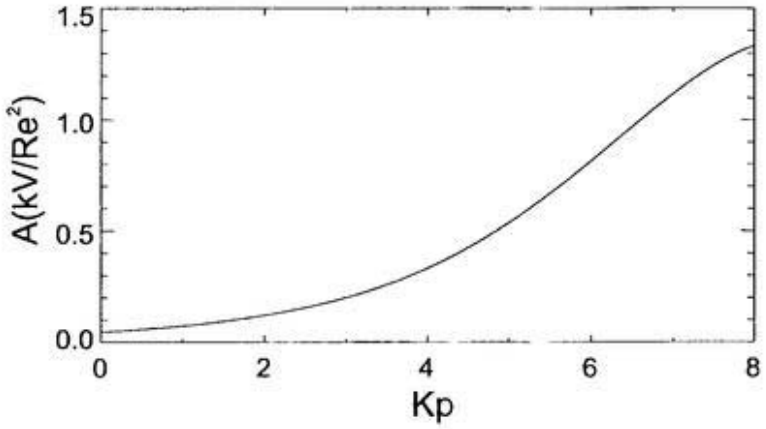

Figure 2.15. The intensity factor A for the Volland-Stern type convection model as a function of Kp, being given by *Maynard and Chen* [1975].

Corotation field

The corotation electric field Φ_{co} in the inertia frame is expressed by

$$\boldsymbol{E}_{co} = -(\boldsymbol{\omega} \times \boldsymbol{R}) \times \boldsymbol{B}, \tag{2.57}$$

where ω is the angular velocity of the earth's rotation. Then the electric potential Φ_{co} becomes

$$\Phi_{co} = -\int_{\infty}^{R} |\boldsymbol{E}_{co}| dR, \tag{2.58}$$

$$= -\frac{\omega R e^3 B_0}{R}, \tag{2.59}$$

where Re is the earth's radius. After substituting the quantities, $\omega = 2\pi/24 \cdot 3600$ rad/s, a=6371 km, $B_0 = 31000$ nT, the electric potential becomes

$$\Phi_{co} = -\frac{C}{R} \text{ [V]}, \tag{2.60}$$

with

$$C = 5.83 \times 10^{12} \text{ [V m]}. \tag{2.61}$$

Hence, the large-scale electric potential Φ, which consists of the convection and the corotation field, is obtained as

$$\Phi = \Phi_{dd} + \Phi_{co}$$

$$= AR^{\gamma} \sin\phi - \frac{C}{R}. \tag{2.62}$$

2.2.7 Drift trajectories of particles

With the assumptions, (1) the first two invariants are conserved; (2) field lines are equipotential; (3) motion of particles includes no additional field, the bounce-average drift trajectories under the dipole magnetic field and the Volland-Stern type convection field can be written [*Ejiri*, 1978] as

$$\frac{dX}{dt} = -\frac{\omega}{\gamma} X^{\gamma+2} \cos\phi, \tag{2.63}$$

$$\frac{d\phi}{dt} = \omega X^{\gamma+1} \sin\phi + \omega - \frac{3\mu G(y_0)}{qR_s^2 X^2}, \tag{2.64}$$

$$\frac{dy_0}{dt} = -\frac{y_0 I(y_0)}{4f(y_0)} \frac{1}{X} \frac{dX}{dt}, \tag{2.65}$$

$$X \equiv \frac{R}{R_s}, \tag{2.66}$$

where $I(y_0), \mu$ and R_s are a function related to the second invariant, the first adiabatic invariant (magnetic moment), a geocentric distance of a stagnation point at MLT of 18h for a zero energy particle, respectively. The geocentric distance of a stagnation point (R_s) for a zero energy particle is

$$R_s = \left(\frac{\omega R e^3 B_0}{A\gamma} \right)^{\frac{1}{\gamma+1}} \tag{2.67}$$

The function $I(y_0)$ is given by

$$I = \frac{1}{R} \int_{s_1}^{s_2} \left[1 - \frac{B(s)}{B_m} \right]^{1/2} ds, \tag{2.68}$$

having no dimension. *Ejiri* [1978] also gives the approximate formula for the function I as

$$\begin{aligned} I(y) &= 2\alpha(1-y) + 2\beta y \ln y + 4\beta(y - y^{1/2}) \\ &\quad +3a_1(y^{1/3} - y) + 6a_2(y^{2/3} - y) + 6a_4(y - y^{4/3}) - 2a_3 y \ln y. \end{aligned} \tag{2.69}$$

The coefficients for Eq.(2.69) are indicated by Eq.(2.50), Eq.(2.51) and Eq.(2.52).

Solving the equations, Eq.(2.63),Eq.(2.64) and Eq.(2.65), one can trace a bounce-average drift trajectory for a given initial condition. The fundamental trajectories under the dipole magnetic field and the Volland-Stern type convection field are drawn in *Ejiri* [1978]. Again, several proton and electron bounce-average trajectories are presented for instance; **Figure 2.16, Figure 2.17** and **Figure 2.18** indicate the energy dependent trajectories, the intensity of the convection dependent trajectories and the pitch angle dependent trajectories, respectively.

2.3 Particle's directional differential flux

2.3.1 Directional differential flux

The previous section has dealt with the motion of single charged particles in the magnetosphere. However, the description of trapped charged particles involves large numbers of particle distribution in space, energy and pitch angle. Hence, the concepts of a directional differential flux has been introduced to describe the characteristic behavior of population of trapped particles.

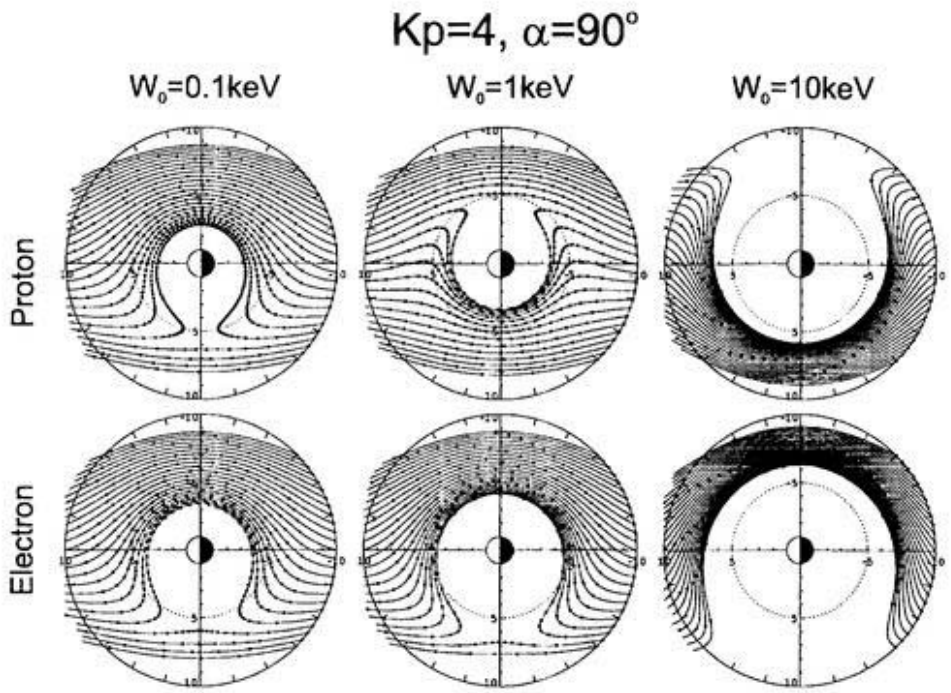

Figure 2.16. Magnetic moment dependence of bounce-average trajectories for protons (top panels) and electrons (bottom panels) with their pitch angles of 90°. From left to right panels, each panel indicates the trajectories for the initial kinetic energies of 0.1, 1, and 10 keV, respectively. They are corresponding to the magnetic moments of 3.23 eV/nT, 32.3 eV/nT and 323 eV/nT, respectively. The trajectories are traced under the dipole magnetic field and the Volland-Stern type convection field with its intensity being Kp=4 for the *Maynard and Chen* [1975] model. All particles start at $L = 10$. Particle positions are represented by dots at 10-minutes steps.

The directional differential flux for a given location, direction and energy is the number of particles at energy W within energy range of dW which cross a unit area perpendicular to the specified direction within a unit solid angle in unit time. The directional differential flux j is given by

$$j = \frac{dN}{dS dW d\Omega dt}, \tag{2.70}$$

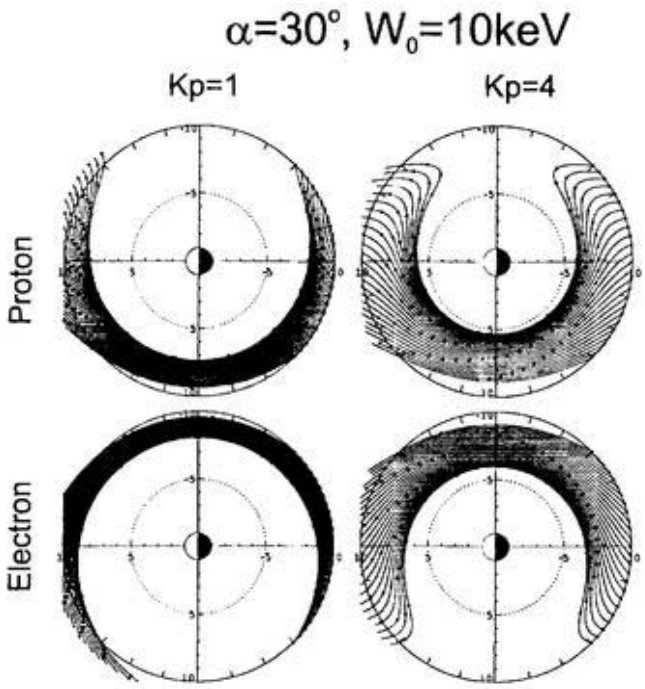

Figure 2.17. Same as previous figure except that the intensity of the convection field dependence of the bounce-average-trajectories for protons (top panels) and electrons (bottom panels) with their pitch angles of 30° and the initial kinetic energy of 10 keV (323 eV/nt). Left panels indicate the trajectories for Kp=1 and bottom panels for Kp=4.

where dS and $d\Omega$ are the element of area an the element of solid angle.

For equatorial trapped particles, the equatorial directional differential flux j_0 passing through the equatorial plane having an area of dS is also given by

$$j_0(W, y) = \frac{dN}{2\pi\tau_b y dy dW}, \tag{2.71}$$

where y, τ_b are sine of the pitch angle and the bounce period of the particle with the energy of W and sine of the pitch angle y. This concept is used to obtain the equatorial directional differential flux throughout this dissertation.

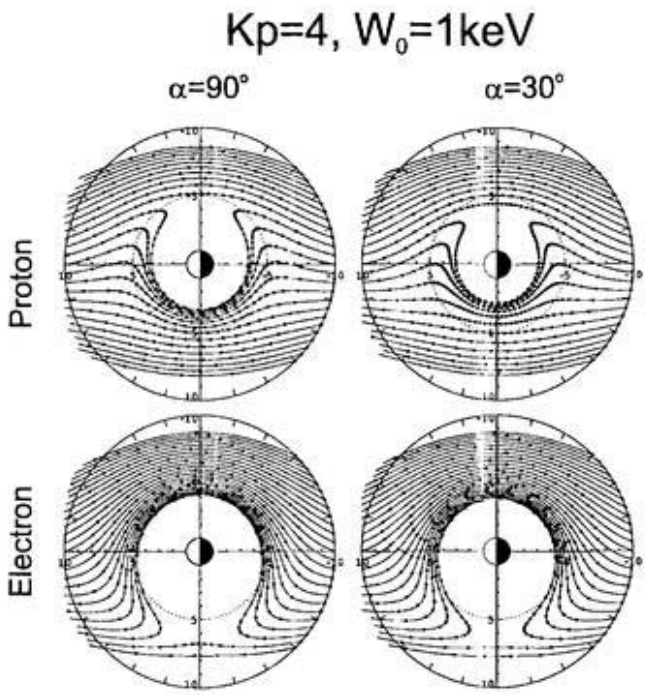

Figure 2.18. Same as previous figure except that the intensity of the convection field dependence of the bounce-average-trajectories for protons (top panels) and electrons (bottom panels) with the initial kinetic energy of 1 keV (32.3 eV/nt) for the convection field for Kp=4. Left panels indicate the trajectories for their initial pitch angle of 90° and bottom panels 30°.

2.3.2 Liouville's theorem and phase space density

The Liouville's theorem describes that the phase space density of particles F specified by the momentum $\boldsymbol{p}$ and spatial coordinate $\boldsymbol{r}$ is conserved in the phase space.

The phase space density (F) is expressed as

$$\begin{aligned} F &= \frac{dN}{d\boldsymbol{r}d\boldsymbol{p}} \\ &= \frac{dN}{dxdydzdp_xdp_ydp_z}, \ [\mathrm{s}^3/\mathrm{m}^6\ \mathrm{kg}^3] \end{aligned} \tag{2.72}$$

where $d\boldsymbol{r}(dx, dy, dz)$ and $d\boldsymbol{p}(dp_x, dp_y, dp_z)$ are a coordinate vector and a momentum vector,

respectively. Here we transform the rectangular coordinates to the spherical coordinates with the polar axis along the velocity vector as

$$\begin{aligned} dxdydzdp_xdp_ydp_z &= (dS \cdot vdt)(p^2dpd\Omega) \\ &= p^2dSdtdWd\Omega, \end{aligned} \tag{2.73}$$

$$\tag{2.74}$$

where v is the velocity. Note that $vdp = dE$ since $E = p^2/2m$, where m is the mass. Thus, the directional differential flux j can be rewritten as

$$\begin{aligned} j &= \frac{dN}{dSdtdWd\Omega} \\ &= p^2F. \end{aligned} \tag{2.75}$$

The Liouville's theorem is applied to map the phase space density at a given location in this simulation.

Chapter 3

Dynamic model of plasmasphere and Coulomb collision loss for energetic ions

3.1 Introduction

The dominant loss processes of energetic ions in the magnetosphere have been considered to be the charge exchange with neutral atoms [e.g., *Frank*, 1967; *Swisher and Frank*, 1968; *Prülss*, 1973; *Tinsley*, 1976; *Lyons and Evans*, 1976; *Smith et al.*, 1978; *Smith and Bewtra*, 1978; *Smith et al.*, 1981; *Kistler et al.*, 1989; *Noël*, 1997; *Ebihara et al.*, 1998b] and the Coulomb collision with dense cold plasmas in the plasmasphere [e.g., *Wentworth et al.*, 1959; *Liemohn*, 1961; *Kistler et al.*, 1989; *Fok et al.*, 1991]. The number densities of scattering particles are required when we consider the lifetimes of the charge exchange and

Coulomb collision losses. Though the distribution of neutral atoms for the charge exchange is relatively steady, the distribution of plasmaspheric cold plasmas for the Coulomb collision is drastically changed with the magnetospheric activity [e.g., *Chappell et al.*, 1970a; *Chappell et al.*, 1970b; *Chappell et al.*, 1971; *Carpenter and Chappell*, 1973; *Maynard and Grebowsky*, 1977; *Chappell*, 1982; *Reasoner et al.*, 1983; *Higel and Wu*, 1984; *Nagai et al.*, 1985; *Horwitz et al.*, 1990] Therefore the time-dependent distribution of the plasmasphere is required to evaluate the Coulomb lifetime of the ring current ions and to discuss the ring current formation and its decay as well.

The plasmasphere is formed by the bulk motion of the cold plasma in the magnetosphere [e.g., *Nishida*, 1966; *Brice*, 1967]. Many authors have discussed the deformation of the plasmapause or detachment of plasmatail [e.g., *Carpenter et al.*, 1966; *Chappell et al.*, 1970; *Chen and Wolf*, 1972; *Grebowsky et al.*, 1974; *Grebowsky and Chen*, 1975; *Maynard and Chen*, 1975; *Horwitz et al.*, 1990; *Moldwin et al.*, 1995; *Gallagher et al.*, 1995]. The thermal plasma of the plasmasphere is supplied from the ionosphere; this physical process is called a refilling process. Many kinds of large-scale refilling models have been proposed; for example, hydrodynamic models [e.g., *Mayr et al.*, 1970; *Moffett and Murphy*, 1973; *Marubashi and Grebowski*, 1976; *Li et al.*, 1983; *Khazanov et al.*, 1984; *Singh and Chan*, 1992; *Guiter et al.*, 1995] and semikinetic models [e.g., *Lin et al.*, 1992; *Wilson et al.*, 1992]. However these models (hydrodynamic and semikinetic models) seem to be inappropriate to obtain the three-dimensional time-dependent distribution of the cold plasma to evaluate the Coulomb collision loss of energetic ions because these models require many computer resources to solve their equations. Here, the total ion contents model described in *Chen*

and Wolf [1972] is applied for modeling the transport of ionospheric plasmas into a flux tube. By solving a differential equation as mentioned below, the saturation density and refilling time constant of the plasmasphere is calculated; this model requires no empirical model for the saturation density and time constant such as *Carpenter and Anderson* [1992] and *Rasmussen et al.*[1993].

The main purpose of this chapter is to evaluate the Coulomb collision loss of the ring current ions by using time-varying three-dimensional plasmaspheric model. To do this, the time-varying three-dimensional plasmaspheric model is presented in Section 3.2. After evaluating both lifetimes of energetic ions (H^+, He^+ and O^+) due to the loss processes in Section 3.3, change of plasma pressure and its ion composition of the ring current during a particular storm are examined in Section 3.4.

3.2 Three-dimensional dynamic model of the plasmasphere

3.2.1 Source of the plasmaspheric thermal protons

The plasmaspheric thermal protons is considered to be supplied from the conjugate ionospheres, where O^+ ions are dominant species. The charge exchange reaction in the topside ionosphere,

$$O^+ + H \rightarrow O + H^+, \tag{3.1}$$

is one of possible sources for the plasmaspheric protons. The resultant protons in the topside ionosphere are carried upward by ambipolar diffusion, and they fill the flux tube in the magnetosphere. The other source for the plasmaspheric protons is the direct photoionization of H atoms in the topside ionosphere as

$$H + h\nu \rightarrow H^+ + e^-. \tag{3.2}$$

However, the photoionization as a source of the plasmaspheric protons has been ignored for the source of the plasmasphere for a long time. In this subsection, a quantitative comparison of the sources, the charge exchange and the photoionization, is made.

Continuity equation

Considering a flux tube that connects with both ionospheres, the continuity equation governing the H^+ density in the flux tube is

$$\frac{\partial n_i}{\partial t} + \frac{\partial (n_i w_i)}{\partial s} = Q - L, \tag{3.3}$$

where n_i, w_i, Q and L are the number density, the bulk velocity, the production rate and the loss rate, respectively. The production rate [*Banks and Kocharts*, 1973] is

$$Q = Q_{cc} + Q_{pi}, \tag{3.4}$$

$$Q_{cc} = \sigma_{cc} n(H) n(O^+) \sqrt{\frac{8k\overline{T_n}}{\pi m(H)}}, \tag{3.5}$$

$$Q_{pi} = I(H) n(H), \tag{3.6}$$

where $Q_{ce}, Q_{pi}, \sigma_{ce}, n(H), n(O^+), k, T_n, m(H)$ and $I(H)$ are the production rate due to the charge exchange, the production rate due to the photoionization, the charge exchange cross section, the number density of H, the number density of O^+, Boltzmann's constant, the temperature of neutral gas, mass of H and the ionization frequency, respectively. By comparing the charge exchange production rate Q_{ce} with the photoionization production rate Q_{pi}, the dominance of the charge exchange process for the source of the plasmaspheric protons will be quantitatively examined.

Production rates

The ionization frequency $I(H)$ is obtained by the integral expressed as

$$\begin{aligned} I(H) &= \int F(\lambda)\sigma_{pi}(\lambda)d\lambda \\ &= \int F_0(\lambda)\exp(-\tau_{opt}(\lambda))\sigma_{pi}(\lambda)d\lambda, \end{aligned} \tag{3.7}$$

where $F, F_0, \sigma_{pi}, \lambda$ and τ_{opt} are the photon flux, the photon flux outside the atmosphere, the ionization cross section, the wave length and the optical depth, respectively.

Samson [1966, pp. 237] gives the ionization cross section σ_{pi} as

$$\sigma_{pi} = \frac{32\pi^2 g q^6 R_c}{3^{3/2} h^3 \nu^3 n_q^5} \tag{3.8}$$

$$= 6.31 \times 10^{-18} g(\lambda/\lambda_0)^3 \ (\mathrm{cm}^{-3}), \tag{3.9}$$

where R_c, n_q, g, q, h and ν are the Rydberg constant, the principal quantum number, the Gaunt factor, the charge, the Planck number, and the frequency, respectively. The Gaunt

factor g varies from 0.8 at the threshold wave length λ_0 to a maximum of 1.0 at approximately 20 nm. The threshold wave length of this reaction λ_0 is taken to be 91.175 nm. The optical depth τ_{opt} can be approximate to ~ 1 in the topside ionosphere [*Banks and Kockarts*, 1973].

The EUV-91 model [*Tobiska*, 1991] gives the spectrum of the solar extreme ultraviolet (EUV) radiation $F_0(\lambda)$ for the wavelength below 105.0 nm. **Figure 3.1** shows the extreme ultraviolet spectrum for the solar maximum (left panel) and the solar minimum (right panel) given by the EUV-91 model.

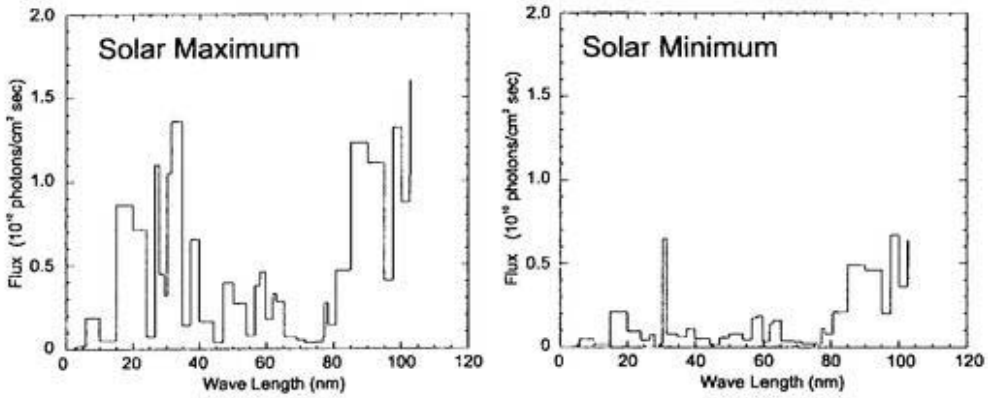

Figure 3.1. EUV spectra obtained by the EUV-91 model for the solar maximum (left panel) and the solar minimum (right panel).

Then the ionization frequencies $I(H)$ become 6.9×10^{-7} sec for the solar maximum and 2.9×10^{-7} sec for solar minimum, respectively. Therefore the production rate due to the photoionization Q_{pi} becomes

$$Q_{pi} = 6.9 \times 10^{-7} n(H)\ (\mathrm{m^{-3}sec^{-1}}) \qquad \text{for solar maximum}$$

$$= 2.9 \times 10^{-7} n(H)\ (\mathrm{m^{-3}sec^{-1}}) \qquad \text{for solar minimum.}$$

Next, the production rate due to the charge exchange is derived. After substituting the charge exchange cross section σ_{ce} being $(1.5 \pm 0.5) \times 10^{-19}$ m^2 [*Banks and Kockarts*, 1973] into Eq.(3.5), we obtain the production rate due to the charge exchange as

$$Q_{ce} = (2.18 \pm 0.73) \times 10^{-17} n(O^+) n(H) T_n^{1/2} \ (\mathrm{m^{-3}sec^{-1}}). \tag{3.10}$$

Altitude profile of the production rates

Typical altitude profiles of the production rates for the solar maximum and the solar minimum are shown in **Figure 3.2**. The IRI-95 [*Bilitza*, 1986] and MSISE-90 [*Hedin*, 1987; *Hedin*, 1991] models are used to obtain these ionospheric and thermospheric quantities. From comparing the production rates at any altitude, it is clear that the charge exchange is the dominant production process for thermal protons by a factor of ~10-1000 in the topside ionosphere. Therefore, the thermal protons produced by the photoionization can be ignored.

3.2.2 Ionosphere-magnetosphere coupling

As discussed in the previous section, the H^+ ions supplying to the plasmasphere are mainly produced by the charge exchange reaction in the conjugate ionospheres, i.e.,

$$O^+ + H \rightarrow O + H^+. \tag{3.1}$$

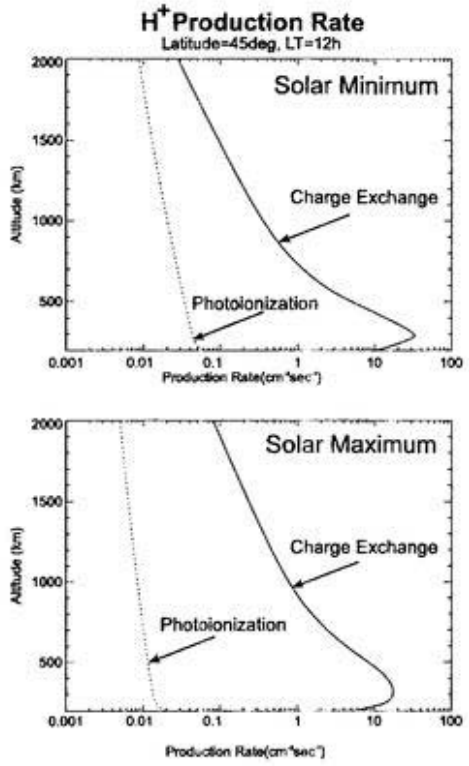

Figure 3.2. Production rates of thermal protons as a function of altitude due to the charge exchange (solid line) and the photoionization (dotted line), respectively, at noon and the geographic latitude of 45 deg. Top and bottom panels show the profile for the solar minimum and the solar maximum, respectively.

The reverse reaction can occur easily because the ionized potentials of H^+ and O^+ are very closed to each other. Therefore the main sink of the H^+ ions is the reactions of

$$H^+ + O \rightarrow H + O^+. \tag{3.11}$$

The continuity equation along a flux tube is given by

$$\frac{\partial F}{\partial s} = Q_{H^+} - L_{H^+}, \tag{3.12}$$

where F is the H^+ flux, s the distance along a field line, Q_{H^+} a production rate of H^+ and L_{H^+} a loss rate of H^+. The production and loss rates, Q_{H^+} and L_{H^+}, are [*Richards and Torr*, 1985],

$$Q_{H^+} = 2.5 \times 10^{-17} T_n^{1/2} n(H) n(O^+) \ (\mathrm{m^{-3}s^{-1}}), \tag{3.13}$$

$$L_{H^+} = 2.2 \times 10^{-17} T_i^{1/2} n(O) n(H^+) \ (\mathrm{m^{-3}s^{-1}}), \tag{3.14}$$

where $n(H), n(O), n(H^+), n(O^+), T_i$ and T_n are densities of neutral hydrogen, neutral oxygen, proton, oxygen ion, and ion and neutral temperatures, respectively. Integrating Eq.(3.12) along a field line, the upward flux becomes

$$F(s) = F_0 \frac{B(s)}{B_0} + B_0 \int_0^s (Q_{H^+} - L_{H^+}) \frac{ds}{B(s)} \ (\mathrm{m^{-2}s^{-1}}), \tag{3.15}$$

where B and s are a magnetic intensity, and the distance along a field line, respectively. The subscript 0 refers to the quantities at the lower boundary altitude z_0 of the production/loss region.

The upward flux will be maximum when the plasmasphere is depleted after a large magnetic storm. In this situation, i.e., $L_{H^+} = 0$, the upward flux becomes maximum and is called as a limiting flux.

The chemical equilibrium is the state that production and loss rates are equal. The concentration of chemical equilibrium H^+ ions in the ionosphere is derived from an equality

of P_{H+} and L_{H+}, i.e.,

$$n(H^+) = \frac{2.5 \times 10^{-17} T_n^{1/2} n(H)}{2.2 \times 10^{-17} T_i^{1/2} n(O)} n(O^+) \ (\mathrm{m}^{-3}). \tag{3.16}$$

The typical profiles of O^+ density and chemical equilibrium H^+ density are shown in **Figure 3.3**. The IRI-95 [*Bilitza*, 1986] and MSISE-90 [*Hedin*, 1987; *Hedin*, 1991] models are used to calculate these ionospheric and thermospheric quantities. The lower boundary z_0 is the altitude where chemical equilibrium H^+ density is equal to O^+ density in **Figure 3.3**. In other words, the bulk motion of the plasma due to the ambipolar diffusion is controlled by H^+ in the region above z_0. The lower boundary altitude is highly sensitive to the solar activity as shown in **Figure 3.4**. The lower boundary in the solar minimum is from 600 km to 800 km depending its local time and latitude, but in the solar maximum (the bottom panel of **Figure 3.4**); the altitudes are roughly twice the altitude in solar minimum (the top panel of **Figure 3.4**).

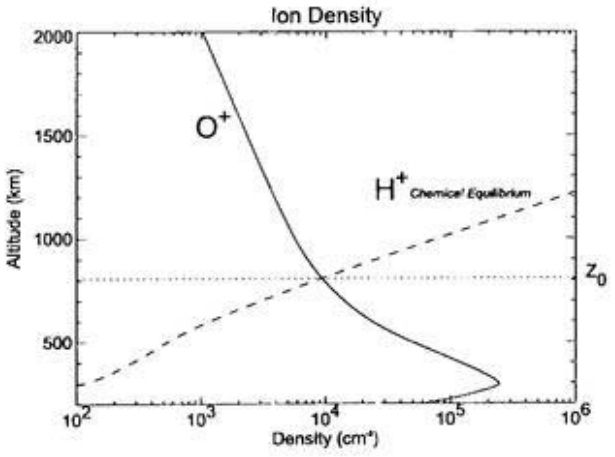

Figure 3.3. Typical profiles of O^+ density (solid line) and the chemical equilibrium H^+ density (dashed line) at noon during summer.

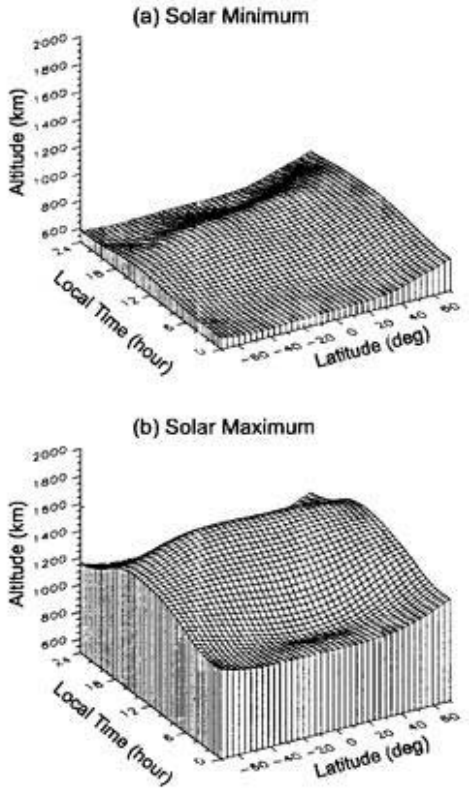

Figure 3.4. The latitudinal and longitudinal variation of the lower boundary altitude z_0 for (a) a solar minimum and (b) a solar maximum.

Since the $n(O^+)$ profile falls off exponentially with altitude, H^+ that escapes to the plasmasphere is produced within one scale height of O^+ [*Raitt et al.*, 1975], and the loss region of H^+ ions also may exist within one scale height of atomic oxygen above z_0. Then, we obtain the flux which can escape to the plasmasphere as,

$$F = P_{H^+} H(O^+) - L_{H^+} H(O) \ (\mathrm{m^{-2}s^{-1}}), \tag{3.17}$$

where $H(O^+)$ is the scale height of O^+ and $H(O)$ the scale height of atomic oxygen at the lower boundary z_0.

Considering a flux tube connecting with both ionospheres, the continuity equation of the total ion content per unit magnetic flux N [*Chen and Wolf*, 1972] is

$$\frac{dN}{dt} = \frac{F_N + F_S}{B_0}, \tag{3.18}$$

where B_0 is the magnetic intensity at the ionosphere, and N is defined as

$$N = \int \frac{n(H^+)h_s}{B} ds \ (\mathrm{Wb}^{-1}), \tag{3.19}$$

where h_s is the coordinate scale factor aligned with a field line. The subscripts N and S represent northern and southern hemispheres, respectively. The average density in a flux tube $\bar{n}$ is

$$\bar{n} = \frac{N}{V} \ (\mathrm{m}^{-3}), \tag{3.20}$$

where

$$V = \int \frac{h_s}{B} ds \ (\mathrm{m}^3\mathrm{Wb}^{-1}). \tag{3.21}$$

Then, the continuity equation of the average density becomes,

$$\frac{d\bar{n}}{dt} = \frac{F_N + F_S}{B_0 V} \ (\mathrm{m}^{-3}\mathrm{s}^{-1}), \tag{3.22}$$

or

$$\frac{d\bar{n}}{dt} = \frac{1}{B_0 V}\Big(\sum_{h=N,S} 2.5\times 10^{-17} T_{n,h}^{1/2} n_h(H) n_h(O^+) H_h(O^+) - n_0 \sum_{h=N,S} 2.2\times 10^{-17} T_{i,h}^{1/2} n_h(O) H_h(O)\Big), \tag{3.23}$$

where n_0 is the H^+ number density at the conjugate ionospheres, corresponding to $n(H^+)$. To solve the ordinary differential equation Eq.(3.23), it is obvious that we must obtain the relation between $\bar{n}$ and n_0.

We assume that the number density along a field line is in hydrostatic equilibrium which is derived from plasma transport equation (e.g.,Eq.(15) of [*Rasmussen et al.*, 1993]) with the following assumptions; (1) pressure is isotropic, (2) temperatures are constant and (3) inertia force is negligible. In the hydrostatic equilibrium state, the distribution with the dipole field as a function of colatitude θ is

$$n(\theta) = n_0 \exp\left\{\frac{Re}{H_0^* L}\left(\frac{1}{\sin^2\theta} - \frac{1}{\sin^2\theta_0}\right)\right\}, \tag{3.24}$$

and

$$H_0^* = \frac{k(T_i + T_e)}{m(H) g_0}, \tag{3.25}$$

where g_0, k, n_0, T_e, T_i and θ_0 are gravity force at surface of the earth, Boltzmann's constant, H^+ density at the altitude of z_0, electron temperature, ion temperature, and colatitude of the production/loss region in the conjugate ionosphere, respectively. In a dipolar geometry,

the colatitude θ_0 is given by

$$\sin^2\theta_0 = \frac{Re + z_0}{LRe}, \tag{3.26}$$

where L and Re are McIlwain's L-value and the earth's radius. The equatorial density n_{eq} is simply given by substituting θ of 90° into Eq.(3.24) as,

$$n_{eq} = n_0 \exp\left\{-\frac{Re}{H_0^* L \tan^2\theta_0}\right\}. \tag{3.27}$$

From Eqs.(3.20) and (3.24), the average density $\bar{n}$ is analytically given by

$$\bar{n} = n_0\Theta, \tag{3.28}$$

where

$$\Theta \equiv \frac{\displaystyle\int_{\pi/2}^{\theta_0} \sin^7\theta \exp\left\{\frac{Re}{H_0^* L}\left(\frac{1}{\sin^2\theta} - \frac{1}{\sin^2\theta_0}\right)\right\} d\theta}{\displaystyle\int_{\pi/2}^{\theta_0} \sin^7\theta d\theta}. \tag{3.29}$$

After substituting Eq.(3.13), (3.14), (3.17) and (3.28) into Eq.(3.22), the differential equation of the average density is obtained as

$$\begin{aligned}\frac{d\bar{n}}{dt} &= \frac{1}{B_0 V}\Big(\sum_{h=N,S} 2.5\times 10^{-17} T_{n,h}^{1/2} n_h(H) n_h(O^+) H_h(O^+) \\ &\quad -\frac{\bar{n}}{\Theta}\sum_{h=N,S} 2.2\times 10^{-17} T_{i,h}^{1/2} n_h(O) H_h(O)\Big).\end{aligned} \tag{3.30}$$

The solution of the ordinary differential equation of Eq.(3.30) clearly has a time constant

τ, so-called refilling time constant,

$$\tau = \frac{B_0 V \Theta}{\sum_{h=N,S} \left(2.2 \times 10^{-17} T_{i,h}^{1/2} n_h(0) H_h(O)\right)}, \tag{3.31}$$

and has the saturation density $\bar{n}_{sat}$,

$$\bar{n}_{sat} = \frac{\Theta \sum_{h=N,S} 2.5 \times 10^{-17} T_{n,h}^{1/2} n_h(H) n_h(O^+) H_h(O^+)}{\sum_{h=N,S} 2.2 \times 10^{-17} T_{i,h}^{1/2} n_h(0) H_h(O)}. \tag{3.32}$$

3.2.3 Formation of the plasmasphere

The thermal protons supplying into a flux tube are radially and azimuthally moved by drift motion in the magnetosphere. The motion is governed by the $E \times B$ drift because plasmaspheric protons are cold with temperature of ~ 1 eV [e.g., *Olsen et al.*, 1987]. In this model, the thermal protons are traced under the dipolar magnetic field and the corotation electric field and the time-dependent convection field whose electric potential is expressed by the Volland-Stern type [*Volland*, 1973; *Stern*, 1975] as

$$\Phi = AR^{\gamma} \sin\phi, \tag{2.55}$$

where R is a geocentric distance, ϕ a magnetic local time, γ a shielding factor and A a factor indicating the strength of the convection. Here, the shielding factor γ is taken to be 2. Following *Maynard and Chen* [1975], the intensity factor A as a function of Kp is given

by

$$A = \frac{0.045}{(1 - 0.159Kp + 0.0093Kp^2)^3} \ (\mathrm{kV/Re^2}). \tag{2.56}$$

Figure 3.5 shows a schematic diagram of this plasmaspheric model; the thermal protons are produced by the charge exchange reaction in the conjugate ionospheres at the altitude of z_0. After transported by the ambipolar diffusion into the magnetosphere, they are azimuthally and radially moved by the $E \times B$ drift motion in the magnetosphere. The number density in the flux tube is obtained by solving the differential equation of Eq.(3.22).

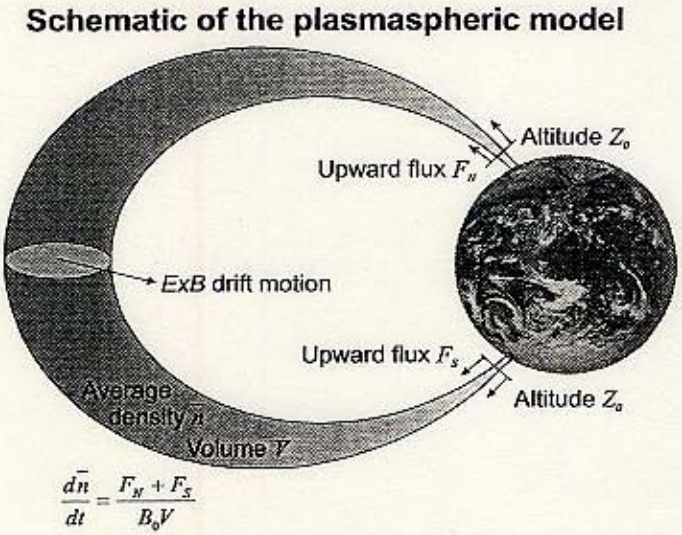

Figure 3.5. Schematic of this plasmaspheric model.

3.2.4 Comparison with satellite observations

The EXOS-B satellite (JIKIKEN) was launched on September 16, 1979 into a near equatorial orbit (the apogee of 5.1 Re, the height of perigee of 225 km and the inclination of

31°). Because of the low inclination orbit, EXOS-B could sweep widely from the ionosphere to beyond the plasmapause in the near equatorial plane. An electron density is directly calculated from an upper hybrid resonance frequency which is measured by a frequency swept impedance probe (IPS) [*Ejiri et al.*, 1981] aboard EXOS-B using a length of 33.4 m antenna, a frequency range from 10 kHz to 3 MHz with a swept period of 2 sec (high bit rate) or 8 sec (low bit rate).

Three days' data sets of EXOS-B from August 11-13, 1981, when EXOS-B had an apogee of near midnight, are used to compare with the result of the numerical simulation. There are three available orbits during the days. One of the orbits of EXOS-B (on August 12, 1981) projected in the equatorial plane is shown in **Figure 3.6** with a snapshot of a contour map of the calculated proton number density at 1400 UT on August 13, 1981. A purple line in the bottom panel indicates the orbit of EXOS-B passing from the dusk side to the dawn side through an apogee of L=5.1. A marked dot on the purple line represents the position of EXOS-B at 1400 UT on August 12, 1981. At this time, a bulge of the plasmasphere is clearly seen in near midnight, being corotated with the earth.

The three days' profiles of the electron density observed by EXOS-B along their trajectories and profiles of the proton density calculated by this numerical model are shown in **Figure 3.7**. The number density of electrons is assumed to be equal to the number density of protons due to charge neutrality. The comparisons between calculated profiles and observed profiles for the three orbits are summarized as followings:

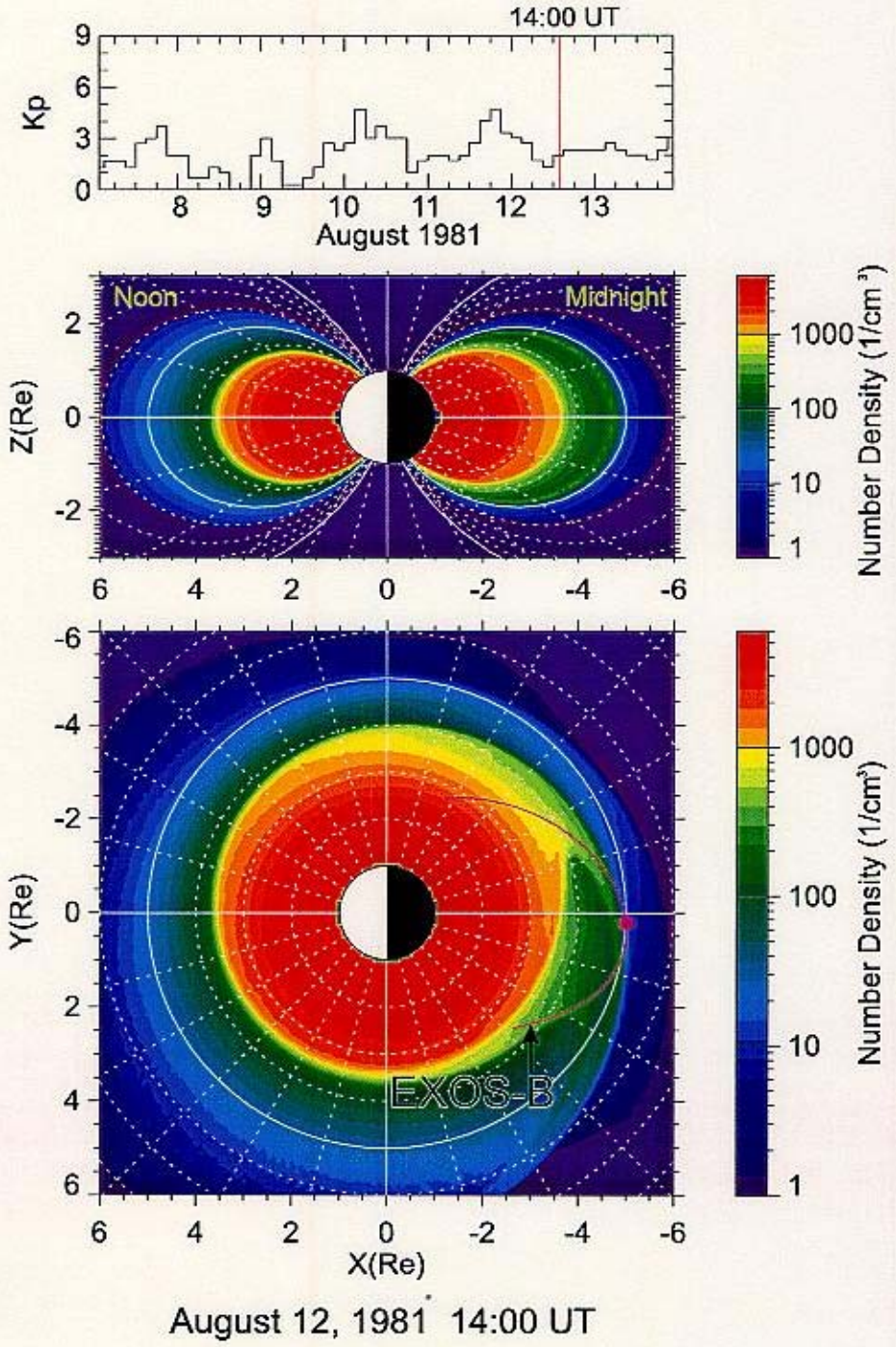

Figure 3.6. A snapshot of calculated number density of the plasmaspheric protons in the noon midnight meridian plane (middle panel) and in the equatorial plane (bottom panel) at 1400 UT of August 12, 1981. A purple line represents the trajectory of EXOS-B and a dot indicates the satellite's position at 1400 UT. The Kp indices are shown in the top panel.

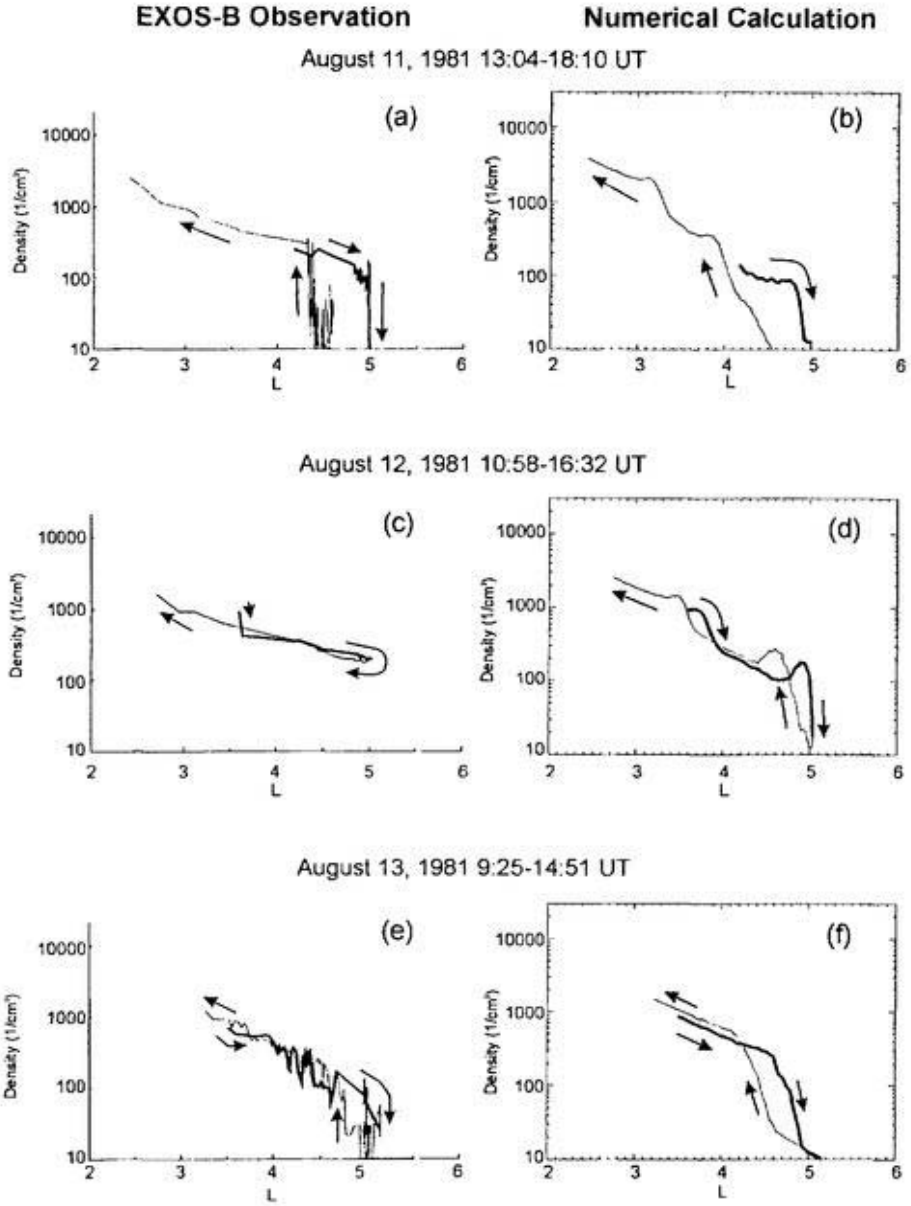

Figure 3.7. Three days' radial profiles of thermal electron density observed by EXOS-B (left side) and profiles of thermal proton density calculated by the model (right side) along the trajectories of EXOS-B in the periods of 1304-1810 UT of August 11, 1981 (top panels), 1058-1632 UT of August 12 (middle panels), 0925-1451 UT of August 13 (bottom panels). The thick lines represent the outbound paths.

Orbit on August 11, 1981

A weak magnetic storm with minimum Dst of -41 nT was occurred on August 11, 1981, being caused by an enhanced convection; an estimated polar cap potential [*Boyle et al.*, 1997] gradually increased and reached its maximum of 120 kV around 2000 UT on August 11. A main phase of the storm lasts from 1000 UT on August 11 until 2100 UT on the same day. In the main phase of the storm, EXOS-B observed the electron density during the period of 1304-1810 UT on August 11; the results are shown in top panels of **Figure 3.7**. EXOS-B intersected the plasmapause at L=4.98 and L=4.34 along the outbound and inbound paths, respectively. The difference between them is ΔL=0.64 whereas the calculation gives ΔL=0.86. Though the observed location of the plasmapause is slightly different, the changes in space and time coincide each other with the accuracy of about 34 %.

Orbit on August 12, 1981

A recovery phase of the storm lasts until 1400 UT on August 12, and the enhanced convection gradually decreased. In the second orbit (1058-1632 UT on August 12; middle panels), EXOS-B didn't encounter the plasmapause in this orbit; it seems as if the plasmasphere was refilled within a day. However it takes more than five days to refill the depleted plasmasphere up to the density of the order of 100 cm^{-3} at L=5 by our calculation. Therefore the ionospheric outflow hardly refills the plasmasphere up to the observed density $\sim$100 cm^{-3} at L=5 within a day. One possible reason is that EXOS-B observed a bulge (or a plasmatail) corotated with the earth from the noon-dusk quadrant in the weak-

ened convection. **Figure 3.8** shows a time series of the equatorial number density during the recovery phase of the weak storm from 2000 UT on August 11 to 1600 UT on August 12. At the most disturbed time (2000 UT on August 11), the dense region extending from the core plasmasphere to the dayside magnetopause (a plasmatail) is clearly seen in the noon-dusk quadrant. As the convection was decreased, the plasmatail began to corotate with the earth because the open-close boundary of zero-energy drift motion was spread out. When the plasmatail (or a bulge) corotated and reached around midnight, the EXOS-B satellite passed through the coroted plasmatail. Therefore EXOS-B did not encounter the plasmapause in the second orbit. **Figure 3.9** shows this explanation schematically.

Orbit on August 13, 1981

The magnetosphere was relatively quiet (Kp $\leq$ 3) in the third orbit (0925-1451 UT on August 13). The calculated profile (panel of 'f' of **Figure 3.8**) shows that the location of the plasmapause segments is $4.6 \leq L \leq 4.9$ (outbound) and $4.1 \leq L \leq 4.6$ (inbound) and the absolute electron density is approximately 900 cm^{-3} at $L = 3.5$ and 300 cm^{-3} at $L = 4.5$ (outbound); the calculation is in good agreement with the observation on the location of the plasmapause and the absolute electron density except for the fine structure.

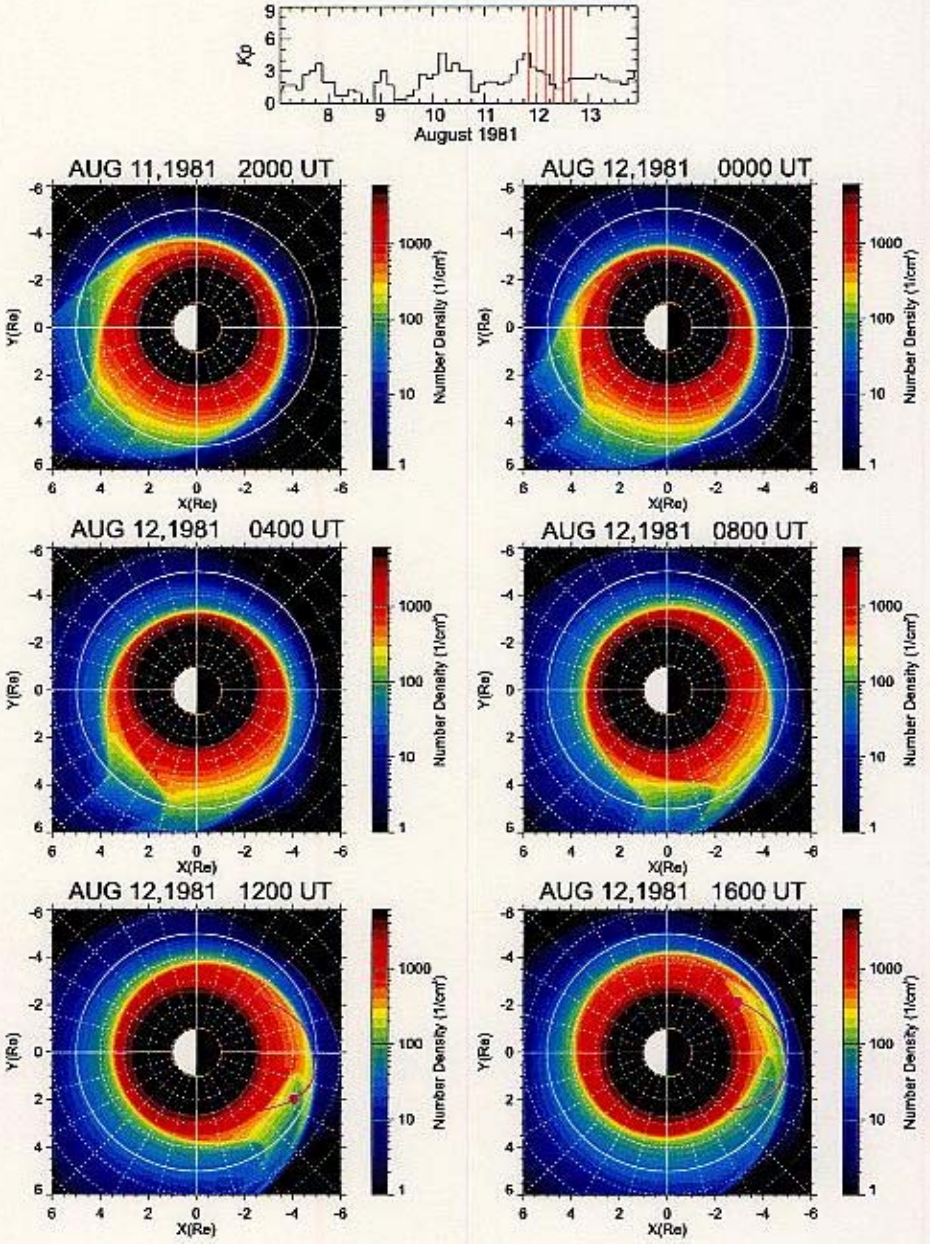

Figure 3.8. A time series of the equatorial number density of cold electrons form 2000 UT on August 11 to 1600 UT on August 12. A purple line drawn in bottom panels indicates the EXOS-B orbit.

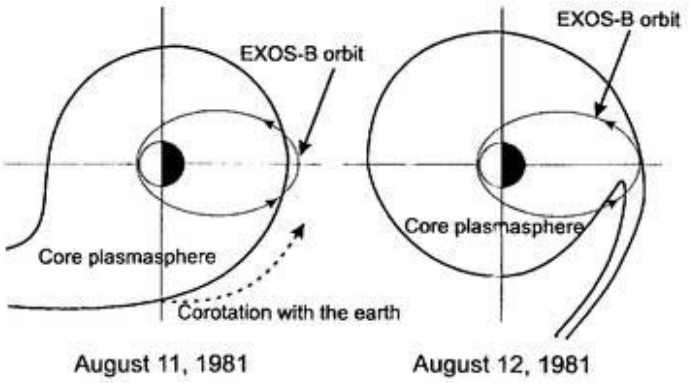

Figure 3.9. Schematic for the explanation of the EXOS-B observation.

3.3 Lifetimes of energetic ions

3.3.1 Coulomb collision lifetime

The Coulomb decay lifetime of the ring current ions is calculated by a method of *Fok et al.*[1991], which has been calculated with the assumption that a distribution function of the plasmaspheric plasmas is Maxwellian with temperature of 1 eV. The normalized Coulomb lifetimes of H^+ He^+ and O^+ ions as a function of energy are plotted in **Figure 3.10**, showing energy dependence of the lifetimes. The Coulomb loss lifetime is short in lower energy. For example, if the ring current ions with energy of 1 keV stay in the plasmasphere whose density is 100 cm^{-3}, the lifetimes of H^+, He^+ and O^+ ions due to the Coulomb collision loss are 1.6, 4.9 and 19 days, respectively. For the energy of 10 keV, the lifetimes are 11, 9.6 and 22 days, respectively.

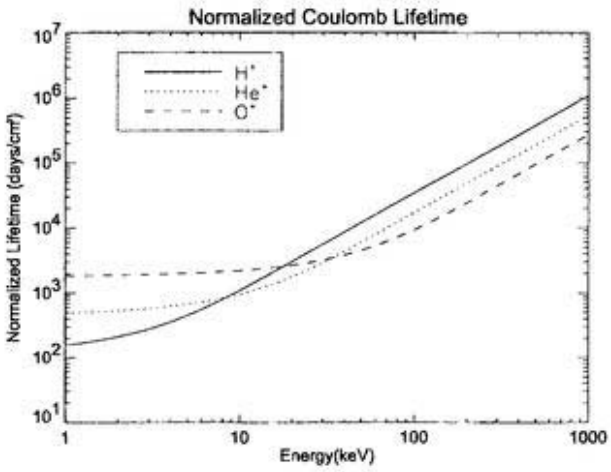

Figure 3.10. The normalized Coulomb lifetimes of H^+(solid line), He^+(dotted line) and O^+(dashed line) ions derived by the formulas of *Fok et al.*[1991].

3.3.2 Charge exchange lifetime

The other major loss process of the ring current ions is the charge exchange. As described in *Kistler et al.*[1989], the dominant charge exchange loss of H^+, He^+ and O^+ ions are due to the reactions of

$$H^+ + H \rightarrow H + H^+, \tag{3.33}$$

$$He^+ + H \rightarrow He + H^+, \tag{3.34}$$

$$O^+ + H \rightarrow O + H^+. \tag{3.35}$$

The charge exchange lifetime for an energetic ions τ_{cc} is given by

$$\tau_{cc} = \frac{1}{n(H)\sigma v}, \tag{3.36}$$

where $n(H), \sigma$ and v are the number density of neutral hydrogen, the charge exchange cross section, and the thermal velocity of an bouncing ion, respectively.

A spherically symmetric model derived by *Chamberlain* [1963] is used to obtain the number density of the neutral hydrogen. Parameters for the Chamberlain model are given by *Rairden et al.* [1986]; the parameters are exobase temperature, 1050 K; exobase density, 44000 cm^{-3}; geocentric distance of exobase r_c, 1.08 Re (500 km altitude); and a critical radius for satellite atoms, 3.0 r_c. The fitting parameters was derived from the ultraviolet photometer imaging by DE1 satellite [*Rairden et al.*, 1986].

The charge exchange cross section is given by *Janev and Smith* [1993] for H^+ ions and *Smith and Bewtra* [1978] for He^+ and O^+ ions. The normalized charge exchange lifetime (defined as $\tau_{cc} \times n(H)$) for H^+, He^+ and O^+ ions as a function of energy are plotted in **Figure 3.11**. For example, the charge exchange lifetimes of the ring current H^+, He^+ and O^+ ions with energy of 1 keV at the geocentric distance of 4 Re are 0.57, 108, 5.3 days, respectively. For the energy of 10 keV, the lifetimes are 0.41, 11 and 2.0 days, respectively. For the energies below 45 keV, the charge exchange lifetime of H^+ ions is shorter than that of O^+ and vice versa.

3.3.3 Spatial distribution of the lifetimes

The lifetimes due to the loss processes depend on the density of scattering particles, i.e., the lifetimes of an energetic ion is a function of its position and time. **Figure 3.12** indicates the spatial distribution of the lifetimes for 10 keV ions with an equatorial pitch angle of 90° due to the Coulomb collision (left panels) and the charge exchange (right

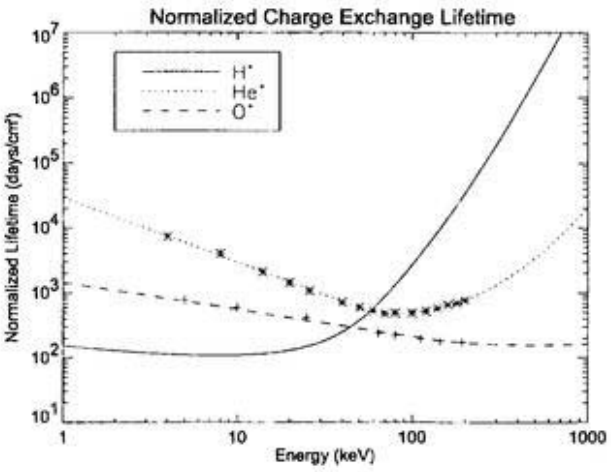

Figure 3.11. The normalized charge exchange lifetimes of H^+(solid line), He^+(dotted line) and O^+(dashed line) ions. The H^+ lifetimes is given by *Janev and Smith* [1993], and the lifetimes of He^+ and O^+ are given by *Smith and Bewtra* [1978]. The data points are the experimental value of *Smith and Bewtra* [1978].

panels). As an example, the Coulomb collision lifetime is obtained by using a snapshot of the calculated plasmaspheric density at 2100 UT of August 11, 1981, when the Dst index reached its minimum in a weak magnetic storm. The Coulomb lifetimes of 10 keV ions, H^+, He^+ and O^+, are resemble each other. There are two characteristics to be noted:

1. The energetic ions with its energy of 10 keV at L=3 have a Coulomb lifetime of a day; the Coulomb collision cannot be ignored for energetic ions in the plasmasphere because the lifetime is shorter than the typical duration of a storm. The Coulomb collision can be ignored in the outer plasmasphere because the lifetime is above ~10 days.

2. Charge exchange loss is important for 10 keV H^+ ions; the lifetime is below a day in the region of $L \leq 5$ and below 3 hours in the region of $L \leq 3$. For the He^+

ions, the charge exchange lifetime is longer than that of the Coulomb collision, i.e., the Coulomb collision loss dominates the charge exchange loss for He^+ ions with energy of 10 keV. On the contrary, for the O^+ ions with energy of 10 keV, the charge exchange lifetime is comparable to the Coulomb lifetime in the plasmasphere whereas the charge exchange becomes the dominant loss process in the outer plasmasphere.

3.4 Discussion

In the previous section, the lifetimes of energetic ions due to the charge exchange and Coulomb collision loss processes have been examined. In this section, loss effects of energetic ions on macroscopic quantities, such as the pressure (energy density), due to the charge exchange and the Coulomb collision loss processes are examined for a particular magnetic storm.

3.4.1 Change of storm time pressure due to the loss processes

To examine the loss effects of the plasma pressure, many ions having various energies and equatorial pitch angles are traced. After tracing the ions under a dipole magnetic field, a corotation electric field and the Volland-Stern type convection field with its intensity depending on Kp indices, the directional differential flux in the equatorial plane is calculated. By integrating the differential flux, the plasma pressure are obtained. The method to derive the plasma pressure is described in below.

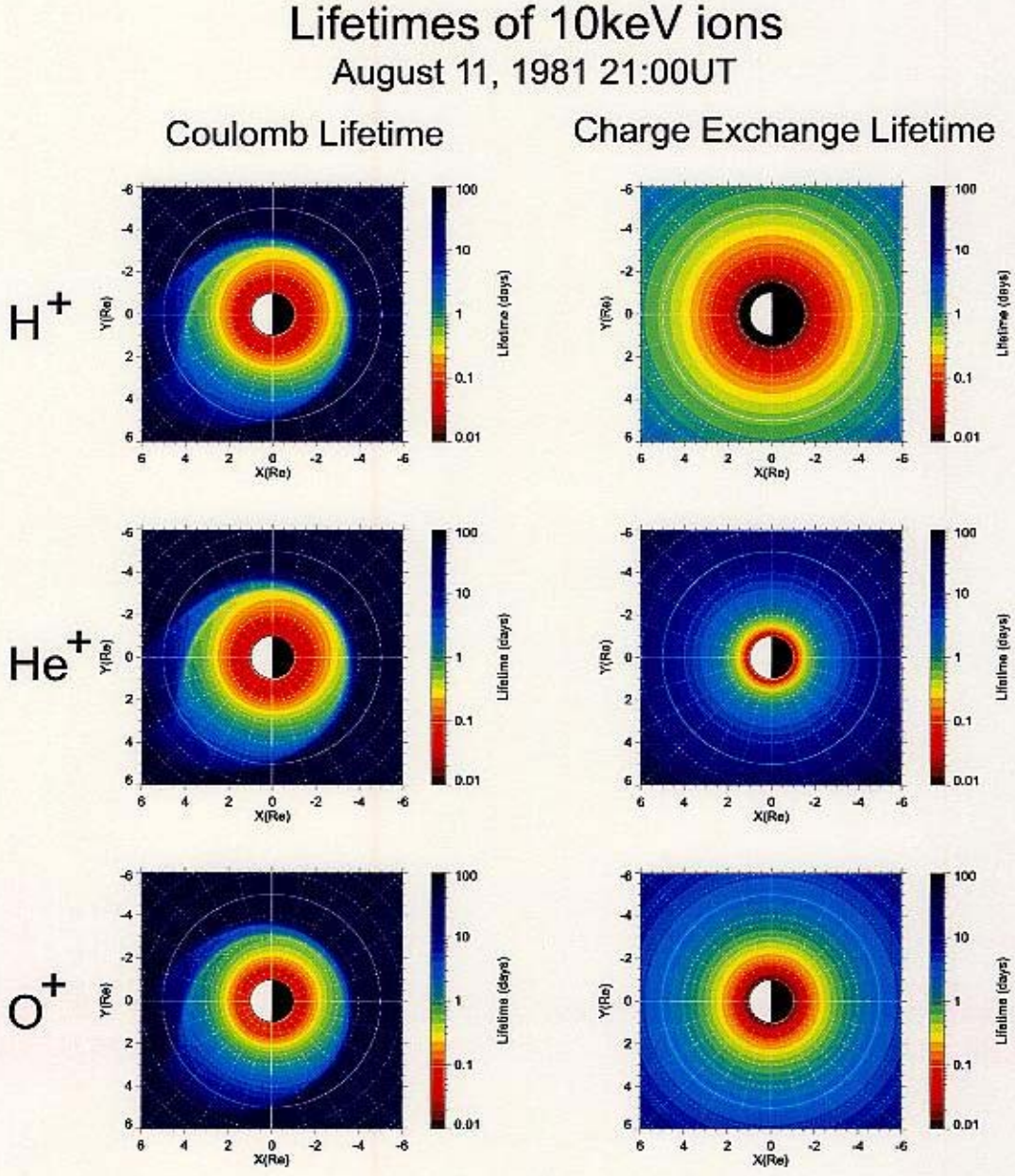

Figure 3.12. The calculated lifetimes in the equatorial plane for 10 keV H^+(top), He^+(middle) and O^+(bottom) ions due to Coulomb collision (left side) and the charge exchange (right side) at 2100 UT of August 11, 1981.

Initial and boundary conditions

The ions whose distribution function is initially isotropic Maxwellian with the temperature of 5 keV and the density of 0.22 cm^{-3} are injected from the boundary azimuthally located at L=8 with 21h $\leq$ MLT $\leq$ 3h. The composition ratio of H^+, He^+ and O^+ ions at the source boundary is fixed to be 0.8, 0.05 and 0.15, respectively. The magnetosphere is initially empty, that is, all ions are transported from the night side boundary by the convection.

Drift trajectories

Drift trajectories of ions are traced by bounce-average approximation under a dipole magnetic field, a time-dependent convection electric field and a corotation electric field. The followings are assumed in this model; (1) the first two invariants are conserved, (2) field lines are equipotential and (3) motion of particles induces no additional field. The numerical method to trace the bounce-average trajectory is described in *Ejiri* [1978]; time development equations of the bounce-average drift motion becomes

$$\frac{dX}{dt} = -\frac{\omega}{\gamma} X^{\gamma+2} \cos\phi, \tag{2.63}$$

$$\frac{d\phi}{dt} = \omega X^{\gamma+1} \sin\phi + \omega - \frac{3\mu G(y_0)}{qR_s^2 X^2}, \tag{2.64}$$

$$X \equiv \frac{R}{R_s}, \tag{2.66}$$

where $q, \omega, \mu, R_s, \gamma$ and G are particle charge, angular velocity of earth's rotation, first adiabatic invariant (magnetic moment), a geocentric distance of a stagnation point at

MLT of 18h for a zero energy particle, a shielding factor being taken to be 2 and a function of an equatorial pitch angle given by *Ejiri* [1978], respectively.

Convection electric field

The Volland-Stern type convection field represents the electric potential Φ as

$$\Phi = AR^{\gamma} \sin \phi, \tag{2.55}$$

where R is a geocentric distance, ϕ a magnetic local time, A a factor indicating the strength of the convection. Here, the shielding factor γ is taken to be 2. Following *Maynard and Chen* [1975], the intensity factor A is given by

$$A = \frac{0.045}{(1 - 0.159Kp + 0.0093Kp^2)^3} \ (\mathrm{kV/Re^2}). \tag{2.56}$$

Charge exchange and Coulomb collision loss processes

The ions are lost by three physical processes; the charge exchange with the neutral hydrogen, the Coulomb collision with thermal plasmas, and convection outflow due to arrival at the magnetopause azimuthally located at L=11.

A trapped ion bouncing between northern and southern mirror points experiences different density of the neutral hydrogen aligned with its bouncing trajectory. The bounce-average density of the neutral hydrogen for an bouncing ion is introduced and is given

by

$$\langle n_H \rangle \equiv \frac{\int \frac{n(s)}{v_\parallel(s)} ds}{\int \frac{1}{v_\parallel(s)} ds} \tag{3.37}$$

$$\simeq \frac{n'_H}{\cos^j \lambda_m}, \tag{3.38}$$

where $v_\parallel, ds, j, n'_H$ and λ_m are parallel velocity of an ion, a line element aligned with a field line, an approximate factor, the equatorial density of the neutral hydrogen, and the mirror latitude, respectively. After substituting Eq.(3.38) into Eq.(3.36), the charge exchange lifetime for a bouncing ion can be approximated as

$$\tau_{ce} \simeq \frac{\cos^j \lambda_m}{n'_H \sigma_H v}. \tag{3.39}$$

Following *Smith and Bewtra* [1978], the approximate factor j is taken to be 3.5. Then the lifetimes due to the charge exchange and the Coulomb collision can be expressed as

$$\frac{1}{\tau} = \frac{1}{\tau_{ce}} + \frac{1}{\tau_{cc}}, \tag{3.40}$$

where τ_{cc} is the lifetime due to the Coulomb collision. Using the lifetimes, number of ions lost by the charge exchange is calculated along with their bounce-average trajectories. This process can be numerically expressed as

$$\frac{\partial f}{\partial t} = -\frac{f}{\tau}, \tag{3.41}$$

where f is the phase space density.

Directional differential number flux

The method to calculate an equatorial differential flux is as follows: First, all packet particles are gathered into a small phase space bin $(\Delta L, \Delta\phi, \Delta W, \Delta y)$, where L, ϕ, W and y are McIlwain's L-value, MLT, the kinetic energy and a sine of a pitch angle, respectively. Next, the directional differential flux in the equatorial plane $j_0(L, \phi, W, y)$ as

$$j_0(L, \phi, W, y) = \frac{\Delta N_{bin}}{2\pi S \tau_b y \Delta y \Delta W}, \tag{3.42}$$

where $\Delta N_{bin}, S$ and τ_b are the real number of gathered particles in the bin, the area of a virtual detector in the equatorial plane and the bounce period of a particle, respectively.

The off-equatorial differential flux j_0 at a latitude of λ can be derived from the Liouville's theorem [*Roederer*, 1970] as

$$j(L, \phi, \lambda, W, y) = j_0(L, \phi, W, h(\lambda)y), \tag{3.43}$$

with

$$h(\lambda) \equiv \frac{\cos^3 \lambda}{(1 + 3\sin^2 \lambda)^{1/4}}. \tag{3.44}$$

Plasma pressure

The perpendicular pressure $P_\perp$ and the parallel plasma pressure $P_\parallel$ are given by

$$P_\parallel = \int mv^2 F(\boldsymbol{v}) \cos^2 \alpha d\boldsymbol{v}, \tag{3.45}$$

$$P_{\perp} = \int \frac{1}{2} m v^2 F(\boldsymbol{v}) \sin^2 \alpha \, d\boldsymbol{v}, \tag{3.46}$$

where F is the velocity distribution function and m the particle's mass. The pressure can be expressed by using the directional differential flux j instead of the velocity distribution function F as

$$P_{\perp} = \pi\sqrt{2m} \int_{\alpha}\int_{W} j\sqrt{W} \sin^3 \alpha \, d\alpha \, dW, \tag{3.47}$$

$$P_{\parallel} = 2\pi\sqrt{2m} \int_{\alpha}\int_{W} j\sqrt{W} \cos^2 \alpha \sin \alpha \, d\alpha \, dW. \tag{3.48}$$

3.4.2 Result

Change of pressure due to the loss processes

On June 4-8, 1991, an intense magnetic storm with minimum Dst of -223 nT occurred, having a complex main phase and two step recovery phase. During the storm, the CRRES satellite observed the ion flux for each species in the near equatorial plane. The CRRES satellite was launched on 25 July 1990 into a geosynchronous transfer orbit (GTO) with the apogee of 33584 km, the perigee of 350 km and the inclination of 18.1° . From the ion composition observation by the CRRES MICS (Magnetospheric Ion Composition Spectrometer) instrument during the intense storm, *Roeder et al.*[1996] reported on the change of plasma pressure (energy density) as follows; (1) the percentage of relative O^+ pressure to the total at L=3-5 increased from 7 % prior to the storm to 29 % in the recovery phase, that means the relative ion composition never became dominated by oxygen, (2) the fastest decreasing ion was O^+ at L=3-6 in the recovery phase.

The results of the calculation are shown in **Figure 3.13**. Dst indices are shown in the top panel, indicating a complex main phase and two step recoveries constituting the rapid initial recovery and the slow recovery. The second panel represents a contour of number density of cold electrons in the meridian of midnight; the plasmasphere drastically shrank during the disturbed period. The last two panels are the radial profiles in the midnight meridian at 0000 UT on June 7, 1991 during the later recovery phase of the storm (denoted by (C) in the top panel). The third panel shows the loss rates of the plasma pressure. In the region of $L \leq 3$, one can find that (1) the Coulomb collision loss of the pressure is effective in the region of $L < 3$ because the core region of the plasmasphere (≥ 100 cm^{-3}) shrank within $L \simeq 3$ at midnight during the storm as shown in the second panel, (2) the Coulomb collision loss is more effective for the He^+ and O^+ than H^+ and (3) on the other hand, the charge exchange loss is more effective for H^+ than He^+ or O^+.

The bottom panel of **Figure 3.13** shows the plasma pressure as a function of L. The pressure has a peak at $L \sim 3.8$. The composition ratio is relatively steady in the high L region whereas the ratio is highly changed in the low L region. It is clear that H^+ becomes a minor composition relative to O^+ and He^+ at $L \leq 2.3$ in the later recovery phase. *Roeder et al.* [1996] reported that the percentage of relative O^+ pressure to the total at L=3-5 increased from 7 % prior to the storm to 29 % in the storm and the O^+ pressure decreased rapidly. However, this cannot be explained by this model calculation. This suggests that the drastic enhancement of O^+ ions in the near-earth plasma sheet may be introduced.

The absolute quantities of the observed pressure around L=3.5 are 32 nPa, 8 nPa and 13 nPa for H^+, He^+ and O^+ ions, respectively. However, the absolute calculated pressure

is smaller than the observed one. More realistic source condition in the near-earth plasma sheet and the convection model will be required to explain the absolute quantities; this will be examined in Chapter 5.

Change of ion composition ratio due to the loss processes

A time series of the composition ratio of the pressure as a function of L is shown in **Figure 3.14**. Three curves in each panel indicate the H^+, He^+ and O^+ composition ratio as a function of L, respectively. Because the ion composition ratio in the near-earth plasma sheet is assumed to be 0.8, 0.05 and 0.15 for H^+, He^+ and O^+ ions, respectively, the ratio is almost constant at high L. However, the ratio is drastically changed by the loss processes at low L; H^+ becomes a minor species in the region of $L \leq 1.8$ at 1900 UT on June 5 (labeled as A), when the initial rapid recovery begins. The composition ratio is almost kept until the rapid recovery phase ends at 0400 UT on June 6 (labeled as B). After then, the composition ratio changes gradually. In fact, CRRES observed the enhancement of the composition ratio of O^+ pressure up to 29 % at L=3-5 in the recovery phase [*Roeder et al.*, 1996]. However, this cannot be explained by this model simulation being the steady initial ion composition ratio. Therefore, the drastic change of O^+ ions in the near-earth plasma sheet may be introduced. Indeed, ionospheric ions (such as O^+ and He^+) obviously increase relative to the solar wind originated ions in the plasmasheet during a storm [*Peterson et al.*, 1981; *Sharp et al.*, 1982; *Lennartsson and Shelly*, 1986; *Daglis et al.*, 1994].

An initial rapid recovery of a magnetic storm has been considered to be caused by the relatively shorter charge exchange lifetime of O^+ ions. However, the calculational result

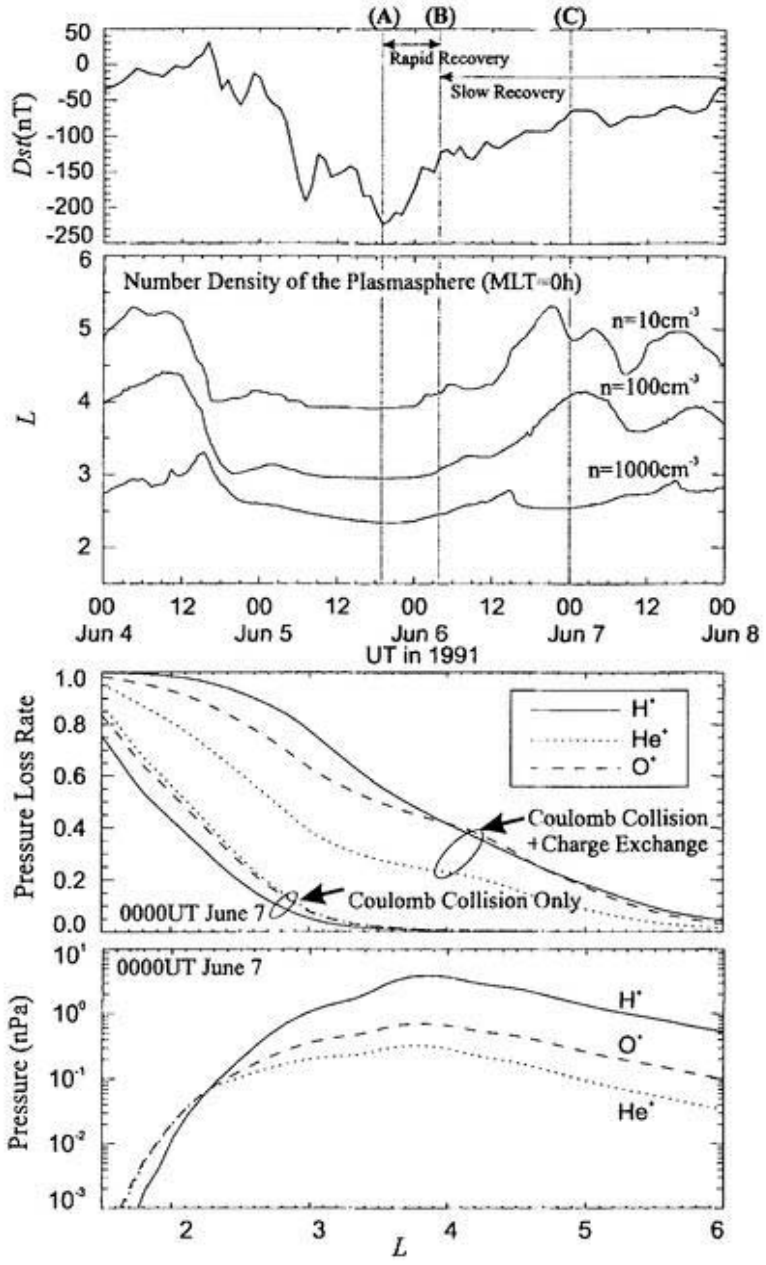

Figure 3.13. The panels show from top to bottom; (top panel) the Dst index of the magnetic storm on June 4-8, 1991, (second panel) a contour showing plasmaspheric number densities of 10 cm^{-3}, 100 cm^{-3} and 1000 cm^{-3} in the midnight meridian, (third panel) the radial profile in the midnight meridian at 0000 UT on June 7, 1991; the loss rate due to Coulomb collision (lower left group) and loss rate due to Coulomb collision and charge exchange (upper right group), (bottom panel) also the radial profile in the midnight meridian of the plasma pressure of H^+, He^+ and O^+. The loss rate of 1.0 means that the pressure is completely lost.

shows that there is no drastic change of O^+ pressure during the initial rapid recovery. Thus the shorter charge exchange lifetime of O^+ ions is not a good explanation for the rapid initial recovery of *Dst* for this particular storm. The sources for the initial rapid recovery also will be mentioned in Chapter 5.

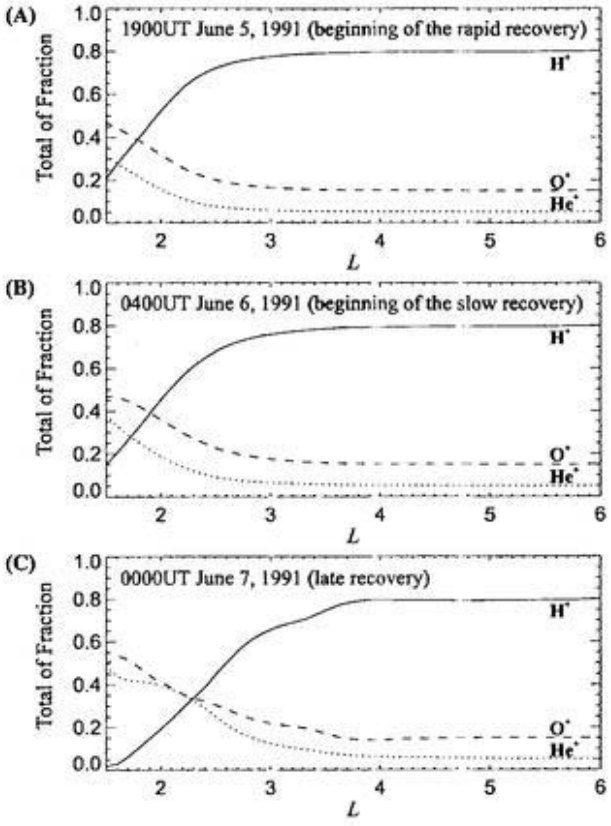

Figure 3.14. The composition ratio of the H^+, He^+ and O^+ pressure in the midnight meridian (A) at 1900 UT on June 5, 1991 (beginning of the rapid recovery), (B) at 0400 UT on June 6, 1991 (end of the rapid recovery and beginning of the slow recovery) and (C) at 0000 UT on June 7, 1991 (late recovery).

3.5 Conclusion

In this chapter, the time-dependent plasmaspheric model is developed to evaluate the Coulomb collision loss for ring current ions. This model is derived from the total flux tube content model of *Chen and Wolf* [1972] with the assumptions; (1) the primary ion species in the plasmasphere is H^+, (2) the main source and sink of the plasmaspheric H^+ ions are the charge exchange reaction in the conjugate ionospheres, and the production and loss regions are the altitude where the chemical equilibrium H^+ density is equal to O^+ density, (3) the distribution aligned with a field line is hydrostatic equilibrium and (4) the magnetic field is a dipole and the electric field consists of the Volland-Stern type convection field and the corotation field.

The accuracy of this model is examined by comparing with the EXOS-B satellite observations during the period of a weak magnetic storm during a period of August 11-13, 1981. The calculated radial profiles of the electron density shown in **Figure 3.7** are in good agreement with the EXOS-B observation with respect to the absolute density, relative displacements of the plasmapause and the dynamical feature of the plasmasphere.

Using this plasmaspheric model, the spatial variation of the Coulomb collision lifetimes of the energetic ions is evaluated; the Coulomb collision loss is comparable to the charge exchange loss for all major species (H^+, He^+ and O^+) with energies below a few tens of keV in the plasmasphere as pointed out by *Fok et al.*[1991]. However, the Coulomb collision loss for energetic ions is almost restricted within the core plasmasphere. Therefore, during a magnetic storm, the Coulomb collision loss hardly affects the ions that contribute to the ring current flowing at L ~4-6 because the plasmasphere shrinks due to an enhanced

convection field.

Chapter 4

Enhancements of a differential flux of energetic ions associated with a substorm

4.1 Introduction

The energetic particles injected from the near-earth plasma sheet have a characteristic energy dispersion signature when they penetrate into the inner magnetosphere due to their energy and pitch angle dependent drift trajectories. Especially, a 'nose' structure can be seen as a common feature in an energy versus time diagram of ions in the energy range of 1-100 keV when a satellite passages in the afternoon region of L ~4-6. The characteristics of the 'nose' structure were clarified by *Smith and Hoffman* [1974] and were statistically examined by *Ejiri et al.* [1980]. Several interpretations of the 'nose' formation have been

attempted [e.g., *Chen*, 1970; *Grebowsky and Chen*, 1975; *Konradi et al.*, 1975; *Ejiri et al.*, 1978; *Ejiri et al.*, 1980]

The Explorer 45 satellite was launched on November 15, 1971, into an elliptical orbit having an apogee of 5.24 Re, a perigee of 224 km, an inclination of 3.6° and a period of 7.8 hours [*Longanecker and Hoffman*, 1973; *Gloeckler et al.*, 1975]. Explorer 45 measured the directional differential flux of energies of 0.84-872 keV for ions and energies of 0.84-405 keV for electrons by the electrostatic particle detector for lower energies and the solid state detector for higher energies.

On February 13, 1972, the Explorer 45 satellite observed an ion 'nose' dispersion structure in the dusk-midnight sector during a main phase of a moderate storm with a minimum Dst of -47 nT [*Cahill et al.*, 1975; *Konradi et al.*, 1975; *Ejiri*, 1978; *Ejiri et al.*, 1978; *Ejiri et al.*, 1980].

E-t (energy versus time) diagrams of the ion differential flux observed by Explorer 45 during the main phase of the storm are shown in **Figure 4.1**; the top panel for a pitch angle of 90° and the bottom panel for 30°. The 'nose' structure can be seen in the both diagrams; the differential flux suddenly enhances at 1145 UT (L=5.1, MLT=18.5 h) around energies of 45 keV. The flux enhancements began to spread to both higher and lower energies at high L and the enhancements remain to be the high flux intensity beyond the apogee. The orbit of Explorer 45 in the L-MLT coordinates is shown in **Figure 4.2**. Three geomagnetic indices during this period, 2.5-minutes value of AL (courtesy of Dr. T. Iyemori), Dst and Kp, are shown in **Figure 4.3**. Kp increases up to 5^- at 0900 UT and decreases gradually. There are three significant activities of auroral electrojets as indicated by AL during the

main phase. Identified from ground magnetograms, a storm sudden commencement (SSC) was recorded at 0939 UT and a first substorm onset at 1110 UT.

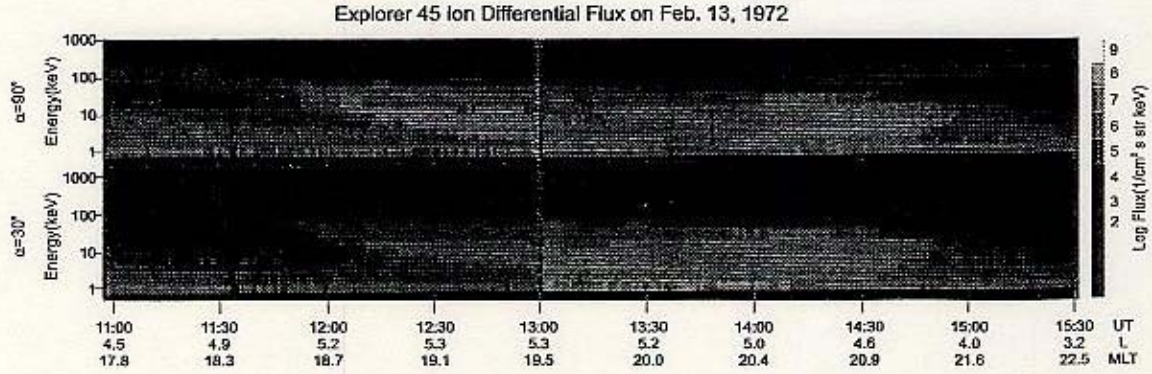

Figure 4.1. E-t (energy versus time) diagrams of the directional differential flux from 1100 UT to 1530 UT on February 13, 1972. The magnetic latitudes during the period are within from -10.22° to -14.15°. Top and bottom panels indicate the differential flux of pitch angles of 90° and 30°, respectively.

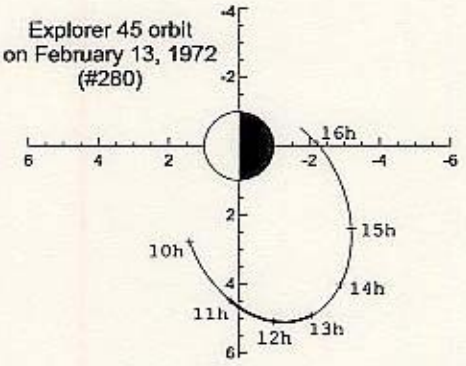

Figure 4.2. Explorer 45 orbit at 1000-1610 UT on February 13, 1972 in the L-MLT coordinates.

This 'nose' structure was often observed during the development of the main phase [*Smith and Hoffman*, 1974; *Ejiri et al.*, 1980], and/or during high substorm activities indicated by AE [*Ejiri et al.*, 1980]. The 'nose' structure has been considered to be caused by the

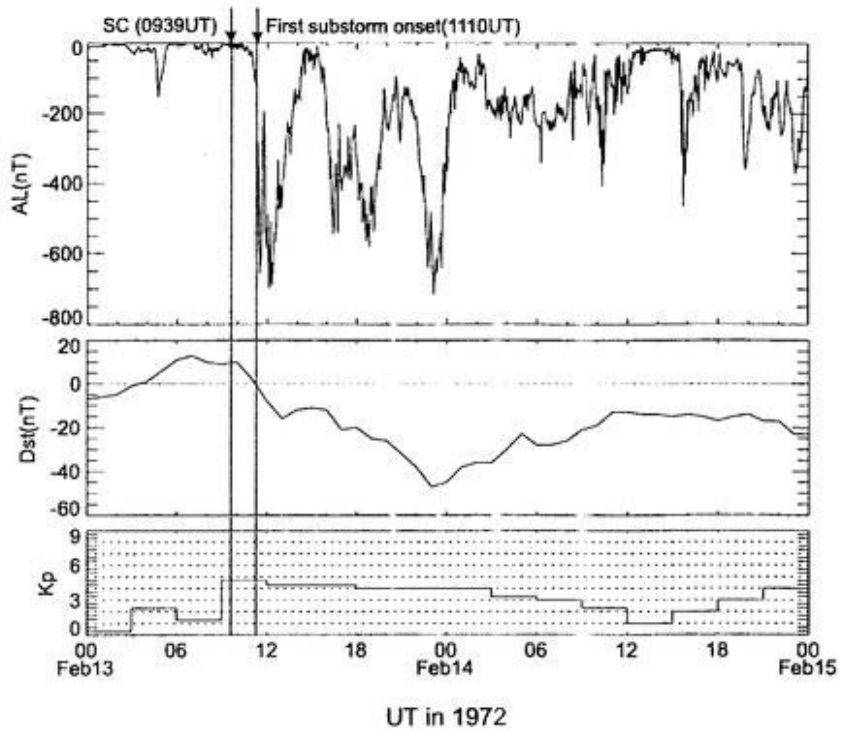

Figure 4.3. From top to bottom panels, 2.5-minutes value of AL, Dst and Kp indices during a moderate storm on February 13-14, 1972.

energy and pitch angle dependence of ions' trajectories under time-dependent convection electric field [e.g., *Smith and Hoffman*, 1974]. *Ejiri* [1978] and *Ejiri et al.*[1978, 1980] numerically confirmed the formation of the 'nose' structure by particle tracing under the time-dependent convection field. To demonstrate the nose structure, *Ejiri et al.*[1978] assumed the particles' start points to be L=10; they determined the injection start time by backtracking the observed 8 keV ions, as a test particle, from the first observed location (L = 5.1 and MLT=18.5 h) to the assumed boundary location of L=10.

The backtracking trajectory under the time-dependent electric field is shown in **Figure 4.4**, indicating the starting time being 0925 UT if the start points are taken to be L=10.

However, as *Ejiri* [1978; pp. 4809] mentioned, there are ambiguities of the estimated

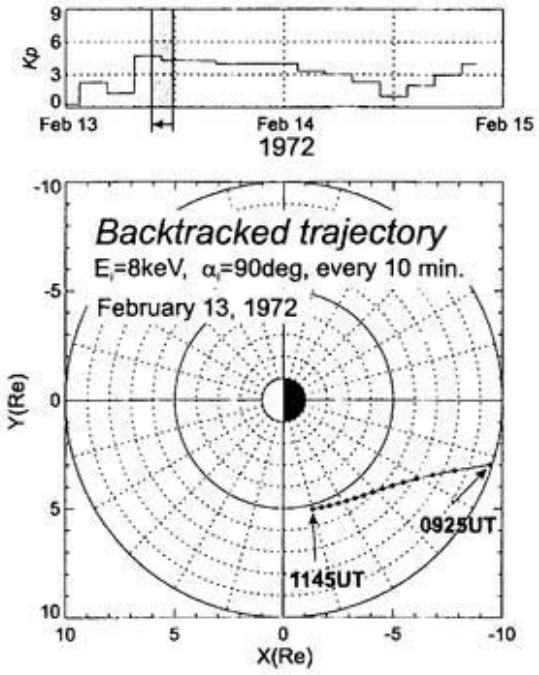

Figure 4.4. Backtracked trajectory from 1145 UT at L = 5.1 and MLT=18.5 to L=10 under time-dependent convection field. The initial energy and pitch angle at L = 5.0 are 8 keV and 90°, respectively.

starting time of the injection and the start points (L=10 Re). The ambiguity of the source location does not affect much the particle trajectories because the drift motion at high L (> 7 Re) are dominated by the $E \times B$ drift that is independent of their energis, charges and pitch angles.

If the substorm-associated injection commences at the first ground substorm onset of 1110 UT, there should exist an additional large-scale or localized electric field over the background convection field to push energetic particles from the boundary location of L=10 into the inner magnetosphere rapidly, i.e., an induction electric field due to dipolarization, when a stretched magnetic field becomes a dipole-like configuration in the near-earth magnetotail rapidly, may be a primary source. The induced electric fields have often been observed by

satellites directly [e.g., *Aggson et al.*, 1983; *Pedersen et al.*, 1985; *Maynard et al.*, 1996].

Although direct satellite observations show that electric fields during an expansion of a substorm tend to be irregular with magnitudes of several millivolts per meter in the near-earth plasma sheet [e.g., *Pedersen et al.*, 1985], the induced electric field has its dominant polarity in dawn-dusk direction [*Aggson et al.*, 1983; *Maynard et al.*, 1996]. Recently, *Maynard et al.*[1996] reported that the impulsive electric fields were observed at the region of L$\geq$5.2 and MLT from 2100 h to 0000 h with their intensity more than 4 mV/m and a time scale of a few minutes.

Although the induction field associated with a substorm often observed by satellites, the spatiotemporal structure of the induction field is still unknown. *Birn et al.* [1997a, 1997b, 1998] investigated the particle injection on the basis of geosynchronous observations in the dynamic fields of a three-dimensional MHD simulations of magnetotail neutral line formation and dipolarization. There are, however, many ambiguous parameters for the MHD simulation; physical meanings of the parameters remain as a matter of debate.

The other manner to model the distribution of the induction field is to calculate the Faraday's law directly by using two specified magnetic configurations given by empirical models [e.g., *Tsyganenko*, 1987; 1989]. *Fok et al.* [1996] modeled the particle injection under the induction field derived by this manner. However, it has been pointed out that the magnetic fields in the near-earth magnetotail given by the empirical model of *Tsyganenko* [1989] obviously lack the magnetotail current during an expansion and a recovery phases of a substorm [*Pulkkinen et al.*, 1992; 1994], i.e., the empirical magnetic field model hardly represents the actual magnetic field during a substorm-associated dipolarization event.

Moreover, the induction field given by the Faraday's law by using the magnetic field model seems to be lacking any physical meanings because of using the empirical models.

Therefore it is extremely difficult to model the spatiotemporal distribution of the induction field. In this chapter, using a simplest model of the induced electric field described below, the sudden flux enhancement associated with a substorm injection observed by Explorer 45 is numerically examined.

4.2 Model description

4.2.1 Induction electric field model

The actual induced electric field associated with a substorm may be a function of local time(ϕ), L-value(L) and time(t), that is,

$$E_\phi = E_\phi(t, \phi, L), \tag{4.1}$$

where E_ϕ is the azimuthal component of the induced electric field. Here, a simplified model expressed as

$$E_\phi = E_0 f_1(t) f_2(\phi) f_3(L), \tag{4.2}$$

where E_0, $f_1(t)$, $f_2(\phi)$ and $f_3(L)$ are a maximum intensity of the electric field, normalized functions of time, MLT and L, respectively, is introduced. The normalized functions,

$f_1(t), f_2(\phi)$ and $f_3(L)$ are simply written here as

$$f_1(t) = \exp\left(-\frac{(t-t_0)^2}{\Lambda}\right), \tag{4.3}$$

$$f_2(\phi) = \begin{cases} \left(1-10^{-\frac{\phi-\phi_1}{\Delta\phi}}\right)\cdot\left(1-10^{-\frac{\phi_2-\phi}{\Delta\phi}}\right) & \text{for } \phi_1 \le \phi \le \phi_2 \\ 0 & \text{for } \phi < \phi_1 \text{ or } \phi > \phi_2 \end{cases} \tag{4.4}$$

$$f_3(L) = \begin{cases} 1-10^{-\frac{L-L_s}{\Delta L}} & \text{for } L \ge L_s \\ 0 & \text{for } L < L_s \end{cases} \tag{4.5}$$

$$\tag{4.6}$$

and

$$\Lambda = \frac{-(\Delta t/2)^2}{\log 0.1}, \tag{4.7}$$

where ϕ_1 and ϕ_2 are the azimuthal boundary of the induced electric field ($\phi_1 < \phi_2$), L_s is an inner edge of the induced electric field, Δt is a time scale of the electric field, and $\Delta\phi$ and ΔL are characteristic widths of the boundary regions on MLT and L, respectively. The normalized functions are illustrated in **Figure 4.5**. The peak time of the induced field t_0 is given by the substorm onset time t' plus $\Delta t/2$; the onset time t' should be determined by the observation.

This induction field is superposed on the corotation field and the large-scale convection field whose electric potential is expressed by the Volland-Stern type [*Volland*, 1973; *Stern*,

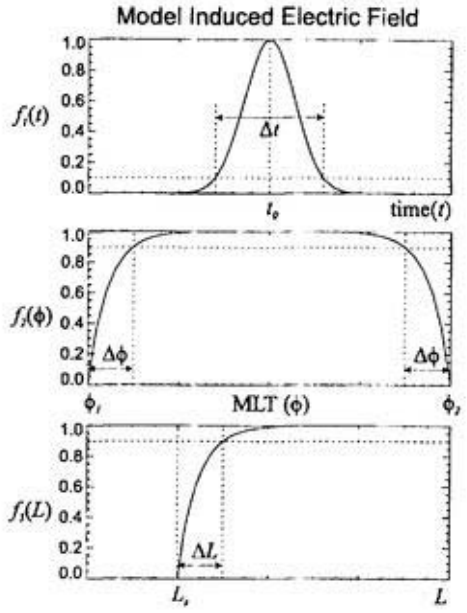

Figure 4.5. Substorm-associated induction field model. From top to bottom, normalized functions $f_1(t), f_2(\phi)$ and $f_3(L)$, where t, ϕ and L are time, magnetic local time (MLT) and McIlwain's L-value, respectively, constituting the inductive electric field model due to the dipolarization associated with the substorm.

1975] as

$$\Phi = AR^{\gamma} \sin \phi, \tag{2.55}$$

where R is a geocentric distance, γ a shielding factor and A a factor indicating the strength of the convection. Here, the shielding factor γ is taken to be 2. Following *Maynard and Chen* [1975], the intensity factor A as a function of Kp is given by

$$A = \frac{0.045}{(1 - 0.159Kp + 0.0093Kp^2)^3} \ (\mathrm{kV/Re^2}). \tag{2.56}$$

4.2.2 Drift trajectory

Drift trajectories of particles having various energies and pitch angles are traced by bounce-average approximation under a dipole magnetic field, a time-dependent convection electric field and a corotation electric field. The followings are assumed in this model; (1) the first two invariants are conserved, (2) field lines are equipotential and (3) motion of particles induces no additional field. The numerical method to trace the bounce-average trajectory is described in *Ejiri* [1978]; time development equations of the bounce-average drift motion becomes

$$\frac{dX}{dt} = -\frac{\omega}{\gamma}X^{\gamma+2}\cos\phi + \frac{E_\phi}{BR_s}, \tag{4.8}$$

$$\frac{d\phi}{dt} = \omega X^{\gamma+1}\sin\phi + \omega - \frac{3\mu G(y_0)}{qR_s^2X^2}, \tag{2.64}$$

$$X \equiv \frac{R}{R_s}, \tag{2.66}$$

where $q, \omega, \mu, R_s, \gamma$ and G are particle charge, angular velocity of earth's rotation, first adiabatic invariant (magnetic moment), a geocentric distance of a stagnation point at MLT of 18h for a zero energy particle, a shielding factor being taken to be 2 and a function of an equatorial pitch angle given by *Ejiri* [1978], respectively. The second term in the right hand side of Eq.(4.8) is the radial drift velocity due to the induced electric field.

4.2.3 Directional differential number flux

The manner to calculate an equatorial differential flux is as follows: First, all packet particles including real number of particles are gathered into a small phase space bin $(\Delta L, \Delta\phi, \Delta W, \Delta y)$, where L, ϕ, W and y are McIlwain's L-value, MLT, the kinetic energy and a sine of a pitch angle, respectively. Next, the directional differential flux in the equatorial plane $j_0(L, \phi, W, y)$ as

$$j_0(L, \phi, W, y) = \frac{\Delta N_{bin}}{2\pi S \tau_b y \Delta y \Delta W}, \tag{3.42}$$

where $\Delta N_{bin}, S$ and τ_b are the real number of gathered particles in the bin, the area of a virtual detector in the equatorial plane and the bounce period of a particle, respectively.

4.2.4 Loss effects of ions

Ions are lost by the charge exchange and the Coulomb collision loss as examined in Chapter 3. Number of ions lost by the both loss processes are calculated along with their bounce-average trajectories. This process can be numerically expressed as

$$\frac{\partial f}{\partial t} = -\frac{f}{\tau}, \tag{3.41}$$

where f and τ are the phase space density and the lifetime of an ion, respectively. The lifetime of an ion is given by

$$\frac{1}{\tau} = \frac{1}{\tau_{cc}} + \frac{1}{\tau_{cc}}, \tag{3.40}$$

where τ_{ce} and τ_{cc} are the lifetime due to the charge exchange and the Coulomb collision, respectively. The ions are also lost by the convection outflow.

4.3 Comparison with Explorer 45 satellite observation

4.3.1 Observed spectra of the differential flux

Figure 4.6 shows spectra of the ion differential flux observed by Explorer 45 at 1145 UT (left panel) and 1200 UT (right panel) on February 13, 1972, when Explorer 45 began to observe the flux enhancement along the outbound path in the near equatorial plane (a magnetic latitude of $\sim -11°$). There are two noticeable characteristics: (1) The differential fluxes with energies from 20 to 80 keV are drastically enhanced, whereas, the background flux with energies below ~10 keV is relatively steady; the ions with the energy range of 20-80 keV are selectively transported into the satellite position of L ~5 in the dusk region. (2) The flux with a pitch angle of 90° is higher than that of 30°.

4.3.2 Parameters of the inductive electric field model

In this chapter, the following assumption is made: (1) The ions that cause the flux enhancement beginning at 1145 UT are rapidly transported from the near-earth plasma sheet azimuthally located at L=8 by a substorm-associated induction field. (2) The injection is initiated at 1110 UT when the ground substorm commenced. (3) The characteristic time

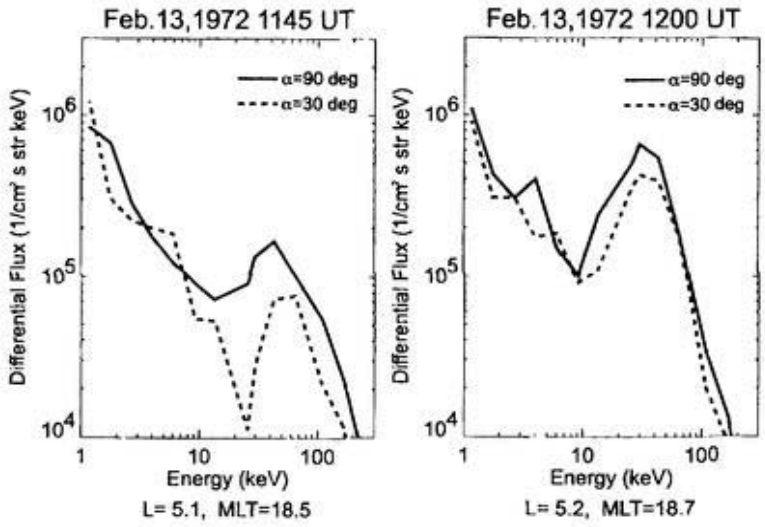

Figure 4.6. Spectra of the directional differential flux of ions observed by Explorer 45 at 1145 UT (left) and 1200 UT (right) on February 13, 1972. A solid line and a dashed line indicate the flux for pitch angles of 90° and 30°, respectively.

scale of the induction electric field Δt is 10 minutes, that is, the peak time of the field t_0 is taken to be 1115 UT. To model this process, indefinite parameters of the inducted field model as expressed by Eq.(4.3), Eq.(4.4) and Eq.(4.5) are determined here.

Radial width of the induction field

Figure 4.7 illustrates backtracked trajectories of ions having initial energy of 50 keV at the start point; backtracking starts at 1145 UT at L=5.1 and MLT=18.1 h where Explorer 45 began to observe the flux enhancements, and lasts until 1110 UT when the first ground substorm were commenced. From comparing between panels of (a) and (b), it is clear that an inner edge of the induction field (L_s) should be lower than 4.5. From comparing between panels of (a) and (c), it is also clear that a maximum intensity of the electric field (E_0) should be greater than 6 mV/m to push ions from the boundary located at L=8 to the

position where Explorer 45 began to observe the flux enhancement. Thus, the parameters, L_s and E_0, are determined as 4.5 and 6 mV/m, respectively.

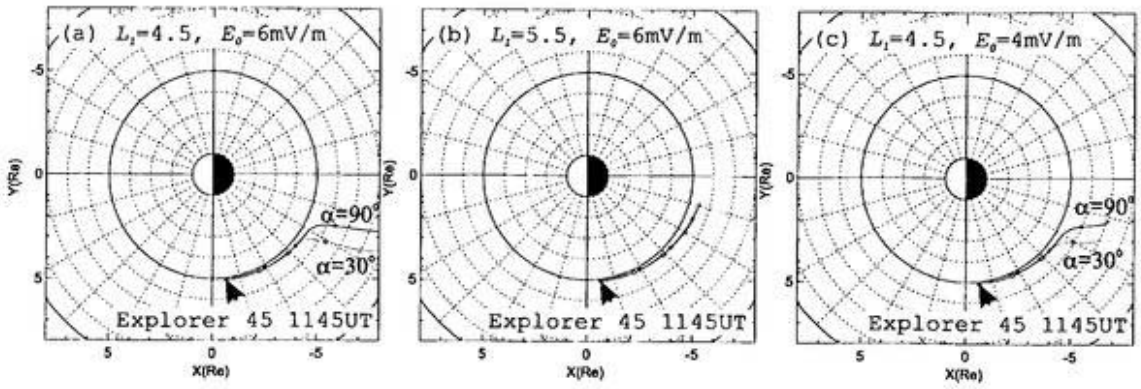

Figure 4.7. Backtracked trajectories of ions whose initial energy is 50 keV from 1145 UT to 1110 UT. Backtracking starts at L=5.1 and MLT=18.5 h where Explorer 45 was situated at 1145 UT. The parameters of the induction field are taken to be (a) L_s=5.5 and E_0=6 mV/m, (b) L_s=6.5 and E_0=6 mV/m and (c) L_s=5.5 and E_0=4 mV/m. A solid line and a dotted line indicate trajectories for ions with pitch angles of 90° and 30°, respectively.

Azimuthal width of the induction field

Next, the azimuthal width of the induction field is determined. **Figure 4.8** also represents the backtracked trajectories of ions having initial energies of 30 keV, 70 keV and 110 keV, respectively, and their equatorial pitch angles are 90°. The trajectories are calculated under the inductive electric field with the parameters determined in the previous subsection (L_s=4.5 and E_0=6 mV/m). It is also clear that the azimuthal width should be from MLT=21 h to 3 h, i.e., ϕ_1 and ϕ_2 should be 21 h and 3 h, respectively, to push ions (with energies of 30-110 keV at L = 5.1) from the boundary located at L=8 to the location of Explorer 45 of 1145 UT.

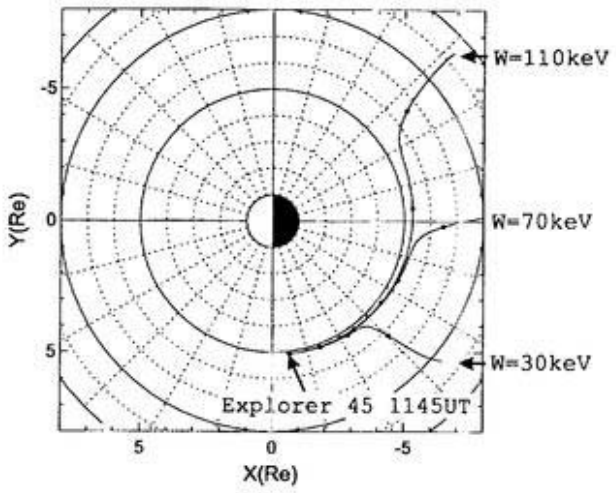

Figure 4.8. Backtracked trajectories of ions whose initial energies are 30 keV, 70 keV and 110 keV from 1145 UT to 1110 UT. Backtracking starts at L=5.1 and MLT=18.5 h where Explorer 45 was situated at 1145 UT.

Source distribution function

The parameters for the induction field model, L_s, ϕ_1, ϕ_2 and E_0 have been determined. In this subsection, using the observed spectra of the ion differential flux, the source distribution function at the source boundary located at L=8 is deduced by particle tracing. Here, two assumptions are made; (1) the source distribution function being isotropic Maxwellian and (2) the source distribution function being independent of MLT and time.

Figure 4.9 shows the calculated and the observed spectra at 1145 UT and 1200 UT. The number density at the boundary is fixed to be 0.3 cm^{-3}, but the temperature is varied from 3 keV to 7 keV. As the source temperature increases, the energy of the maximum differential flux also increases; the source temperature of 5 keV may be suitable for explaining the observed spectra.

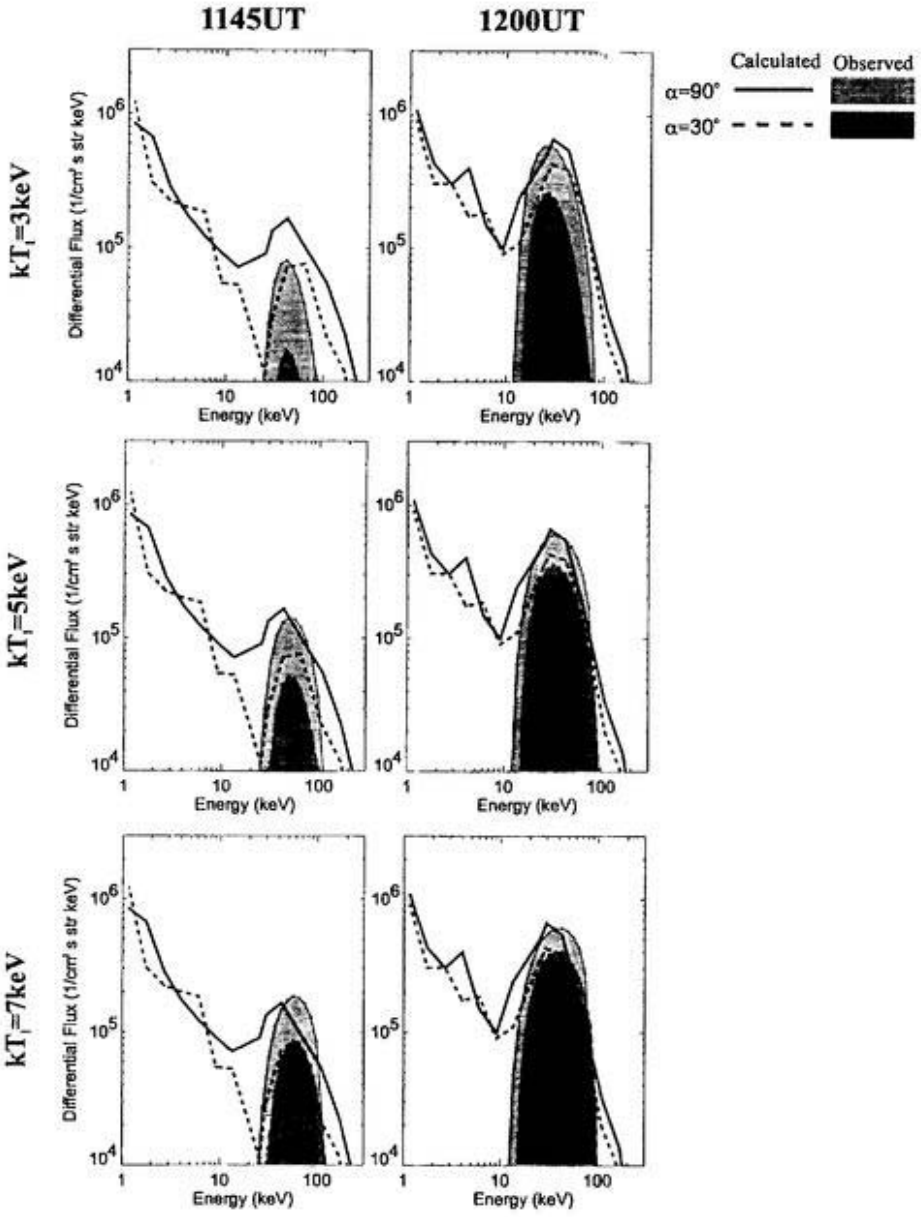

Figure 4.9. Spectra of the differential flux at 1145 UT (left panels) and at 1200 UT (right panels). The calculated spectra indicated by filled lines are compared with the observed spectra indicated by lines. The number density at the boundary is fixed to be 3 cm^{-3}, but the temperature are varied from 3 keV to 7 keV.

Figure 4.10 shows the calculated and the observed spectra at 1145 UT and 1200 UT. The temperature at the boundary is fixed to be 5 keV, but the number density is varied from 0.1 to 0.5 cm^{-3}. As the source number density increases, the peak flux increases linearly; the source number density of 0.3 cm^{-3} may be suitable. From **Figure 4.9** and **Figure 4.10**, the suitable distribution function at the boundary is deduced as isotropic Maxwellian with the temperature of 5 keV and the number density of 0.3 cm^{-3}.

Using the deduced parameters for the induction field model, the calculated E-t (energy versus time) diagram of the differential flux is compared with the observed diagram by Explorer 45 as shown in **Figure 4.11**. The absolute quantity of the calculated differential flux and its energy dispersion structure illustrated in the middle panel are in good agreement with the observed spectra given by Explorer 45 represented in the bottom panel. In the calculated diagram shown in the middle panel, a banded structure with its energy of ~100 keV appears from 1227 UT. This structure is so-called 'drift echo', that is, newly injected ions, which are penetrating into the inner magnetosphere by the transient induction electric field, drift around the earth westward and they return to the same local time. The drift echo feature associated with a substorm is well observed at the geosynchronous satellites [e.g., *Arnoldy and Chan*, 1969; *Belian et al.*, 1978; *Baker et al.*, 1978]. However, the 'drift echo' feature is not clearly seen in the observed diagram.

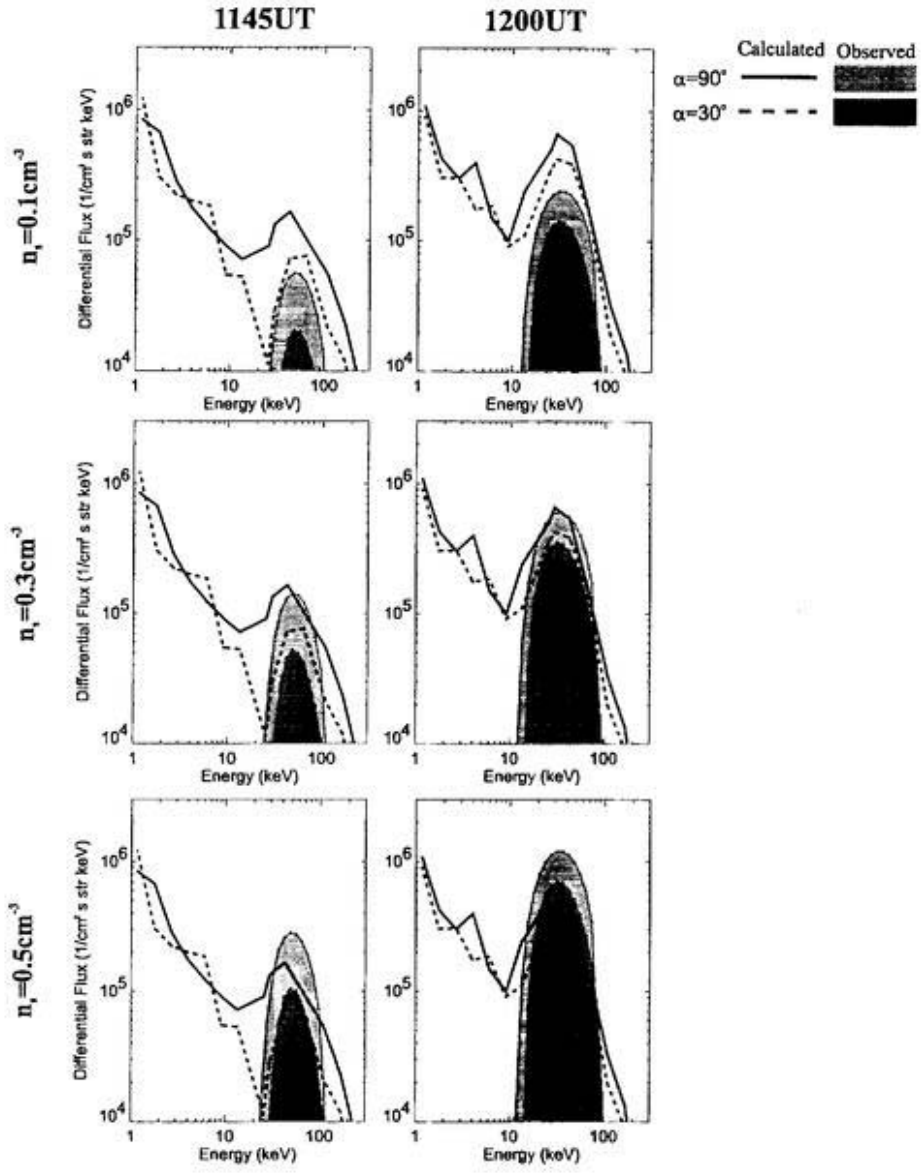

Figure 4.10. Spectra of the differential flux at 1145 UT (left panels) and at 1200 UT (right panels). The calculated spectra indicated by filled lines are compared with the observed spectra indicated by lines. The temperature at the source boundary is fixed to be 5 keV, but the density are varied from 0.1 to 0.5 cm^{-3}.

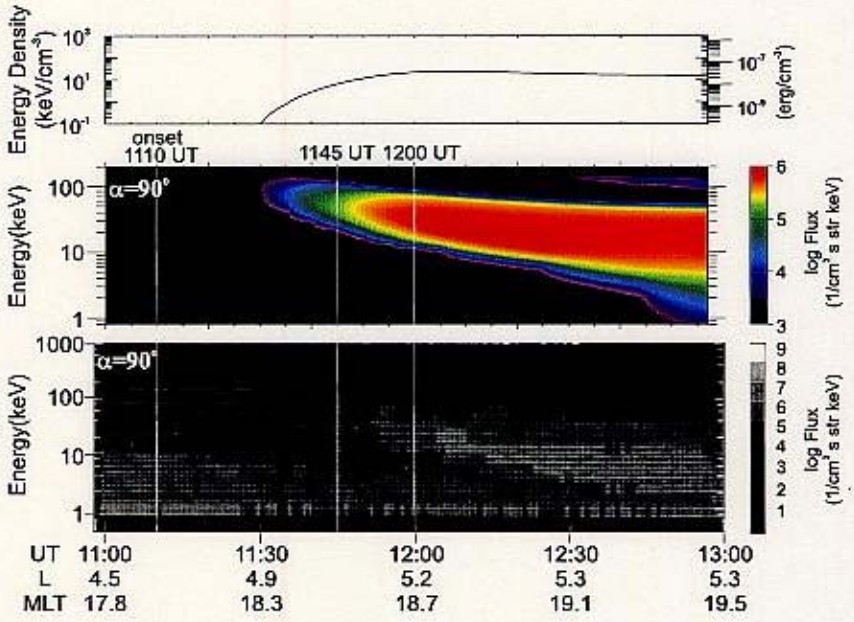

Figure 4.11. Calculated (middle) and observed (bottom) E-t diagrams for ions with pitch angle of 90°. Top panel indicates the energy density.

4.4 Discussion

4.4.1 Magnetic response to an isolate substorm injection

The magnetic response at the center of the earth to an isolate substorm-associated injection is examined here. The manner to calculate the magnetic disturbance due to the particles' motion is described below.

Plasma pressure

The perpendicular and parallel pressures, $P_\perp$ and $P_\parallel$, are given by

$$P_\parallel = \int mv^2 F(\boldsymbol{v}) \cos^2 \alpha d\boldsymbol{v}, \tag{3.45}$$

$$P_\perp = \int \frac{1}{2} m v^2 F(\boldsymbol{v}) \sin^2 \alpha \, d\boldsymbol{v}, \tag{3.46}$$

where F is the velocity distribution function and m the particle's mass. The pressure can be expressed by using the directional differential flux j instead of the velocity distribution function F as

$$P_\perp = \pi \sqrt{2m} \int_\alpha \int_W j \sqrt{W} \sin^3 \alpha \, d\alpha \, dW, \tag{3.47}$$

$$P_\parallel = 2\pi \sqrt{2m} \int_\alpha \int_W j \sqrt{W} \cos^2 \alpha \sin \alpha \, d\alpha \, dW. \tag{3.48}$$

Current density

The current density perpendicular to the magnetic field in the ring current has been considered as a combination of the three currents [*Parker*, 1957]; the magnetization current $\boldsymbol{J}_M$, the curvature drift current $\boldsymbol{J}_R$ and the grad-B drift current $\boldsymbol{J}_B$. The total current density $\boldsymbol{J}_\perp$ is given by

$$\begin{aligned} \boldsymbol{J}_\perp &= \boldsymbol{J}_M + \boldsymbol{J}_R + \boldsymbol{J}_B, \\ \boldsymbol{J}_\perp &= \frac{\boldsymbol{B}}{B^2} \times \left[\nabla P_\perp + (P_\parallel - P_\perp) \frac{(\boldsymbol{B} \cdot \nabla)\boldsymbol{B}}{B^2} \right]. \end{aligned} \tag{2.3}$$

A detail for the derivation of the current density $\boldsymbol{J}_\perp$ is described in Appendix B. In the dipolar magnetic field, the azimuthal component of the current density J_ϕ becomes

$$J_\phi = \frac{1}{B^2} \left(\frac{B_r}{r} \frac{\partial P_\perp}{\partial \lambda} - B_\lambda \frac{\partial P_\perp}{\partial r} \right)$$

$$+\frac{1}{B^3}\left(P_{\parallel}-P_{\perp}\right)\left(\frac{B_r}{r}\frac{\partial B}{\partial \lambda}-B_{\lambda}\frac{\partial B}{\partial r}\right) \tag{4.9}$$

$$= \frac{r^3}{M\left(1+3\sin^2\lambda\right)}$$
$$\Big[-\frac{2}{r}\sin\lambda\frac{\partial P_{\perp}}{\partial \lambda}-\cos\lambda\frac{\partial P_{\perp}}{\partial r}$$
$$+\frac{P_{\parallel}-P_{\perp}}{r}\left(-\frac{6\sin^2\lambda\cos\lambda}{1+3\sin^2\lambda}+3\cos\lambda\right)\Big], \tag{4.10}$$

where B_r, B_λ, r and M are the radial component of the magnetic field, the latitudinal component of the magnetic field, the radial distance from the center of the earth, and the magnetic moment of the earth, respectively.

Magnetic disturbance and corrected Dst*

After integrating the three-dimensional distribution of the current density, the magnetic disturbance induced by the current can be derived from the Biot-Savart's law. Especially, the magnetic disturbance parallel to the earth's dipole at the center of the earth ΔB_C is given by

$$\Delta B_C = \frac{\mu_0}{4\pi}\int_r\int_\lambda\int_\phi \cos\lambda J_\phi(r,\lambda,\phi)drd\lambda d\phi, \tag{4.11}$$

where μ_0 is the permeability in vacuum and J_ϕ the azimuthal component of the current density $\boldsymbol{J}_\perp$.

Results

The results are illustrated in **Figure 4.12**, **Figure 4.13** and **Figure 4.14**. **Figure 4.12** shows a time series of the plasma pressure perpendicular to the magnetic field $P_\perp$ in the equatorial plane during the period from 1120 UT to 1220 UT on February 13, 1972. At 1120 UT, it can be seen that the ions just begin to drift azimuthally after they are quickly injected into the magnetosphere radially by the induced electric field. At 1220 UT, the pressure distribution forms a 'ring'. Ions with high energies drifting westward encounter ions with low energies dominantly drifting eastward by $E \times B$ drift in the dawn region. The 'zipper' distribution [e.g., *Fennel et al.*, 1981; *Kaye et al.*, 1981] can be seen around there.

In **Figure 4.13**, a time series of the azimuthal component of the current density $J_\perp$ in the equatorial plane is shown. At 1120 UT, the azimuthal current densities reached maximum intensities of 3.2 nA/m^2 for eastward current at L of 4.9 and 2.5 nA/m^2 for westward current at L of 5.6 in MLT of 24 h. Until 1200 UT, after 50 minutes from the commencement of the injection, the current density distributes a 'partial ring current'. At 1220 UT, the distribution of the current density becomes 'symmetric'.

The calculated Dst* responding to the isolated injection is shown in **Figure 4.14**. The calculated magnetic disturbance at the center of the earth parallel to the earth's dipole ΔB_C (or Dst*) is compared with the observed Dst*. Dst* is so-called corrected Dst, indicating the strength of the ring current. The calculated Dst* indicated by a solid line starts with

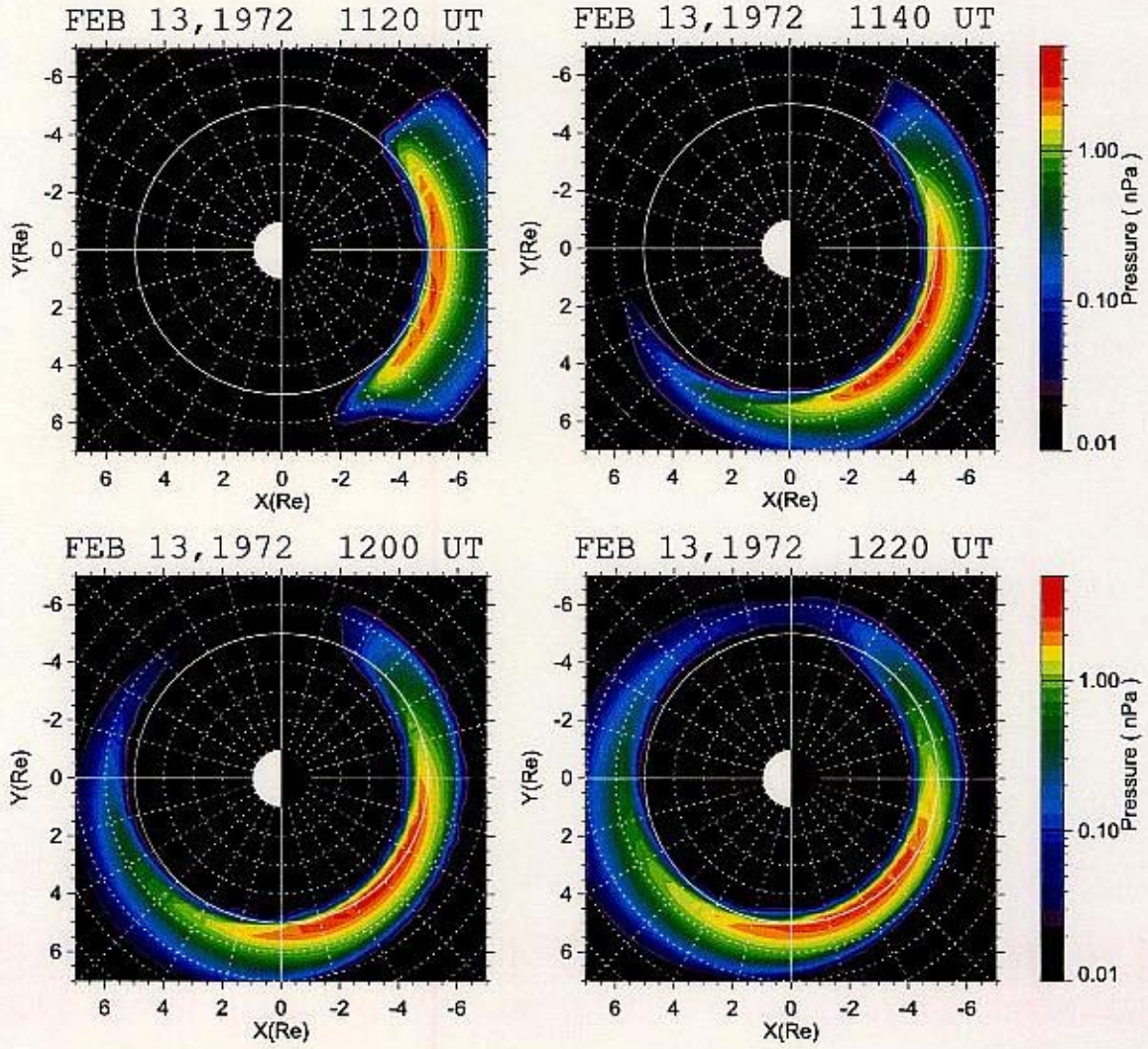

Figure 4.12. A time series of the plasma pressure perpendicular to the magnetic field $P_{\perp}$ in the equatorial plane during a period 1120-1220 UT on February 13, 1972. A color code indicates the intensity of the perpendicular pressure.

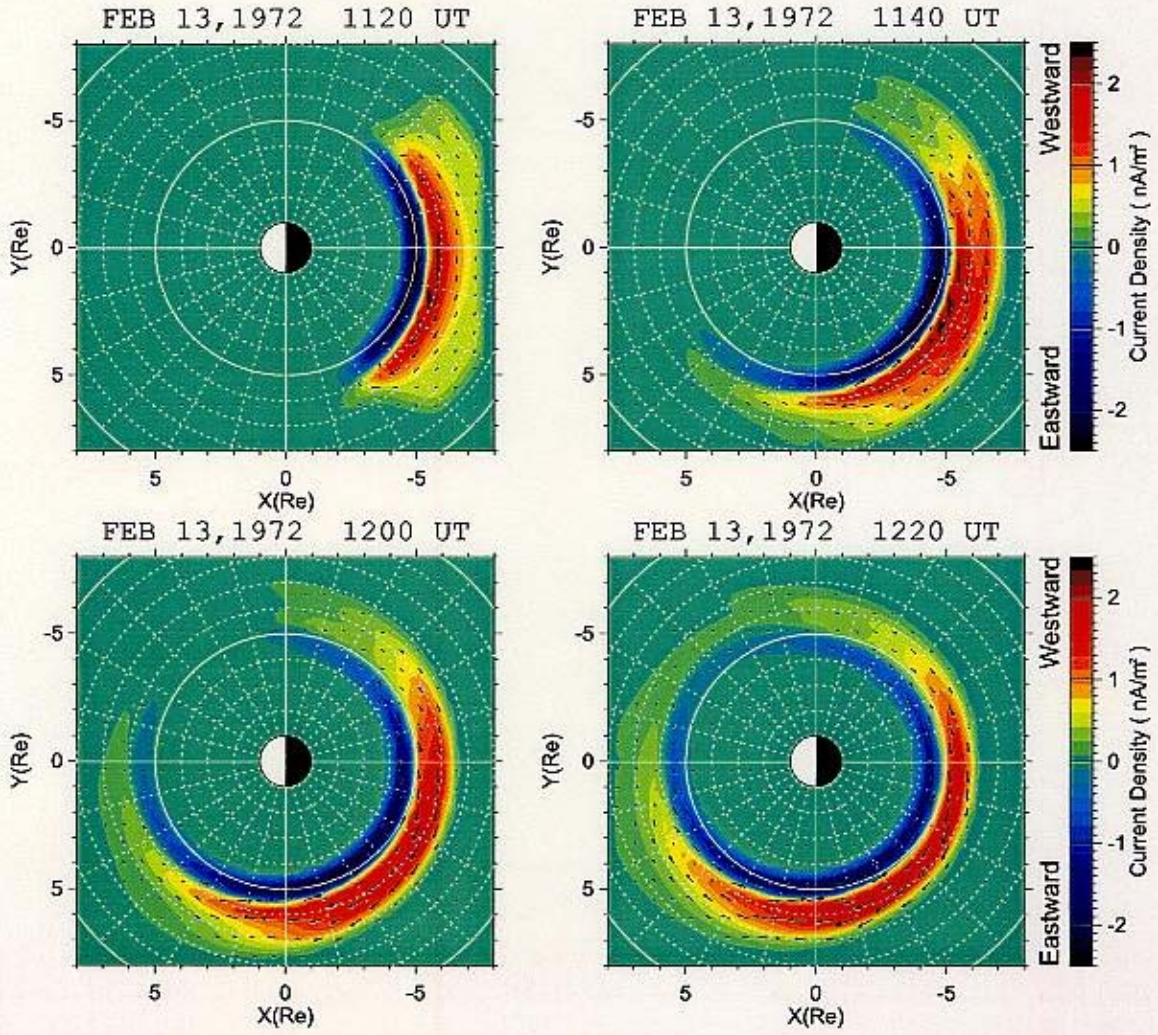

Figure 4.13. A time series of the azimuthal current density J_ϕ in the equatorial plane during a period 1120-1220 UT on February 13, 1972. A color code indicates the intensity of the perpendicular pressure. Color codes of red and blue represent that the currents flow toward westward and eastward, respectively.

Dst* of 0 because the magnetosphere is initially empty. The observed Dst* is obtained by

$$Dst* = \left(Dst - c_1 P_{sw}^{1/2} + c_2\right)/\xi, \tag{4.12}$$

where P_{sw} is the dynamic pressure of the solar wind, which is given by $N_{sw} m V_{sw}^2$, and ξ a coefficient for the earth's induction which is taken to be 1.5, and c_1 and c_2 are empirical coefficients, respectively. Typically, the coefficients, c_1 and c_2, are 0.2 nT/(eV cm^{-3})$^{1/2}$ and 20 nT, respectively [e.g., *Gonzalez et al.*, 1994]. Using the OMNI data sets provided by NASA/NSSDC, the solar wind dynamic pressure P_{sw} is calculated. There is a time lag between the peaks of the inductive electric field and Dst* by 65 minutes. The minimum Dst*, however, is quite small, being only -1.8 nT, even though the intensity and the duration of the induction field are enough large and are comparable to a major substorm [e.g., *Maynard et al.*, 1996]. Hence, an isolate substorm-associated injection hardly affects Dst*.

4.4.2 Ring current buildup caused by multiple injections

Historically, a magnetic storm had been considered to be composed of substorms. *Chapman* [1962] stated that:

> A magnetic storm consists of sporadic and intermittent polar disturbances, the lifetimes being usually one or more hours. These I call polar substorms. Although polar substorms occur most often during magnetic storms, they also appear during rather quiet periods when no significant storm is in progress.

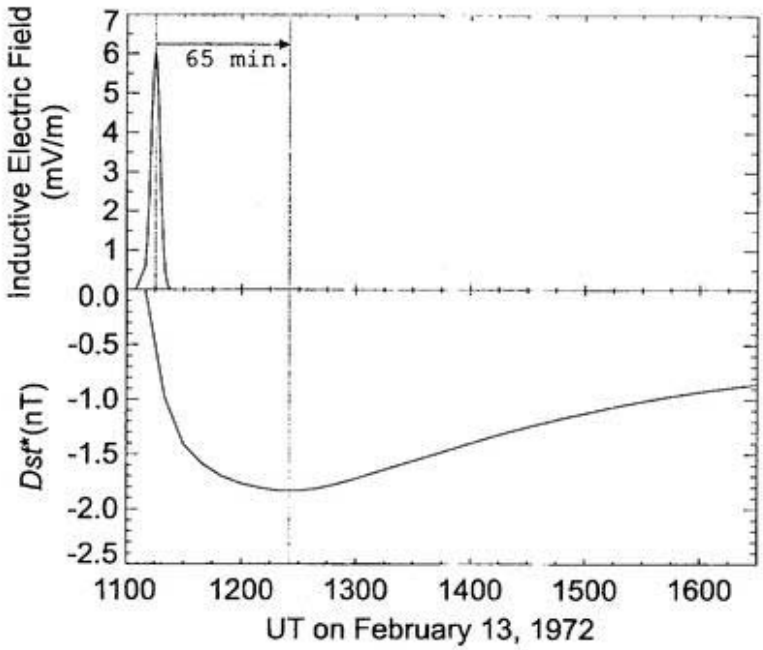

Figure 4.14. Change of Dst* responding to the substorm-associated induction field. Intensity of the induced electric field (top panel) and calculated Dst* (bottom panel) are indicated.

If it is true, the intensity of a magnetic storm can simply be determined by number of substorms as

$$\text{A storm consists of} \sum \text{substorm.}$$

In this subsection, following this concept, the ring current buildup is examined by superposing many substorm injections. Although the definition of the word of 'substorm' has been controversial, it is assumed that the word of 'substorm' includes the meanings of the followings in this chapter; (1) particle injection due to dipolarization in the magnetotail, (2) the transient development of the auroral electrojets, which can be seen in the high-latitude magnetograms, and (3) the transient development of the current wedge, which can be seen

in the mid- and low-latitude magnetograms.

To identify the substorm onset times, magnetograms observed by 27 stations are used. Geographic latitudes, longitudes and magnetic latitudes of the stations are listed in **Table 4.1**. Taking criteria to identify substorm onsets are a positive bay for mid- or low-latitude stations in the nightside region, and a sudden decrease for auroral latitude stations, there are 13 substorm onsets during a main phase of the storm on February 13, 1972; the onset times are 1115, 1200, 1230, 1550, 1610, 1635, 1720, 170, 1930, 2000, 2130, 2240 and 2330 UT.

The followings are assumed for this simulation; (1) the injections occur at the onset times identified above, (2) the source distribution function for all injections are corresponding to that of the first injection that is mentioned in the previous subsection, i.e., isotropic Maxwelllian with the temperature of 5 keV and the density of 3 cm^{-3}, (3) the spatiotemporal structure of the inductive electric field for each injection is also corresponding to that of the first injection.

The result is shown in **Figure 4.15**. There are three characteristics to be noted:

1. Decrease of observed Dst* starts with -10 nT and reaches its minimum of -36 nT at 2300 UT on February 13.

2. Calculated Dst* is responding to the substorm onsets; each sudden decrease of calculated Dst* is initiated by the induction electric field. The curve is composed of 13 notches. Calculated Dst* reaches its minimum of -26 nT at 2340 UT on February 13.

Although calculated Dst* resembles that of observed Dst* in the decrease rate and intensity of the decrease, the calculational result seems to be unnatural for the reasons: (1)

Station Name	Geographic Lat. (deg)	Geographic Long. (deg)	Magnetic Lat. (deg)
Barrow	71.30	203.25	68.8
Dixon	73.55	80.57	63.1
Dourbes	50.10	4.60	51.7
Dumnt d'Urville	-66.66	140.01	-75.4
Eskdalemuir	55.32	356.80	58.2
Fort Churchill	58.80	265.90	68.8
Fredericksburg	38.20	282.63	49.5
Gnangara	-31.78	115.95	-43.1
Godhavn	69.23	306.48	79.6
Great Whale River	55.30	282.25	66.5
Guam	13.58	144.87	4.2
Hartland	50.98	355.52	54.3
Honolulu	21.32	202.00	21.3
Huancayo	-12.05	284.67	-0.7
Irkutsk	52.17	104.45	40.8
Kakioka	36.23	140.18	26.3
Kanoya	31.42	130.88	20.7
Kiruna	67.83	20.42	65.1
Leirvogur	64.18	338.30	69.9
Leningrad	59.95	30.70	56.1
Meanook	54.62	246.67	62.0
Moscow	55.48	37.32	50.7
Murmansk	68.25	33.08	63.3
Narssarssuaq	61.20	314.60	71.0
Novolazarevskaya	-70.77	11.82	-66.5
Tahiti	-17.34	211.00	-14.8
Tixie Bay	71.58	129.00	60.6

Table 4.1. Station list with geographic latitude, longitude and magnetic latitudes. Magnetograms observed by the stations are used to identify the substorm onsets.

In general, the notch feature responding to the induction field (or an injection) during a main phase of a storm hardly appears in the low-latitude magnetograms. The decrease of Dst or an H-component of low-latitude magnetogram during a main phase of a storm is relatively smooth. (2) More than 50 substorm-associated injections (or more than 50 major substorms) will be required for the development of an intense storm having minimum Dst of -100 nT, however, such number of major substorms seems to be unrealistic for an ordinary storm. Hence, it is deduced that the storm time ring current is hardly developed by the sum of substorm-associated injections alone, that is, a storm is not composed of substorms only; other sources play an important role for storm time ring current development. In the next chapter, the storm time ring current buildup controlled by the solar wind and IMF will be examined.

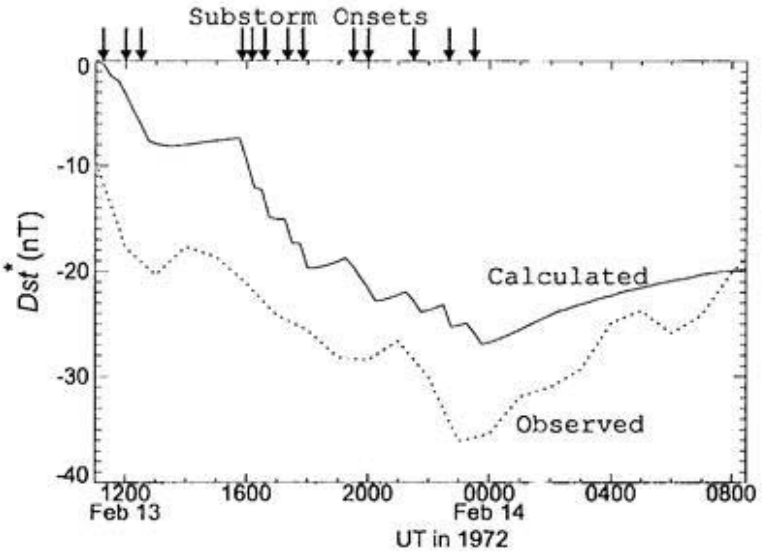

Figure 4.15. Calculated Dst* (solid line) and observed Dst* (dotted line) in the weak storm on February 13, 1972. Arrows indicate the substorm onsets.

4.5 Conclusion

In this chapter, a 'nose' energy dispersion structure [e.g., *Grebowsky and Chen*, 1975; *Konradi et al.*, 1975; *Ejiri et al.*, 1978; *Ejiri et al.*, 1980] has been examined by using particle tracing scheme to explain the sudden enhancement of the ion differential flux observed by Explorer 45 in the dusk region on February 13, 1972 associated with an isolate substorm. If the ions contributing the flux enhancement observed by Explorer 45 started at the first substorm on the weak storm of 1115 UT in the near-earth plasma sheet, an additional electric field superposed on the convection field was required to push ions into the inner magnetosphere radially. To explain the flux enhancement, a simple induction field model is introduced and parameters are deduced from single particle tracing. Using the additional induction electric field, the results is obtained; the calculated differential flux is in good agreement with the observed differential flux in the absolute quantity of the flux and its energy dispersion structure.

The magnetic disturbance at the center of the earth due to the isolate substorm injection is investigated. The result of the simulation shows that the isolate injection hardly affects the magnetic disturbance; the intensity is approximately $\sim$ 2 nT. Next, following the concept that a storm is composed of substorms, the ring current buildup is examined by superposing many substorm injections. There were 13 substorms during the storm of February 13, 1972. Parameters for 13 injections are corresponding to those of the first injection. The result suggests that the curve of calculated Dst* is unnatural for this particular weak storm and that an intense or a large storm are hardly explained this concept. Therefore other parameters' dependent sources as well as other mechanisms of

particle flux enhancements may play an important role for the storm time ring current buildup.

Chapter 5

Solar wind and IMF dependent model of the ring current

5.1 Introduction

Many authors have numerically modeled the ring current development. *Lee et al.* [1983], *Wodnicka* [1989] and *Takahashi et al.* [1990] have examined energy transport from the near-earth plasma sheet to the ring current under a simple assumption that the number density and the temperature in the plasma sheet are steady. Their primary results are that the energy transport due to an enhanced convection electric field has a potential for realistic change of the magnetic disturbance in the earth's surface during a main phase of a magnetic storm. *Chen et al.* [1994] traced bounce-average trajectories of ions and they calculated temporal evolution of equatorial normalized phase space density during a magnetic storm. Their model calculation including radial diffusion due to impulsive fluctuation of the large

scale electric field with a time scale of 20 minutes shows a reasonable radial distribution of the energy density and magnetic disturbance in the equatorial plane. *Kistler et al.* [1989] studied the time evolution of the equatorial phase space density of ring current ions by point-to-point mappings. *Fok et al.* [1993, 1995] and *Jordanova et al.* [1994, 1996] examined the decay of the storm time phase space density of H^+, $He^+$and O^+ions by solving the Fokker-Planck equation. An initial condition of their model is given by energy spectra observed by AMPTE/CCE. *Sheldon et al.*[1993] examined diffusive ion transport of ring current ions due to magnetic and electric fluctuations for the quiet time ring current. *Noël*[1997] studied the ring current decay by using a Monte Carlo type calculation, showing the result that the charge exchange is the dominant energy loss process of the ring current for a particular storm. *Ebihara et al.*[1998] concluded that the decay of ring current ions is mainly due to the charge exchange process.

The numerical models described above mainly discuss on the transport and the decay of ring current ions. So far, the quantitative study on the storm time ring current buildup, being one of topics on the magnetic storm, has been superficial. Recently, *Jordanova et al.*[1998] numerically showed that the superdense plasma sheet is one of main sources for the ring current buildup for a particular storm. Indeed, their model whose boundary condition is given by direct observations by two geosynchronous satellites well explains the ring current buildup as indicated by Dst for a particular storm. They concluded that there are two main factors contributing to ring current buildup; the plasma sheet population of ions and the convection electric field.

After examining the solar wind density and the near-earth plasma sheet density, *Borovsky*

et al. [1997] and *Terasawa et al.* [1997] have concluded that they are highly correlated. As shown in **Figure 5.1**, *Borovsky et al.* [1997] statistically examined that the relation between the solar wind density N_{sw} and the plasma sheet density N_{ps} is well fitted by $N_{ps} = 0.020N_{sw} + 0.12$ (cm^{-3}) with a linear correlation coefficient of 0.69 at the geocentric distance of 17.5 to 22.5 Re, and $N_{ps} = 0.040N_{sw} + 0.48$ (cm^{-3}) with a linear correlation coefficient of 0.67 at the geosynchronous altitude. This means that the near-earth plasma sheet density is well responsive to change of the solar wind density. However, the physical mechanism of the transport of ions from the solar wind into the plasma sheet is still unknown.

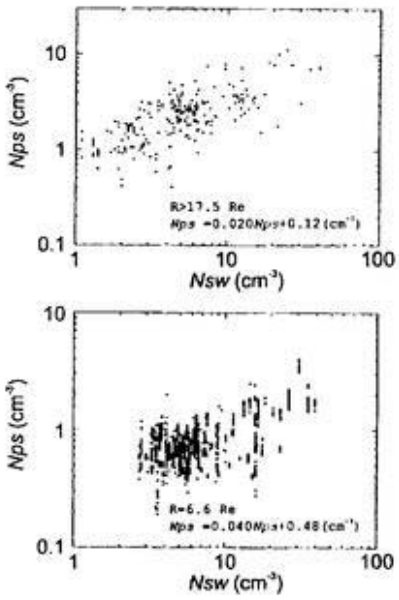

Figure 5.1. The plasma sheet density N_{ps} as a function of the solar wind density N_{sw}. The top panel shows the relation observed at L=17.5-22.5 and the bottom panel shows the relation observed at L=6.6. (After *Borovsky et al., 1997.*)

If the plasma sheet density is well correlated with the solar wind density, the source density of the ring current ions in the near-earth plasma sheet can be directly estimated

from the solar wind density, that is, a satellite observing in the magnetosphere is not necessary to give the boundary condition for a ring current model as *Jordanova et al.*[1998] modeled. In this chapter, the ring current buildup depending on the solar wind is mainly examined based on the assumption that the plasma sheet density is well correlated with the solar wind density. In Section 5.2 the relation between the solar wind density and the plasma sheet density is statistically examined by using WIND and GEOTAIL satellite. In Section 5.3, a simulation scheme of this ring current model is described. In Section 5.4, results of the numerical simulation are shown and are compared with ground and satellite observations. In Section 5.5, the following items are discussed; (1) the energy injection rate from the near-earth plasma sheet into the ring current, (2) dependence of corrected Dst on the plasma sheet temperature, (3) electric current distribution of the ring current, (4) effects of charge exchange loss, (5) energy composition of the pressure, (6) response time of the plasma sheet density to the solar wind density, (7) the relation of total kinetic energy of the ring current ions, and (8) a diamagnetic effect of the ring current. In section 5.6, a conclusion is described.

In this chapter, the contribution of electrons to the ring current is not mentioned because the plasma sheet temperature of electrons is approximately 5 times lower than that of ions [e.g., *Baumjohann et al.*, 1989]; the electrons may slightly contribute to the ring current formation.

5.2 Statistical analysis of the solar wind dependence of the plasma sheet density

5.2.1 Data and criteria

As mentioned above, *Terasawa et al.* [1997] and *Borovsky et al.* [1997] reported that the number density in the plasma sheet is well correlated with the solar wind density. *Terasawa et al.* [1997] statistically investigated the solar wind dependence of the plasma sheet density at the geocentric distance of 15-50 Re observed by GEOTAIL and they found that the relation between them obviously has the dependence of the polar angle of IMF. They speculated from the statistics as follows: When IMF points northward, the solar wind ions diffusively penetrate into the plasma sheet through the LLBL with a time scale of ~6 hours. On the other hand, when IMF turns southward, the solar wind ions are directly carried into the plasma sheet by the reconnection with a time scale of ~1 hour. *Borovsky et al.* [1997] also studied their relation at the geocentric distance of 6.6 Re (geosynchronous altitude) and 17.5-22.5 Re but they described that there is no IMF dependence between them.

So far, the statistical analysis of the solar wind dependence of the plasma sheet density has been examined at the geocentric distance of 15-50 Re [*Terasawa et al.*, 1997], 6.6 Re and 17.5-22.5 Re [*Borovsky et al.*, 1997]. The geocentric distance of $\geq$15 Re is quite too far for the boundary condition of the ring current model assuming a dipolar magnetic field because the earth's magnetic field around there is dominated by the 'tail current'; the magnetic field at the geocentric distance of $\geq$15 Re is hardly approximated by a dipole field. The

geosynchronous altitude, the geocentric distance of 6.6 Re, is too near for the boundary condition because it is well known that the ring current flows beyond the geosynchronous altitude. Therefore the geocentric distance of 8-10 Re is considered to be appropriate for the boundary condition of the ring current model. However, the relation between the solar wind density and the plasma sheet density at the geocentric distance of 8-10 Re has never yet been examined. Fortunately, the GEOTAIL satellite during the near-earth orbital phase has been passing through the near-earth plasma sheet at the geocentric distance of $\geq$ 9 Re with wide azimuthal coverage. In this section, by comparing the plasma sheet density observed by GEOTAIL at the geocentric distance of 9-11 Re with the solar wind density observed by WIND simultaneously, the relation between them is statistically investigated to derive the boundary condition at 10 Re of the ring current model.

The GEOTAIL satellite was launched on July 24, 1992. The primary purpose of the mission is to study the structure and dynamics of the tail region of the magnetosphere. The GEOTAIL mission is divided into two phases. During the first two years, the GEOTAIL satellite surveyed the distant magnetotail (about 200 Re). In February 1995, the second phase commenced as the apogee was reduced to 30 Re and the perigee 10 Re. The perigee was, moreover, reduced to 9 Re in the northern summer of 1997.

The number density and temperature of ions in the plasma sheet are provided by GEOTAIL LEP [*Mukai et al.*, 1994], and the magnetic field is provided by GEOTAIL MGF [*Kokubun et al.*, 1994]. The solar wind and the IMF data sets are provided by SWE [*Ogilvie et al.*, 1995] and MFI [*Lepping et al.*, 1995] instruments aboard the WIND satellite, respectively. The momentum data sets for the plasma sheet density and temperature

provided by the GEOTAIL LEP term are used. The momentum data is calculated from the observation of the energy-per-charge analyzer (EA-ion) of GEOTAIL LEP which gives three-dimensional velocity distributions of ions over the energy-per-charge ranges of 32 eV/q-39 keV/q. The criteria to select the available data sets are listed in **Table 5.1**. To except the data observed in the lobe, identified from high ion beta value defined as $2\mu_0 N_{ps} kT/B^2$, where k and T are Boltzmann's constant and the temperature, respectively, the high ion beta value is added to the criteria. The data observed during umbras and penumbras of GEOTAIL are also excepted. A time lag from WIND to the earth is adjusted by using the solar wind velocity being fixed to be 400 km/s. However, the delay of the penetration of the solar wind medium into the plasma sheet is not considered here. During the periods when the perigee of GEOTAIL was located in the plasma sheet (April 1995 - August 1995, May 1996 - October 1996, April 1997 - October 1997), there were 89 GEOTAIL orbits and 170 thirty-minutes intervals which satisfied the criteria. Position of GEOTAIL satisfying the criteria listed in **Table 5.1** is shown in **Figure 5.2**.

GEOTAIL LEP	available
MLT of GEOTAIL	21h - 3h
Radial distance of GEOTAIL	9 - 11 Re
|GSM-Z| of GEOTAIL	<2 Re
Radial distance of WIND	>15 Re
Ion beta ($=2\mu_0 nkT/B^2$)	>0.8

Table 5.1. Criteria for the selection of GEOTAIL and WIND data sets.

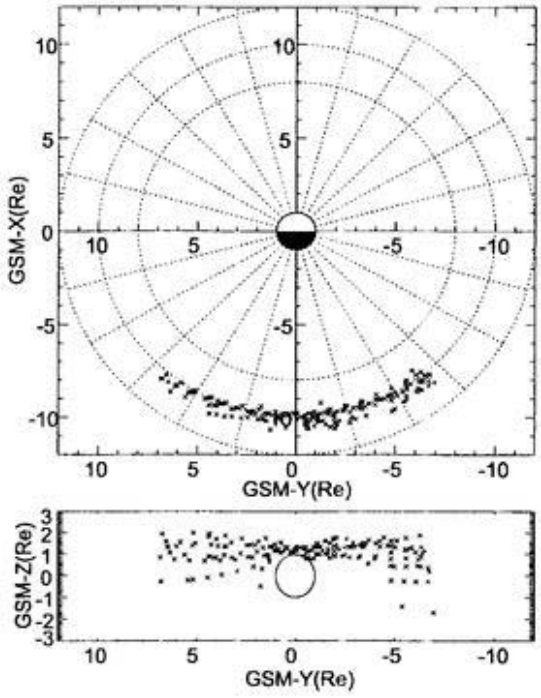

Figure 5.2. Position of GEOTAIL satisfying the criteria in 1995-1997. Top and bottom panels show the position in the GSM-X-Y plane and the GSM-Y-Z plane, respectively.

5.2.2 Results

The result of the statistical analysis is shown in **Figure 5.3**. As shown in **Figure 5.3**, the plasma sheet density N_{ps} in the near-earth plasma sheet at the geocentric distance of 9-11 Re is well correlated with the solar wind density N_{sw}; the result is consistent with the previous studies [*Terasawa et al.*, 1997; *Borovsky et al.*, 1997]. The data indicated in **Figure 5.3** can be fitted by $N_{ps} = 0.025N_{sw} + 0.395$ (cm^{-3}). The color codes indicate the IMF-Bz averaged in the each interval, however, the dependence of the IMF-Bz is not clear. The fitted equation derived here is used to estimate the plasma sheet density at the geocentric distance of 10 Re for the boundary condition of this ring current model.

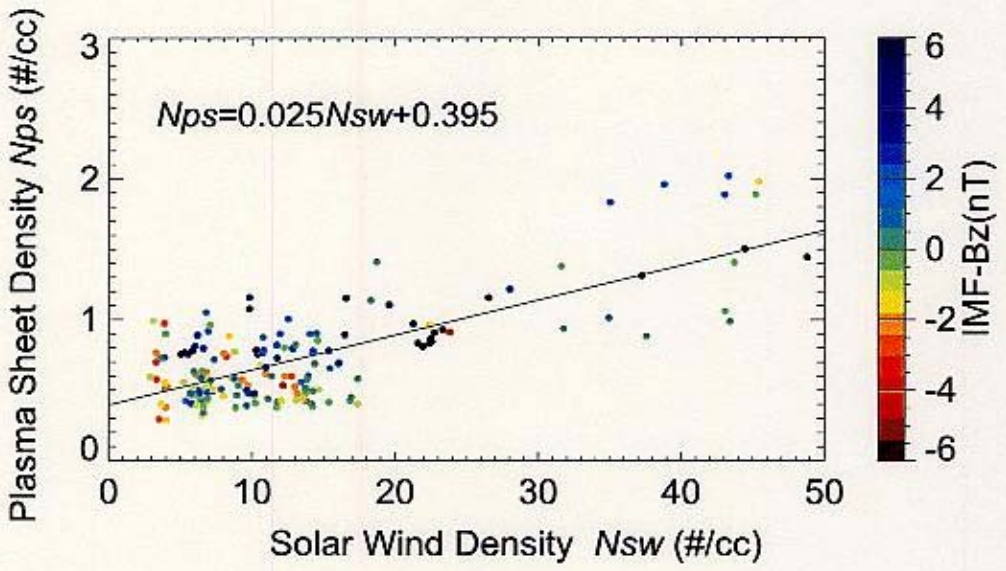

Figure 5.3. The plasma sheet density at the geocentric distance of 9-11 Re (N_{ps}) as a function of the solar wind density (N_{sw}). The color codes indicate the GSM-Z component of IMF.

5.3 Simulation scheme

A simulation scheme is schematically summarized in **Figure 5.5**. All ions whose distribution function is assumed to be isotropic Maxwellian are injected through the 'injection boundary' azimuthally located at L of 10 with MLT of 21h-3h. The temperature at the boundary is fixed to be 5 keV and the number density depends on the solar wind density. After tracing the ions under a dipole magnetic field, the corotation electric field and the Volland-Stern type convection field with its intensity depending on the solar wind velocity and IMF, the directional differential flux in the equatorial plane is calculated. The ions are lost by two processes; the charge exchange with the neutral hydrogen and the convection outflow. Because of the reason that the differential flux in the equatorial plane has information of a pitch angle, the off-equatorial differential flux can be mapped from

the equatorial differential flux. By integrating the differential flux in velocity space, the plasma pressure and the current density are obtained. The magnetic disturbance due to the current density can be directly obtained by the Biot-Savart integral over the whole three-dimensional distribution of the calculated current density.

5.3.1 Convection electric field model depending on solar wind and IMF

Many coupling functions between the polar cap potential and the solar wind condition have been proposed since *Reiff et al.*[1981] examined coupling functions by direct satellite observations. Recently, *Boyle et al.*[1997] reexamined the previously presented coupling functions using more than 58000 polar passes of DMSP with stringent criteria to provide updated estimates of the polar cap potential. *Boyle et al.*[1997] found that the function expressed as

$$\begin{aligned}\Phi_{PC} &= -4.1 + 0.5\sin(\phi + 0.056 + 0.015B_y(\mathrm{nT})) \\ &\quad \left(1.1\times10^{-4}V_{sw}(\mathrm{km/s})^2 + 11.1B_{IMF}(\mathrm{nT})\sin^3(\theta_{IMF}/2)\right) \quad (\mathrm{kV}), \qquad (5.1)\end{aligned}$$

where $\Phi_{PC}, \phi, B_y, V_{sw}, B_{IMF}$ and θ_{IMF} are the polar cap potential, magnetic local time, a GSM-Y component of IMF, a bulk velocity of the solar wind, a magnetic intensity of IMF and a polar angle of IMF, respectively, has the highest correlation with satellite observations in the functions that they examined. After removing the skewed angle of the potential, Eq.(5.1) can be applied to the Volland-Stern type convection field model [*Volland*, 1973;

Stern, 1975] with a shielding factor of 2 in the equatorial plane as

$$\Phi \approx \left[1.1 \times 10^{-4} V(\mathrm{km/s})^2 + 11.1 B_{IMF}(\mathrm{nT}) \sin^3(\theta_{IMF}/2)\right] \frac{\sin\phi}{2} \left(\frac{R}{R_B}\right)^2 \quad (\mathrm{kV}), \qquad (5.2)$$

where Φ, R and R_B are the electric potential, the geocentric distance and the geocentric distance of the magnetopause at MLT of 6 hour or 18 hour, respectively. In a dipolar magnetic field, the geocentric distance of the magnetosphere boundary R_B in the equatorial plane is given by

$$R_B = \frac{1}{\cos^2 \lambda_{PC}} \quad (\mathrm{Re}), \qquad (5.3)$$

where λ_{PC} is a latitude of the polar cap boundary, which is taken to be 72° corresponding to R_B of 10.47 Re. Although the magnetosphere boundary R_B is sensitive to the solar wind dynamic pressure [e.g., *Spreiter and Hyett*, 1963; *Sibeck et al.*, 1991; *Shue et al.*, 1997], the magnetosphere boundary R_B is assumed to be steady in this simulation.

An example of the estimated polar cap potential is shown in **Figure 5.4**. The potential derived from the Kp dependent model by *Maynard and Chen*[1975] is also shown in the same panel to make a comparison. The solar wind bulk velocity (V_{sw}), the intensity of IMF (B_{IMF}) and the polar angle of IMF (θ_{IMF}) are plotted in the first three panels of **Figure 5.4**; these quantities are used to estimate the polar cap potential Φ_{PC} as expressed in Eq.(5.2). The solar wind and the IMF data sets are provided by SWE [*Ogilvie et al.*, 1995] and MFI [*Lepping et al.*, 1995] instruments aboard the WIND satellite, respectively. The fourth panel indicates the Kp history for the Kp dependent potential model [*Maynard and*

Chen, 1975]. Two lines in the fifth panel of **Figure 5.4** indicate the polar cap potential Φ_{PC} estimated by the solar wind velocity and the IMF dependent model [*Boyle et al.*, 1997] (thick line) and Kp [*Maynard and Chen*, 1975)] (thin line). Both estimated potentials resemble each other except for a sudden increase of Kp index at 0300 UT on April 11, 1997. There are two reasons to use the solar wind and IMF dependent model better than the Kp dependent model: One is the time resolution of controlling quantities; Kp indices are provided only 3 hours values. Another is due to a physical meaning; the solar wind and IMF are considered to control the polar cap potential directly though Kp is one of resultant quantities indicating the magnetospheric activity.

5.3.2 Distribution function at an 'injection boundary'

All ions pass through an 'injection boundary' azimuthally located at L of 10 Re with MLT of 21 h to 3 h. The distribution function at the injection boundary located at L of 10 is assumed to be isotropic Maxwellian with the temperature of 5 keV and various densities. The distribution function is independent of MLT. As examined in Section 5.2, the plasma sheet density N_{ps} at the injection boundary is given by the solar wind density N_{sw} as

$$N_{ps}(\mathrm{cm}^{-3}) = 0.025 N_{sw}(\mathrm{cm}^{-3}) + 0.395.$$

The temperature of plasma sheet hardly depends on the solar wind temperature [e.g., *Terasawa et al.*, 1997], but *Baumhohann* [1996] and *Birn et al.* [1997] statistically examined and concluded that the plasma sheet temperature increases after substorm onsets. However, from two reasons, the plasma sheet temperature is assumed to be steady in this simulation:

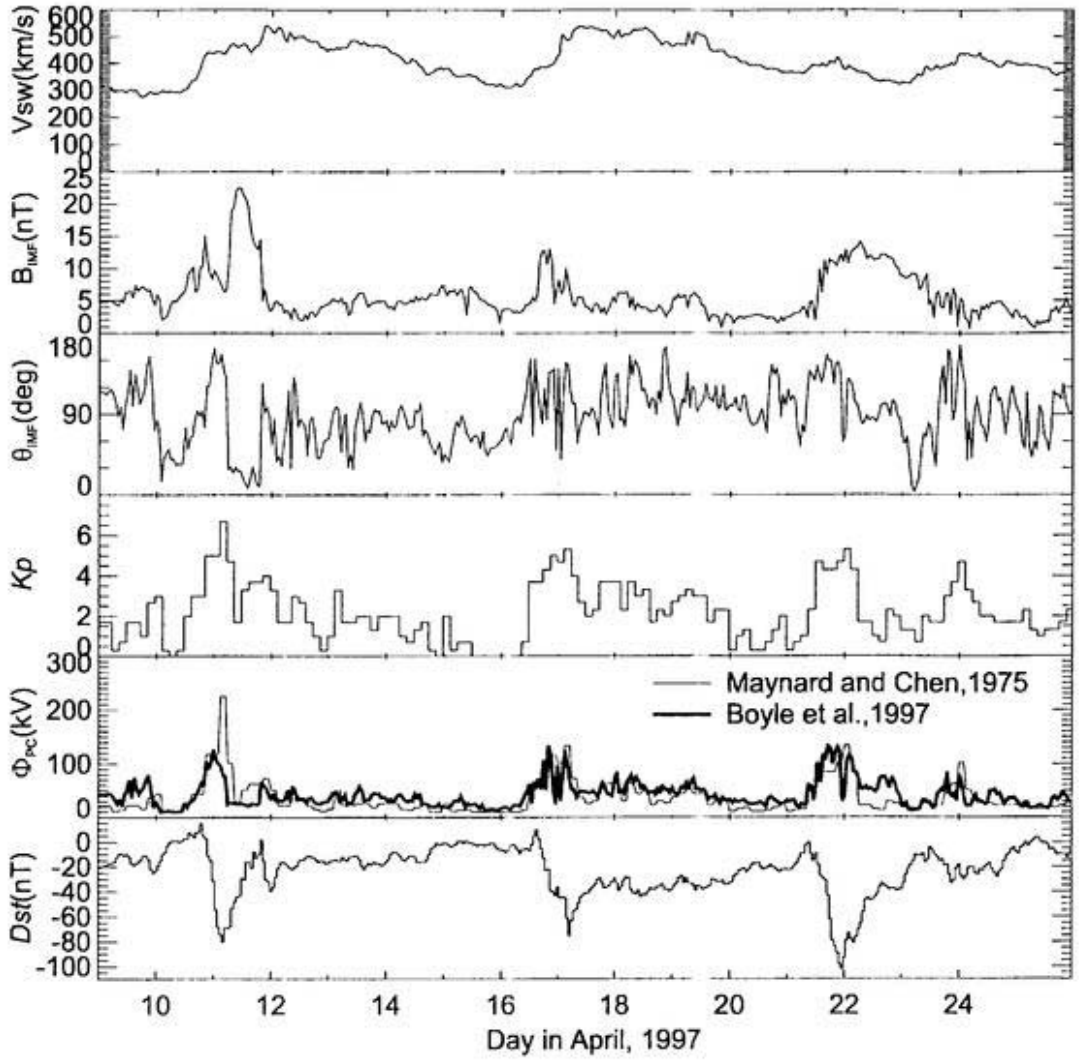

Figure 5.4. From top panel, the solar wind bulk velocity (V_{sw}), the magnetic intensity of IMF (B_{IMF}), the polar angle of IMF (θ_{IMF}), the Kp history, the total polar cap potential drop Φ_{PC}, Dst indices on April, 9-26, 1997, when three successive magnetic storms occurred. The solar wind and IMF quantities are hourly averaged. A thick line in the fifth panel indicates the polar cap potential drop calculated by *Boyle et al.* [1997] depending on V_{sw}, B_{IMF} and θ_{IMF}. A thin line indicates the potential calculated by *Maynard and Chen et al.* [1975] depending on Kp indices.

First, the determination of a substorm onset is too difficult. Second, the time scale of a temperature enhancement associated with a substorm is quite shorter than the time scale of a storm; the typical enhancements of the temperature last within an hour. On the other hand, typical main phases of moderate or intense storms sustain for more than a half of a day. The dependence of the temperature on the ring current buildup as indicated by corrected Dst is examined in Section 5.5.2.

5.3.3 Drift trajectories

Drift trajectories of packet particles including the real number of ions in a small phase space bin (various energies and pitch angles) are traced by bounce-average approximation under a dipole magnetic field, a time-dependent convection electric field and a corotation electric field. The follows are assumed in this model; (1) the first two invariants are conserved, (2) field lines are equipotential and (3) motion of particles induces no additional field. The numerical method to trace the bounce-average trajectory is described in *Ejiri* [1978]; time development equations of the bounce-average drift motion becomes

$$\frac{dX}{dt} = -\frac{\omega}{\gamma} X^{\gamma+2} \cos\phi, \tag{2.63}$$

$$\frac{d\phi}{dt} = \omega X^{\gamma+1} \sin\phi + \omega - \frac{3\mu G(y_0)}{qR_s^2 X^2}, \tag{2.64}$$

$$X \equiv \frac{R}{R_s}, \tag{2.66}$$

where $q, \omega, \mu, R_s, \gamma$ and G are particle charge, angular velocity of earth's rotation, first adiabatic invariant (magnetic moment), a geocentric distance of a stagnation point at

MLT of 18h for a zero energy particle, a shielding factor being taken to be 2 and a function of an equatorial pitch angle given by *Ejiri* [1978], respectively.

5.3.4 Charge exchange loss process

The ions are lost by two physical processes; the charge exchange with the neutral hydrogen and convection outflow due to arrival at the magnetopause azimuthally located at L=10. The charge exchange is one of significant loss processes of ring current ions [e.g., *Frank*, 1967; *Swisher and Frank*, 1968; *Prülss*, 1973; *Tinsley*, 1976; *Lyons and Evans*, 1976; *Smith and Bewtra*, 1978; *Smith et al.*, 1981]. The lifetime of an ion due to the charge exchange τ_{ce} is given by

$$\tau_{ce} = \frac{1}{n_H \sigma_H v}, \tag{3.36}$$

where n_H is the density of neutral hydrogen, σ_H charge exchange the cross section and v thermal velocity of an ion. A trapped ion bouncing between northern and southern mirror points experiences different density of the neutral hydrogen aligned with its bouncing trajectory. The bounce-average density of the neutral hydrogen for an bouncing ion is introduced and is given by

$$\langle n_H \rangle \equiv \frac{\int \frac{n(s)}{v_{\parallel}(s)} ds}{\int \frac{1}{v_{\parallel}(s)} ds} \tag{3.37}$$

$$\simeq \frac{n'_H}{\cos^j \lambda_m}, \tag{3.38}$$

where $v_{\|}, ds, j, n'_H$ and λ_m are parallel velocity of an ion, a line element aligned with a field line, an approximate factor, the equatorial density of the neutral hydrogen, and the mirror latitude, respectively. After substituting Eq.(3.38) into Eq.(3.36), the charge exchange lifetime for a trapped ion can be rewritten as

$$\tau_{ce} \simeq \frac{\cos^j \lambda_m}{n'_H \sigma_H v}. \tag{3.39}$$

Following *Smith and Bewtra* [1978], the approximate factor j is taken to be 3.5.

A spherically symmetric model derived by *Chamberlain* [1963] is used to obtain the number density of the neutral hydrogen. Parameters for the Chamberlain model are given by *Rairden et al.* [1986]; the parameters are exobase temperature, 1050 K; exobase density, 44000 cm^{-3}; geocentric distance of exobase r_c, 1.08 Re (500 km altitude); and a critical radius for satellite atoms, 3.0 r_c. The fitting parameters was derived from the ultraviolet photometer imaging by DE-1 satellite [*Rairden et al.*, 1986].

Number of ions lost by the charge exchange is calculated along with their bounce-average trajectories. This process can be numerically expressed as

$$\frac{\partial f}{\partial t} = -\frac{f}{\tau_{ce}}, \tag{3.41}$$

where f is the phase space density.

5.3.5 Directional differential number flux

The manner to calculate an equatorial differential flux is as follows: First, all packet particles are gathered into a small phase space bin $(\Delta L, \Delta\phi, \Delta W, \Delta y)$, where L, ϕ, W and y are McIlwain's L-value, MLT, the kinetic energy and a sine of a pitch angle, respectively. Next, the directional differential flux in the equatorial plane $j_0(L, \phi, W, y)$ is calculated as

$$j_0(L, \phi, W, y) = \frac{\Delta N_{bin}}{2\pi S \tau_b y \Delta y \Delta W}, \tag{3.42}$$

where ΔN_{bin}, S and τ_b are the real number of gathered particles in the bin, the area in the equatorial plane and the bounce period of a particle, respectively.

The off-equatorial differential flux j_0 at a latitude of λ can be derived from the Liouville's theorem [*Roederer*, 1970] as

$$j(L, \phi, \lambda, W, y) = j_0(L, \phi, W, h(\lambda)y), \tag{3.43}$$

with

$$h(\lambda) \equiv \frac{\cos^3 \lambda}{(1 + 3\sin^2 \lambda)^{1/4}}. \tag{3.44}$$

5.3.6 Plasma pressure

The perpendicular and parallel pressures, $P_\perp$ and $P_\parallel$, are given by

$$P_\parallel = \int m v^2 F(\boldsymbol{v}) \cos^2 \alpha \, d\boldsymbol{v}, \tag{3.45}$$

$$P_\perp = \int \frac{1}{2} m v^2 F(\boldsymbol{v}) \sin^2 \alpha d\boldsymbol{v}, \tag{3.46}$$

where F is the velocity distribution function and m the particle's mass. The pressure can be expressed by using the directional differential flux j instead of the velocity distribution function F as

$$P_\perp = \pi\sqrt{2m} \int_\alpha \int_W j\sqrt{W} \sin^3 \alpha d\alpha dW, \tag{3.47}$$

$$P_\parallel = 2\pi\sqrt{2m} \int_\alpha \int_W j\sqrt{W} \cos^2 \alpha \sin \alpha d\alpha dW. \tag{3.48}$$

5.3.7 Current density

The current density perpendicular to the magnetic field in the ring current has been considered as a combination of the three currents [*Parker*, 1957]; the magnetization current $\boldsymbol{J}_M$, the curvature drift current $\boldsymbol{J}_R$ and the grad-B drift current $\boldsymbol{J}_B$. The total current density $\boldsymbol{J}_\perp$ is given by

$$\begin{aligned} \boldsymbol{J}_\perp &= \boldsymbol{J}_M + \boldsymbol{J}_R + \boldsymbol{J}_B, \\ \boldsymbol{J}_\perp &= \frac{\boldsymbol{B}}{B^2} \times \left[\nabla P_\perp + (P_\parallel - P_\perp) \frac{(\boldsymbol{B} \cdot \nabla)\boldsymbol{B}}{B^2} \right]. \end{aligned} \tag{2.3}$$

A detail for the derivation of the current density $\boldsymbol{J}_\perp$ is described in Appendix B. In the dipolar magnetic field, the azimuthal component of the current density J_ϕ becomes

$$J_\phi = \frac{1}{B^2} \left(\frac{B_r}{r} \frac{\partial P_\perp}{\partial \lambda} - B_\lambda \frac{\partial P_\perp}{\partial r} \right)$$

$$+\frac{1}{B^3}\left(P_{\parallel}-P_{\perp}\right)\left(\frac{B_r}{r}\frac{\partial B}{\partial \lambda}-B_{\lambda}\frac{\partial B}{\partial r}\right) \tag{4.9}$$

$$= \frac{r^3}{M\left(1+3\sin^2\lambda\right)} \left[-\frac{2}{r}\sin\lambda\frac{\partial P_{\perp}}{\partial \lambda}-\cos\lambda\frac{\partial P_{\perp}}{\partial r} + \frac{P_{\parallel}-P_{\perp}}{r}\left(-\frac{6\sin^2\lambda\cos\lambda}{1+3\sin^2\lambda}+3\cos\lambda\right)\right], \tag{4.10}$$

where B_r, B_λ, r and M are the radial component of the magnetic field, the latitudinal component of the magnetic field, the radial distance from the center of the earth, and the magnetic moment of the earth, respectively.

5.3.8 Magnetic disturbance and corrected Dst*

After integrating the three-dimensional distribution of the current density, the magnetic disturbance induced by the current can be derived from the Biot-Savart's law. Especially, the magnetic disturbance parallel to the earth's dipole at the center of the earth ΔB_C is given by

$$\Delta B_C = \frac{\mu_0}{4\pi}\int_r\int_\lambda\int_\phi \cos\lambda J_\phi(r,\lambda,\phi)drd\lambda d\phi, \tag{4.11}$$

where μ_0 is the permeability in vacuum and J_ϕ the azimuthal component of the current density $\boldsymbol{J}_\perp$. Here, ΔB_C is considered to be equivalent to corrected Dst (hereinafter referred to Dst*).

Corrected Dst, which is widely accepted as a good indicator of the strength of the ring current, is given by subtracting D_{CF} (due to the Chapman-Ferraro current) from the

observed Dst and removing the earth's induction as

$$Dst* = \left(Dst - c_1 P_{sw}^{1/2} + c_2\right)/\xi, \tag{4.12}$$

where P_{sw} is the dynamic pressure of the solar wind, which is given by $N_{sw} m V_{sw}^2$, and ξ a coefficient for the earth's induction, and c_1 and c_2 are empirical coefficients, respectively. Typically, the coefficients, c_1 and c_2, are 0.2 nT/(eV $cm^{-3})^{1/2}$ and 20 nT, respectively [e.g., *Gonzalez et al.*, 1994]. *Dessler and Parker* [1959] mentioned that the observed Dst is 1.5 times larger than the impressed field in the vicinity of a perfectly diamagnetic earth. Therefore the coefficient for the induction ξ is taken to be 1.5.

5.3.9 Simulation flow

The simulation flow is as follows.

1. Set the solar wind density N_{sw}, the solar wind bulk velocity V_{sw} and IMF.

2. Calculate the polar cap potential Φ_{PC} deduced from the solar wind velocity and IMF. Also calculate the plasma sheet density N_{ps} deduced from the solar wind density N_{sw}.

3. Inject ions, having a distribution function of isotropic Maxwellian, passing through the injection boundary azimuthally located at R_i=10 Re. Each packet particle has a real number of ions.

4. Trace bounce-average trajectories of the particles under a dipole magnetic field and the time-dependent convection field.

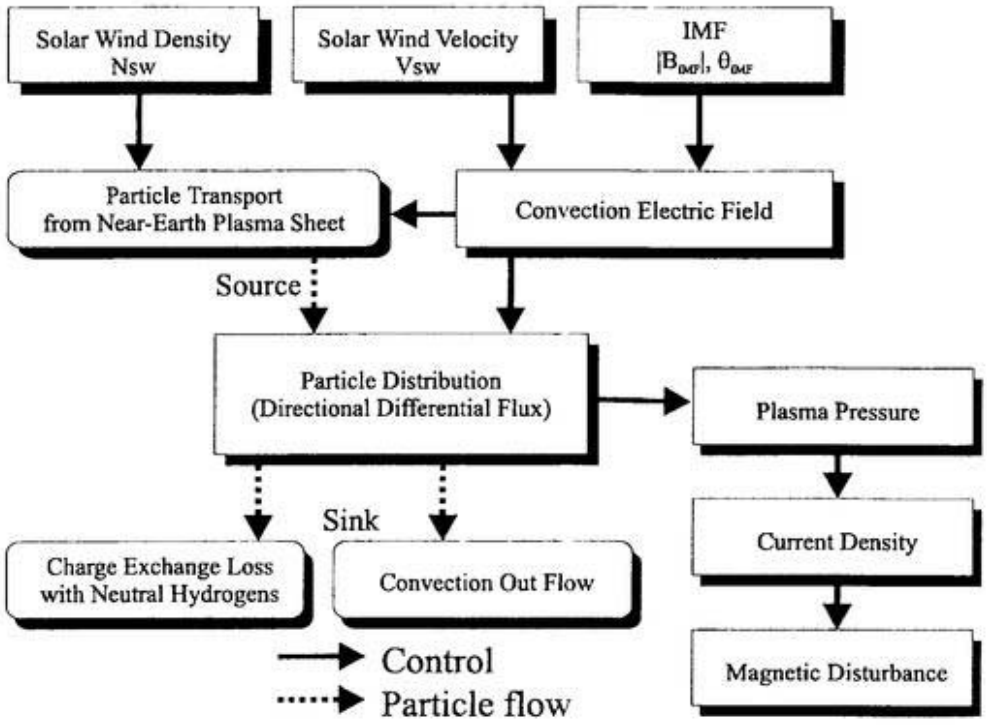

Figure 5.5. A block diagram of this simulation depending on the solar wind and IMF. Rectangles and round rectangles indicate physical quantities and physical process, respectively. The primary output of this simulation is the directional differential flux in the equatorial plane.

5. Calculate the directional differential flux at every time step.

6. After calculating the charge exchange lifetime for each ion, the number of particles in the phase space are lost.

7. Return to 1.

5.4 Magnetic storm in April, 1997

5.4.1 Outline of the storm

In this section, three successive magnetic storms occurred in April 1997 are examined. The solar wind bulk velocity (V_{sw}), the solar wind proton number density (N_{sw}), the GSM-X, -Y and -Z components of the interplanetary magnetic field (IMF-Bx, -By and -Bz), and the final Dst index during the storms are plotted in **Figure 5.6**. The solar wind data and the IMF data are obtained from SWE [*Ogilvie et al.*, 1995] and MFI [*Lepping et al.*, 1995] instruments aboard the WIND satellite, respectively. NOAA (National Oceanic and Atmospheric Administration) reported that there were three major storms in April 1997; the storms began at 1300 UT on April 10, 1997 (hereinafter denoted as Storm I), at 1320 UT on April 16 (Storm II) and at 0500 UT on April 21 (Storm III), which are indicated by vertical lines in **Figure 5.6**. An SC (sudden commencement) was clearly observed at the beginning of the Storm II. The minima of Dst are -82 nT, -77 nT and -107 nT, respectively. Therefore the storms are categorized to a moderate or an intense storm. Especially, the Storm III was caused by a passage of a large magnetic cloud with an estimated diameter

of 0.4 AU [R. Lepping, personal communication, 1998].

5.4.2 Model calculation

Ebihara and Ejiri [1998] examined the ring current buildup and its decay of the same storms in April, 1997 using the convection electric field depending on the Kp index. Instead of the Kp dependent convection model, the solar wind and IMF dependent model is used in this chapter. The magnetosphere is initially empty, and the injection begins at 0000 UT on April 9, 1997 before a commencement of the storm I. The calculation summarized in **Figure 5.5** continues with a time step of 5 minutes and lasts at 0000 UT on April 26, 1997.

5.4.3 Comparison with the observed Dst*

In **Figure 5.7**, calculated Dst* is compared with observed Dst* during the period of April 9-25, 1997. Because the magnetosphere is initially empty, calculated Dst* begins with Dst* of 0 at 0000 UT on April 9, 1997. Before a commencement of the Storm I, both calculated and observed Dst* decrease in response to a negative excursion of IMF-Bz during a period of 1640-2200 UT on April 9, 1997. After then, three successive storms began at 1300 UT on April 10, 1997 (Storm I), at 1320 UT on April 16 (Storm II) and at 0500 UT on April 21 (Storm III), respectively.

It can easily be found that calculated Dst* is in fairly good agreement with observed Dst* for these particular storms except for periods around minima of Dst*. Details of comparisons are mentioned below.

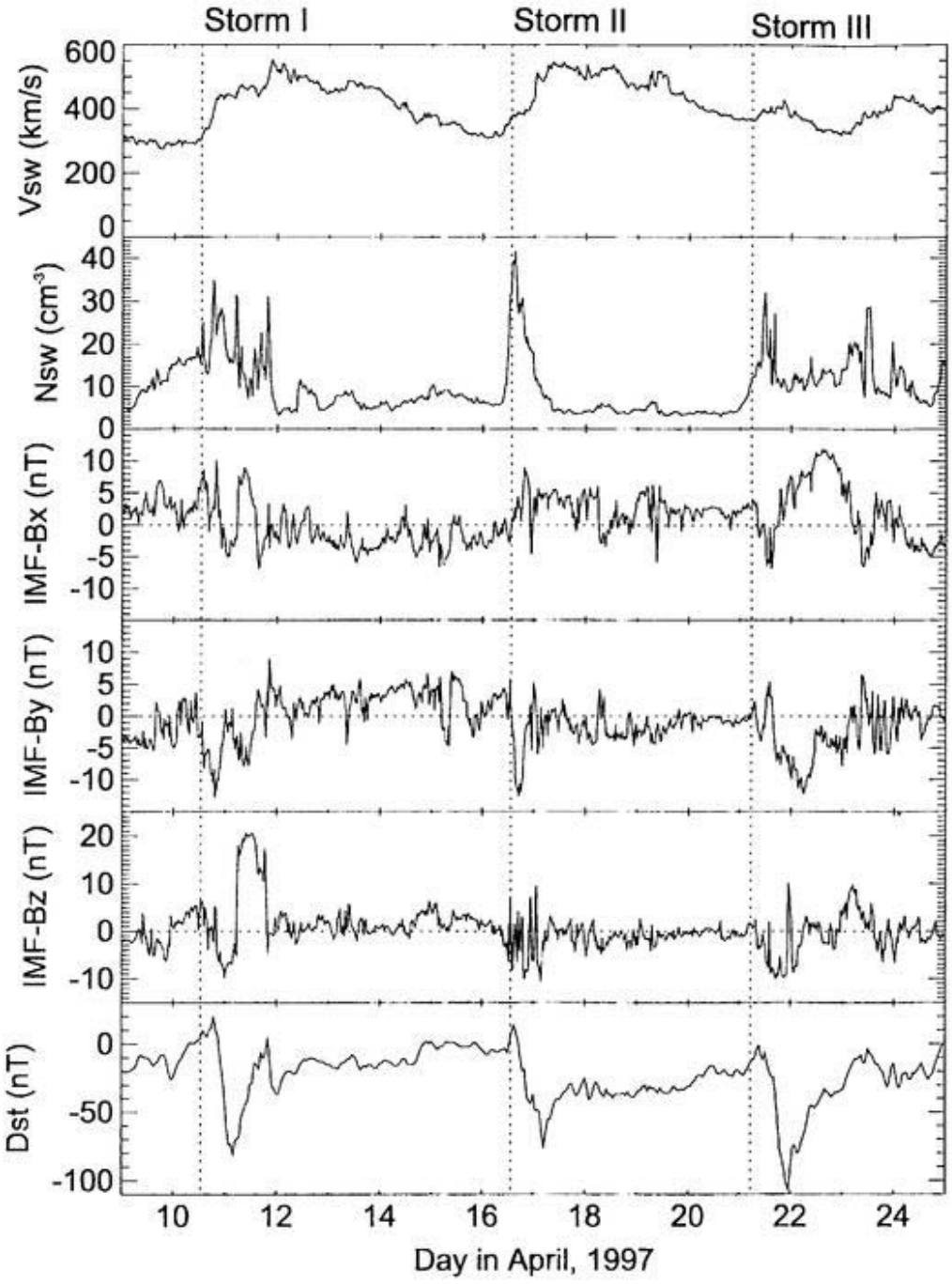

Figure 5.6. The solar wind, IMF and Dst during a period the storms on April 9-25, 1997. From the top to the bottom panels, the solar wind bulk velocity V_{sw}, the number density of the solar wind protons N_{sw}, the GSM-X, -Y and -Z components of the IMF and final Dst are shown. Vertical lines indicate the start times of the storms.

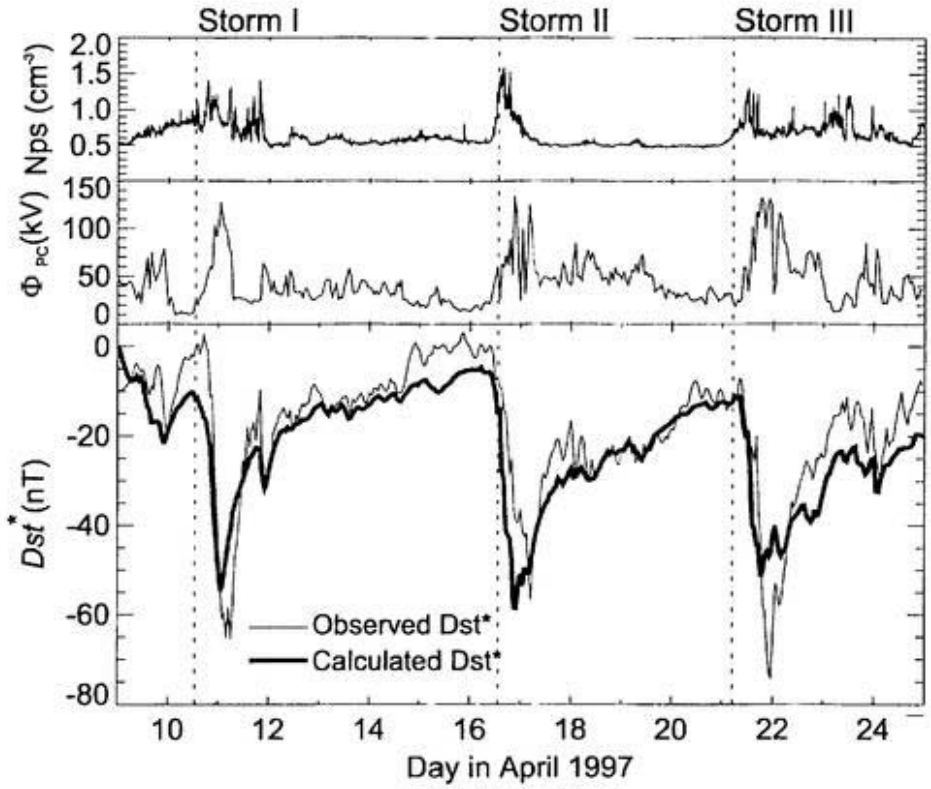

Figure 5.7. Comparison between calculated and observed Dst*. From the top panel, the plasma sheet number density deduced from the solar wind density, the polar cap potential drop derived by *Boyle et al.* [1997] and calculated Dst* (thick line) with observed Dst* (dotted line) during the period of April 9-25, 1997 are shown.

Storm I

Figure 5.8 shows calculated and observed Dst* during the Storm I. After a commencement of an initial phase of the real Storm I at 1300 UT on April 10, 1997, a main phase began at 1900 UT on April 10. Since the effect of Chapman-Ferarro magnetopause current flowing eastward is removed from observed Dst, the change of phases from the initial phase to the main phase, usually identified from a commencement of a negative excursion of Dst, is ambiguous. The decrease of calculated Dst* (corresponding to the ring current buildup)

begins at 1100 UT on April 10, 1997 due to an enhancement of Φ_{PC}. While calculated Dst* reaches its minimum of -55 nT at 0100 UT on April 11, the decrease of observed Dst* lasts until 0600 UT on April 11 with its minimum Dst* of -65 nT; calculated minimum Dst* is lacking by 15 % of observed minimum Dst*, and calculated Dst* recovers faster than observed Dst*. One possible reason for the time lag between the minima is that the plasma sheet density responds to the solar wind density with a time lag [*Terasawa et al.*, 1997], however, the time lag is ignored in this simulation. The time lag between them will be examined in Section 5.5.6. The other reasons for the difference is the underestimated polar cap potential Φ_{PC}; observed Dst* begins to increase at 0600 UT on April 11 when the IMF-Bz suddenly turns northward. Therefore the actual polar cap potential Φ_{PC} may be continuously enhanced until 0600 UT on April 11 though the deduced Φ_{PC} begins to decrease at 0100 UT on April 11.

In the recovery phase, a second decrease of Dst* appears during a period of 2100-2200 UT on April 11. The southward turning of IMF and the enhanced solar wind density up to 30 cm^{-3} cause the second decrease in the recovery phase of the storm. The decrease is in agreement with the observation. After then, small fluctuations also appear; these fluctuations are caused by change of polar cap potential.

Storm II

Figure 5.9 shows calculated and observed Dst* during the Storm II. Since the polar cap potential is highly fluctuated during the main phase, observed Dst* decreases with multiple steps. While observed Dst* peaks to its minimum of -57 nT at 0500 UT on April

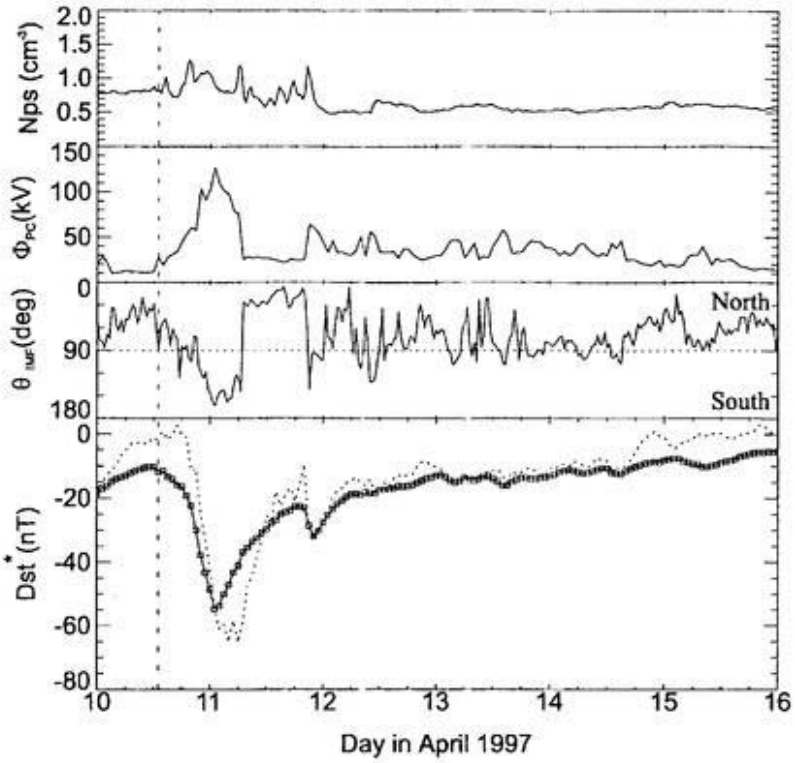

Figure 5.8. Comparison between calculated and observed Dst* for the Storm I. From the top panel, the plasma sheet number density (N_{ps}) deduced from the solar wind density, the polar cap potential (Φ_{PC}) derived by *Boyle et al.* [1997], the polar angle of IMF (θ_{IMF}) and calculated Dst* (thick line) with observed Dst* (thin line) during the period of April 10-16, 1997 (Storm I) are shown.

17, calculated Dst* peaks to the minimum of -59 nT at 2200 UT on April 16; the time for the peak of calculated Dst* is earlier than that for the observed peak by about 7 hours, however, their minima of Dst* resemble each other.

In the recovery phase, there are three obvious enhancements of the polar cap potential at 1800 UT on April 17, 1997; at 0000 UT on April 18 and at 0430 UT on April 18, respectively. As the polar cap potential enhances, observed and calculated Dst* decrease in response to the enhancements. Although both onset times of the decreases resemble each

other, the absolute value of the calculated decrease is smaller than that of the observation. This may be caused by the underestimated plasma sheet density. *Terasawa et al.* [1997] concluded that the solar wind ions diffusively penetrate into the plasma sheet through the LLBL with a characteristic time delay of ~6 hours when IMF points northward. Therefore the long duration of northward IMF leads the plasma sheet to become 'cold and dense'. Thus it is speculated that the real plasma sheet may be 'cold and dense' just prior to the enhancements because northward IMF lasts for about two hours.

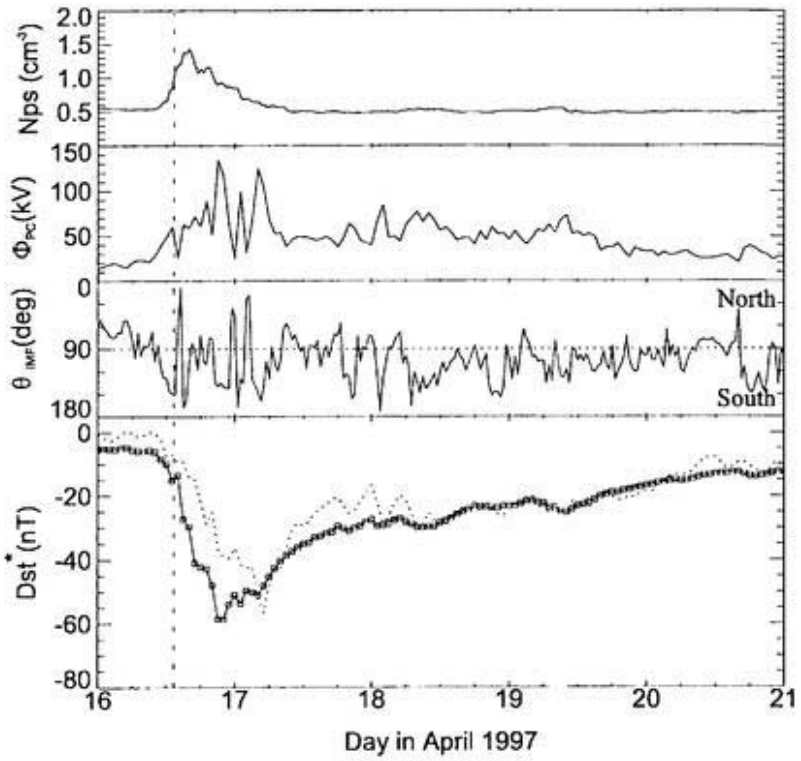

Figure 5.9. Same as previous figure except that calculated and observed Dst* during the period of April 16-21, 1997 (Storm II) are plotted.

Storm III

Figure 5.10 shows calculated and observed Dst* during the Storm III. As described above, this storm is caused by a large magnetic cloud accompanied with a positive excursion of IMF-Bx and a bipolar excursion of IMF-Bz. Calculated minimum Dst* is -51 nT whereas observed minimum Dst* is -74 nT; calculated minimum Dst* is lacking by 32 % of observed minimum Dst*. While a recovery phase of calculated Dst* begins at 1800 UT on April 21, the recovery phase of observed Dst* begins at 2300 UT on April 21; the time lag of 5 hours between them is similar to the case of the Storm I.

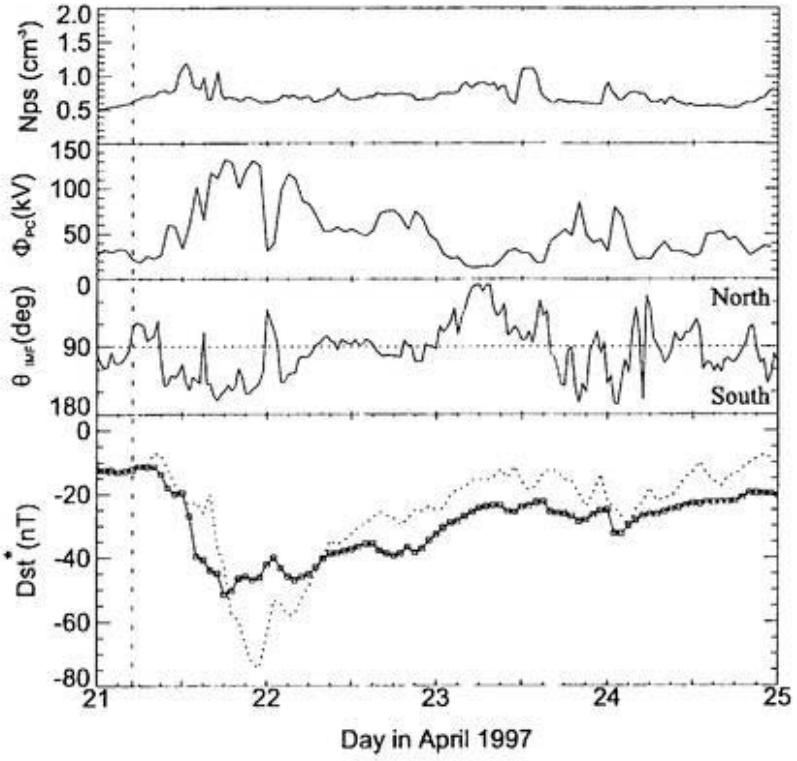

Figure 5.10. Same as previous except that calculated and observed Dst* during the period of April 21-25, 1997 (Storm III) are plotted.

Summary of the comparison

In general, the differences between calculated and observed Dst* arise from some possible reasons listed below.

First, although it is assumed in this simulation that the plasma sheet density responds to the solar wind density immediately, *Terasawa et al.* [1997] statistically examined and found that the plasma sheet density responds to the solar wind density with characteristic time lags of $\sim$ 1 hour for north IMF and $\sim$ 6 hours for south IMF; no time lag between them seems to be unrealistic. The effect of the time lag to the ring current buildup will be examined below.

Secondly, high energy ions with energies above $\sim$ 80 keV which are mainly transported by the radial diffusion also contributes to the ring current [e.g., *Smith and Hoffman*, 1973; *Lui et al.*, 1987; *Hamilton et al.*, 1988]. However the ions transported by the diffusion are ignored in this simulation. The contribution of the higher energy ions will be discussed below in more detail.

Thirdly, this simulation considers no other ion species, especially O^+. Energetic O^+ions dominantly increase as a storm develops. *Hamilton et al.* [1986], *Roeder et al.* [1996] and *Daglis* [1997] reported that the energy density of O^+ions in the ring current dominates the H^+ions during a strong magnetic storm. However, for a moderate storm with minimum Dst of -80 nT, the composition rate of the O^+energy density rose only up to 30 % [*Daglis*, 1997]. This fact supports that the enhanced O^+energy density is a reasonable reason for the difference between the calculated and observed minimum Dst* because the calculated Dst* being lacking by 15 % for the Storm I and by 32 % for the Storm III.

Fourthly, an induction electric field due to dipolarization during an expansion phase of a substorm may change the energy injection rate into the ring current. Although the effect of the induction field hardly contributes to a major variation of storm time Dst* as discussed in the previous section, a minor variation with a short time scale of Dst* may be a result of the substorm effect.

Fifthly, there is an ambiguity of the estimated polar cap potential due to an empirical model. Furthermore, the solar wind and IMF observed by WIND is not always corresponding to the quantities in the vicinity of the earth's magnetosphere. In fact, the WIND satellite was in far away from the earth at the geocentric distance of ~200 Re in April, 1997.

5.5 Discussion

5.5.1 Energy inject rate

As shown in **Figure 5.5**, number of ions passing through the 'injection boundary' is determined by the polar cap potential Φ_{PC} and the plasma sheet number density N_{ps}. In order to reveal the efficiency of them to the ring current buildup as indicated by Dst*, two situations are set and are examined; one is the steady convection with Φ_{PC} of 20 kV, and another is the steady plasma sheet density with N_{ps} of 0.4 cm^{-3}.

Figure 5.11 shows the results for the two cases. For the case of the steady plasma sheet density N_{ps} indicated by a thick solid line, the ring current is changed by the polar cap potential Φ_{PC} only. On the other hand, for the case of the steady polar cap potential Φ_{PC}

indicated by a solid line, the ring current is changed by the plasma sheet density N_{ps} only. By comparing the two curves with observed Dst* indicated by a thin line, it is concluded that the major variation of Dst* is mainly due to the polar cap potential Φ_{PC} and the plasma sheet density N_{ps} as well; these two curves, for the steady convection and for the steady plasma sheet density, are quite different from the observed Dst*. This means that the convection field itself cannot contribute to the ring current buildup alone for these particular storms.

The result can be explained by an analytical expression. To do this, an input rate of total kinetic energy into the ring current is formulated here. In the first, the total energy Γ injected from the near-earth plasma sheet through the 'injection boundary' is defined as

$$\begin{aligned} \Gamma &\equiv \int \frac{1}{2} m v^2 F(\boldsymbol{v}) d\boldsymbol{x} d\boldsymbol{v} && (5.4) \\ &= \int \frac{1}{2} m v^2 F(\boldsymbol{v}) dA v dt \cos\alpha v^2 d\Omega dv \\ &= 2\pi m \int dA \int F(\boldsymbol{v}) v^4 S_b(y) y dy dv, && (5.5) \end{aligned}$$

where $F(\boldsymbol{v}), m, A, \alpha, y, \tau_b$ and $S_b(y)$ are the velocity distribution function, the mass, the area, a pitch angle, a sine of a pitch angle, a bounce period and an integral quantity defined as

$$\begin{aligned} \tau_b &= \frac{2}{v} \int \left(1 - \frac{B_m}{B}\right)^{-1/2} ds && (5.6) \\ &\equiv \frac{2}{v} S_b(y), && (5.7) \end{aligned}$$

where B_m and ds are a magnetic field at a mirror point, a line element align with a field

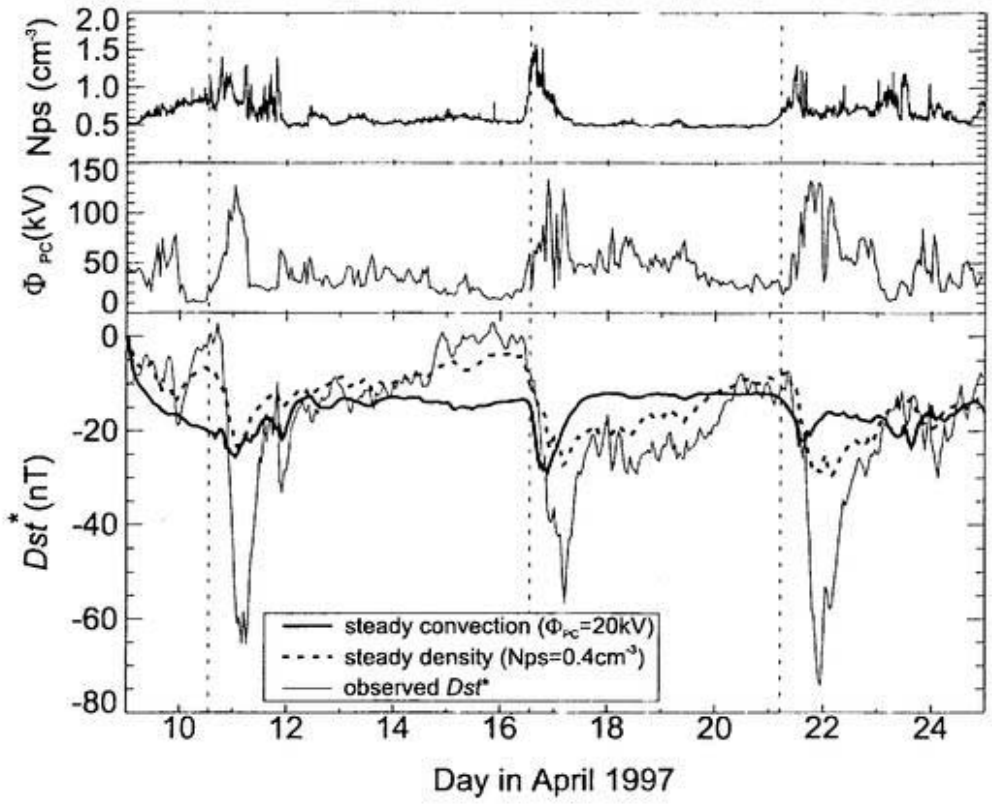

Figure 5.11. Plasma sheet density (top), polar cap potential drop (middle) and Dst* (bottom). Three curves in the bottom panel indicate observed Dst* (thin line), calculated Dst* with steady convection field of 20 kV (thick line) and calculated Dst* with steady plasma sheet density of 0.4 cm^{-3} (dashed thick line), respectively.

line, respectively.

In dipolar geometry, S_b can be obtained by

$$S_b = 2Rf,$$

$$f(y) \simeq 1.38 - 0.32(y + y^{1/2}) + 0.055y^{1/3} - 0.037y^{2/3} - 0.074y + 0.056y^{4/3}, \quad (2.46)$$

where f is a function depending on an equatorial pitch angle. An approximate formula of

f is given by *Ejiri*[1978].

Since the velocity distribution function at the 'injection boundary' is assumed to be an isotropic Maxwellian in this simulation, the velocity distribution function F becomes

$$F = \frac{N_{ps}}{(\pi v_0^2)^{3/2}} \exp\left(-\frac{v^2}{v_0^2}\right), \tag{5.8}$$

where N_{ps} and v_0 are the number density in the plasma sheet and the most probable velocity, respectively.

In polar coordinates, the area dA in the equatorial plane is given by

$$\begin{aligned} dA &= R_0 d\phi dR \\ &= R_0 d\phi dt \frac{dR}{dt} \\ &= R_0 d\phi dt \frac{E_\phi}{B}, \end{aligned} \tag{5.9}$$

where R_0, ϕ and E_ϕ are the geocentric distance of the 'injection boundary', the local time and the azimuthal component of the electric field, respectively. If the convection field is expressed by the Volland-Stern type, the azimuthal component of the electric field is easily led as

$$E_\phi = \frac{1}{R}\frac{\partial \Phi}{\partial \phi} \tag{5.10}$$

$$= AR\cos\phi, \tag{5.11}$$

$$A = \frac{\Phi_{PC}}{2R_B^2}, \tag{5.12}$$

where Φ, R_B and Φ_{PC} are the electric potential, the geocentric distance of the magnetopause and the polar cap potential, respectively. Then the area dA becomes

$$dA = \frac{\Phi_{PC}}{2B}\left(\frac{R_0}{R_B}\right)^2 dt\cos\phi d\phi. \tag{5.13}$$

After substituting Eq.(5.8), Eq.(5.9) and Eq.(5.13) into Eq.(5.5), the total energy Γ is given by

$$\Gamma = \frac{3}{2}N_{ps}E_0\frac{\Phi_{PC}}{2B}\left(\frac{R_0}{R_B}\right)^2\int dt\int\cos\phi d\phi\int S_b y dy, \tag{5.14}$$

where E_0 is the temperature, being corresponding to $mv_0^2/2$. Now, the energy input rate γ is introduced as

$$\begin{aligned}\gamma &= \Gamma/\int dt \\ &= \frac{3N_{ps}E_0\Phi_{PC}}{4B}\left(\frac{R_0}{R_B}\right)^2 Y(R)\int\cos\phi d\phi \text{ (in watt)}, \qquad (5.15)\\ Y(R_0) &\equiv \int S_b(y)ydy. \qquad (5.16)\end{aligned}$$

The quantity Y as a function of geocentric distance is summarized in **Table 5.2**.

After substituting the quantities, R_0 of 10 Re, ϕ of 21 h - 3 h (27 h) and R_B of 10.47 Re, which are used in this simulation, into Eq.(5.15), the energy input rate γ becomes

$$\gamma = 0.286N_{ps}(\text{cm}^{-3})\Phi_{PC}(\text{kV})E_0(\text{keV}) \text{ (in gigawatt)}. \tag{5.17}$$

Eq.(5.17) indicates that the energy injection rate is proportional to the number density in

R(Re)	Y(Re)	R(Re)	Y(Re)
2	1.83	9	8.23
3	2.74	10	9.14
4	3.66	11	10.1
5	4.57	12	11.0
6	5.49	13	11.9
7	6.40	14	12.8
8	7.31	15	13.7

Table 5.2. Y as a function of the radial distance R. Y is used to derive analytically the energy input rate into the magnetosphere.

the plasma sheet (N_{ps}) times the polar cap potential drop (Φ_{PC}) times the temperature in the plasma sheet (E_0).

Because the plasma sheet temperature is insensitive to Dst* as mentioned below (Section 5.5.2), the energy input rate is approximately as a function of the plasma sheet density N_{ps} and the polar cap potential Φ_{PC}. Since the plasma sheet temperature E_0 is fixed to be 5 keV in this calculation, the energy injection rate becomes simply as

$$\gamma = 1.43 N_{ps}(\mathrm{cm}^{-3})\Phi_{PC}(\mathrm{kV}) \quad \text{(in gigawatt)}.$$

For a typical case in a main phase of a storm, the quantities are N_{ps} of 1.5 cm^{-3}, E_0 of 5 keV and Φ_{PC} of 120 kV. Then the energy input rate for the typical case becomes 260 gigawatts.

5.5.2 Dependence of Dst* on plasma sheet temperature

The temperature at the 'injection boundary' located at L of 10 is fixed to be 5 keV in this simulation. Indeed, the average temperature in the near-earth plasma sheet is ~5 keV [e.g., *Peterson et al.*, 1981; *Lennartsson and Shelley*, 1986; *Baumjohann et al.*, 1989; *Paterson et al.*, 1998]. The temperature in the near-earth plasma sheet is poorly correlated with the solar wind average energy [e.g., *Terasawa et al.*, 1997]. However, *Baumjohann* [1996] statistically concluded that the ion temperature in the near-earth plasma sheet between 10 to 19 Re increases after a substorm expansion determined by AE index, and furthermore, *Birn et al.* [1997] also statistically shows that the temperature in the near-earth plasma sheet at 6.6 Re increases around a substorm onset as indicated by a dispersionless particle injection.

As mentioned in the previous subsection (Section 5.5.1), the analytic expression of the energy input rate (Eq.(5.17)) indicates that the energy input rate into the ring current is a function of the temperature in the near-earth plasma sheet E_0 as well as the polar cap potential and the plasma sheet density. As the plasma sheet temperature increases, the relative number of ions with higher energies increases but the relative number of ions with lower energies decreases. Because ions with higher energies tend to drift azimuthally, it becomes hard for the high energy ions to move radially inward. Therefore these ions flow away in the magnetosphere immediately, slightly contributing to the ring current buildup; the strength of the ring current as indicated by Dst* is not proportional to the plasma sheet temperature.

Figure 5.12 shows minimum Dst* of the Storm I on April 10-11, 1997 as a function of

the plasma sheet temperature E_0. It is revealed that the ring current buildup as indicated by Dst* is insensitive to the temperature in the near-earth plasma sheet for the temperature above 3 keV with the variation being within 10 %. However, for the temperature below 3 keV, minimum Dst* is sensitive to the plasma sheet temperature.

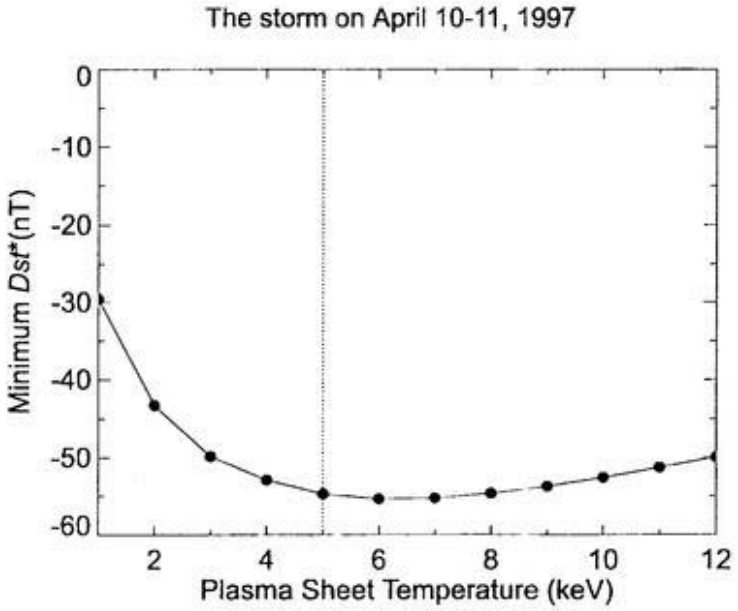

Figure 5.12. Temperature dependence of the ring current buildup. A curve indicates minimum Dst* as a function of the plasma sheet temperature for the Storm I occurred on April 10-11, 1997.

5.5.3 Electric current distribution

An equivalent westward line current flowing at the geocentric distance of 4-5 Re has been previously considered to explain a storm time negative bay of Dst (references to be surveyed). However, the classical idea is incorrect. The actual distribution of electric currents is complex as *Akasofu and Chapman* [1961] and *Hoffman and Bracken* [1965, 1967]

presented, which is not a wire current. In this subsection, the spatiotemporal distributions of the plasma pressure and the current density during a magnetic storm are examined.

Figure 5.13 shows the temporal evolution of the plasma pressure perpendicular to the magnetic field $P_{\perp}$ and the current density perpendicular to the magnetic field $J_{\perp}$ in the equatorial plane in the Storm I. There are three characteristics to be noted:

1. At the beginning of the Storm I (at 1800 UT on April 10, 1997; labeled as A), a peak of the plasma pressure is located at the geocentric distance of 6.0 Re with the perpendicular plasma pressure of 5 nPa in the dusk region.

2. As the storm most develops at 0100 UT on April 11 (labeled as B), the plasma pressure drastically increases in the dusk region; the peak is located at 5.3 Re with the perpendicular plasma pressure of 20 nPa, that is, the peak of the pressure shifts 0.7 Re inward and its intensity increases simultaneously due to the enhanced convection. Moreover, both westward and eastward currents also enhance simultaneously. The peak of the eastward current is located at 4.5 Re and westward current at 7.0 Re. The spatial structure of the currents is classified as the 'partial ring current' in classical terms because the currents partially intense in the dusk region.

3. In the recovery phase at 0700 UT on April 11 (labeled as C), the previously enhanced plasma pressure and the current density decreases. The peak of the plasma pressure is still located at 5.3 Re, but the pressure decreases to 9 nPa. The spatial structure is classified as the 'symmetric ring current' in classical terms.

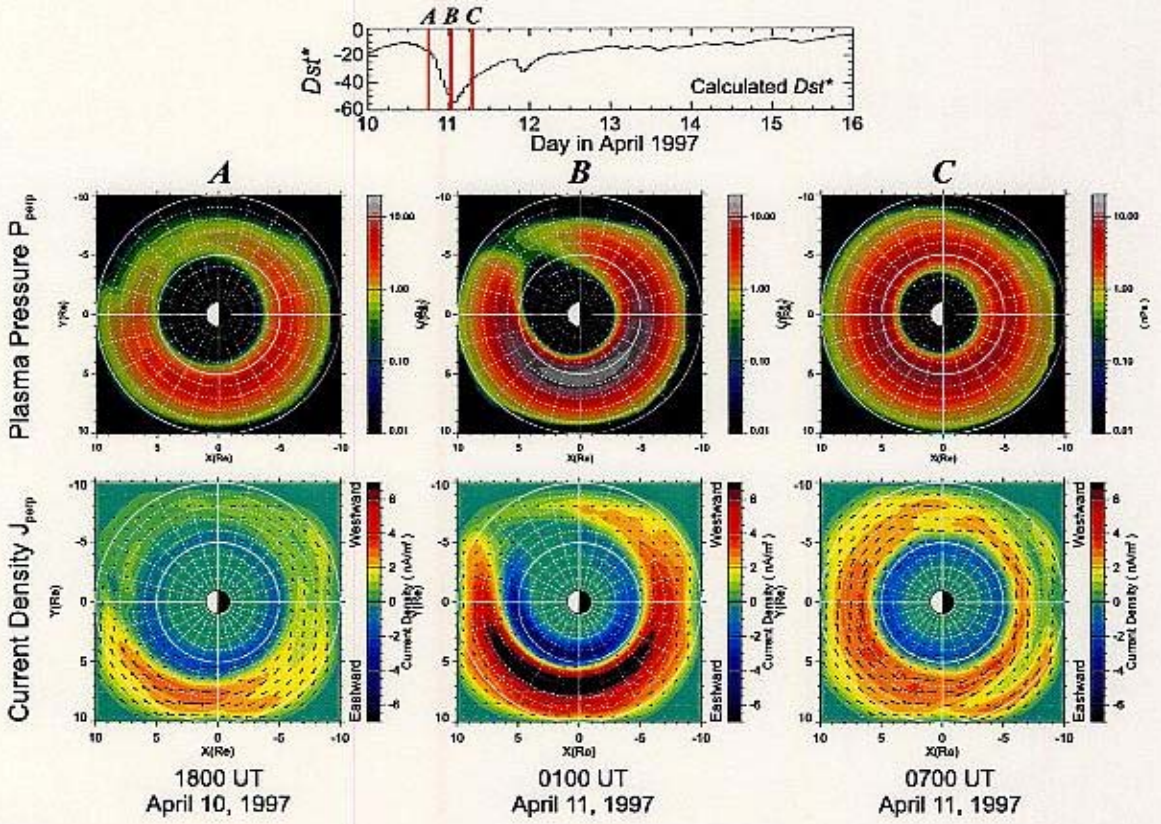

Figure 5.13. Temporal evolution of the equatorial pressure and current density in Storm I. Top panel shows calculated Dst*. Middle and bottom panels show the pressure perpendicular to the magnetic field and the current density perpendicular to the magnetic field in the equatorial plane, respectively, at 1800 UT on April 10, 1997 (left panels; denoted as A), 0100 UT on April 11, (middle panels; denoted as B) and 0700 UT on April 11, 1997 (right panels; denoted as C). In the bottom panels (current density), the pseudo-color code indicates the strength of the azimuthal component of the current density; red as westward and blue as eastward currents. Arrows indicate the direction of the current density.

To examine details, cross sections of the electric current and the plasma pressure in the equatorial plane at MLT of 18h are presented in **Figure 5.14**. Four curves in the top panel in **Figure 5.14** indicate the total azimuthal current J_ϕ, the magnetization current J_M, the curvature drift current J_R and the grad-B drift current J_B, respectively. The maxima of the magnetic drift currents (the curvature drift current J_R and the grad-B drift current J_B) are located at L of 6.0, which correspond to a maximum of the plasma pressure. Since the anisotropy of the plasma pressure, defined as $P_\parallel/P_\perp$, is approximately equal to 1.2, it is deduced that the total azimuthal current density J_ϕ is approximately produced by the ∇P term in Eq.(2.3) because the second term in the right hand side of Eq.(2.3) can be negligible.

Next, the contribution of eastward and westward currents to Dst* are examined. The total current J_ϕ has peaks of 8 nA/m^2 at L=5.3 for the eastward current and 10.8 nA/m^2 at L=6.9 for the westward current. Therefore the ratio of the current density between the peaks is approximately 1.4. Because the total amount of the volume where the westward current flows dominates the volume where the eastward current flows, the negative magnetic disturbance at the center of the earth dominates the positive magnetic disturbance. The dominance of the total volume where the westward current flows is clearly seen in **Figure 5.15** showing the cross section of the current density and the plasma pressure at MLT of 6 h and 18 h.

It is impossible for observed Dst* to be divided into two components; Dst* induced by the westward ring current and Dst* induced by the eastward ring current. Three lines in **Figure 5.16** indicate Dst* induced by the westward ring current, the eastward ring

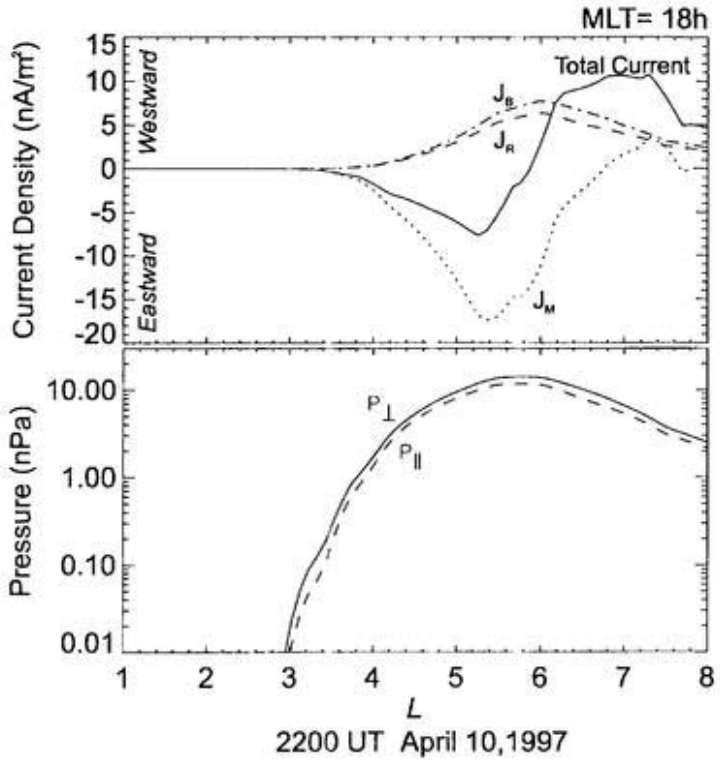

Figure 5.14. Cross sections of the equatorial current density (top panel) and plasma pressure (bottom panel) as a function of L in the meridian at MLT of 18h at 2200 UT on April 10, 1997. In the top panel, solid, dotted, dashed and dashed-dotted lines indicate the total azimuthal current J_ϕ, the magnetization current J_M, the curvature drift current J_R and the grad-B drift current J_B, respectively. The positive quantity denotes the westward current. In the bottom panel, a solid line indicates the perpendicular plasma pressure $P_\perp$ and a dashed line the parallel plasma pressure $P_\parallel$.

current and Dst* induced by both currents, respectively. It is found that Dst* induced by the westward current is approximately 3~4 times larger than Dst* induced by the eastward current.

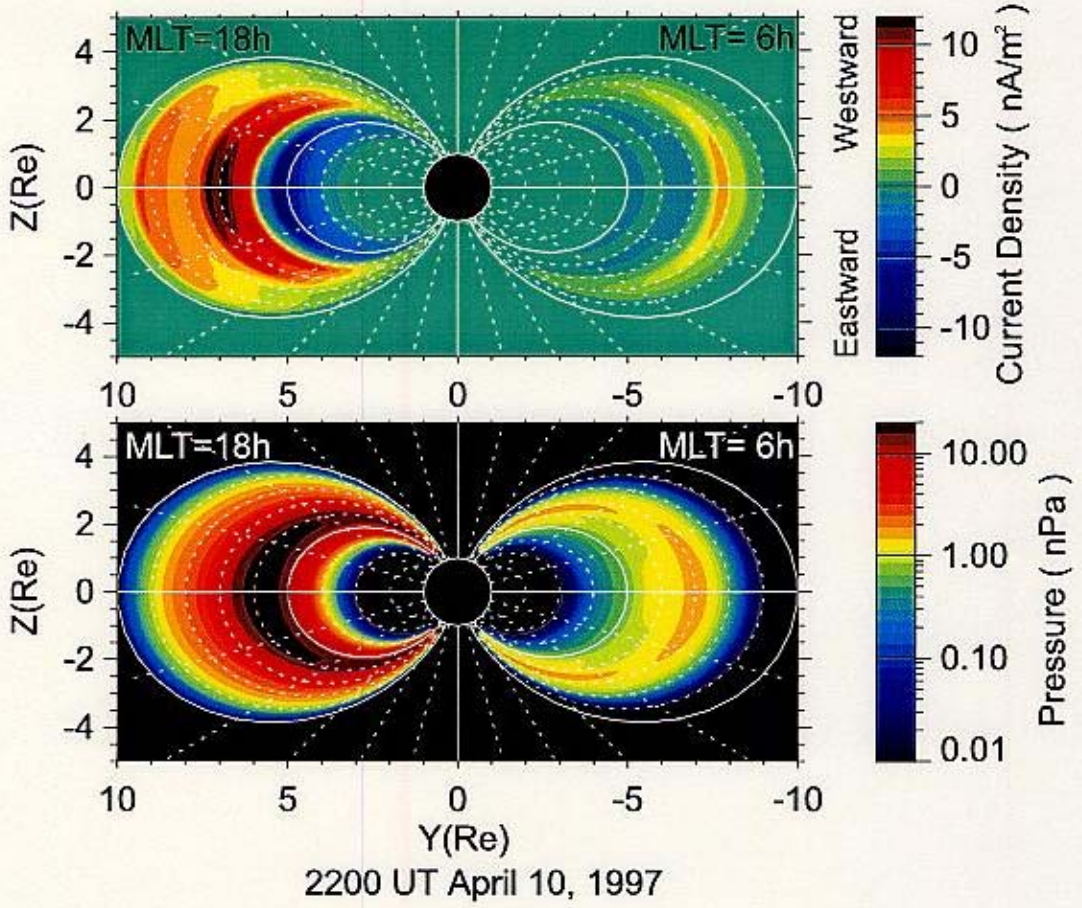

Figure 5.15. Top and bottom panels show the azimuthal current density J_ϕ and the perpendicular plasma pressure $P_\perp$, respectively, in the cross section of the dawn-dusk meridian at 2200 UT on April 10, 1997.

5.5.4 Effects of charge exchange loss

The loss effect of energetic ions on the ring current due to the charge exchange is examined here. The charge exchange loss effect on the Dst* during the storms is clearly shown in **Figure 5.17**. Two curves that indicate the observed Dst* (thin solid line) and calculated Dst* with the charge exchange loss (thick solid line) are corresponding to the bottom panel of **Figure 5.7**. A dotted line indicates calculated Dst* without the charge exchange loss;

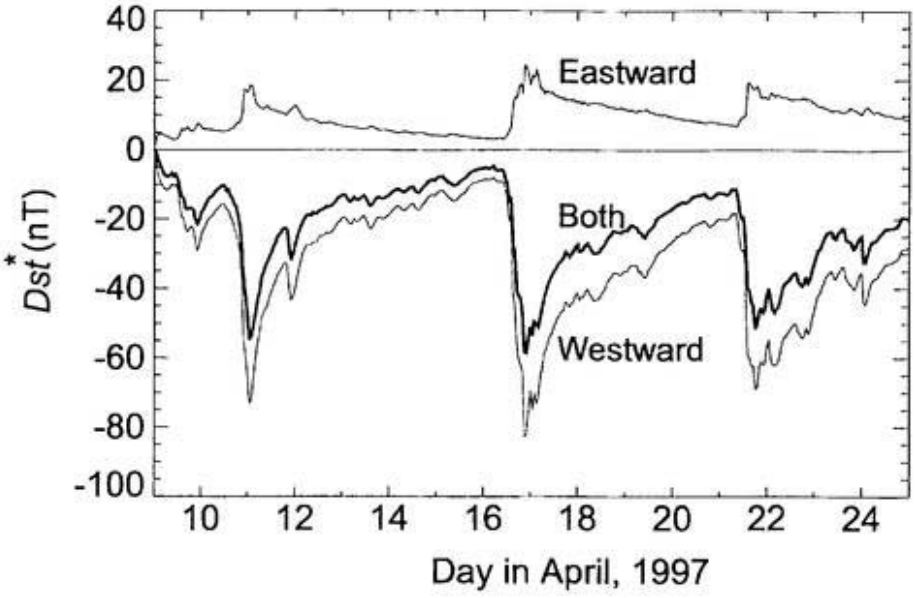

Figure 5.16. Calculated Dst* during the period of April 9-25, 1997 (thick line; denoted as 'both'). Thin lines indicate Dst* induced by the westward current (denoted as 'westward') and Dst* induced by the eastward current (denoted as 'eastward').

the convection outflow is the only loss process. It is noted that Dst* without the charge exchange loss begins to recover rapidly when recovery phases begin. This means that the initial rapid recovery in the early recovery phase is mainly due to convection outflow. After flowing out major energetic ions due to the convection, Dst* decays slowly due to the charge exchange in the late recovery phase. Dst* with the charge exchange loss recovers slowly within 4-5 days, being resemble to observed Dst*. On the other hand, Dst* without the charge exchange hardly recovers in the late recovery phases; the next storm occurs before the ring current decays sufficiently. Therefore the base value of Dst* decreases with time; this is unrealistic.

The plasma pressure as a function of L at 0000 UT on April 16, 1997, just before the beginning of Storm II, is shown in **Figure 5.18**. It is noted that the plasma pressure

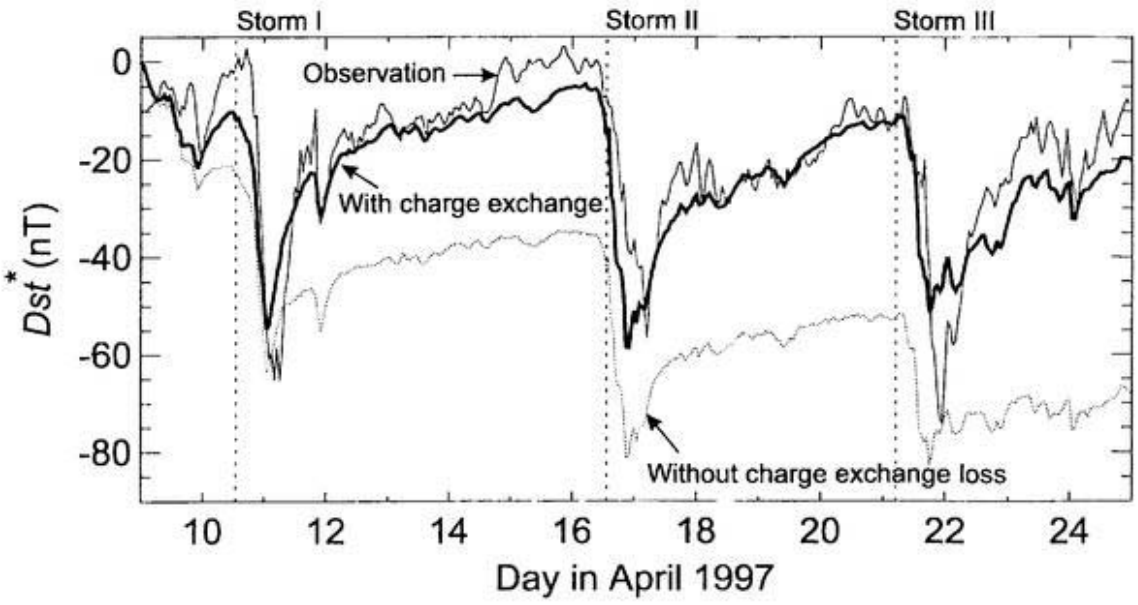

Figure 5.17. Decay of the perpendicular plasma pressure due to the charge exchange loss effects. Observed Dst* (thin line), calculated Dst* with charge exchange loss process (thick line) and calculated Dst* without charge exchange loss process (dotted line) are plotted for the period of April 9-25, 1997.

(equivalent to energy density) are strongly lost by the charge exchange; the perpendicular pressure decreases from 5.2 to 1.7 nPa (decrease to 32.7 %) at L=6, from 8.1 to 0.8 nPa (9.9 %) at L=5, from 6.2 to 0.2 nPa (3.2 %) at L=4.

The effect of the charge exchange on the pressure (energy density) is also clearly seen in **Figure 5.19**. Two panels of **Figure 5.19** show a time series of the perpendicular pressure as a function of time and L. A left panel shows the pressure in the case including the charge exchange loss and a right panel in the case excluding the loss. After beginning of recovery phases of the storms, the previously enhanced pressure begins to decrease drastically, decaying fast at low L because the charge exchange lifetime of an ion is short at low L. For example, the charge exchange lifetime for an ion with the energy of 10 keV

is roughly within a day in the region of $L \leq 5$ [**Figure 7** in *Ebihara et al.*, 1998b].

White lines in **Figure 5.19** indicate the peak L-value of the perpendicular pressure. The peaks of the pressure locate at L of 5-6 in the case including the charge exchange loss and at L of 4.5-5.5 in the case of excluding the loss.

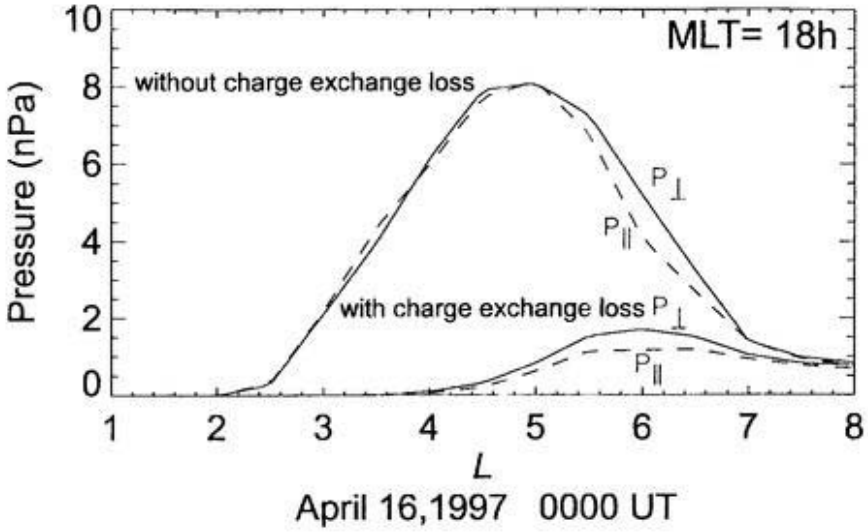

Figure 5.18. Cross section of the plasma pressure terms as a function of L at MLT of 18h at 0000 UT on April 16, 1997

5.5.5 Energy composition of the plasma pressure

The differential perpendicular pressure, which is defined as $dP_\perp/dE$ having a dimension of number density, is introduced here. **Figure 5.20** shows the calculated differential pressure at different L-value of 4, 5 and 6. White lines in **Figure 5.20** indicate the peak energy of the differential perpendicular pressure $dP_\perp/dE$, i.e., ions having the energies indicated by the white lines most contribute to the perpendicular pressure. It is noted that a major contributor to the perpendicular plasma pressure is the ions with an energy range of $\simeq$

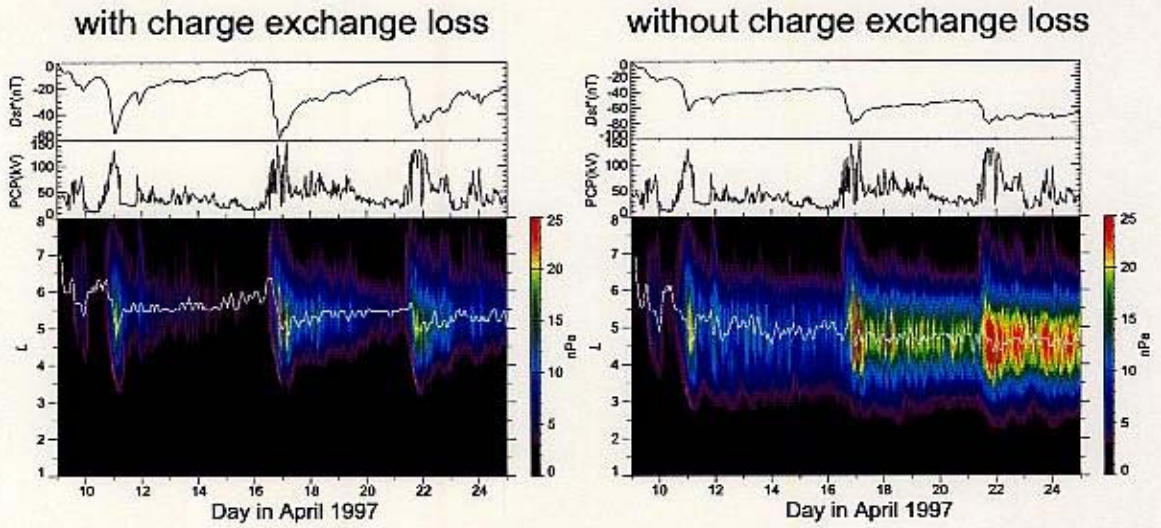

Figure 5.19. Perpendicular plasma pressure with the charge exchange loss (left) and without the loss (right) as a function of L and time. Top panels show calculated Dst* and middle panels show the polar cap potential (PCP) drop deduced from the solar wind and IMF. A white line in the bottom panel indicates the peak L-value of the pressure.

15-30 keV for $L = 4$, $\simeq$ 30-40 keV for $L = 5-6$ during a main phase and an early recovery phase, while the energy of a major contributor is $\simeq$ 15 keV in quiet periods. Compared with the panel (a) of **Figure 5.20** for the case of the steady convection, the rise of the most contribution energy to the perpendicular pressure is due to the enhancement of the convection field. For example, ions with a kinetic energy of 30 keV at L=4 only appear when the polar cap potential Φ_{PC} strongly enhances.

As the convection field enhances, an open-close boundary of drift trajectories of energetic ions shrinks [e.g., *Ejiri*, 1978], and then more energetic ions can penetrate into the inner magnetosphere. **Figure 5.21** indicates the equipotential lines which satisfy $q\Phi + \mu B = constant$, where μ is the magnetic moment of an ion. The equipotential lines are equivalent to drift trajectories for an ion with the magnetic moment of 61.94 keV/nT (corresponding

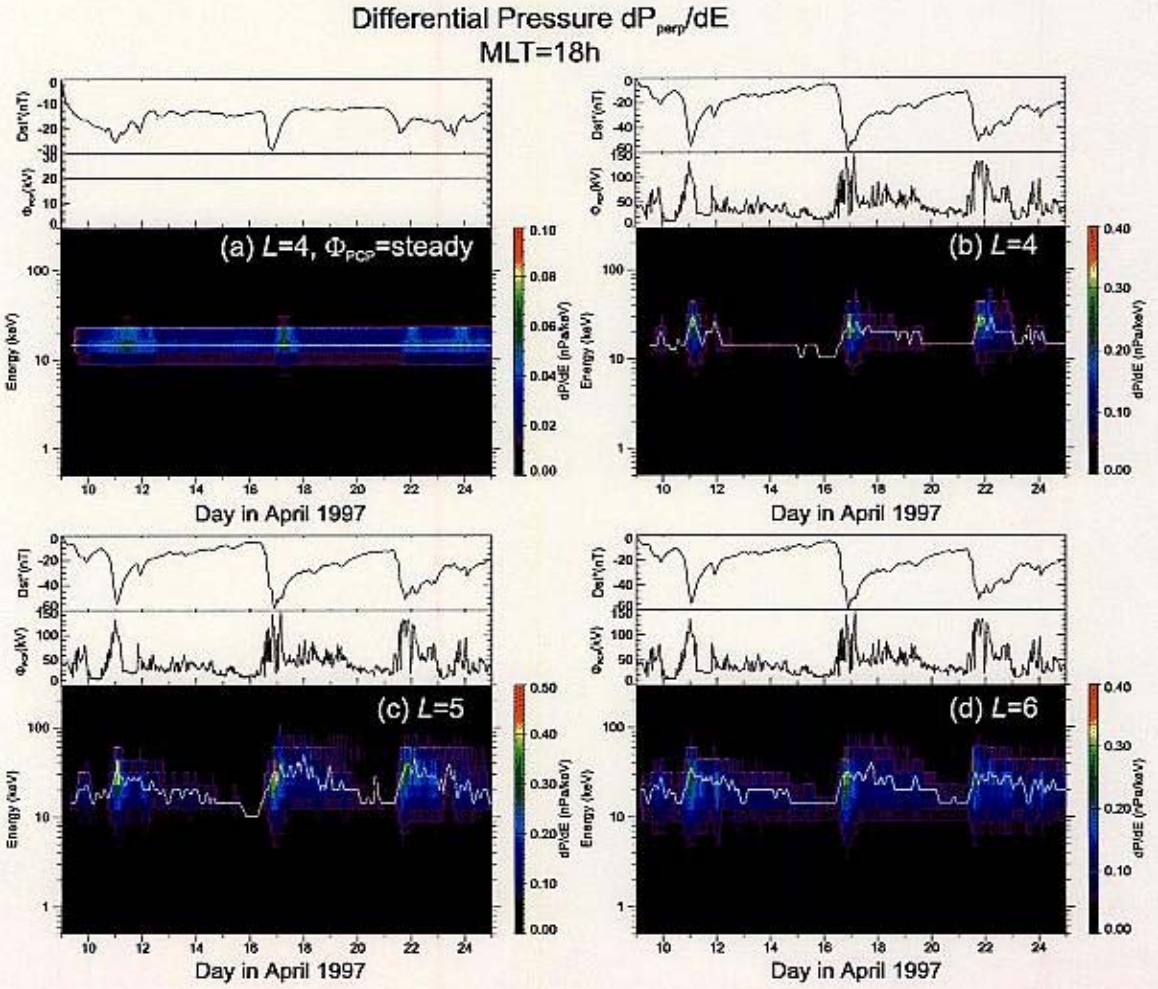

Figure 5.20. The differential pressure defined as $dP_{\perp}(\mathrm{nPa})/dE(\mathrm{keV})$ at (a) and (b) $L = 4$, (c) $L = 5$, (d) $L = 6$ in cross section at MLT of 18h at 0000 UT on April 16, 1997. White lines indicate a peak of the differential energy. Especially, Top left panel (a) is the case of the steady convection Φ_{PC} of 20 kV. Each panel shows calculated Dst* (top), the polar cap potential Φ_{PC} (middle) and a time series of the differential pressure (bottom).

to the kinetic energy of 30 keV at L=4) with an equatorial pitch angle of 90°. For the polar cap potential of 20.0 kV (left panel in **Figure 5.21**), the open-close boundary drawn by a closed thick line intersects the MLT of 18h at L=4.7, that is, the newly injected ions with kinetic energy of 30 keV cannot be found in the region of L <4.7 at MLT of 18h. On the other hand, under the enhanced convection field with the polar cap potential of 58.0 kV (right panel), the open-close boundary intersects MLT of 18h at L=4, that is, if the polar cap potential enhances above Φ_{PC} of 58.0 kV, the newly injected ions with the energy of 30 keV can be found at L=4 of MLT=18h.

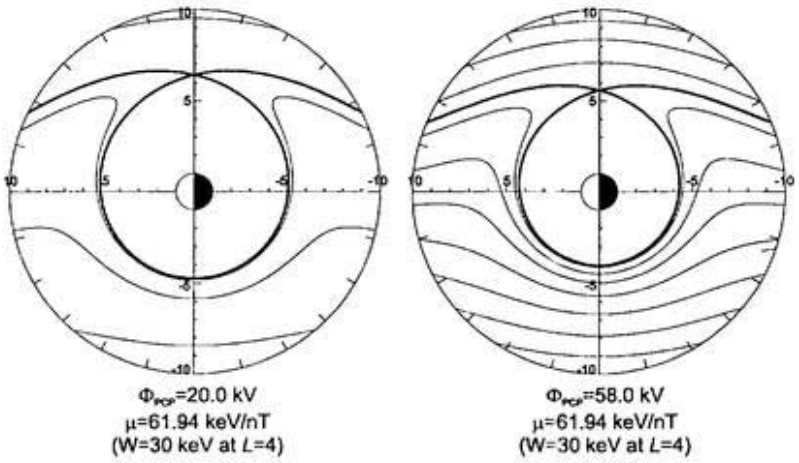

Figure 5.21. Equipotential lines satisfying $q\Phi + \mu B = constant$, where μ is the magnetic moment. The lines indicate the drift trajectories for an ion with an equatorial pitch angle of 90 ° with the magnetic moment of μ=61.94 keV/nT corresponding to the kinetic energy of 30 keV at L=4. Left and right panels show the case of the polar cap potential Φ_{PC} of 20.0 kV and 58.0 kV, respectively. A thick line represents a separatrix of the potential lines. Especially, a inner closed thick line is called an open-close boundary (or a last closed equipotential line).

From the numerical simulation, it is found that the ions with energies of around 15-40 keV at L=4-5 in the dusk region most contribute to the perpendicular pressure. Previous

satellite observations by the AMPTE/CCE satellite (Active Magnetospheric Particle Tracer Explorer/Charge Composition Explorer) [*Williams*, 1985] show that there is another peak around energies of 100 keV in the dusk region [*Gloeckler et al.*, 1985b]. AMPTE/CCE is the satellite placed into a nearly equatorial orbit with an apogee of 8.8 Re and an initial perigee altitude of 1108 km. **Figure 5.22** shows the differential number density observed by AMPTE/CCE in a main phase of a large storm on September 5, 1984 when AMPTE/CCE was between L=3.7-4.7 on the inbound pass, being reported by *Gloeckler et al.*[1985b]. The differential number density defined by *Gloeckler et al.*[1985b] corresponds to the differential pressure defined above. A curve of the differential number density versus the energy for H^+ions shown in **Figure 5.22** has prominent peaks around energies of 15-20 keV and 80-200 keV. The double peaks were also observed by the Explorer 45 satellite [*Smith and Hoffman*, 1973]. The first peak with energies of 15-20 keV observed by AMPTE/CCE is in agreement with the model calculation, that is, the first peak appears due to the convective transport from the near-earth plasma sheet. However, the second peak with energies of 80-200 keV observed by AMPTE/CCE is hardly explained by the convective transport; a strong enhanced convection field, the polar cap potential Φ_{PC} exceeding 563 kV, is necessary to push an ion with magnetic moment of 0.413 keV/nT with an equatorial pitch angle of 90° (corresponding to the kinetic energy of 200 keV at L=4) from L of 10 into L of 4. This highly enhanced polar cap potential may be unrealistic.

One possible reason for the appearance of the second peak is due to the radial diffusion caused by fluctuation of the magnetic field or the electric field. Under the simple estimation, *Lyons and Schulz* [1989] suggests that the radial diffusion due to fluctuation of the large-

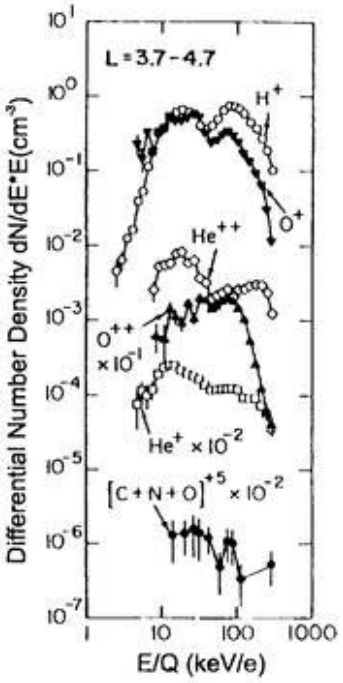

Figure 5.22. Differential number density versus energy/charge in the energy range of 1 - 300 keV/q observed by the AMPTE/CCE CHEM instrument for H^+, O^+, He^{++}, O^{++}, He^+, and $[C + N + O]^+5$ at L=3.7 to 4.7 in a main phase of the storm occurred on September 5, 1984. The local time of the satellite was in 1400 - 1800 LT. (After *Gloeckler et al.* [1985b].)

scale electric field associated with a substorm leads to move ions with energies above 40 keV at L=3 inward during a main phase of a storm. Moreover, *Chen et al.* [1994] investigated the radial diffusion effect by a guiding-center particle simulation with an impulsive enhanced convection whose cross-tail potential is 200 - 400 kV (corresponding to a large storm) with time scale of 20 minute. Then they concluded that the ions with these higher energies can be transported by the impulsive convection electric field during storms having long duration of main phases. Additionally, *Chen et al.*[1997] deduced that the effectiveness of the impulsive fluctuated convection limits to a particular main phase having a time scale

above 12 hours. The time scale of 12 hours of a main phase is relatively comparable to or longer than a characteristic time scale of a main phase of a moderate or an intense storm [e.g., *Yokoyama and Kamide*, 1997]. Therefore it is suggested that the diffusive transport due to the fluctuated convection field may be less effectiveness than the convective transport for the storm time development of the plasma pressure (or the ring current) for a moderate or an intense storm.

In the previous subsection, it was shown that the peak of the calculated pressure is located at L=5-5.5 in the dusk region during the storms (**Figure 5.19**). However, in general, most of observational results of the ring current have shown that the peak of the pressure is approximately located at L=3-3.5 during a magnetic storm [*Frank*, 1967; *Hoffman and Bracken*, 1965; *Hoffman and Cahill*, 1968; *Smith and Hoffman*, 1973; *Williams*, 1981; *Krimigis et al.*, 1985; *Lui et al.*, 1987; *Hamilton et al.*, 1988; *Roeder et al.*, 1996]. Besides, the peak of the pressure is also located at L=3-3.5 during magnetically quiet periods [e.g., *Williams*, 1981; *Lui and Hamilton*, 1992; *De Michelis et al.*, 1997]. If the actual pressure observed by satellites consists of ions transported by the convection only, an unusual strength of the convection field is necessary to push ions originated in the plasma sheet into the inner magnetosphere. Furthermore, the actual peak of the pressure should strongly depend on the strength of the convection if the ions are transported by the convection only. However, the peak of the pressure remains relatively steady at L=3-3.5 during quiet and active periods. Indeed, *Lui et al.* [1987] reported the time evolution of the pressure profile of ions with energies of 25 keV - 1 MeV during main and recovery phases during a storm on September 4-5, 1984, showing that there is no significant change in the

pressure profile around the peak during the phases of the storm. The fact can be explained by considering the pressure composed of two constituents; one is due to the convective transport (for lower energies) that is responsible to the convection field, and another is due to a diffusive transport (for higher energies) that can push high energy ions into the inner magnetosphere L ~3 - 3.5, not depending on magnetic activities [e.g., *Korth and Friedel*, 1996, Figure 4]. This idea is schematically drawn in **Figure 5.23**; this is consistent with the time evolution profile of the pressure that were directly observed by AMPTE/CCE with energy range of 25 keV - 1 MeV [*Lui et al.*, 1987].

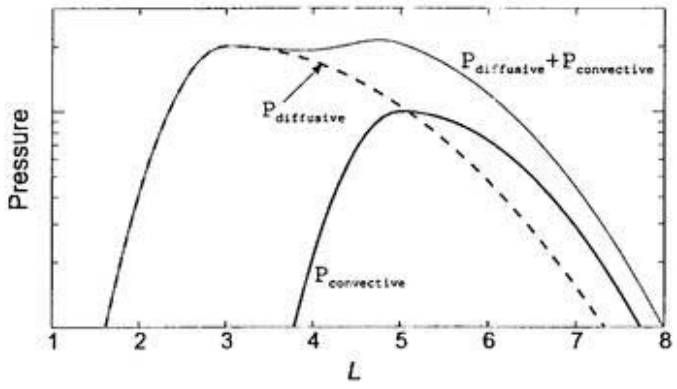

Figure 5.23. Schematic storm time pressure as a function of L for the MLT of 18h. A thick solid line indicates the pressure due to the convective transport $P_{convective}$, a thick dashed line the pressure due to the diffusive transport $P_{diffusive}$ and thin line the total pressure $(P_{convective} + P_{diffusive})$.

If the pressure can be separated into the two components, the current density perpendicular to the magnetic field $\boldsymbol{J}_\perp$ is also separated into two terms as

$$\begin{aligned} \boldsymbol{J}_\perp &= \frac{\boldsymbol{B}}{B^2} \times \left[\nabla P_\perp + (P_\parallel - P_\perp) \frac{(\boldsymbol{B} \cdot \nabla)\boldsymbol{B}}{B^2} \right] \\ &= \frac{\boldsymbol{B}}{B^2} \times \left[\nabla P_{\perp,convective} + (P_{\parallel,convective} - P_{\perp,convective}) \frac{(\boldsymbol{B} \cdot \nabla)\boldsymbol{B}}{B^2} \right] \end{aligned}$$

$$+\frac{\boldsymbol{B}}{B^2}\times\left[\nabla P_{\perp,diffusive}+(P_{\parallel,diffusive}-P_{\perp,diffusive})\frac{(\boldsymbol{B}\cdot\nabla)\boldsymbol{B}}{B^2}\right] \quad (5.18)$$

$$\equiv \boldsymbol{J}_{\perp,convective}+\boldsymbol{J}_{\perp,diffusive}, \quad (5.19)$$

where the subscripts *convective* and *diffusive* represent quantities due to the convective transport and the diffusive transport, respectively. Moreover, the magnetic disturbance $\Delta\boldsymbol{B}$ induced by the current density $\boldsymbol{J}_{\perp}$ also can be separated as

$$\Delta\boldsymbol{B}=\Delta\boldsymbol{B}_{convective}+\Delta\boldsymbol{B}_{diffusive}. \quad (5.20)$$

As shown in **Figure 5.7**, calculated Dst* deduced from $J_{\perp,convective}$ (not including $J_{\perp,diffusive}$) is in relatively good agreement with observed Dst*, except for the most disturbed periods; e.g., 0100-1200 UT on April 11, 1997 and 1200 UT on April 21-1200 UT on April 22. The diffusive transport during a storm may be one of candidates for the difference between calculated and observed Dst* around their minima. In future, the effect of the diffusive transport on temporal and spatial changes of the pressure, the current density and Dst* during a storm should be examined.

5.5.6 Response time of the plasma sheet density to the solar wind density

As mentioned above, it is assumed that the plasma sheet density responds to the solar wind density immediately in this simulation. However, *Terasawa et al.* [1997] statistically examined and found that the plasma sheet density responds to the solar wind density with

a characteristic time delay of $\sim$ 1 hour for northward IMF and $\sim$ 6 hours for southward IMF. Because the plasma sheet density is one of major sources of the ring current buildup as discussed in Section 5.5.1, the time delay of the response will be one of essential elements for the ring current buildup.

Figure 5.24 shows the effects of the time delay of the plasma sheet density responding to the solar wind density for the three storms. Curves for no delay time are indicated by open squares in each panel and they are corresponding to **Figure 5.8**, **Figure 5.9** and **Figure 5.10**. A curve indicated by filled squares shows calculated Dst* with a delay time of 3 hours, and a curve indicated by filled circles shows calculated Dst* with a delay time of 7 hours. It is clear that the calculated Dst* with the time delay of 7 hours is resemble the observed Dst*. The time delay affects Dst* drastically when the solar wind density changes noticeably in a main phase such as the Storm II and the Storm III. It seems reasonable to concluded that the time delay causes a significant change to Dst* during a main and an early recovery phases when the solar wind density changes noticeably.

5.5.7 Dst* and total kinetic energy of the ring current ions

The magnetic disturbance has been calculated by the Biot-Savart integral over the whole three-dimensional distribution of the calculated current density in this simulation. Although the Biot-Savart integral is a complete method to calculate Dst*, the method has hardly been used because the actual calculation of the integral spends a lot of time and many computer resources. Therefore the well-known Dessler-Parker-Sckopke (hereinafter referred to DPS) relation [*Dessler and Parker*, 1959; *Sckopke*, 1966] has been used. The

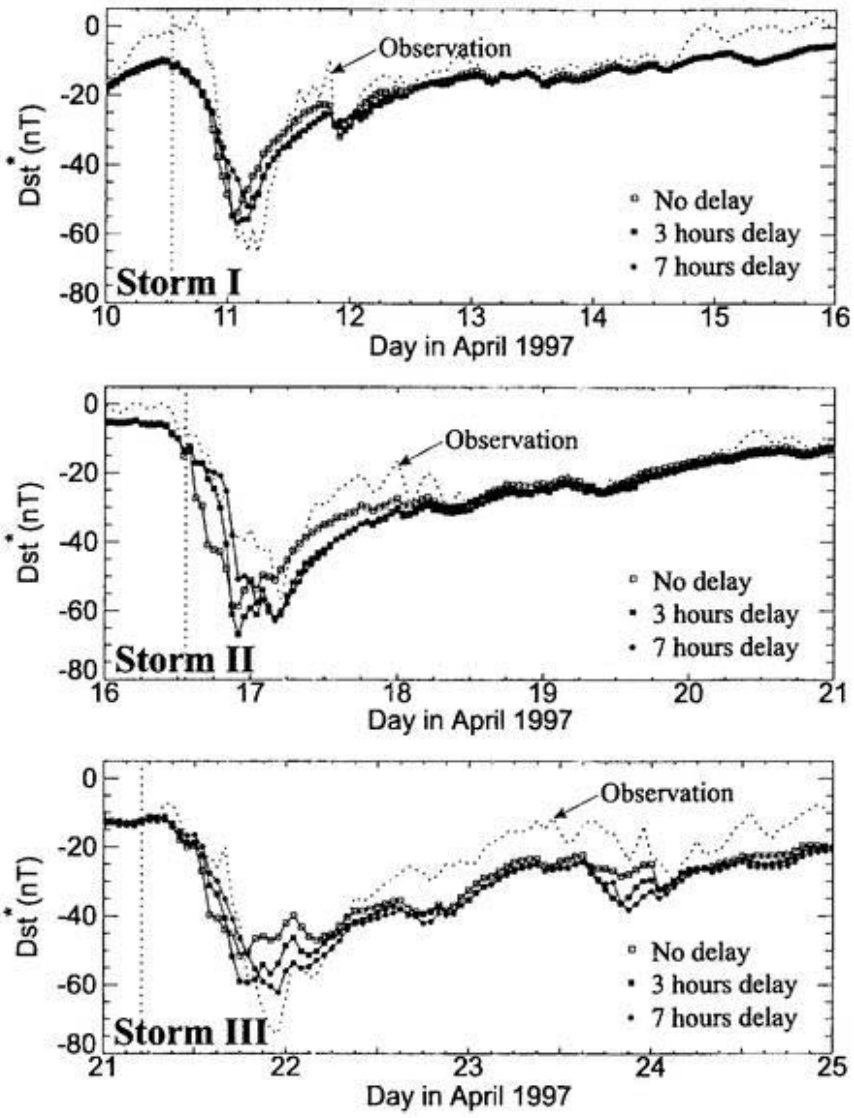

Figure 5.24. Effects of the time delay of the plasma sheet density responding to the solar wind density for the three storms; the top panel for Storm I, the middle panel for Storm II and the bottom panel for Storm III. Three solid lines in a panel indicate calculated Dst* with no time delay (open square), with 3 hours delay (filled square) and with 7 hours delay (filled circle), respectively. A dashed line indicates observed Dst*. A vertical line in a panel indicates the commencement time of a storm reported by NOAA.

DPS relation is the relation between the total kinetic energy of ring current protons and the magnetic disturbance at the center of the earth, and is expressed as

$$\Delta B(\mathrm{nT}) = 2.495 \times 10^{-14} W_{\perp}(\mathrm{Joule}), \tag{5.21}$$

where $W_{\perp}$ is the total kinetic energy of protons perpendicular to a magnetic field, i.e., the DPS relation indicates that the magnetic disturbance parallel to the earth's dipole at the center of the earth is proportional to the total kinetic energy of protons. The manner to derive the DPS relation is described in appendix A. **Figure 5.25** shows the relation between calculated Dst* and the total kinetic energy during the storms. The calculational result indicates that the magnetic disturbance obtained by the Biot-Savart integral is approximately proportional to the total kinetic energy of ring current ions; the ratio is approximately 0.5 to 1.0×10^{-14} nT/J. From comparing with the DPS relation expressed in Eq.(5.21), it is concluded that the magnetic disturbance obtained by the DPS relation is overestimated with an approximate factor of 2.5 to 5. The overestimation of the DPS relation may be arising from the unrealistic assumption of its derivation; the DPS relation is derived under the assumption that the magnetic disturbance is caused by grad-B drift current of protons with a pitch angle of 90° and the protons' dipole magnetic moment due to gyration. In fact, the grad-B drift current $\boldsymbol{J}_B$ is canceled by one of terms of the magnetization current $\boldsymbol{J}_M$. Moreover, an essential of the magnetization effect is not the dipole moment produced by gyrating protons, but the pressure gradient ∇P.

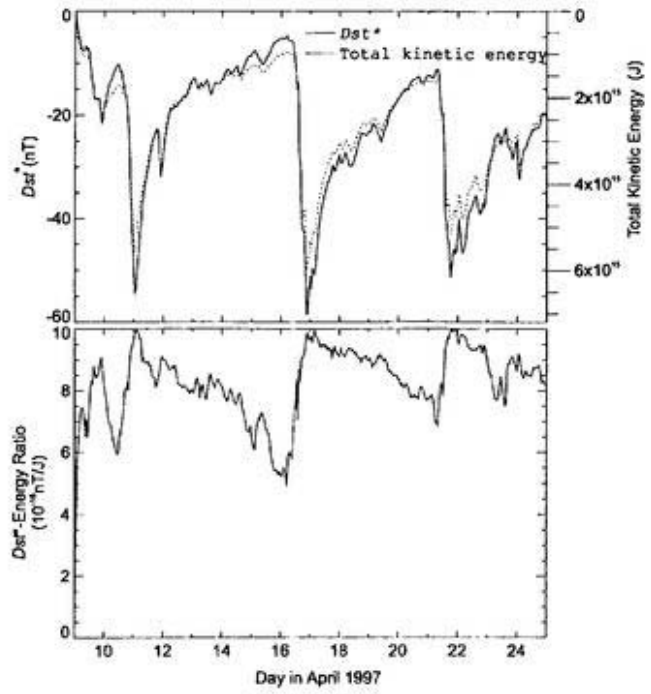

Figure 5.25. Top and bottom panels show Dst* (solid line) and total kinetic energy (dashed line), and the ratio of Dst* and total kinetic energy, respectively, during the period of the storms.

5.5.8 Diamagnetic effect

Previous works

Existence of the high plasma pressure causes distortion of local magnetic fields; this is called the diamagnetic effect. In fact, the distorted magnetic field due to the ring current has been observed by satellites; Explorer 6 [*Smith et al.*, 1960], Explorer 26 [*Cahill*, 1966; *Hoffman and Cahill*, 1968], Explorer 45 [e.g., *Cahill*, 1973] and AMPTE/CCE [e.g., *Potemra et al.*, 1985]. The characteristic feature of the observed distortion of the equatorial magnetic field has been explained by existence of the ring current. *Akasofu and Chapman* [1961] initially developed the symmetric ring current model using an ideal parti-

cle distribution, and they compared with the satellite observation by Explorer 6. *Hoffman and Bracken* [1967] calculated radial distribution of the distorted magnetic field including self-consistent effects. Recently, *Chen et al.* [1994, 1997] traced newly injected ions with a highly fluctuated convection field in order to consider the radial diffusive transport. After obtaining a radial profile of the pressure, they calculated the magnetic disturbance by assuming that the pressure distributes axially symmetric and that the currents flow in the equatorial plane. Therefore the local time dependence of the distorted magnetic field cannot be discussed by their model calculation. However, it is expected that the distorted magnetic field due to the ring current distributes asymmetrically because the storm time pressure develops partially. In this subsection, spatial distribution of the distorted magnetic field is examined.

Spatial distribution of equatorial distorted magnetic field

A time series of contour plots of the distorted equatorial magnetic field induced by the ring current during the main and the early recovery phases of the storm on April 10-11, 1997 is shown in **Figure 5.26**. The distorted field is derived from the Biot-Savart integral over the whole three-dimensional distribution of the calculated current density; this is the same manner as Dst* is calculated. Since this calculation includes no self-consistency, the current density is obtained under an assumption that the magnetic field is fixed to be dipolar.

If the magnetic field is purely dipolar, the contour lines become axially symmetric. However it is clear that the magnetic field is highly distorted by the ring current. There are

five characteristics to be noted:

1. At a commencement of the main phase (1300 UT, April 10, 1997; labeled as (a)), the magnetic field is slightly distorted by ions which are newly injected under the weak convection field and the lower plasma sheet density. In the cross section at MLT of 18h, the weak ring current decreases the the equatorial magnetic field ΔB of ~10-20 nT at the region of $L < 8$, while the equatorial magnetic field is increased at $L > 9$. A reversed 'S' structure in the contour appears in the dusk region at $L > 8$.

2. After 3 hours from the commencement (1600 UT, April 10; labeled as (b)), the contour becomes complicated; the reversed 'S' structure is expanding in the dusk to the noon region. As the main phase develops, the structure shifts slowly to the early local time.

3. A 'depression' of the equatorial magnetic field can be seen in the panel of (d) in the region of MLT=12-15 h and $L \sim 8$. The 'depression' is the region where each vector of ∇B points to inside.

4. A 'hill' of the equatorial magnetic field can be seen in the panel of (e) in the dusk side. The 'hill' is the region where each vector of ∇B. points to inside.

5. In generally, the distortion is prominent in the dusk region rather than the dawn region because the ring current develops partially in the dusk region as shown in **Figure 5.13**.

The contour is a line equivalent to the drift trajectory due to ∇B. A particle having a sufficiently high kinetic energy (greater than a few hundreds keV) with a pitch angle of

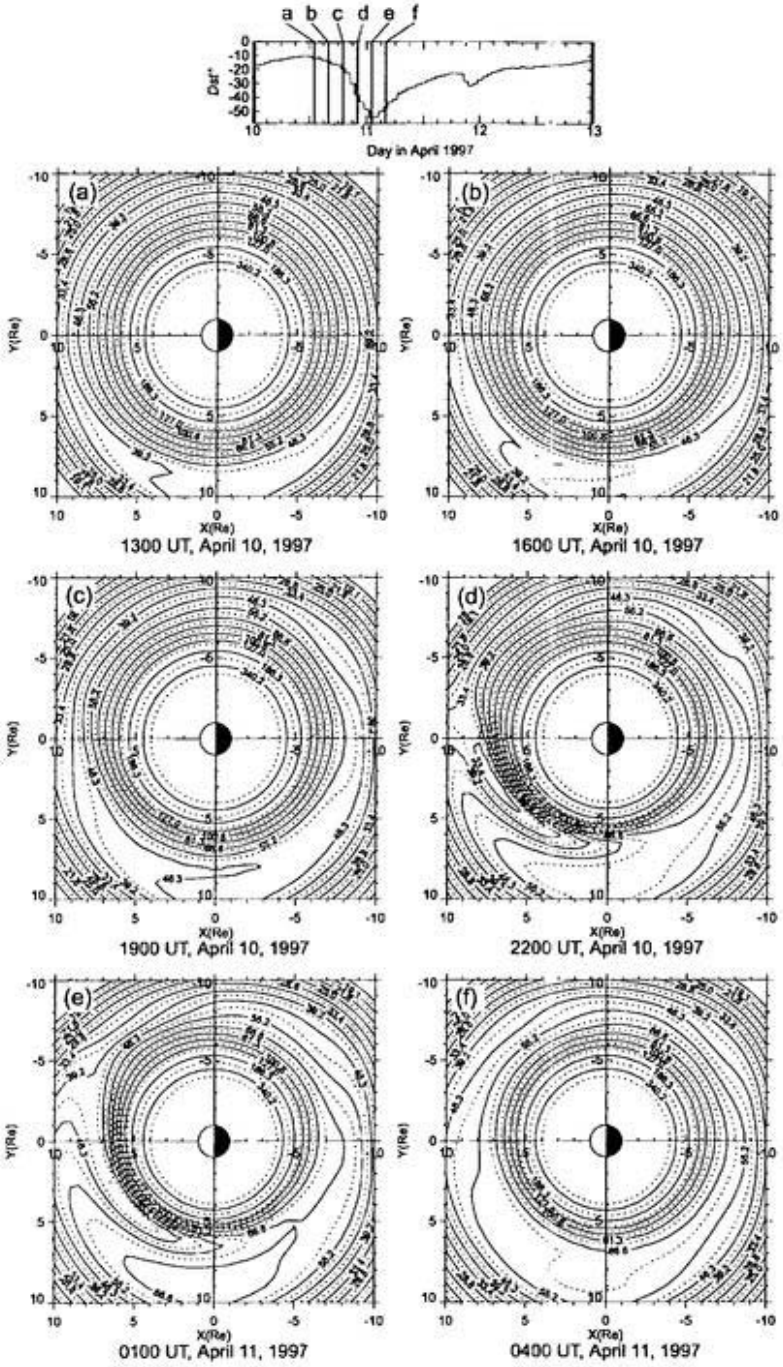

Figure 5.26. Distorted equatorial magnetic field due to the ring current. Top panel indicates calculated Dst*. Each panel labeled as (a)-(f) shows a contour map of constant equatorial magnetic fields during the main and the early recovery phases of the storm on April 10-11, 1997 at (a) 1300 UT, April 10, 1997 (b) 1600 UT, (c) 1900 UT, (d) 2200 UT, (e) 0100 UT, April 11 and (f) 0400 UT, April 11. Quantities written in the contour are the intensity of the magnetic field in nanotesla.

90° drifts along the contour line because the drift motion of such a high energy particle is dominated by the ∇B drift; the $E \times B$ drift can be ignored under the ordinary convection (except for a sudden compressive shock such as a SC). Although the drift trajectory of ∇B is axially symmetric in a dipole magnetic field, the drift trajectory is drastically changed due to the distorted magnetic field. For example, considering ions whose equatorial pitch angle is 90°, the ∇B drift trajectories can classify into four categories;

1. an ion drifting around the earth westward (Type 1),
2. an ion drifting around the earth westward but partly drifting eastward in the reversed 'S' shape structure (Type 2),
3. an ion locally drifting around the 'depression' anticlockwise (Type 3),
4. an ion locally drifting around the 'hill' clockwise (Type 4).

The trajectories for electrons are opposite to the case of ions. Type 2 is the trajectory that a particle can radially drift in the reversed 'S' shape structure (more than 2 Re). Type 3 and Type 4 are the trajectories that a particle is locally trapped, never drifting around the earth. These categorized trajectories are schematically shown in **Figure 5.27**.

It seems that the distorted magnetic field due to the ring current affects drift motion of the radiation belt particles. *Williams et al.* [1968] reported that counts of the relativistic electrons suddenly decreased in the outer radiation belt during a main phase of a storm, and began to increase when a recovery phase commenced. After then, many authors have been studied the negative excursion of the relativistic electrons' flux during a main phase of a magnetic storm [e.g., *Korth and Friedel*, 1997; *Li et al.*, 1997; *Obara et al.*, 1998]. Most

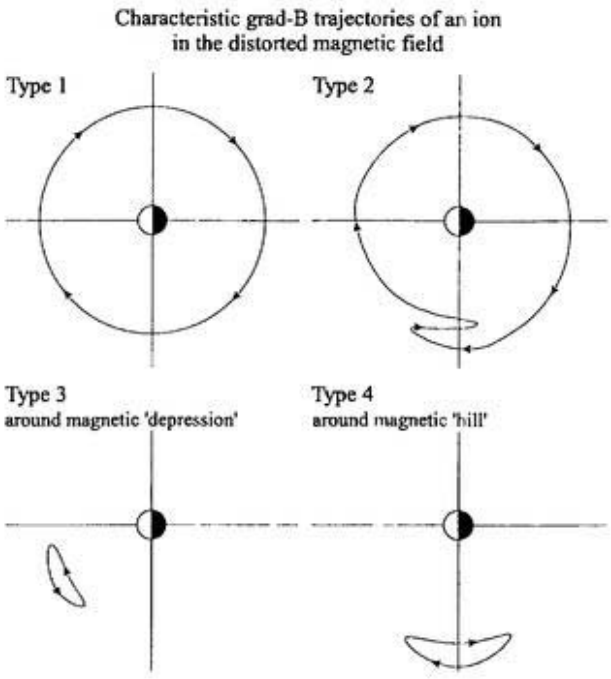

Figure 5.27. Schematic ∇B drift trajectories of an ion. The trajectories are categorized into 4 characteristics.

of the authors have speculated that the storm time decrease of the relativistic electrons' flux is caused by the adiabatic cooling of the electrons due to the depletion of the equatorial magnetic field. However, a whole mechanism which leads the drastic change of relativistic electrons' flux in the outer radiation belt during a storm has never yet been understood. From the calculational results, it is expected that not only the adiabatic effect due to the depletion of the magnetic field but also the drastic change of the drift trajectories of the relativistic electrons due to the distorted magnetic field affect the storm time change of the electrons' flux in the outer radiation belt. In future, the dynamics of relativistic electrons should be studied by using a realistic ring current model.

It is also expected that the distorted magnetic field may change the drift motion of ions

that contribute to the ring current. If the drift motion changed by the ring current affects the ring current itself, the effect is considered to be non-linear. The non-linear effect on the ring current ions also should be studied in future.

Cross section of the distorted magnetic field

A cross section of the equatorial distorted magnetic field at 0100 UT on April 11, 1997 as a function of L is shown in **Figure 5.28**. A left panel of **Figure 5.28** represents the distortion of the equatorial magnetic field parallel to the earth's dipole ΔBz due to the ring current at different MLT of 0h, 6h, 12h and 18h; it is clear that the distortion has strong local time dependence. In the dusk region (MLT of 18h), the distortion ΔBz reaches minimum of -110 nT. On the other hand, in the dawn region(MLT of 6h), the magnetic field slightly decreases. In fact, the strong local dependence of the distortion was observed by AMPTE/CCE [*Potemra et al.*, 1985] in a main phase of a large storm at 0330-0450 UT on September 5, 1985; the magnetic distortion reached its minimum ΔB of -130 nT in the dusk side, while the magnetic field slightly distorted in the dawn side.

A right panel of **Figure 5.28** shows the intensity of the magnetic field Bz as a function of L at MLT of 18h. A peak of the distorted magnetic field is located at L=6.6, and the field exceeds the intensity of a dipole field indicated by a dotted line in the region of L >7.8. The feature is similar to previous satellite observations.

It is remarkable that the calculated distortion is deduced from the current density constituted by the ions that are transported by the convection. The contribution of the ions transported by the diffusion is not included in **Figure 5.28**. Therefore, as discussed in the

Section 5.5.5, the actual peak of the distorted magnetic field may be located at L of 3-3.5 due to the pre-existing or relatively steady ring current.

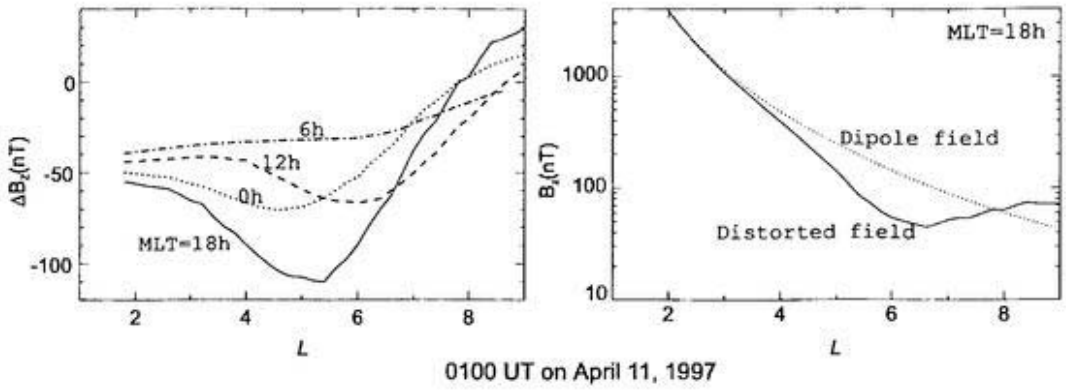

Figure 5.28. Distorted equatorial magnetic field parallel to the earth's dipole Bz as a function of L due to the ring current. Left panel shows the MLT dependence of the distortion. Right panel represents the magnetic field at MLT of 18h; a dashed line indicates the dipole field and a solid line the distorted field.

5.6 Conclusion

In this chapter, the ring current buildup depending on the solar wind and IMF, and its spatiotemporal structure have been examined. The plasma sheet density as a boundary condition located at L=10 is given by the statistical analysis using two satellites, GEOTAIL for the plasma sheet density at L=9-11 and WIND for the solar wind density. The result of the statistical analysis shows that the plasma sheet density at L=9-11 is well correlated with the solar wind density; this is consistent with the previous studies. After tracing newly injected ions having various pitch angles and energies under a dipole magnetic field and the Volland-Stern type convection field depending on the solar wind and IMF, the

three-dimensional distribution of a directional differential flux, plasma pressure and current density are calculated. All ions pass through an 'injection boundary' azimuthally located at L of 10 with MLT of 21-3h. A distribution function of the ions at the 'injection boundary' independing of MLT is assumed to be isotropic Maxwellian with the temperature of 5 keV and the number density depending on the solar wind density. The ions are lost by two processes; the charge exchange and convection outflow. The magnetic disturbance induced by the ring current can be directly obtained by the Biot-Savart integral over the whole three-dimensional distribution of the calculated current density.

As an example, three successive storms in April, 1997 are studied. The calculated magnetic disturbance at the center of the earth is compared with observed corrected Dst(Dst*), and it is found that calculated Dst* is in fairly good agreement with observed Dst*. There are five noticeable characteristics:

1. The major variation of Dst* is mainly due to the convection electric field and the plasma sheet density deduced from the solar wind density as well. This result can be explained by an analytical expression; the energy injection rate into the ring current is given by 0.286 $N_{ps}(\mathrm{cm}^{-3})$ $\Phi_{PC}(\mathrm{kV})$ $E_0(\mathrm{keV})$ in gigawatt, where N_{ps}, Φ_{PC} and E_0 are the plasma sheet density, the polar cap potential and the plasma sheet temperature, respectively. However, the plasma sheet temperature E_0 is insensitive to the ring current buildup for the temperature above 3 keV.

2. Dst* induced by the westward current is approximately 3~4 times larger than Dst* induced by the eastward current.

3. The ions with energies of around ~15-30 keV at L =4, and around ~30-40 keV at L=5-6 in the dusk region most contribute to the perpendicular pressure. The most contribution energy rises due to an enhancement of the convection field during a main phase of a storm.

4. Previous satellite observations by AMPTE/CCE show that there is another peak, the energy of around 100 keV in the dusk region. Because an unusual convection stronger than Φ of 563 kV is necessary to push an ion with kinetic energy of 200 keV at L=4 convected from L=10, the second peak observed by the satellite is considered to be transported by the radial diffusion.

5. Therefore, the pressure and the current density can be separated into two terms; one is due to the convectional transport and another due to the diffusive transport. Since the convectional transport well explains the time scale of the decrease of Dst* during a main phase, the ring current buildup as indicated by Dst* is mainly due to the convectional transport for these particular storms.

6. From comparing with Dst* derived from the well-known Dessler-Parker-Sckopke (DPS) relation, it is deduced that Dst* given by the DPS relation is overestimated with an approximate factor of 2.5 to 5. The overestimation of the DPS relation may be arising from the unrealistic assumption of its derivation.

7. The equatorial distorted magnetic field due to the ring current is calculated. The distortion is prominent in the equatorial dusk region. The contour showing the equatorial distorted magnetic field is equivalent to the drift trajectory due to ∇B, that

is, a high energy particle (greater than a few hundreds keV) with a pitch angle of 90° drifts along with a contour line. The drift trajectory of such a particle is drastically changed due to the distortion. Considering ions with a pitch angle of 90°, the drift trajectories can classify into four categories; (1) an ion drifting westward around the earth (Type 1), (2) an ion drifting eastward around the earth but partly drifting eastward in the reversed 'S' structure (Type 2), (3) an ion locally drifting anticlockwise around the magnetic 'depression' (Type 3) and (4) an ion locally drifting clockwise around the magnetic 'hill' (Type 4). The trajectories for electrons with a pitch angle of 90° are opposite to the case of ions. Therefore trajectories of the high energy particles with a pitch angle of 90° are complicated during a main phase of a storm. This is considered to be one of reasons for the cause for the storm time flux decrease of relativistic electrons.

There are differences between observed and calculated Dst*; calculated minimum Dst* is lacking by 3 % - 32 % of observed Dst* and the peaks of calculated minimum Dst* are earlier than the observed peak by about 5 - 7 hours. These differences arise from some possible reasons:

1. It is assumed that the plasma sheet density responds to the solar wind density immediately in this calculation. It has been reported that there is a characteristic time delay between them, i.e., about 1-6 hours. A delay of 7 hours from the solar wind density to the plasma sheet density well explains the time lag between the peak times.

2. The ions that are radially transported by the diffusion are not included. The ions having relatively higher energies transported by the diffusion also contribute to the

ring current. Although the characteristic time scale of the diffusive transport the ions is still unknown, the contribution of the diffusive transported ions may be negligible because the ions transported by the convection well explains the ring current buildup both in the time scale and in strength.

3. The other ion species, especially O^+, may be contribute to the ring current buildup. In the solar minimum, it is speculated from the previous direct observation that 30 % of O^+ ions contribute to the ring current.

4. An induction electric field due to dipolarization during an expansion phase of a substorm may also contribute to the ring current. However, the estimation of the substorm effect is difficult.

In future, the followings should be examined for understanding the physics of a magnetic storm;

1. contribution of ions transported by the radial diffusion to the ring current,

2. contributions of O^+ ions and electrons to the ring current,

3. characteristic delay time of ion transport from the solar wind to the near-earth plasma sheet,

4. non-linear effects of the ring current itself due to the diamagnetic effect,

5. dynamics of relativistic particles during a main phase of a magnetic storm.

Concluding remarks

In this dissertation, the dynamic behavior concerned with the development and decay of the ring current has been studied by using newly developed particle simulation scheme.

The general introduction toward the objects of this dissertation is described in Chapter 1.

The historical survey of the dynamics of the ring current and related phenomena associated with a magnetic storm is made in Chapter 2. Particles' motion in the dipolar magnetic field and the concept of the differential flux are also mentioned.

In Chapter 3, after constructing time-dependent three-dimensional plasmaspheric model, the Coulomb collision loss of ions in the magnetosphere is evaluated. This plasmaspheric model is derived from the total flux tube content model with the assumptions; (1) the primary cold ion species is H^+, (2) cold ions distribute in hydrostatic equilibrium align a field line and (3) bulk motion of cold ions are governed by the Kp dependent Volland-Stern type convection field and the corotation field. The accuracy of this model is examined by comparing with the EXOS-B satellite observations during a weak magnetic storm; the calculated radial profiles of the thermal plasma are in good agreement with the EXOS-B observation with respect to the absolute density, relative displacements of the plasmapause.

Using this plasmaspheric model, the spatial variation of the Coulomb collision lifetimes of the energetic ions is evaluated; the Coulomb collision loss is comparable to the charge exchange loss for all major species (H^+, He^+ and O^+) with energies below a few tens of keV in the plasmasphere. However, the Coulomb collision loss for energetic ions is almost restricted within the core plasmasphere. Therefore, during a magnetic storm, the Coulomb collision loss hardly affects the ions that contribute to the ring current because the plasmasphere shrinks due to an enhanced convection field.

In Chapter 4, an enhancement of the differential flux accompanied with a 'nose' energy dispersion structure has been examined by using particle tracing simulation. Results of the calculation well explain the sudden enhancement of the ion differential flux observed by Explorer 45 in the dusk region on February 13, 1972 associated with an isolate substorm. An additional temporal electric field having its maximum intensity of 6 mV/m and a time scale of 10 minutes is introduced to push ions suddenly from the near-earth plasma sheet into the inner magnetosphere where Explorer 45 observed the dispersion. Using this additional electric field, the calculated differential flux fairly agrees with that observed. The additional electric field is considered as a substorm-associated induction field. The magnetic disturbance at the center of the earth (Dst* field) due to the particle injection by this substorm-associated induction field is examined. The result shows that the isolate substorm injection hardly affects the magnetic disturbance with its minimum intensity of $\sim$2 nT. Next, following the concept that a storm is composed of substorms, the ring current buildup is examined by superposing many substorm injections. There were 13 substorms during the storm of February 13, 1972; the result suggests that the accumulation of the

substorm injections hardly explains the actual magnetic disturbance as compared with the observed Dst* index. This means that other mechanisms may play an important role for the storm time ring current buildup.

In Chapter 5, a model that deals with the ring current buildup and its decay depending on the solar wind density and the interplanetary magnetic field (IMF) is developed. First, the plasma sheet density as a boundary condition located at L=10 is given by the statistical analysis using two satellites, GEOTAIL for the plasma sheet density and WIND for the solar wind density. The results indicates that the plasma sheet density is well correlated with the solar wind density; this is consistent with the previous studies. After tracing newly injected ions having various pitch angles and energies under a dipole magnetic field and the Volland-Stern type convection field depending on the solar wind and IMF, the three-dimensional distribution of a directional differential flux, the plasma pressure and the current density are calculated. A distribution function of the ions at the 'injection boundary' independing of MLT is assumed to be isotropic Maxwellian with the temperature of 5 keV and the number density depending on the solar wind. The ions are lost by two processes; the charge exchange and convection outflow. The Coulomb collision loss is ignored because the plasmasphere during storms drastically shrinks so that the Coulomb collision with the plasmaspheric thermal plasma can be ignored for the ring current ions as compared with the charge exchange loss. The magnetic disturbance induced by the ring current can be directly obtained by the Biot-Savart integral over the whole three-dimensional distribution of the calculated current density. This is a new attempt; previous models calculate the magnetic disturbance at the center of the earth (Dst*) by the well-known Dessler-Parker-Sckopke

relation.

Three successive storms in April 1997 are studied for instance. The calculated magnetic disturbance at the center of the earth (Dst*) is compared with observed one, and it is found that calculated Dst* is in fairly good agreement with observed Dst*. There are five noticeable characteristics:

1. The major variation of Dst* is mainly due to the convection electric field and the plasma sheet density deduced from the solar wind density as well. This result can be explained by an analytical expression as the energy injection rate into the ring current being 0.286 $N_{ps}(\mathrm{cm}^{-3})\Phi_{PC}(\mathrm{KV})E_0(\mathrm{keV})$ in gigawatt, where N_{ps}, Φ_{PC} and E_0 are the plasma sheet density, the polar cap potential and the plasma sheet temperature, respectively. The plasma sheet temperature E_0 is insensitive to the ring current buildup for the temperature above 3 keV.

2. Dst* induced by the westward current is approximately 3~4 times larger than Dst*.

3. The ions with energies of around ~15-30 keV at L =4, and around ~30-40 keV at L=5-6 in the dusk region most contribute to the perpendicular pressure. The most contribution energy rises due to an enhancement of the convection field during a main phase of a storm.

4. Previous satellite observations by AMPTE/CCE show that there is another peak, the energy of around 100 keV in the dusk region. Because an unusual convection stronger than Φ of 563 kV is necessary to push an ion with kinetic energy of 200 keV at L=4 convected from L=10, the second peak observed by the satellite is considered

to be transported by the radial diffusion.

5. Therefore, the pressure and the current density can be separated into two terms; one is due to the convectional transport and another due to the diffusive transport. Since the convectional transport well explains the time scale of the decrease of Dst* during a main phase, the ring current buildup as indicated by Dst* is mainly due to the convectional transport for these particular storms.

6. From comparing with Dst* derived from the well-known Dessler-Parker-Sckopke (DPS) relation, it is deduced that Dst* given by the DPS relation is overestimated with an approximate factor of 2.5 to 5. The overestimation of the DPS relation may be arising from the unrealistic assumption of its derivation.

7. The equatorial distorted magnetic field due to the ring current is calculated. The distortion is prominent in the equatorial dusk region. The contour showing the equatorial distorted magnetic field is equivalent to the drift trajectory due to ∇B, that is, a high energy particle (greater than a few hundreds keV) with a pitch angle of 90° drifts along with a contour line. The drift trajectory of such a particle is drastically changed due to the distortion. Considering ions with a pitch angle of 90°, the drift trajectories can classify into four categories; (1) an ion drifting westward around the earth (Type 1), (2) an ion drifting eastward around the earth but partly drifting eastward in the reversed 'S' structure (Type 2), (3) an ion locally drifting anticlockwise around the magnetic 'depression' (Type 3) and (4) an ion locally drifting clockwise around the magnetic 'hill' (Type 4). The trajectories for electrons with a pitch angle

of 90° are opposite to the case of ions. Therefore trajectories of the high energy particles with a pitch angle of 90° are complicated during a main phase of a storm. This is considered to be one of reasons for the cause for the storm time flux decrease of relativistic electrons.

Appendix A

Dessler-Parker-Scopke relation

For an equatorial ring current of strength of I flowing the radius of r, the magnetic disturbance at the center of the earth is given by

$$\delta B_r = \frac{\mu_0 I}{2\pi r}, \tag{A.1}$$

where μ_0 is the permeability in vacuum. For a single particle drifting in the equatorial plane, the current produced by drift is

$$I = \frac{q v_d}{2\pi r}, \tag{A.2}$$

where v_d is the drift velocity and q the charge. In a dipolar field, the equatorial drift velocity v_d is given by

$$v_d = -\frac{3 E_\perp r^2}{q a^3 B_0}, \tag{A.3}$$

where a is earth's radius, $E_\perp$ the particle's kinetic energy perpendicular to the local magnetic field, and B_0 the magnetic strength at L=1. Combing these relations, the magnetic disturbance due to the particle's drift is

$$\delta B_1 = -\frac{3\mu_0 E_\perp}{4\pi a^3 B_0}. \tag{A.4}$$

The effect of gyration as well as drift is also included. A single gyration particle creates dipole due to a current loop with its moment antiparallel to the earth's field. This dipole creates a positive axial field at the center of the earth as

$$\delta B_2 = \frac{\mu_0 \mu}{4\pi r^3}, \tag{A.5}$$

where μ is the dipole moment. The dipole moment of a gyration particle is

$$\begin{aligned} \mu &= \frac{E_\perp}{B} \\ &= \frac{r^3 E_\perp}{B_0 a^3}. \end{aligned} \tag{A.6}$$

Thus the magnetic disturbance due to the drift is given by

$$\delta B_2 = \frac{\mu_0 E_\perp}{4\pi B_0 a^3}. \tag{A.7}$$

Summing the two contributions, the magnetic disturbance can be written as

$$\delta B = \delta B_1 + \delta B_2$$

$$= -\frac{\mu_0 E_\perp}{2\pi B_0 a^3}. \tag{A.8}$$

The total magnetic energy outside the earth's surface U_M is generally given by

$$U_M = \frac{1}{2\mu_0}\int B^2 dV, \tag{A.9}$$

where V is volume and B the magnetic strength. In the dipolar field, the total magnetic field U_M is

$$\begin{aligned} U_M &= \frac{1}{2\mu_0}\int_r\int_\theta 2\pi r^2 \sin\theta B^2 d\theta dr \\ &= \frac{\pi a^6 B_0^2}{\mu_0}\int_r\int_\theta \frac{\sin\theta\,(1+3\cos^2\theta)}{r^2} d\theta dr \\ &= \frac{4\pi a^3 B_0^2}{3\mu_0}. \end{aligned} \tag{A.10}$$

Combing the relations, the magnetic disturbance as a function of the total particle's energy is finally written as

$$\frac{\delta B}{B_0} = -\frac{2}{3}\frac{E_\perp}{U_M}. \tag{A.11}$$

Appendix B

Current density in the ring current

For the case of no gravity force, no inertia force and steady fields, the current density perpendicular to the magnetic field $\boldsymbol{J}_\perp$ can be express as [*Parker*, 1957]

$$\boldsymbol{J}_\perp = \boldsymbol{J}_M + \boldsymbol{J}_R + \boldsymbol{J}_B, \tag{B.1}$$

where $\boldsymbol{J}_M, \boldsymbol{J}_R$ and $\boldsymbol{J}_B$ are the magnetization current, the curvature drift current and the grad-B drift current, respectively.

B.1 Magnetization current

Considering loop currents produced by the Larmor motion of charged particles in a locally uniform field, the net currents appears only at the edge of a small surface C. Therefore

the net current penetrating the small surface C is given by

$$\begin{aligned} I &= \oint -n(\pi r_L^2 \boldsymbol{b}) \cdot \frac{\omega}{2\pi} q d\boldsymbol{l} \\ &= -\int \nabla \times \left(n\pi r_L^2 \boldsymbol{b} \frac{\omega}{2\pi} q \right) \cdot d\boldsymbol{S} \\ &\equiv \int \boldsymbol{J}_M \cdot d\boldsymbol{S}, \end{aligned} \tag{B.2}$$

where $n, r_L, \boldsymbol{b}, \omega, d\boldsymbol{l}, d\boldsymbol{S}$ and q are the number density, the Larmor radius, a unit vector of the local magnetic field, the gyro angular velocity, a line element around the surface C, the area of the surface C and charge, respectively. Then the magnetization current J_M is given by

$$\begin{aligned} \boldsymbol{j}_M &= -\nabla \times \left(n \cdot \frac{1}{2} m v_\perp^2 \cdot \frac{\boldsymbol{B}}{B^2} \right) \\ &= -\nabla \times \left(P_\perp \frac{\boldsymbol{B}}{B^2} \right), \qquad \text{(B.3)} \\ &= -\nabla P_\perp \times \frac{\boldsymbol{b}}{B} - P_\perp \nabla \frac{1}{B} \times \boldsymbol{b} - \frac{P_\perp}{B} (\nabla \times \boldsymbol{b}), \qquad \text{(B.4)} \end{aligned}$$

where m is mass and B is the local magnetic field.

B.2 Curvature drift current

The centrifugal force due to a curved mangetic field is

$$\boldsymbol{F}_R = \frac{m v_\parallel^2}{R^2} \boldsymbol{R}, \tag{B.5}$$

where $\boldsymbol{R}$ is the position vector. The drift velocity owning to the centrifugal force $\boldsymbol{v}_R$ is deduced as

$$\begin{aligned}
\boldsymbol{v}_R &= \frac{\boldsymbol{F}_R \times \boldsymbol{B}}{qB^2} \\
&= \frac{mv_{\parallel}^2 \boldsymbol{R} \times \boldsymbol{B}}{qB^2R^2} \\
&= -\frac{mv_{\parallel}^2}{qB^3}\nabla_{\perp}B \times \boldsymbol{B} \\
&= \frac{mv_{\parallel}^2}{qB^4}\boldsymbol{B} \times (\boldsymbol{B}\cdot\nabla)\boldsymbol{B}
\end{aligned}$$

where $P_{\perp}$ and $P_{\parallel}$ are the plasma pressure peppendicular to the magnetic field and the pressure parallel to the magnetic field, respectively. Then the curvature drift current density $\boldsymbol{J}_R$ is given by

$$\boldsymbol{J}_R = \frac{P_{\parallel}}{B^4}\boldsymbol{B} \times (\boldsymbol{B}\cdot\nabla)\boldsymbol{B}. \tag{B.6}$$

B.3 Grad-B drift current

Since the drift velocity due to grad-B $\boldsymbol{v}_B$ is expressed as

$$\boldsymbol{v}_B = -\frac{\frac{1}{2}mv_{\perp}^2\nabla B \times \boldsymbol{B}}{qB^3}, \tag{B.7}$$

the grad-B drift current $\boldsymbol{J}_B$ becomes

$$\boldsymbol{J}_B = \frac{P_{\perp}}{B^3}\boldsymbol{B} \times \nabla B. \tag{B.8}$$

B.4 Total currents

After summing up the three currents, the total perpendicular current $\boldsymbol{J}_\perp$ is obtained as

$$\begin{aligned}
\boldsymbol{J}_\perp &= \boldsymbol{J}_M + \boldsymbol{J}_R + \boldsymbol{J}_B \\
&= -\nabla P_\perp \times \frac{\boldsymbol{b}}{B} - P_\perp \nabla \frac{1}{B} \times \boldsymbol{b} - \frac{P_\perp}{B}(\nabla \times \boldsymbol{b}) + \frac{P_\parallel}{B^4}\boldsymbol{B} \times (\boldsymbol{B}\cdot\nabla)\boldsymbol{B} + \frac{P_\perp}{B^3}\boldsymbol{B} \times \nabla B \\
&= \frac{1}{B^2}\boldsymbol{B} \times \nabla P_\perp - \frac{P_\perp}{B^3}\boldsymbol{B} \times \nabla B - \frac{P_\perp}{B^4}\boldsymbol{B} \times (\boldsymbol{B}\cdot\nabla)\boldsymbol{B} \\
&+ \frac{P_\parallel}{B^4}\boldsymbol{B} \times (\boldsymbol{B}\cdot\nabla)\boldsymbol{B} + \frac{P_\perp}{B^3}\boldsymbol{B} \times \nabla B \\
&= \frac{\boldsymbol{B}}{B^2} \times \left[\nabla P_\perp + \frac{P_\parallel - P_\perp}{B^2}(\boldsymbol{B}\cdot\nabla)\,\boldsymbol{B}\right]. \qquad \text{(B.9)}
\end{aligned}$$

References

Aggson, T. L., J. P. Heppner, N. C. Maynard, Observations of large magnetospheric electric fields during the onset phase of a substorm *J. Geophys. Res.*, **88**, 3981-3990, 1983

Akasofu, S. -I., Energy coupling between the solar wind and the magnetosphere, *Space Sci. Rev.*, **28**, 111, 1981

Akasofu, S. -I., and S. Chapman, The ring current, geomagnetic disturbance, and the Van Allen radiation belts, *J. Geophys. Res.*, **66**, 1321-1350, 1961

Akasofu, S. -I, J. C. Cain, and S. Chapman, The magnetic field of a model radiation belt, numerically computed, *J. Geophys. Res.*, **66**, 4013-4026, 1961

Arnoldy, R. L., and K. W. Chan, Particle substorms observed at geostationary orbit, *J. Geophys. Res.*, **74**, 5019, 1969

Banks, P. M. and G. Kockarts, *Aeronomy*, Part B, Academic Press, New York, 192, 1973

Baker, D. N., P. R. Higbie, E. W. Hones, Jr., and R. D. Belian, High-resolution energetic particle measurements at 6.6 Re, 3. Low-energy electron anisotropies and short-term

substorm predictions, *J. Geophys. Res.*, **83**, 4863-4868, 1978

Baumjohann, W., Near-earth plasma sheet dynamics, *Adv. Space Res.*, **18**, (8)27-(8)33, 1996

Baumjohann, W., G. Paschmann, and C. A. Cattell, Average plasma properties in the central plasma sheet, *J. Geophys. Res.*, **94**, 6597-6606, 1989

Baumjohann, W., G. Paschmann, T. Nagai, and H. Luhr, Superposed epoch analysis of the substorm plasma sheet, *J. Geophys. Res.*, **96**, 11605-11608, 1991

Belian, R. D., D. N. Baker, P. R. Higbie, and W. W. Hones, Jr., High-resolution energetic particle measurements at 6.6 Re, 2. High-energy proton drift echos, *J. Geophys. Res.*, **83**, 4857-4862, 1978

Berko, F. W., L. J. Chahill, Jr., and T. A. Fritz, Protons as the prime contributors to storm time ring current, *J. Geophys. Res.*, **80**, 3549-3552, 1975

Beutier, J. -A. Sauvaud, D. Boscher, and S. Bourdarie, Global imaging by energetic neutral particles, *Geophys. Monogr. Ser.*, Vol. 97, edited by J. F. Lemaire, D. Heynderickx, and D. N. Baker, pp. 281-284, AGU, Washington, D. C., 1996

Bilitza, D., International reference ionosphere: recent developments, *Radio Sci.*, **21**, 343-346, 1986

Birn, J., M. F. Thomsen, J. E. Borovsky, G. D. Reeves, D. J. McComas, and R. D. Belian, Characteristic plasma properties during dispersionless substorm injections at geosynchronous orbit, *J. Geophys. Res.*, **102**, 2309-2324, 1997a

Birn, J., M. F. Thomsen, J. E. Borovsky, G. D. Reeves, D. J. McComas, R. D. Belian, M. Hesse, Substorm ion injections: Geosynchronous observatoins and test orbits in three-dimensional dynamic MHD fields, *J. Geophys. Res.*, **102**, 2325-2341, 1997b

Birn, J., M. F. Thomsen, J. E. Borovsky, G. D. Reeves, D. J. McComas, R. D. Belian, M. Hesse, Substorm electron injections: Geosynchronous observations and test particle simulations, *J. Geophys. Res.*, **103**, 9235-9248, 1998

Bishop, J., Multiple charge exchange and ionization collisions within the ring current-geocorona-plasmasphere system: Generation of a secondary ring current on inner L shells, *J. Geophys. Res.*, **101**, 17325-17336, 1996

Borovsky, J. E., M. F. Thomsen, and D. J. McComas, The superdense plasma sheet: Plasmaspheric origin, solar wind origin, or ionospheric origin?, *J. Geophys. Res.*, **102**, 22089-22097, 1997

Bourdarie, S., D. Boscher, T. Beutier, J. -A. Sauvaud, M. Blanc, Electron and proton radiation belt dynamic simulations during storm periods: A new asymmetric convection-diffusion model, *J. Geophys. Res.*, **102**, 17541-17552, 1997

Brice, N. M., Bulk motion of the magnetosphere, *J. Geophys. Res.*, **72**, 5193-5211, 1967

Burton, R. K., R. L. McPherron, and C. T. Russell, An empirical relationship between interplanetary conditions and Dst, *J. Geophys. Res.*, **80**, 4204, 1975

Cahill, Jr., L. J., Inflation of the inner magnetosphere during a magnetic storm, *J. Geophys. Res.*, **71**, 4505-4519, 1966

Cahill, Jr., L. J., Magnetic storm inflation in the evening sector, *J. Geophys. Res.*, **78**, 4724-4730, 1973

Cahill, Jr., L. J., and Y. C. Lee, Development of four magnetic storms in February 1972, *Planet. Space Sci.*, **23**, 1279-1292, 1975

Chapman, S., Earth storms: retrospect and prospect, *J. Phys. Soc. Jpn.*, **17**, 6-, 1962

Carpenter, D. L., New experimental evidence of the effect of magnetic storms on the magnetosphere, *J. Geophys. Res.*, **67**, 135-145, 1962

Carpenter, D. L., Whistler evidence of a 'knee' in the magnetospheric ionization density profile, *J. Geophys. Res.*, **68**, 1675-1682, 1963

Carpenter, D. L., Whistler studies of the plasmapause in the magnetosphere, *J. Geophys. Res.*, **71**, 693-709, 1966

Carpenter, D. L., Some aspects of plasmapause probing by whistlers, *Radio Sci.*, **18**, 917, 1983

Carpenter, D. L., and R. R. Anderson, An ISEE/Whistler model of equatorial electron density in the magnetosphere, *J. Geophys. Res.*, **97**, 1097-1108, 1992

Carpenter, D. L., and C. R. Chappell, Satellite studies of magnetospheric substorms on August 15, 1968. 3. Some features of magnetospheric convection, *J. Geophys. Res.*, **78**, 3062-3067, 1973

Chamberlain, J. W., Planetary coronae and atmospheric evaporation, *Planet. Space Sci.*, **11**, 901-960, 1963

Chamberlain, J. W., Charge exchange in a planetary corona: Its effect on the distribution and escape of hydrogen, *J. Geophys. Res.*, **82**, 1-9, 1977

Chandler, M. O., and C. R. Chappell, Observations of the flow of H^+ and He^+ along magnetic field lines in the plasmasphere, *J. Geophys. Res.*, **91**, 8847-8860, 1986

Chappell, C. R., Detached plasma regions in the magnetosphere, *J. Geophys. Res.*, **79**, 1861, 1974

Chappell, C. R., Initial observations of thermal plasma composition and energetics from Dynamics Explorer-1, *Geophys. Res. Lett.*, **9**, 929-932, 1982

Chappell, C. R., K. K. Harris and G. W. Sharp, A study of the influence of magnetic activity on the location of the plasmapause as measured by Ogo 5, *J. Geophys. Res.*, **75**, 50, 1970a

Chappell, C. R., K. K. Harris and G. W. Sharp, The morphology of the bulge region of the plasmasphere, *J. Geophys. Res.*, **75**, 3848-3861, 1970b

Chappell, C. R., K. K. Harris, and G. W. Sharp, Day side plasmasphere measurements, *J. Geophys. Res.*, **76**, 7631, 1971

Chen, A. J., Penetration of low-energy protons deep into the magnetosphere, *J. Geophys. Res.*, **75**, 2458-2467, 1970

Chen, A. J., and J. M. Grebowsky, Plasma tail interpretations of pronounced detached plasma regions measured by Ogo 5, *J. Geophys. Res.*, **79**, 3851-3855, 1974

Chen, A. J., J. M. Grebowsky, and H. A. Taylor, Jr., Dynamics of mid-latitude light ion trough and plasma tails, *J. Geophys. Res.*, **80**, 968-976

Chen, A. J., and R. A. Wolf, Effects on the plasmasphere of a time-varying convection electric field, *Planet. Space Sci.*, **20**, 483-509, 1972

Chen, M. W., L. R. Lyons, and M. Schulz, Simulations of phase space distributions of storm time proton ring current, *J. Geophys. Res.*, **99**, 5745-5759, 1994

Chen, M. W., J. L. Roeder, J. F. Fennell, L. R. Lyons, and M. Schulz, *J. Geophys. Res.*, **103**, 165-178, 1998

Chen, M. W., M. Schulz, and L. R. Lyons, Modeling of ring current formation and decay: A review, in *Magnetic Storms, Geophys. Monogr. Ser.*, Vol. 98, edited by B. T. Tsurutani, W. D. Gonzalez, Y. Kamide, and J. K. Arballo, AGU, Washington, DC, 1997

Chen, M. W., M. Schulz, L. R. Lyons, and D. J. Gorney, Stormtime transport of ring current and radiation belt ions, *J. Geophys. Res.*, **98**, 3835-3849, 1993

Cladis, J. B. and W. E. Francis, The polar ionosphere as a source of the storm time ring current, *J. Geophys. Res.*, **90**, 3465-3473, 1985

Comfort, R. H., J. H. Waite, Jr., and C. R. Chappell, Thermal ion temperatures from the retarding ion mass spectrometer on DE 1, *J. Geophys. Res.*, **90**, 3475-3486, 1985

Cowley, S. W. H, Energy transport and dissipation, paper

Cowley, S. W. H., and M. Ashour-Abdalla, Adiabatic plasma convection in a dipole field: Proton forbidden-zone effects for a simple electric field model, *Planet. Space Sci.*, **24**, 821-833, 1976

Daglis, I. A., The role of magnetosphere-ionosphere coupling in magnetic storm dynamics, in *Magnetic Storms, Geophys. Monogr. Ser.*, vol. 98, edited by B. T. Tsurutani, W. D. Gonzalez, Y. Kamide, and J. K. Arballo, pp. 107-116, AGU, Washington, D. C., 1997

Daglis, I. A., W. I. Axford, Fast ionospheric response to enhanced activity in geospace: Ion feeding of the inner magnetotail, *J. Geophys. Res.*, **101**, 5047-5065, 1996

Daglis, I. A., S. Livi, E. T. Sarris and B. Wilken, Energy density of ionospheric and solar wind origin ions in the near-Earth magnetotail during substorms, *J. Geophys. Res.*, **99**, 5691-5703, 1994

De Michelis, P., I. A. Daglis, and G. Consolini, Average terrestrial ring current derived from AMPTE/CCE-CHEM measurements, *J. Geophys. Res.*, **102**, 14103-14111, 1997

Delcourt, D. C., J. A. Sauvaud, and T. E. Moore, Cleft contribution to ring current formation, *J. Geophys. Res.*, **95**, 20937-20943, 1990

Dessler, A. J., and E. N. Parker, Hydrodynamic theory of geomagnetic storms, *J. Geophys. Res.*, **64**, 2239-2252, 1959

Doyle, M. A., and W. J. Burke, S^3-2 measurements of the polar cap potential, *J. Geophys. Res.*, **88**, 9125, 1983

Ebihara, Y., and M. Ejiri, Modeling of solar wind control of the ring current buildup: A case study of the magnetic storms in April 1997, *Geophys. Res. Lett.*, **25**, 3751-3754, 1998

Ebihara, Y., M. Ejiri, and H. Miyaoka, Enhancements of differential flux of energetic particles in the inner magnetosphere associated with a magnetic storm, *Proc. NIPR Symp. Upper Atmos. Phys.*, **11**, 150-153, 1998a

Ebihara, Y., M. Ejiri, and H. Miyaoka, Coulomb lifetime of the ring current ions with time varying plasmasphere, *Earth Planet. Space*, **50**, 371-382, 1998b

Ebihara, Y., M. Ejiri, and H. Miyaoka, Simulation on ring current formation: A case study of a storm on February 13, 1972 *Proc. NIPR Symp. Upper Atmos. Phys.*, **12**, in press, 1998c

Ebihara, Y., H. Miyaoka, F. Tohyama and M. Ejiri, Loss effects for energetic protons associated with a magnetic storm in the inner magnetosphere, *Proc. NIPR Symp. Upper Atmos. Phys.*, **10**, 16-28, 1997

Ejiri, M., Trajectory traces of charged particles in the magnetosphere, *J. Geophys. Res.*, **83**, 4798-4810

Ejiri, M., R. A. Hoffman, and P. H. Smith, The convection electric field model for the magnetosphere based on Explorer 45 observations, *J. Geophys. Res.*, **83** 4798-4810,

1978

Ejiri, M., R. A. Hoffman, and P. H. Smith, Energetic particle penetrations into the inner magnetosphere, *J. Geophys. Res.*, **85**, 653-663, 1980

Ejiri, M., K. Tsuruda, Y. Watanabe, A. Nishida and T. Obayashi, Impedance and electric field observations in the magnetosphere with satellite JIKIKEN(EXOS-B), *J. Geomag. Geoelectr.*, **33**, 101-110, 1981

Elphic, R. C., M. F. Thomsen, and J. E. Borovsky, The fate of the outer plasmasphere, *Geophys. Res. Lett.*, **24**, 365-368, 1997

Fennel, J. F., D. R. Croley, Jr., and S. M. Kaye, Low-energy ion pitch angle distributions in the outer magnetosphere: Ion zipper distributions, *J. Geophys. Res.*, **86**, 3375-3382, 1981

Fok, M. -C., J. U. Kozyra and A. F. Nagy, Lifetime of ring current particles due to Coulomb collisions in the plasmasphere, *J. Geophys. Res.*, **96**, 7861-7867, 1991

Fok, M., -C., J. U. Kozyra, A. F. Nagy, C. E. Rasmussen, and G. V. Khazanov, Decay of equatorial ring current ions and associated aeronomical consequences, *J. Geophys. Res.*, **98**, 19381-19393, 1993

Fok, M. -C., T. E. Moore, J. U. Kozyra, G. C. Ho, and D. C. Hamilton, Three-dimensional ring current decay model, *J. Geophys. Res.*, **100**, 9619-9632, 1995

Fok, M. -C., Moore, T. E., and Greenspan, M. E., Ring current development during storm main phase, *J. Geophys. Res.*, **101**, 15311-15322, 1996

Frank, L. A., On the extraterrestrial ring current during geomagnetic storm, *J. Geophys. Res.*, **72**, 3753-3767, 1967

Gallagher, D. L., P. D. Craven, R. H. Comfort and T. E. Moore, On the azimuthal variation of core plasma in the equatorial magnetosphere, *J. Geophys. Res.*, **100**, 23597-23605, 1995

Geisler, J. E., On the limiting daytime flux of ionization into the protonosphere, *J. Geophys. Res.*, **72**, 81-85, 1967

Gonzalez, W. D., J. A. Joselyn, Y. Kamide, H. W. Krochl, G. Rostoker, B. T. Tsurutani, and V. M. Vasyliunas, What is a geomagnetic storm ?, *J. Geophys. Res.*, **99**, 5771-5792, 1994

Gonzalez, W. D., and F. S. Mozer, A quantitative model for the potential resulting from reconnection with an arbitrary interplanetary magnetic field, *J. Geophys. Res.*, **79**, 4186, 1974

Gonzalez, W. D., B. T. Tsurutani, A. L. C. Gonzalez, E. J. Smith, F. Tang, and S. -I. Akasofu, Solar wind-magnetosphere coupling during intense magnetic storms (1978-1979), *J. Geophys. Res.*, **94**, 8835, 1989

Grebowsky, J. M., and A. J. Chen, Effects of convection electric field on the distribution of ring current type protons, *Planet. Space Sci.*, **23**, 1045-1052, 1975

Grebowsky, J. M., Y. Tulunay and A. J. Chen, Temporal variations in the dawn and dusk midlatitude trough and plasmapause, *Planet. Space Sci.*, **22**, 1089-1099, 1974

Groeckler, G., N. K. Bewtra, P. J. Denatale, P. H. Smitih, and R. A. Hoffman, Software systems for Explorer 45 (S^3-A) data analysis, *NASA/GSFC X Doc.*, 626-75-286, November 1975

Gloeckler, G., F. M. Ipavich, W. Studemann, B. Wilken, D. C. Hamilton, G. Kremser, D. Hovestadt, F. Gliem, R. A. Lundgren, W. Rieck, E. O. Tums, J. C. Cain, L. S. Masung, W. Weiss, P. Winterhof, The charge-energy-mass spectrometer for 0.3-300 keV/e ions on the AMPTE CCE, *IEEE Trans. on Geosci. and Remote Sensing*, **GE-23**, 234-240, 1985a

Groeckler, G., B. Wilken, W. Studemann, F. M. Ipavich, D. Hovestadt, D. C. Hamilton, and G. Kremser, First composition measurement of the bulk of the storm-time ring current (1 to 300 keV/e) with AMPTE-CCE, *Geophys. Res. Lett.*, **12**, 325-328, 1985b

Guiter, S. M., T. I. Gombosi and C. E. Rasmussen, Two-stream modeling of plasmaspheric refilling, *J. Geophys. Res.*, **100**, 9519-9526, 1995

Hamilton, D. C., G. Gloeckler, F. M. Ipavich, W. Studemann, B. Wilken and G. Kremser, Ring current development during the great geomagnetic storm of February 1986, *J. Geophys. Res.*, **93**, 14343-14355, 1988

Hedin, A. E., MSIS-86 thermospheric model, *J. Geophys. Res.*, **92**, 4649-4662, 1987

Hedin, A. E., Extension of the MSIS thermosphere model into the middle and lower atmosphere, *J. Geophys. Res.*, **96**, 1159-1172, 1991

Henderson, M. G., G. D. Reeves, H. E. Spence, R. B. Sheldon, A. M. Jorgensen, J. B. Blake, and J. F. Fennell, *Geophys. Res. Lett.*, **24**, 1167-1170, 1997

Higel, B., and L. Wu, Electron density and plasmapause characteristics at 6.6 Re: A statistical study of the GEOS 2 relaxation sounder data, *J. Geophys. Res.*, **89**, 1583-1601, 1984

Hoffman, R. A., and P. A. Bracken, Magnetic effects of the quiet-time proton belt, *J. Geophys. Res.*, **70**, 3541-3556, 1965

Hoffman, R. A., and P. A. Bracken, Higher-order ring currents and particle energy storage in the magnetosphere, *J. Geophys. Res.*, **72**, 6039-6049, 1967

Hoffman, R. A., and L. J. Cahill, Jr., Ring current particle distributions derived from ring current magnetic field measurements, *J. Geophys. Res.*, **73**, 6711-6722, 1968

Hoffman, R. A., and W. H. Dodson, Light ion concentrations and fluxes during magnetically quiet times, *J. Geophys. Res.*, **85**, 626, 1990

Horwitz, J. L., L. H. Brace, R. H. Comfort, and C. R. Chappell, Dual-spacecraft measurements of plasmasphere-ionosphere coupling, *J. Geophys. Res.*, **91**, 11203-11216, 1986

Horwitz, J. L., R. H. Comfort and C. R. Chappell, A statistical characterization of plasmasphere density structure and boundary locations, atmosphere, *J. Geophys. Res.*, **95**, 7937-7947, 1990

Hudson, M. K., S. R. Elkington, J. G. Lyon, V. A. Marchenko, I. Roth, M. Temerin, J. B. Blake, M. S. Gussenhoven, and J. R. Wygant, Simulations of radiation belt formation during storm sudden commencements, *J. Geophys. Res.*, **102**, 14087-14102, 1997

Ipavich, F. M., A. B. Galvin, M. Scholer, G. Gloeckler, D. Hovestadt, and B. Klecker, Suprathermal O^+ and He^+ion behavior during the March 22, 1979 (CDAW 6), substorms, *J. Geophys. Res.*, **90**, 1263-1272, 1985

Janev, R. K. and J. J. Smith, Cross sections for collision processes of hydrogen atoms with electrons, protons, and multipli-charged ions, *Atomic and Plasma-Material Interaction Data for Fusion*, IAEA, **4**, 78-79, 1993

Jordanova, V. K., C. J. Farrugia, L. Janoo, J. M. Quinn, R. B. Torbert, K. W. Ogilvie, R. P. Lepping, J. T. Steinberg, D. J. McComas, and R. D. Belian, October 1995 magnetic cloud and accompanying storm activity: Ring current evolution, *J. Geophys. Res.*, **103**, 79-92, 1998

Jordanova, V. K., L. M. Kistler, J. U. Kozyra, G. V. Khazanov, and A. F. Nagy, Collisional losses of ring current ions, *J. Geophys. Res.*, **101**, 111-126, 1996

Jordanova, V. K., J. U. Kozyra, G. V. Khazanov, A. F. Nagy, C. E. Rasmussen, and M. -C. Fok, A bounce-averaged kinetic model of the ring current ion population, *Geophys. Res. Lett.*, **21**, 2785-2788, 1994

Kamide, Y., and N. Fukushima, Positive geomagnetic bays in evening high-latitudes and their possible connection with partial ring current, *Rep. Ionos. Space Res. Jpn.*, **25**,

125, 1971

Kan, J. R., and L. C. Lee, Energy coupling functions and solar wind-magnetosphere dynamic, *Geophys. Res. Lett.*, **6**, 577, 1979

Kaye, S. M., E. G. Shelley, R. D. Sharp, and R. G. Johnson, Ion composition of zipper events, *J. Geophys. Res.*, **86**, 3383-3388, 1981

Khazanov, G. V., M. A. Koen, Yu. V. Konikov and I. M. Sidorov, Simulation of ionosphere-plasmasphere coupling into account ion inertia and temperature anisotropy, *Planet. Space Sci.*, **32**, 585-598, 1984

Kistler, L. M., F. M. Ipavich, D. C. Hamilton, G. Gloeckler, B. Wilken, G. Kremser, and W. Stüdemann, Energy spectra of the major ion species in the ring current during geomagnetic storms, *J. Geophys. Res.*, **94**, 3579-3599, 1989

Kokubun, S., T. Yamamoto, M. H. Acuna, K. Hayashi, K. Shiokawa, and H. Kawano, The Geotail magnetic field experiment, *J. Geomag. Geoelectr.*, **46**, 7-21, 1994

Konradi, A., C. L. Semar, and T. A. Fritz, Substorm-injected protons and electrons and the injection boundary model, *J. Geophys. Res.*, **80**, 543-552, 1975

Korth, A., and R. H. W. Friedel, Dynamics of the near earth radiation environment: Observations over the whole CRRES mission, *AIP Conf. Proc., Workshop on the Earth's Trapped Particle Environment*, no.383, 19-24, 1996

Korth, A., and R. H. W. Friedel, Dynamics of energetic ions and electrons between L=2.5 and L=7 during magnetic storms, *J. Geophys. Res.*, **102**, 14113-14122, 1997

Kozyra, J. U., V. K. Jordanova, R. B. Horne, and R. M. Thone, Modeling of the contribution of electromagnetic ion cyclotron (EMIC) waves to stormtime ring current erosion, *Geophys. Monogr. Ser.*, Vol. 98, edited by B. T. Tsurutani, W. D. Gonzalez, Y. Kamide, and J. K. Arballo, pp. 187-202, AGU, Washington, D. C., 1997

Krimigis, S. M., G. Gloeckler, R. W. McEntire, T. A. Potemra, F. L. Scarf, and E. G. Shelley, Magnetic storm of September 4, 1984: A synthesis of ring current spectra and energy densities measured with AMPTE/CCE, *Geophys. Res. Lett.*, **12**, 329-332, 1985

Lee, L. C., G. Corrick, and S. -I. Akasofu, On the ring current energy injection rate, *Planet. Space Sci.*, **31**, 901-911, 1983

Lennartsson, W., and E. G. Shelley, Survey of 0.1- to 16-keV/e plasma sheet ion composition, *J. Geophys. Res.*, **91**, 3061-3076, 1986

Lepping, R. P., M. Acuna, L. Burlaga, W. Farrell, J. Slavin, K. Schatten, F. Mariani, N. Ness, F. Neubauer, Y. C. Whang, J. Byrnes, R. Kennon, P. Panetta, J. Scheifele, and E. Worley, The Wind Magnetic Field Investigation, *Space Sci. Rev.*, **71**, 207-229, 1995

Li, X., D. N. Baker, M. Temerin, T. E. Cayton, E. G. D. Reeves, R. A. Christensen, J. B. Blake, M. D. Looper, R. Nakamura, and S. G. Kanekal, Multisatellite observations of the outer zone electron variation during the November 3-4, 1993, magnetic storm, *J. Geophys. Res.*, **102**, 14123-14140, 1997

Li, W., J. J. Sojka and W. J. Raitt, A study of plasmaspheric density distributions for diffusive equilibrium conditions, *Planet. Space Sci.*, **31**, 1315-1327, 1983

Liemohn, H., The lifetime of radiation belt protons with energies between 1 keV and 1 MeV, *J. Geophys. Res.*, **66**, 3593-3595, 1961

Lin, J., J. L. Horwitz, G. R. Wilson, C. W. Ho and D. G. Brown, A semikinetic model for early stage plasmasphere refilling 2. effects of wave-particle interactions, *J. Geophys. Res.*, **97**, 1121-1134, 1992

Longanecker, G. W., and R. A. Hoffman, S^3-A spacecraft and experiment description, *J. Geophys. Res.*, **78**, 4711-4717, 1973

Lui, A. T. Y., Radial transport of storm time ring current ions, *J. Geophys. Res.*, **98**, 209-214, 1993

Lui, A. T. Y., D. C. Hamilton, Radial profiles of quiet time magnetosphere parameters, *J. Geophys. Res.*, **97**, 19325-19332, 1992

Lui, A. T. Y., R. W. McEntire, and S. M. Krimigis, Evolution of the ring current during two geomagnetic storms, *J. Geophys. Res.*, **92**, 7459-7470, 1987

Lui, A. T. Y., D. J. Williams, E. C. Roelof, R. W. McEntire, and D. G. Mitchell, First composition measurements of energetic neutrals, *Geophys. Res. Lett.*, **23**, 2641-2644, 1996

Lyons, L. R., and D. S. Evans, 'The inconsistency between proton charge exchange and the observed ring current decay, *J. Geophys. Res.*, **81**, 6197-6200, 1976

Lyons, L. R., and M. Schulz, Access of energetic particles to storm time ring current through enhanced radial "diffusion", *J. Geophys. Res.*, **94**, 5491-5496, 1989

Lyons, L. R., and R. M. Thone, and C. F. Kennel, Pitch-angle diffusion of radiation belt electrons within the plasmasphere, *J. Geophys. Res.*, **77**, 3455-3474, 1972

Lyons, L. R., and D. J. Williams, A source for the geomagnetic storm main phase ring current, *J. Geophys. Res.*, **85**, 523-530, 1980

Marubashi, K. and J. M. Grebowsky, A model study of diurnal behavior of the ionosphere and the protonosphere coupling, *J. Geophys. Res.*, **81**, 1700-1706, 1976

Maynard, N. C., W. J. Burke, E. M. Basinska, G. M. Erickson, W. J. Hughes, H. J. Singer, A. G. Yahnin, D. A. Hardy, and F. S. Mozer, Dynamics of the inner magnetosphere near times of substorm onsets, *J. Geophys. Res.*, **101**, 7705-7736, 1996

Maynard, N. C., and A. J. Chen, Isolated cold plasma regions: observations and their relation to possible production mechanisms, *J. Geophys. Res.*, **80**, 1009-1013, 1975

Maynard, N. C., and J. M. Grebowsky, The plasmapause revisited, *J. Geophys. Res.*, **82**, 1591, 1977

Mayr, H. G., J. M. Grebowsky and H. A. Taylor, Jr., Study of the thermal plasma on closed field lines outside the plasmasphere, *Planet. Space Sci.*, **18**, 1123-1135, 1970

McIlwain, C. E., Coordinates for mapping the distribution of magnetically trapped particles, *J. Geophys. Res.*, **66**, 3681-3691, 1961

Mewaldt, R. A., R. S. Selesnick, and J. R. Cummings, Anomalous cosmic rays: The principal source of high energy heavy ions in the radiation belts, *Geophys. Monogr. Ser.*, Vol. 97, edited by J. F. Lemaire, D. Heynderickx, and D. N. Baker, pp. 35-41, AGU, Washington, D. C., 1996

Moffett, R. J. and J. A. Murphy, Coupling between the F-region and protonosphere: numerical solution of the time-dependent equations, *Planet. Space Sci.*, **21**, 43-52, 1973

Moldwin, M. B., M. F. Thomsen, S. J. Bame, D. McComas and G. D. Reeves, The fine-scale structure of the outer plasmasphere, *J. Geophys. Res.*, **100**, 8021-8029, 1995

Mukai, T., S. Machida, Y. Saito, M. Hirahara, T. Terasawa, N. Kaya, T. Obara, M. Ejiri, and A. Nishida, The low energy particle (LEP) experiment onboard the GEOTAIL satellite, *J. Geomag. Geoelectr.*, **46**, 669-92, 1994

Nagai, T., J. L. Horwitz, R. R. Anderson, and C. R. Chappell, Structure of the plasmapause from ISEE 1 low-energy ion and plasma wave observations, *J. Geophys. Res.*, **90**, 6622-6626, 1985

Nishida, A., Formation of plasmapause, or magnetospheric plasma knee, by the combined action of magnetospheric convection and plasma escape from the tail, *J. Geophys. Res.*, **71**, 5669-5679, 1966

Noël, S., Decay of the magnetospheric ring current: A Monte Carlo simulation, *J. Geophys. Res.*, **102**, 2301-2308, 1997

Northrop, T. G, The adiabatic motion of charged particles, Interscience publishers, New York, 1963

Obara. T., T. Nagatsuma, M. Den, and E. Sagawa, Enhancement of the trapped radiation electrons at 6.6 Re during the storm recovery phase — Results from analysis of GMS/SEM —, *Proc. NIPR Symp. Upper Atmos. Phys.*, **12**, in press, 1998

Ogilvie, K. W., D. J. Chorney, R. J. Fitzenreiter, F. Hunsaker, J. Keller, J. Lobell, G. Miller, J. D., Scudder, E. C. Sittler Jr., R. B. Torbert, D. Bodet, G. Needell, A. J. Lazarus, J. T. Steinberg, J. H., Tappan, A. Mavretic, and E. Gergin, SWE, a comprehensive plasma instrument for the Wind spacecraft, *Space Sci. Rev.*, **71**, 55-77, 1995

Olsen, R. C., C. R. Chappell, D. L. Gallagher, J. L. Green, and D. A. Gurnett, The hidden ion populations: Revisited, *J. Geophys. Res.*, **90**, 12121, 1985

Olsen, R. C., S. D. Shawhan, D. L. Gallagher, J. L. Green, C. R. Chappell and R. R. Anderson, Plasma observations at the Earth's magnetic equator, *J. Geophys. Res.*, **92**, 2385-2407, 1987

Paterson, W. R., L. A. Frank, S. Kokubun, and T. Yamamoto, Geotail survey of ion flow in the plasma sheet: Observations between 10 and 50 Re, *J. Geophys. Res.*, **103**, 11811-11825, 1998

Park, C. G., Some features of plasma distribution in the plasmasphere deduced from antarctic whistlers, *J. Geophys. Res.*, vol79, 169-173, 1974

Pedersen, A., C. A. Cattell, C. -G. Fälthammar, K. Knott, P. -A. Lindqvist, R. H. Manka, and F. S. Mozer, Electric fields in the plasma sheet and plasma sheet boundary layer, *J. Geophys. Res.*, **90**, 1231-1242, 1985

Peroomian, Vahé, and M. Ashour-Abdalla, Population of the near-earth magnetotail from the auroral zone, *J. Geophys. Res.*, **101**, 15387-15401, 1996

Peterson, W. K., R. D. Sharp, E. G. Shelley, and R. G. Johnson, H. Balsiger, Energetic ion composition of the plasma sheet, *J. Geophys. Res.*, **96**, 761-767, 1981

Prülss, decay of the magnetic storm ring current by the charge-exchange mechanism, *Planet. Space Sci.*, **21**, 983-992, 1973

Potemra, T. A., L. J. Zanetti, and M. H. Acuna, AMPTE/CCE magnetic field studies of the September 4, 1984 storm, *Geophys. Res. Lett.*, **12**, 313-316, 1985

Pulkkinen, T. I., D. N. Baker, R. J. Pellinen, J. Büchner, H. E. J. Koskinen, R. E. Lopez, R. L. Dyson, and L. A. Frank, Particle scattering and current sheet stability in the geomagnetic tail during the substorm growth phase, *J. Geophys. Res.*, **97**, 19283-19297, 1992

Pulkkinen, T. I., D. N. Baker, P. K. Toivanen, R. J. Pellinen, R. H. W. Friedel, and A. Korth, Magnetospheric field and current distributions during the substorm recovery phase, *J. Geophys. Res.*, **99**, 10955-10966, 1994

Rairden, R. L, L. A. Frank, and J. D. Craven, Geocoronal imaging with Dynamics Explorer, *J. Geophys. Res.*, **91**, 13613-13630, 1986

Raitt, W. J., R. W. Schunk and P. M. Banks, A comparison of the temperature and density structure in high and low speed thermal proton flows, *Planet. Space Sci.*, **23**, 1103-1117, 1975

Rasmussen, C. E., S. M. Guiter and S. G. Thomas, A two-dimensional model of the plasmasphere: refilling time constants, *Planet. Space Sci.*, **41**, 35-43, 1993

Reasoner, D. L., P. D. Craven, and C. R. Chappell, Characteristics of low-energy plasma in the plasmasphere and plasma trough, *J. Geophys. Res.*, **88**, 7913-7925, 1983

Reiff, P. H., R. W. Spiro, and T. W. Hill, Dependence of polar cap potential drop on interplanetary parameters, *J. Geophys. Res.*, **86**, 7639-7648, 1981

Richards, P. G. and D. G. Torr, Seasonal, diurnal, and solar cyclical variations of the limiting H^+flux in the Earth's topside ionosphere, *J. Geophys. Res.*, **90**, 5261-5268, 1985

Riley, P., and R. A. Wolf, Comparison of diffusion and particle drift descriptions of radial transport in the earth's inner magnetosphere, *J. Geophys. Res.*, **97**, 16865-16876, 1992

Roeder, J. L., J. F. Fennell, M. W. Chen, M. Grande, S. Livi and M. Schulz, CRRES observations of stormtime ring current ion composition, *AIP Conf. Proc., Workshop on the Earth's Trapped Particle Environment*, no.383, 131-135, 1996

Roederer, J. G., Dynamics of geomagnetically trapped radiation, Springer-Verlag, Berlin Heidelberg, 1970

Roelof, E. C., Energetic neutral atom image of a storm-time ring current, *Geophys. Res. Lett.*, **14**, 652, 655, 1987

Roelof, E. C., and D. G. Sibeck, Magnetopause shapes as a bivariate function of interplanetary magnetic field Bz and solar wind dynamic pressure, *J. Geophys. Res.*, **98**, 21421-21450, 1993

Rostoker, G., Geomagnetic indices, *Rev. Geophys.*, **10**, 935, 1972

Sckopke, N., A general relation between the energy of trapped particles and the disturbance field near the earth, *J. Geophys. Res.*, **71**, 3125-3130, 1966

Sharp, R. D., W. Lennartsson, W. K. Peterson and E. G. Shelley, The origins of the plasma in the distant plasma sheet, *J. Geophys. Res.*, **87**, 10420-10424, 1982

Sheldon, R. B., and D. C. Hamilton, Ion transport and loss in the earth's quiet ring current. 1. Data and standard model *J. Geophys. Res.*, **98**, 13491-13508, 1993

Shue, J. -H, J. K. Chao, H. C. Fu, C. T. Russell, P. Song, K. K. Khurana, and H. J. Singer, A new functional form to study the solar wind control of the magnetopause size and shape, *J. Geophys. Res.*, **102**, 9497-9511, 1997

Sibeck, D. G., R. E. Lopez, and E. C. Roelof, Solar wind control of the magnetopause shape, location, and motion, *J. Geophys. Res.*, **96**, 5489-5495, 1991

Singh, N. and C. B. Chan, Effects of equatorially trapped ions on refilling of the plasmasphere, *J. Geophys. Res.*, **97**, 1167-1179, 1992

Smith, E. J., P. J. Coleman, D. L. Judge, and C. P. Sonett, Characteristics of the extraterrestrial current system: Explorer VI and Pioneer V, *J. Geophys. Res.*, **65**, 1958-1861, 1960

Smith, P. H., and N. K. Bewtra, Charge exchange lifetimes for ring current ions, *Space Sci. Rev.*, **22**, 301-318, 1978

Smith, P. H., N. K. Bewtra, and R. A. Hoffman, Inference of the ring current ion composition by means of charge exchange decay, *J. Geophys. Res.*, **86**, 3470-3480, 1981

Smith, P. H., and R. A. Hoffman, Ring current particle distributions during the magnetic storms of 16-18 December 1971, *J. Geophys. Res.*, **78**, 4731, 1973

Smith, P. H., and R. A. Hoffman, Direct observation in the dusk hours of the characteristics of the storm time ring current particles during the beginning of magnetic storms, *J. Geophys. Res.*, **79**, 966-967, 1974

Smith, P. H., R. A. Hoffman, and T. A. Fritz, Ring current proton decay by charge exchange, *J. Geophys. Res.*, **81**, 2701-2708, 1976

Solomon, J., and O. Picon, Charge exchange and wave-particle interaction in the proton ring current, *J. Geophys. Res.*, **86**, 3335-3344, 1981

Spreiter, J. R., and B. J. Hyett, The effect of a uniform external pressure on the boundary of the geomagnetic field in a steady solar wind, *J. Geophys. Res.*, **68**, 1631-1642, 1963

Stern, D. P., The motion of a proton in the equatorial magnetosphere, *J. Geophys. Res.*, **80**, 595-599, 1975

Swisher, R. L., and L. A. Frank, Lifetimes for low-energy protons in the outer radiation zone, *J. Geophys. Res.*, **73**, 5655-5672, 1968

Takahashi, S., T. Iyemori, and M. Takeda, A simulation of the storm-time ring current, *Planet. Space Sci.*, **38**, 1133-1141, 1990

Taylor, Jr., H. A., H. C. Brinton, and M. W. Pharo, III, Contraction of the plasmasphere during geomagnetically disturbed periods, *J. Geophys. Res.*, **73**, 961-968, 1968

Terasawa, T., M. Fujimoto, T. Mukai, I. Shinohara, Y. Saito, T. Yamamoto, S. Machida, S. Kokubun, A. J. Lazarus, J. T. Stenberg, and R. P. Lepping, Solar wind control of density and temperature in the near-earth plasma sheet: WIND/GEOTAIL collaboration, *Geophys. Res. Lett.*, **24**, 935-938, 1997

Thomsen, M. F., J. E. Borovsky, D. J. McComas and M. B. Moldwin, Observations of the Earth's plasmasheet at geosynchronous orbit, *AIP Conf. Proc., Workshop on the Earth's Trapped Particle Environment*, no.383, 25-31, 1996

Tinsley, B. A., Evidence that the recovery phase ring current consists of helium ions, *J. Geophys. Res.*, **81**, 6193-6195, 1976

Tobiska, K., Revised solar extreme ultraviolet flux model, *J. Atmos. Terr. Phys.*, **53**, 1005-1018, 1991

Tsyganenko, N. A., Global quantitative models of the geomagnetic field in the cislunar magnetosphere for different disturbance levels, *Planet. Space Sci.*, **35**, 1347-1358, 1987

Tsyganenko, N. A., A magnetospheric magnetic field model with a warped tail current sheet, *Planet. Space Sci.*, **37**, 5-20, 1989

Vasyliunas, V. M., J. R. Kan, G. L. Siscoe, and S. -I. Akasofu, Scaling relations governing magnetosphere energy transfer, *Planet. Space Sci.*, **30**, 359, 1982

Volland, H., A semiempirical model of large-scale magnetospheric electric fields, *J. Geophys. Res.*, **78**, 171-181

Watanabe, S., B. A. Whalen, and A. W. Yau, Thermal ion observations of depletion and refilling in the plasmaspheric trough, *J. Geophys. Res.*, **97**, 1081-1096, 1992

Wentworth, R. C., W. M. MacDonald and S. F. Singer, Lifetimes of trapped radiation belt particles determined by Coulomb scattering, *Phys. Fluids*, **2**, 499-509, 1959

Williams, D. J., Ring current composition and sources: An update, *Planet. Space Sci.*, **29**, 1195-1203, 1981

Williams, D. J., Exploration and understanding in space physics, *Geophys. Res. Lett.*, **12**, 303, 1985

Williams, D. J., J. F. Arens, and L. J. Lanzerotti, Observations of trapped electrons at low and high altitudes, *J. Geophys. Res.*, **73**, 5673-5696, 1968

Williams, D. J., and M. Sugiura, The AMPTE Charge Composition Explorer and the 4-7 September 1984 geomagnetic storm, *Geophys. Res. Lett.*, **12**, 305-308, 1985

Wilson, G. R., J. L. Horwitz and J. Lin, A semikinetic model for early stage plasmasphere refilling 1. effects of Coulomb collisions, *J. Geophys. Res.*, **97**, 1109-1119, 1992

Wodnicka, E. B., The magnetic storm main phase modeling, *Planet. Space Sci.*, **37**, 525-534, 1989

Wolf, R. A., J. W. Freeman, Jr., B. A. Hausman, R. W. Spiro, R. V. Hilmer, and R. L. Lambor, Modeling convection effects in magnetic storms, in *Magnetic Storms, Geophys. Monogr. Ser.*, Vol. 98, edited by B. T. Tsurutani, W. D. Gonzalez, Y. Kamide, and J. K. Arballo, AGU, Washington, DC, 1997

Yau, A. W., E. G. Shelley, W. K. Peterson, and L. Lenchyshyn, Energetic auroral and polar ion outflow at DE 1 altitudes: Magnitude, composition, magnetic activity dependence, and longterm variations, *J. Geophys. Res.*, **90**, 8417-8432, 1985

Young, D. T., H. Balsiger, and J. Geiss, Correlations of magnetospheric ion composition with geomagnetic and solar activity, *J. Geophys. Res.*, **87**, 9077-9096, 1982

Yokoyama, N, and Y. Kamide, Statistical nature of geomagnetic storms, *J. Geophys. Res.*, **102**, 14215-14222, 1997